Title

Continuum Modeling of Porous Electrodes for Electrochemical Synthesis

Journal

Chemical Reviews, 122(12)

ISSN

0009-2665

Authors

Bui, Justin C

Lees, Eric W

Pant, Lalit M

et al.

Publication Date

2022-06-22

DOI

10.1021/acs.chemrev.1c00901

Peer reviewed

Continuum modeling of porous electrodes for electrochemical synthesis

Justin C. Bui[1,2], Eric W. Lees[3,4], Lalit M. Pant[3,5], Iryna V. Zenyuk[6], Alexis T. Bell[1,2], and Adam Z. Weber[2]*

[1] Department of Chemical and Biomolecular Engineering
University of California, Berkeley
Berkeley, CA 94720, USA

[2] Liquid Sunlight Alliance
Lawrence Berkeley National Laboratory
Berkeley, CA 94720, USA

[3] Energy Technologies Area
Lawrence Berkeley National Laboratory
Berkeley, CA 94720, USA

[4]Department of Chemical and Biological Engineering
University of British Columbia
Vancouver, BC V6T 1Z3, Canada

[5]Department of Sustainable Energy Engineering
Indian Institute of Technology, Kanpur
Kanpur-208016, India

[6]Department of Chemical and Biomolecular Engineering
University of California, Irvine
Irvine, CA 92697, USA

Chemical Reviews
March 15th, 2022

*Corresponding Author
email: azweber@lbl.gov
phone : (510) 486-6308

Abstract

Electrochemical synthesis possesses substantial promise to utilize renewable energy sources to power the conversion of abundant feedstocks to value-added commodity chemicals and fuels. Of the potential system architectures for these processes, only systems employing 3-D structured porous electrodes have the capacity to achieve the high rates of conversion necessary for industrial scale. However, the phenomena and environments in these systems are not well understood and challenging to probe experimentally. Fortunately, continuum modeling is well-suited to rationalize the observed behavior in electrochemical synthesis, as well as to ultimately provide recommendations for guiding the design of next-generation electrochemical synthesis devices employing porous electrodes. In this Review, we begin by presenting a historical review of modeling of porous electrode systems, with the aim of showing how past knowledge of macroscale modeling can contribute to the rising challenge of electrochemical synthesis. We then present a detailed overview of the governing physics and assumptions required to simulate porous electrode systems for electrochemical synthesis. Leveraging the developed understanding of porous electrode theory, we survey and discuss the present literature on simulating multiscale phenomena in porous electrodes in order to demonstrate their relevance to understanding and improving the performance of devices for electrochemical synthesis. Lastly, we provide our perspectives regarding future directions in the development of models that can most accurately describe and predict the performance of such devices and discuss the best potential applications of future models.

Table of Contents

1. Introduction

Nearly 7% of anthropogenic carbon dioxide (CO_2) emissions come from the manufacturing of industrial chemicals (*e.g.,* plastics, ammonia, methanol), a consequence of the use of fossil-fuel-based feedstocks (natural gas and petroleum) for thermochemical synthesis.[1-4] Electrochemical synthesis—the conversion of low-value feedstocks to high-value products using electricity—could provide a means of eliminating these emissions, if the electricity is generated using renewable energy sources such as wind or solar irradiation.[5-8] However, improvements in efficiency and lifetime are needed for electrochemical synthesis to become cost-competitive with existing practices in the chemical industry.

One of the major challenges for the electrochemical synthesis of chemicals (nominally from CO_2 or CO) carried out in an aqueous electrolyte is the low rate of mass transfer of the reactant to the cathode. This is a direct consequence of both the low reactant solubility in water and its low mass-transfer coefficient, which is inversely proportional to the mass-transfer boundary-layer thickness. 3-D-structured porous electrodes can be used to overcome these challenges because they enable rapid mass transfer and enhanced contact between liquid, gas, and solid phases. However, tailoring the design of porous electrodes to specific applications is challenged by a lack of structure-property-performance relationships that are necessary for optimization. This gap arises due to the complex multiphase flow, mass transfer, and (electro)chemical reaction phenomena that control the performance of porous electrodes.

Physics-based continuum-based modeling is a key tool for designing porous electrodes because it can link device-scale performance (*e.g.* current density and reaction selectivity) to electrode properties and operating conditions. Historically, the development of electrochemical technologies (*e.g.* batteries, fuel cells, and water electrolyzers) have benefitted greatly from these

models and their ability to predict polarization behavior, product and reactant transport, and lifetime limitations, as have been discussed in numerous reviews.[9-16] These models are often complemented by experimental studies to provide fundamental physical insights that accelerate the design of efficient devices. Notwithstanding, the use of such detailed porous-electrode modeling has not yet been firmly established in the electrochemical synthesis community.

The electrochemical synthesis literature is primarily composed of experimental studies aimed at discovering new electrocatalysts[3, 17] or designing new reactor architectures.[18, 19] Density functional theory (DFT) models have also been widely employed to predict and explain the activity and selectivity of electrocatalysts.[20-22] Collectively, these research efforts have been documented in several reviews.[3, 17-19, 23, 24] However, the electrochemical synthesis community has not given significant attention to continuum modeling of porous electrodes. Moreover, there are no reviews summarizing this topic in the context of electrochemical synthesis. This review aims to fill this need by providing a tutorial on continuum models for porous electrodes, and linking those topics to applications in electrochemical synthesis.

The majority of this review focuses on electrochemical reduction of carbon dioxide (CO_2). CO_2 reduction (CO_2R) is an ideal model reaction for studying electrochemical synthesis in porous electrodes because of its wide product distribution and acute sensitivity to the chemical environment near the electrocatalyst.[25, 26] The transport of gases, liquids, and ions dictate this chemical environment, and, consequently, the performance of the electrochemical synthesis. An understanding of how to control the composition of this chemical environment is therefore critical to boosting catalytic activity. However, it is generally challenging to quantify experimentally the concurrent rates of mass transfer and (electro)chemical reactions during electrochemical synthesis because these processes span a wide range of length and time scales.

We show here how modeling can be used to correlate the dynamic chemical environment within porous electrodes with experimental observables, such as product distribution, total current density (i), and thermodynamic efficiency. The goal of these models is not only to enable the design of porous electrodes from first principles, but also to provide fundamental insights by identifying the roles of transport and reaction processes not accessible using current experimental methods.

This review is outlined as follows. First, we begin by presenting the history and motivation for modeling porous electrodes for electrochemical synthesis. Next, the general equations governing the thermodynamics, transport, and kinetics of these systems are discussed, along with a review of model parameterization for these systems. An electrochemical synthesis device is then deconstructed into its constitutive components (liquid electrolyte, polymer electrolyte including membrane separator, porous electrodes composed of a catalyst layer perhaps on a transport layer, reactant/product flow channels) with discourse focusing on models of the relevant multiphase, component-level phenomena across multiple length- and timescales. The electrolyte consists of a dissolved salt (usually aqueous) that supports ionic conduction. The polymer electrolyte is an ion-conducting polymer (ionomer) that enables separation of the evolved products while still maintaining ionic contact between and within the porous electrodes, where the electrochemical reactions take place. It is pertinent to note that the terms porous electrodes and catalyst layers are often used synonymously. The flow channels feed and distribute the reactants along the surface of the electrode and provide an outlet for the evolved products. The coupling of these phenomena into a comprehensive device model is then explored, with an emphasis on the impacts of device configuration. Next, computational methods for achieving these simulations are discussed, followed by examining the coupling of models of

various scales, temporally or spatially. Lastly, we explore future directions for continuum models, focusing on applications of machine learning in macroscale modeling to increase throughput and reduce the number of required model evaluations, as well as the coupling of models with topology optimization and advanced manufacturing methods to produce idealized architectures for electrochemical synthesis.

1.1 Motivation for Electrochemical Synthesis

The demand for industrial chemicals has rapidly grown over the past two decades and continues to increase (**Figure 1a**). Unfortunately, these processes largely rely on fossil-fuels as the primary energy source for driving high temperature and pressure thermochemical reactions, as well as being the reactants. Indeed, chemical manufacturing is responsible for 26% of global energy demand,[27, 28] and consequently, 875 Megatons per year of CO_2 emissions.[1, 4, 29-31] These CO_2 emissions are not only produced indirectly (as a result of combustion), but also directly as a byproduct of the chemical reaction. For example, several important industrial processes, such as ammonia (NH_3) and methanol (CH_3OH) synthesis, and petroleum hydrotreating, require hydrogen.[32] Since hydrogen is most commonly produced by steam reforming of natural gas, a significant amount CO_2 is emitted (5.5 ton_{CO2}/1 ton_{H2}). These aspects of thermochemical processes present significant challenges for reducing CO_2 emissions from the chemical industry. In particular, the generation of plastics (in particular, chemicals derived from petrochemicals that are precursors to plastic generation, such as ethylene), methanol, and ammonia, are responsible for the bulk of CO_2 emissions from the chemical industry (**Figure 1b**).

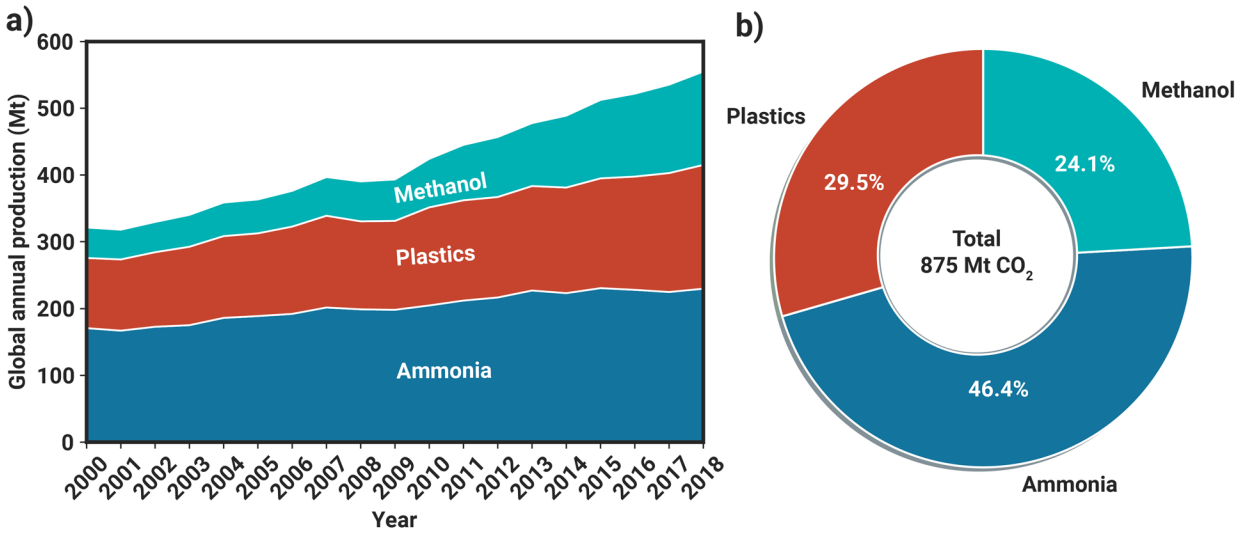

Figure 1: (a) Global annual production of primary chemical commodities from 2000-2018.[33-36] **(b)** Breakdown of total CO_2 emissions from the chemical industry in 2018.[36]

Electrochemical synthesis processes use electricity (instead of heat) to drive the formation of valuable products at more benign conditions than thermochemical processes, which could enable the direct use of renewable electricity in the chemical-manufacturing industry.[37] Moreover, electrochemical synthesis processes can source atomic building blocks such as hydrogen, carbon, nitrogen, and oxygen from air and water instead of using fossil resources to supply carbon and hydrogen.[6] It is notable, though, that there are relatively few commercialized electrochemical processes, with the largest being the Chloro-Alkali process, the industrial production of aluminum, and the organic electrochemical synthesis of adiponitrile (ADN) from acrylonitrile (AN).[37] Historically, this paucity of industrial electrochemical processes is due to the relatively high cost of electrical energy relative to thermal energy. (In 2020 the cost of natural gas was ca. 0.005$/kWh, whereas the cost for industrial electricity was 0.066 $/kWh).[28]

As renewable electricity prices decrease and incentives to reduce CO_2 emissions increase,[38-40] electrochemical synthesis is projected to disrupt the chemical industry.[27, 41] New electrochemical processes that convert N_2, CO_2, and water into the most widely used chemicals

(*e.g.* ethylene, ammonia) are rapidly being developed to replace the incumbent thermochemical processes (**Figure 2**).[42] However, even with carbon taxes, these processes still require considerable technological advancements in order to produce chemicals at industrially-relevant conditions and rates.[42-44]

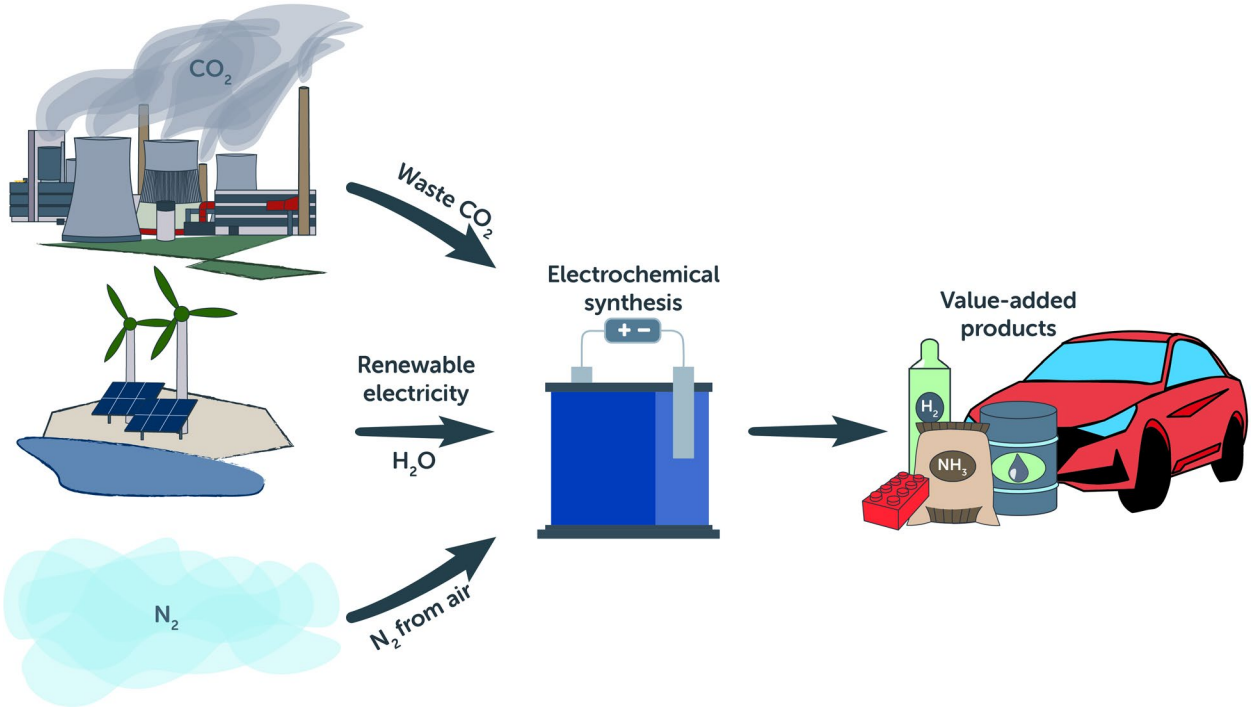

Figure 2: Schematic depiction of an ideal electrochemical synthesis process economy. Waste CO_2, along with H_2O, N_2 feedstocks are upconverted to value-added products using and renewable electricity via electrochemical synthesis.

1.2 Motivation for Porous Electrodes in Electrochemical Synthesis

The most widely deployed electrochemical processes (*e.g.* Chloro-Alkali and electrowinning) convert reactants that are soluble in the (aqueous) electrolyte (*e.g.* Cl^-, Cu^{2+}).[45, 46] The focus of this review is to address electrochemical reactions with reactants that are sparingly soluble in aqueous media (*e.g.* N_2, CO_2) because these reactions (*i.e.* CO_2 and N_2 reduction) have the potential to displace the largest emitting processes in the chemical industry (*e.g.* ethylene and ammonia production).[41, 47, 48] The challenge with these reactions is that they are susceptible to mass-transfer limitations because the gaseous reactant must dissolve in the electrolyte and transport to the electrocatalyst surface to react.[49, 50] The structure of the electrode has a marked influence on the transport of these chemical species, and, therefore, the efficiency of electrochemical synthesis.

Planar electrodes (**Figure 3a**) with well-defined surface areas are commonly used to investigate new electrocatalysts.[3] However, thick diffusion boundary layers (50-200 um) formed during electrolysis can cause mass transport to be the slowest step in the overall process.[25, 51] In this situation, the rate of the electrochemical reaction is limited by reactant transport to the catalytic surface. Taking CO_2 reduction for example, the pioneering work by Hori,[52, 53] and a growing body of literature, have shown that the chemical environment proximal to the electrocatalyst has a high pH and is generally depleted of CO_2 relative to the bulk phase.[54, 55] It is therefore challenging to achieve high current densities (i >100 mA cm^{-2}) with planar electrodes. Planar electrodes are appropriate for studying the intrinsic kinetics of electrocatalysts at low current densities, but not for industrial applications, where high rates are required due to capital cost considerations.[56]

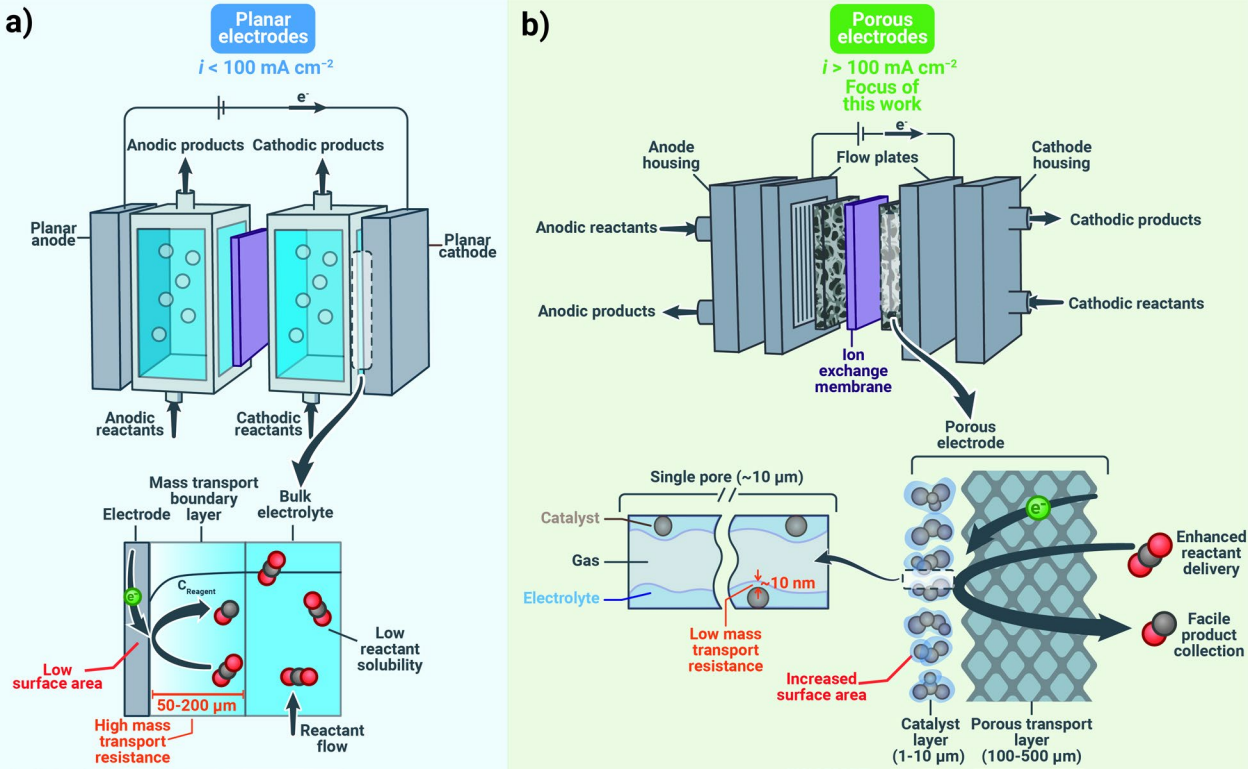

Figure 3: (a) Schematic representation of a planar flow-cell for electrochemical synthesis. Inset depicts local mass transport at the planar electrode surface. **(b)** Schematic representation of an electrochemical synthesis device utilizing porous electrodes. Insets depict local mass transport through the porous transport layer and within the individual pores of the porous electrode.

The 3-D geometry of porous electrodes enables a significant enhancement in catalytic surface area relative to planar electrodes (**Figure 4**).[57, 58] Batteries, water electrolyzers, fuel cells, and other electrochemical reactors leverage this property of porous electrodes to achieve higher geometric current densities (i >100 mA cm^{-2}; **Figure 3**b).[59] For example, in hydrogen fuel cells, reactant gas flows through pores in the electrode and diffuses through thin films of polymer electrolyte (*e.g.*, 5 to 100 nm) to the electrode, which enables rapid mass transfer.[60] The thin film of electrolyte in these porous electrodes is necessary to allow for the conduction of ions to and from the catalyst particles. Porous transport layers (PTLs) are used to support the catalyst layer while ideally providing good thermal and mass transport properties. Electrochemical synthesis devices and hydrogen fuel cells are often designed with similar porous-electrode architectures

because both of these systems must manage multiphase flows and result in relatively high power or current densities.[14, 15, 61] The added challenge with electrochemical synthesis reactions is that the selectivity for the desired products is highly dependent on the local microenvironment surrounding the electrocatalyst, and by extension, the multiscale transport of products and reactants throughout the device as a whole.[62] Porous electrodes enable control of the local microenvironments within an electrochemical synthesis device through tuning of their structure-property-performance relationships to control the relative ratios of reactants, products, and electrolyte/solvent throughout the cell. For example, porous-electrode properties can be tuned to attenuate water transport that promotes the unfavorable hydrogen-evolution reaction (HER) during electrochemical synthesis.[63, 64] Design principles for controlling mass transfer in porous electrodes are therefore key to enabling efficient and selective electrochemical synthesis.

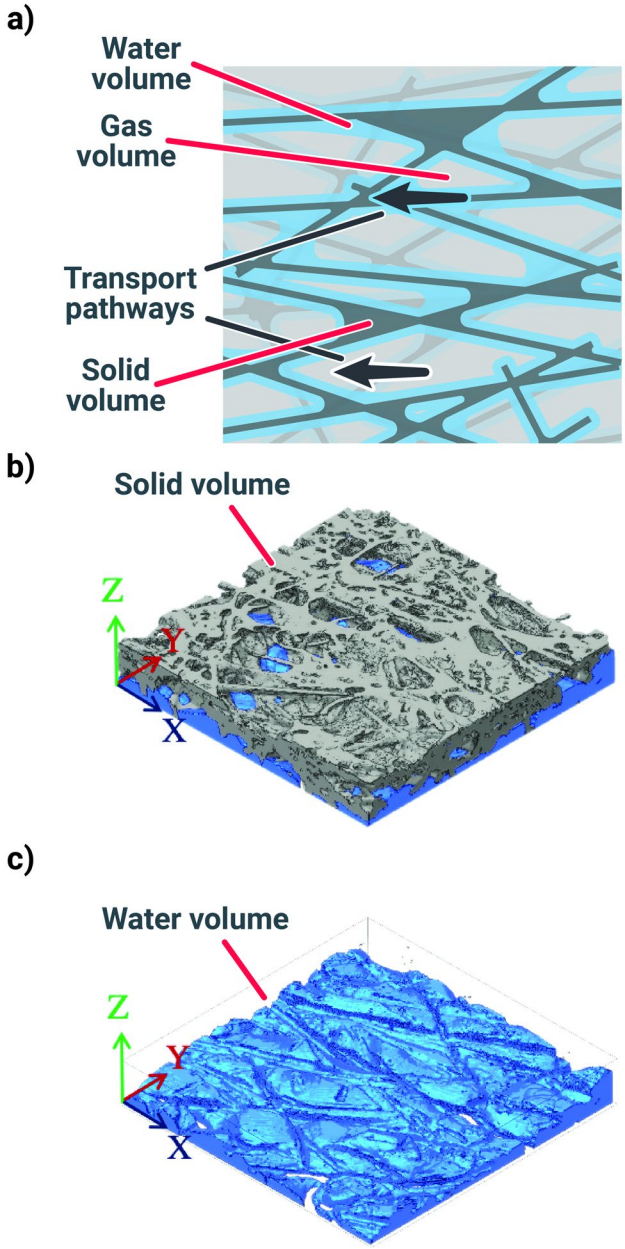

Figure 4: (a) Schematic of dual percolated pathways for transport in a porous electrode. **(b-c)** 3-D-computed geometry of a porous electrode depicting dual percolated pathways calculated from x-ray tomography. **(b)** Full porous electrode with partial wetting. **(c)** Water volume in porous electrode. Adapted with permission from Liu *et al*. Copyright 2021 American Chemical Society.[65]

2. Historical Discussion of Continuum Modeling in Electrochemical Synthesis

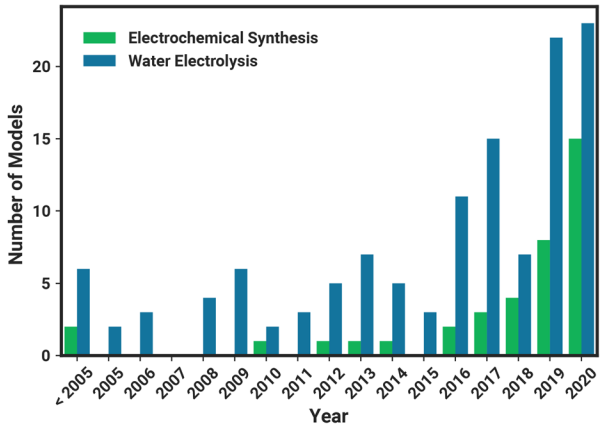

Figure 5: Bar graph depicting the number of continuum-based models published per year that simulate porous electrodes for electrochemical synthesis (green) or water electrolysis (blue).

Within the last ten years, the importance of macroscale modeling of porous electrodes for electrochemical synthesis has been recognized,[3, 19, 49] and within the last five years (2015-2020), the academic output in this area has grown exponentially (see **Figure 5**). Most continuum-based models of porous electrodes for electrochemical synthesis have focused on modeling electrochemical CO_2 reduction[25, 49, 50, 60, 63, 66-81] or acrylonitrile reduction,[82] although many other electrochemical synthesis reactions have been shown to benefit from the use of a porous electrode, such as methane oxidation[83] and ammonia synthesis.[84] Given the steadily increasing interest in shifting towards electrochemical-based synthesis, the number of reactions for which porous electrodes are used are expected to keep expanding, and the importance of macroscale modeling continue to grow.

Unfortunately, the field of macroscale modeling for electrochemical synthesis is still very much in its infancy. Many models for electrochemical CO_2 reduction are merely descriptive (used to estimate local reactants concentrations or pH within experimental devices).[63, 70, 71, 76, 81, 82, 85-90] These models use experimentally derived current densities as boundary conditions and thus are not predictive of electrochemical device performance or product distributions. While

such models provide fundamental insight into the local environments in electrochemical synthesis, the ultimate goal is to have models that predict the product distributions and efficiencies of electrochemical synthesis devices based on underlying physical phenomena.[19]

Several physics-based electrochemical-synthesis models in the literature have provided thorough guidance to experimentalists regarding component- and device-level engineering.[49, 60, 66, 67, 74, 91, 92] However, the majority of these types of models are 1-D (through-plane of the porous electrode), and do not capture pore-level heterogeneity or spatial variations in activity throughout the electrode. Recently, Yang *et al.*[66] and Kas *et al.*[78] developed macroscale models that included 2-D effects along the flow channel of a CO_2 reduction device; however, these models neglect pore-level transport and instead treat the porous transport layers as uniform continua. Bohra *et al.*[71] recently attempted to model pore-level transport for electrochemical CO_2 reduction, but the model had convergence difficulties at higher applied overpotentials, limiting its applicability and predictive power. Understanding transport across multiple length scales is critical to optimizing electrochemical synthesis because the local microenvironments have a strong influence on the observed product distributions.

Fortunately, the state of modeling device architectures for ion-exchange membrane (IEM) water electrolyzers is quite mature and can be used to guide the development of complex, multi-dimensional, multiscale models for electrochemical synthesis. Continuum models used to simulate porous electrodes for water electrolysis far predate those used to simulate electrochemical synthesis.[9, 93] Moreover, in contrast to electrochemical synthesis, water electrolysis continues to be a subject of intense research interest because it is relevant to hydrogen production using renewable energy sources (**Figure 5**).[10, 94] However, the majority of models for water electrolysis are more physically complete and therefore predictive of device

performance than models of electrochemical synthesis.[9, 10] For instance, 3-D pore-network models have been developed to describe composition, potential, and current-density distributions in the microenvironments within porous electrodes used for water electrolysis.[95, 96] The field of water electrolysis has also begun to explore the question of simulating transient operation and degradation modes,[97-100] which have yet to be well explored for electrochemical synthesis. Modeling degradation phenomena in electrochemical synthesis will be critical to understanding and mitigating failure mechanisms that occur in industrial settings and scales.[19]

The field of electrochemical synthesis is beginning to follow the trajectory of water electrolyzers and hydrogen fuel cells through the development of sophisticated continuum models. However, competing reactions and multi-component mass transfer in electrochemical synthesis devices add significant complexity to the models.[3, 68, 101] Accounting for species/species interactions and complex homogeneous reaction kinetics greatly increases the degrees of freedom and causes convergence issues.[49, 67] While not all of these challenges have been faced in the development of water-electrolysis and fuel-cell models, the commonalties between the fields can be used as a starting point to solve the development and implementation challenges associate with models for electrochemical-synthesis systems.[9, 19, 102]

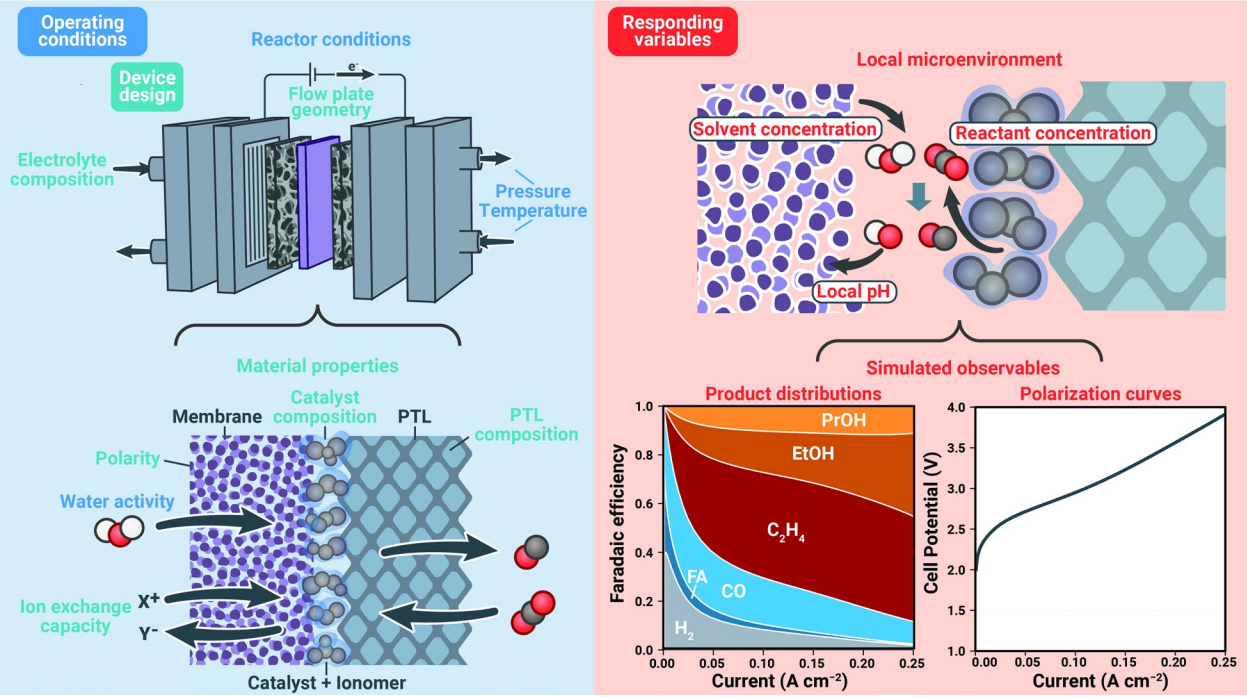

Figure 6: Schematic depicting the objective of macroscale models for electrochemical synthesis: Given a set of materials and experimentally controlled variables at the device level, simulate the response of the electrochemical system at the scale of the catalyst microenvironment, and from that microenvironment simulate product distributions and other observables that can be validated against experiment. Product distribution adapted with permission from Weng *et al.*[67] Copyright 2020 Royal Society of Chemistry.

This review aims to facilitate the transfer of knowledge from the fields of electrochemical engineering and transport phenomena developed for the IEM fuel cell to that of electrochemical synthesis, primarily focused on systems operating near ambient temperature (< 100°C) and pressure (< 5 bar). We note that there is an interest in application of high-temperature systems (*e.g.,* solid oxide cells) for electrosynthesis, and while some of the phenomena governing the operation of such systems are similar to those pertaining to IEM systems, many are different. Thus, a detailed description on modeling high-temperature systems is beyond the scope of this review, and the readers are referred to other recent modeling reviews of these systems.[103-105] Our approach will be to review the IEM and fuel-cell literature and compare it with current electrochemical synthesis models to identify gaps and overlap. Moreover, we highlight

reasonable simplifications that can be made to reduce the computational cost of electrochemical synthesis models. We contend that these simpler models can still be adequately predictive of device performance and provide relevant guidance to experimentalists. Moreover, we posit that the ideal continuum model for electrochemical synthesis is one that accurately simulates the local chemical microenvironments and predicts device efficiencies as a function of variables commonly controlled in experiments (**Figure 6**). The goal of these types of comprehensive simulations is to accelerate the optimization of electrochemical-synthesis devices by reducing the need for extensive experimentation.

3. General Aspects and Equations

3.1 Modeling Methodologies

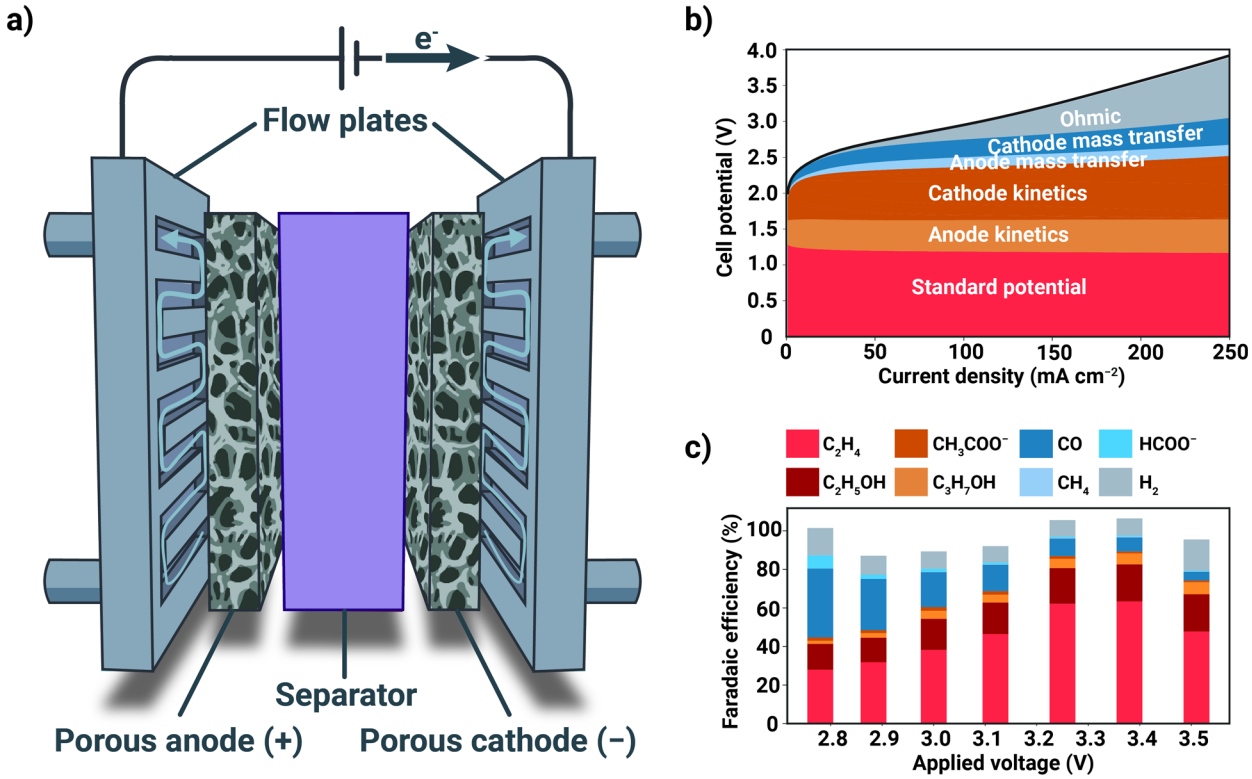

Figure 7: (a) Schematic depicting a typical porous-electrode device used for electrochemical synthesis. **(b)** Typical polarization-curve data taken from experiment, broken down by voltage contribution (applied-voltage breakdown). **(c)** Typical product distribution obtained from

experiment of electrochemical CO_2 reduction.[67] Applied voltage breakdown adapted with permission from Weng *et al*.[67] Copyright 2020 Royal Society of Chemistry.

Porous-electrode devices for electrochemical synthesis typically consist of a membrane or separator situated between two porous electrodes (one anode, one cathode), which are themselves situated between two flow plates (**Figure 7a**) that act as well as current collectors. In these devices, the performance is usually characterized by the results of two key metrics. The first is its IV-(*i.e.,* current-voltage) characteristics, taken from polarization experiments, which provide a polarization curve depicting the applied cell potential required to achieve a certain current density in the device (**Figure 7b**). At low current densities, the performance of the device is dictated mainly by kinetic losses at the anode and cathode, due to the high kinetic overpotentials required to drive the respective electrochemical synthesis reactions.[106] At higher current densities, the mass transport of the reactants to the electrocatalytic sites, as well as ohmic losses throughout the cell, become relevant and increase the cell potential required to achieve a given current density in linear and nonlinear ways.

The second key metric for evaluating the performance of an electrochemical synthesis device is its product distribution (**Figure 7c**). These product distributions are usually evaluated through constant current-density (galvanostatic) or constant voltage (potentiostatic) measurement, where the synthesis products are analyzed simultaneously. While gas-phase products produced during galvanostatic experiments can be measured on-line, analysis of liquid-phase products usually requires their accumulation so that the amount of product is sufficient for analysis by high-performance liquid chromatography (HPLC) or nuclear-magnetic resonance (NMR). These measurements are combined with polarization data to estimate product formation rates. The thermal energy efficiency (EE_{th}) of an electrochemical synthesis reaction can be

determined analogously to traditional chemical processes by using the lower heating value (LHV) of the products as,

$$\mathrm{EE_{th}} = \frac{\frac{A_S}{nF}\sum_i i_i LHV_i}{V_{app} I_{total}}, \quad (1)$$

where A_S is the geometric electrode surface area, i_i is the geometric partial current density for product *i, I* is the total current passed through the device, V_{app} is the applied cell potential, *n* is the number of electrons transferred in the electrochemical reaction, and *F* is Faraday's Constant. The LHV is derived from the enthalpy of combustion of the generated fuel, assuming that the water generated is in the vapor phase, and can be determined by looking at the net change in the enthalpy of formation between reactants and products upon combustion of a given fuel, nominally at 150° C.[107]

It is also common form to compute the energy efficiency (EE) (which is distinct from the thermal energy efficiency) in terms of the standard Gibbs Free Energy for reaction *l* (ΔG_l^0),

$$\mathrm{EE} = \frac{\sum_l \mathrm{FE_l}\, \Delta G^0_{cell,l}}{V_{app} nF}, \quad (2)$$

where FE_l represents the Faradaic Efficiency (*i.e.,* electrochemical selectivity) for reaction *l* which produces product *i*,

$$\mathrm{FE}_l = \frac{i_l}{i_{total}}. \quad (3)$$

FE values measured during electrochemical synthesis experiments are often plotted as a function of voltage or current density, resulting in the product distributions reported in literature. It is important to note that the FE only quantifies the selectivity for a given product, and not the

associated electrical energy consumption. To this end, the voltage efficiency (VE) is used to determine the total electrical energy consumption relative to thermodynamic equilibrium,

$$\mathrm{VE} = \frac{\sum_l \mathrm{FE}_l U^0_{\mathrm{cell},l}}{V_{app}}, \tag{4}$$

where $U^0_{cell,l}$ is the standard cell potential for reaction for each overall reaction l, calculated as the change in Gibbs Free Energy at standard conditions (298 K and 1 atm pressure) divided by the number of electrons that participate in the reaction and Faraday's constant (96485 C mol^{-1}), is also shown.

$$\mathrm{U}^0 = -\frac{\Delta G^0}{nF}, \tag{5}$$

3.2 Conservation Equations

Detailed modeling of electrochemical-synthesis systems at the continuum scale requires mathematical expressions for the conservation of charge, mass, momentum, and energy. The conservation equations need to be combined with constitutive thermodynamic, transport, and (electrochemical) kinetics relationships. The conservation of any quantity ϕ in a defined control volume is given as

$$\frac{\partial \phi}{\partial t} + \boldsymbol{\nabla} \cdot \mathbf{N}_\phi = S_\phi, \tag{6}$$

where $\frac{\partial \phi}{\partial t}$ is the accumulation of any quantity ϕ, N_ϕ is the flux of property ϕ and S_ϕ is the volumetric generation/consumption rate of ϕ. The flux N_ϕ is usually described by a transport model (for example, the Nernst-Planck equation as described later) and the source term S_ϕ is obtained using expressions of the relevant physics for consuming or generating ϕ (also described later). The first term in Eq. (6) represents changes in the quantity ϕ with time and is required for

studying dynamic system behavior, such as operating cycles, degradation during system life, and operational uncertainties. The second term represents the change in quantity ϕ due to its flux in/out of the system. Finally, S_ϕ represents the volume specific rate of change due to generation or consumption of quantity ϕ; this term incorporates changes due to reactions, phase change, etc.

3.3 Thermodynamics

3.3.1 Full- and Half-Cell Potentials

In the development of devices for electrochemical synthesis, strong attention must be paid to the thermodynamics of the reactions occurring at each electrode. At the cathode, electrochemical reduction occurs, with **Table 1** showing common reduction reactions that are of interest for electrochemical synthesis. To calculate the standard reduction potential for each half-reaction, *l,* the following procedure (shown below for the example of the reduction of AN to ADN) was followed to determine the equilibrium potential against the standard hydrogen electrode (SHE), wherein all reactants and products of the reaction possess unit activity:

First, we state the half reaction of interest at the cathode, which in this case is AN reduction.

$$2\mathrm{AN} + 2\mathrm{H}^+ + 2\mathrm{e}^- \rightarrow \mathrm{ADN} \tag{7}$$

Since we want to measure against a SHE, we choose the hydrogen oxidation reaction as our anodic reaction.

$$\mathrm{H}_2 \rightarrow 2\mathrm{H}^+ + 2\mathrm{e}^- \tag{8}$$

Combining the two half reactions provides the overall (full cell) reaction:

$$2\mathrm{AN} + \mathrm{H}_2 \rightarrow \mathrm{ADN}. \tag{9}$$

The species in the above reaction possess the following Gibbs free energies of formation at standard conditions of 298 K and 1 bar pressure:[108]

$$\Delta G^0_{\mathrm{ADN}} = 253.3 \frac{\mathrm{kJ}}{\mathrm{mol}} \tag{10}$$

$$\Delta G^0_{\mathrm{AN}} = 191.1 \frac{\mathrm{kJ}}{\mathrm{mol}} \tag{11}$$

$$\Delta G^0_{H_2} = 0 \frac{\mathrm{kJ}}{\mathrm{mol}} \tag{12}$$

Calculation of the Gibbs free energy change of the overall reaction results in the following result.

$$\Delta G^0_l = 253.3 - (2 * 191.1) \frac{\mathrm{kJ}}{\mathrm{mol}} = -128.9 \frac{\mathrm{kJ}}{\mathrm{mol}} \tag{13}$$

Dividing by $-nF$ for the reaction provides the standard reduction potential against the standard hydrogen electrode (SHE) at pH 0 (unit activity of protons and all other species).

$$U^0_l = -\frac{\Delta G^0_l}{2F} = 0.67 \text{ V vs. SHE at pH 0} \tag{14}$$

We can alternatively calculate the potential against the SHE at pH 14 (unit activity of hydroxides and all other species), as most of these reactions will optimally occur in alkaline environments. To calculate the SHE potential at pH 14, we can calculate the change in Gibbs free energy for the half reaction itself assuming unit activity (1 M concentration) of OH^- anions.

First, we state the alkaline version of the AN reduction reaction.

$$2\mathrm{AN} + 2\mathrm{H_2O} + 2\mathrm{e^-} \rightarrow \mathrm{ADN} + 2\mathrm{OH^-} \tag{15}$$

The Gibbs free energies of the involved species in this half cell reaction are as follows:

$$\Delta G^0_{\mathrm{ADN}} = 253.3 \frac{\mathrm{kJ}}{\mathrm{mol}} \tag{16}$$

$$\Delta G^0_{\mathrm{AN}} = 191.1 \frac{\mathrm{kJ}}{\mathrm{mol}} \tag{17}$$

$$\Delta G^0_{\mathrm{H_2O}} = -237.14 \frac{\mathrm{kJ}}{\mathrm{mol}} \tag{18}$$

$$\Delta G^0_{\mathrm{OH^-}} = -157.2 \frac{\mathrm{kJ}}{\mathrm{mol}} \tag{19}$$

The standard Gibbs free energy change of the half reaction can be determined using the above free energies of formation.

$$\Delta G^0_l = (253.3 - 2 * 157.2) - (2 * 191.1 - 2 * 237.14) = 30.98 \frac{\mathrm{kJ}}{\mathrm{mol}} \tag{20}$$

Again, dividing by $-nF$ for the reaction results in the reduction potential, now against an SHE at pH = 14 (unit activity of hydroxide anions).

$$U^0_{l,pH=14} = -\frac{\Delta G^0}{2F} = -0.16 \text{ V vs. SHE at pH} = 14 \tag{21}$$

In many cases in electrochemical synthesis modeling, however, it is more prudent to adjust the half-cell potentials to local conditions (U_l), as opposed to referencing to standard conditions (U^0_l, pH = 0 or pH = 14, all species at unit activity).

$$U_l = U^0_l + \frac{RT}{nF} \ln\left(\frac{\prod_{r=1}^{a} a_r^{s_{r,l}}}{\prod_{p=1}^{b} a_p^{s_{p,l}}}\right) \tag{22}$$

where n is the number of electrons transferred, R is the ideal gas constant, T is the operating temperature, a_i is the activity of species i, and s_i is the stoichiometric coefficient of species i. The subscripts r and p represent species in the reactants and products, respectively, of the reduction reaction. The continued products term is often referred to as the Nernst correction.

Returning to the case-study reaction of AN reduction, shifting from the SHE at pH = 0 to the local conditions:

$$U_l = U^0_{l,pH=0} + \frac{RT}{F}\ln(a_{H^+}) + \frac{RT}{F}\ln(a_{AN}) - \frac{RT}{2F}\ln\left(a_{ADN}\right) \tag{23}$$

Invoking the definition that $pH = -\log_{10}(a_H)$:

$$U_l = 0.67\ [\text{V vs. SHE}] - \frac{2.303RT}{F}\text{pH} + \frac{RT}{F}\ln(a_{AN}) - \frac{RT}{2F}\ln\left(a_{ADN}\right) \tag{24}$$

It is also demonstrative to show that the alkaline form of the reaction, referenced to SHE at pH = 14, provides the same value for local conditions (U_l):

$$U_l = U^0_{l,pH=14} + \frac{RT}{F}\ln(a_{AN}) + \frac{RT}{F}\ln\left(a_{H_2O}\right) - \frac{RT}{F}\ln(a_{OH^-}) - \frac{RT}{2F}\ln\left(a_{ADN}\right) \tag{25}$$

Invoking the equilibrium of water dissociation, $K_w = 1.0 \times 10^{-14} = \frac{a_{H^+}a_{OH^-}}{a_{H_2O}}$ (*i.e.,* $\text{pH} + \text{pOH} = 14$, where $\text{pOH} = -\log_{10}(a_{OH})$). The above expression can be recast as:

$$U_l = -0.16\ [\text{V vs. SHE}]\ + \frac{2.303RT}{F} \times 14 - \frac{2.303RT}{F}\text{pH} + \frac{RT}{F}\ln(a_{AN}) - \frac{RT}{2F}\ln\left(a_{ADN}\right) \tag{26}$$

Combining the first two terms:

$$U_l = 0.67\ [\text{V vs. SHE}]\ - \frac{2.303RT}{F}\text{pH} + \frac{RT}{F}\ln(a_{AN}) - \frac{RT}{2F}\ln\left(a_{ADN}\right) \tag{27}$$

which is equivalent to Eq. (24). Therefore, the choice to use the alkaline form, referenced to pH 14, or the acidic form, referenced to pH 0, are equivalent when the Nernstian shift to local conditions is accounted for. It is important to note, however, that standard conditions are defined such that reactants and products are at unity; therefore, SHE potentials reported at pHs other than 0 or 14 are not well-defined and should be avoided.

Table 1: List of cathodic half-cell reactions and their standard reduction potentials.

Product	Reaction	U^0 (V vs. SHE) (pH = 0)
Hydrogen (H_2)	$2H^+ + 2e^- \rightarrow H_{2(g)}$	0
Ammonia	$N_2 + 6H^+ + 6e^- \rightarrow 2NH_{3(g)}$	0.03
Adiponitrile	$2AN + 2e^- + 2H^+ \rightarrow ADN_{(aq)}$	0.67
Ethylamine	$CH_3CN + 4H^+ + 4e^- \rightarrow CH_3CH_2NH_{2(aq)}$	0.17
From CO_2		
Formic Acid	$CO_2 + 2H^+ + 2e^- \rightarrow HCOOH_{(aq)}$	−0.12
Carbon Monoxide	$CO_2 + 2H^+ + 2e^- \rightarrow CO_{(g)} + H_2O$	−0.10
Methanol	$CO_2 + 6H^+ + 6e^- \rightarrow CH_3OH_{(aq)} + H_2O$	0.03
Methane	$CO_2 + 8H^+ + 8e^- \rightarrow CH_{4(g)} + 2H_2O$	0.17
Oxalic Acid	$2CO_2 + 2H^+ + 2e^- \rightarrow (COOH)_{2(s)}$	−0.47
Acetic Acid	$2CO_2 + 8H^+ + 8e^- \rightarrow CH_3COOH_{(aq)} + 2H_2O$	0.11
Acetaldehyde	$2CO_2 + 10H^+ + 10e^- \rightarrow CH_3CHO_{(aq)} + 3H_2O$	0.06
Ethanol	$2CO_2 + 12H^+ + 12e^- \rightarrow C_2H_5OH_{aq} + 3H_2O$	0.09
Ethylene	$2CO_2 + 12H^+ + 12e^- \rightarrow C_2H_{4(g)} + 4H_2O$	0.08

Ethane	$2CO_2 + 14H^+ + 14e^- \rightarrow C_2H_{6(g)} + 4H_2O$	0.14
Propionaldehyde	$3CO_2 + 16H^+ + 16e^- \rightarrow C_2H_5CHO_{(aq)} + 5H_2O$	0.09
Propanol	$3CO_2 + 18H^+ + 18e^- \rightarrow C_3H_7OH_{aq} + 5H_2O$	0.10
From CO		
Methane	$CO + 6H^+ + 6e^- \rightarrow CH_{4(g)} + H_2O$	0.27
Acetate	$2CO + 4H^+ + 4e^- \rightarrow CH_3COOH_{aq}$	0.07
Ethanol	$2CO + 8H^+ + 8e^- \rightarrow C_2H_5OH_{(aq)} + H_2O$	0.19
Ethylene	$2CO + 8H^+ + 8e^- \rightarrow C_2H_{4(g)} + 2H_2O$	0.17
Propanol	$3CO + 12H^+ + 12e^- \rightarrow C_3H_7OH_{(aq)} + 2H_2O$	0.19

As shown in **Table 1**, several of the possible reduction products have extremely similar equilibrium potentials, especially in the case of electrochemical reduction of CO_2 or CO. Therefore, it is difficult to discriminate between various electrochemical synthesis products by modulating the applied potential alone, and thus it is necessary to know how the local microenvironment (*e.g.,* concentrations CO_2 and H_2O, pH, cation identity and concentration) affects the partial current density for each product.

At the anode, electrochemical oxidation occurs, and the oxidation reactions of interest for electrochemical synthesis are shown in **Table 2** along with their standard reduction potentials. For electrochemical synthesis reactions that target reduced products, water oxidation is commonly used as the anodic reaction. The use of green hydrogen (from water electrolysis) or blue hydrogen (from steam methane reforming with carbon capture) at the anode has the

potential to lower the open circuit potential (defined as the difference between the anodic and cathodic potential) of the overall cell and reduce energy costs for operating electrochemical synthesis devices.[109] Glycerol oxidation has also been proposed as a promising co-synthesis reaction.[110]

Table 2: List of anodic half-cell reactions and their standard reduction potentials.[a]

Product or Reaction Name	**Reaction**	**U^0 (V vs. SHE) pH = 0**
Hydrogen oxidation reaction (HOR)	$H_2 \rightarrow 2H^+ + 2e^-$	0
Oxygen (O_2)	$2H_2O \rightarrow O_{2(g)} + 4H^+ + 4e^-$	1.23
From Glycerol		
Oxalic Acid	$2C_3H_8O_3 + 6H_2O \rightarrow 3C_2H_2O_{4(aq)} + 22e^- + 22H^+$	0.32
Formic Acid	$C_3H_8O_3 + 3H_2O \rightarrow 3HCOOH_{(aq)} + 8e^- + 8H^+$	0.46

It is important to note that the reactions listed in **Table 1** and **Table 2** are global half-cell reactions that proceed through a series of electron and proton transfer steps; more comments on the microkinetic steps of electrochemical synthesis reactions can be found in Section 3.5.

When multiple reactions occur simultaneously at each electrode, the "standard potential" of the overall device can be obtained by weighting the equilibrium potentials for each reaction by their FE,

$$\overline{U}^0 = \overline{U}^0_{\text{cathode}} - \overline{U}^0_{\text{anode}} = \sum_{\text{n}}(\text{FE})_{\text{n}} U^0_{\text{n}} - \sum_{\text{m}}(\text{FE})_{\text{m}} U^0_{\text{m}}, \quad (28)$$

where $\overline{U}^0$ is defined herein as a FE-averaged standard potential of a cell with multiple reactions, $\overline{U}^0_{\text{anode}}$ is a FE-averaged standard half-cell potential of the anode, $\overline{U}^0_{\text{cathode}}$ is a FE-averaged standard half-cell potential of the cathode, $(\text{FE})_n$ is the FE of a given cathode reaction, $(\text{FE})_m$ is the FE of a given anode reaction, U^0_n is the standard reduction potential of a given cathode reaction, and U^0_m is the standard reduction potential of a given anode reaction. Since the product distribution changes with current density and potential, this FE-weighted standard potential is not necessarily constant and results in a transcendental equation. Additionally, an electrochemical system with multiple reactions would never have all reactions fully in equilibrium, because full equilibrium requires all reactions be at their given standard reduction potential, which is impossible since all of these reactions have different standard reduction potentials based on the free energies of their reactants and products. When actually solving the coupled reaction equations individually, the appropriate mixed potential is calculated together with the resultant FE, but this convolutes a simple metric to compare the applied cell potential and thermodynamic efficiency for the system, which is what the above approximation allows.

Figure 8: Thermodynamic cell diagram for a typical electrochemical synthesis device.

A generic electrochemical synthesis device can be represented as shown in **Figure 8**. In the diagram, the Greek letters represent distinct phases, the straight lines represent an abrupt phase boundary, and wavy lines represent a phase boundary that is not necessarily abrupt. For instance, the ionomer within the electrode can extend into the membrane due to the mobility of the polymer chains. These non-abrupt phase transitions can be represented as distinct boundaries

in a model, but it is important to understand how this simplification may lead to inaccurate estimates of local species concentrations and potential gradients.

The potential measured experimentally for the cell shown in **Figure 8** is defined as the difference in the chemical potential of the electrons at each current collector (□). This quantity can be related to the electrostatic potential, and thus the overall cell potential as follows,

$$U = -\frac{\mu_{e^-}^{\alpha'} - \mu_{e^-}^{\alpha}}{F} = \left(\phi^{\alpha'} - \phi^{\alpha}\right), \tag{29}$$

where F is Faraday's constant, U is the thermodynamic reversible cell potential, ϕ^{α} is the electrostatic potential of phase $\mu_{e^-}^{\alpha}$, and $\mu_{e^-}^{\alpha}$ is the electrochemical potential of electrons in phase α. The overall cell potential can be rewritten as a difference of the electrochemical half-cell potentials for the half-reactions occurring at each electrode,[111, 112]

$$U = U^{\beta'} - U^{\beta} \tag{30}$$

In the above expression, $U^{\beta'}$ and U^{β} are the electrochemical half-cell potential for each electrode, taking into consideration Nernstian shifts due to the local activities of reactant and product species at each electrode, as defined by Eq. (22).

Additionally, the enthalpy dependence of the thermodynamic potential is particularly relevant in electrochemical synthesis, because the enthalpy dependence will dictate whether the reactions require or generate heat, which will be relevant to consider, especially in solar driven electrochemical systems where heat can be generated from near-IR adsorption or in coupled thermo-electrochemical approaches to synthesis.[113] The full form of the enthalpy potential, defined as the change in potential associated with changes in enthalpy, is shown below. For a complete derivation of this relationship the reader should look at Newman and Alyea.[111]

$$U_H(\mathrm{T}) = -\frac{\Delta H(T)}{nF} = \frac{-1}{nF}\left(\Delta H|_{T_0} + \Delta a(T - T_0) + \frac{\Delta b\left(T^2 - T_0^2\right)}{2} - \Delta c\left(\frac{1}{T} - \frac{1}{T_0}\right) + \frac{\Delta\gamma\left(T^3 - T_0^3\right)}{3}\right) \quad (31)$$

In the above expression, $\Delta H|_{T_0}$ is the enthalpy change of the overall reaction at a reference temperature T_0. $\Delta a, \Delta b, \Delta c$, and $\Delta\gamma$ are the net change during the overall reaction (*e.g.,* $\Delta a = \Sigma_i s_i a_i$, where s_i is the stoichiometric coefficient of species i) of the integration constants for the definition of the heat capacity, defined as $C_{p,i} = a_i + b_i T + \frac{c_i}{T^2} + \gamma_i T^2$.

The enthalpy potential can be related to the overall cell potential by the relationship between the Gibbs free energy and enthalpy. The enthalpy potential can equivalently be expressed in terms of the cell potential by the definition of Gibbs free energy invoking the relationship $\frac{\partial U}{\partial T}|_V = \frac{\Delta S}{nF}$, which is only true at constant volume. This substitution facilitates writing a direct expression for the temperature dependence of the equilibrium potential.

$$U(T) = \frac{-1}{nF}\left(\Delta G|_{T_0}\left(\frac{T}{T_0}\right) + \Delta H|_{T_0}\left(1 - \frac{T}{T_0}\right) + \Delta a\left(T - T_0 - T\ln\left(\frac{T}{T_0}\right)\right) - (T - T_0)^2\left(\frac{\Delta b}{2} + \frac{\Delta c}{2TT_0^2}\right) - \frac{\Delta\gamma}{6}(T^3 - 3TT_0^2 + 2T_0^3)\right), \quad (32)$$

where $\Delta G|_{T_0}$ is the free energy change of the overall reaction at a reference temperature T_0. A complete derivation of Eq. (32) can be found in the text of Newman and Thomas-Alyea.[111] The above expression for the temperature dependence of the cell potential is quite complex, largely due to the definition of the heat capacity. However, in many cases, when the temperature range for the targeted electrochemical synthesis in low, it is acceptable to assume that the potential is

linear with respect to temperature. This has been shown to be valid for the hydrogen evolution reaction for temperatures between 273 and 373 K.[114, 115]

3.3.2 Chemical and Electrochemical Potential

In modeling electrochemical synthesis, proper expressions for the electrochemical potentials of the various species are required to construct a thermodynamically consistent model.

$$\mu_i = \mu_i^0 + RT\ln(a_i) + z_i F\phi + \overline{V}_i\left(p - p_{ref}\right) \tag{33}$$

where μ_i is the electrochemical potential of species *i,* μ_i^0 is the electrochemical potential of species *i* at the reference state of 298 K, unit activity, 1 bar pressure, and no applied electrostatic potential, z_i is the charge of species *i,* c_i is the concentration of species *i*, $\overline{V}_i$ is the partial molar volume of species *i, p* is the local pressure, p_{ref} is a reference pressure of 1 bar, and ϕ is the electrostatic potential. In defining the species activity, a_i, multiple scalings can be used, such as comparison to the standard molar reference, or a molal or molar ratio reference.[116, 117] However, one must be careful to ensure that all thermodynamic quantities (*e.g.,* equilibrium constants) are employed with a consistent reference.

It is important to note that the expressions shown in Eq. (33) for the (electro)chemical potential do not explicitly consider excess free energies and are thus only valid in dilute solution. These neglected non-idealities will be critical to consider when modeling devices operating at high current densities, or in ionomer-phase environments, where local concentrations of species can reach up to 10 M ionic strength.[49] The following model for species chemical potential accounts for mixing and excess properties.[116]

$$\mu_i = \mu_i^{\theta} + z_i F\phi + \mu_i^{id} + \mu_i^{slv} + \mu_i^{els} + \mu_i^{phy} + \mu_i^{swe} + \mu_i^{stc} \tag{34}$$

In this definition of the chemical potential, all species, including the solvent, are treated explicitly in both the external solution and the ionomer domains. In the ionomer domains, the polymer groups are idealized as free ions in the hydrophilic domains. μ_i^θ is the reference chemical potential for species *i*, which is defined as the chemical potential of species *i* in a pure liquid solvent, in the limit of ideal solution, in a fully dissociated state, and in which all polymer domains are unswollen. μ_i^{id} results from the change in free energy from ideal mixing. The remaining terms constitute excess chemical potential due to specific effects: μ_i^{slv} arises from the solvation of ions; μ_i^{els} accounts for electrostatic interactions between ions; μ_i^{phy} describes short-range physical interaction between ions; and μ_i^{swe} and μ_i^{stc} result from the swelling of the polymer and steric interactions with the polymer, respectively, and only appear in the ionomer phase. Expressions for these terms are shown below in **Table 3.**

Table 3: Expressions for ideal mixing potential and excess chemical potentials, where subscript 0 denotes the solvent.[a]

Contribution	Term	Expression
Ideal Mixing	μ_i^{id}	$RTln(x_i)$
Solvation	$\mu_{i\neq0}^{slv}$	$RTln(\frac{\alpha_i}{\alpha_{i,\infty}})$
	μ_0^{slv}	$RTln(\alpha_0)$
Electrostatics	$\mu_{i\neq0}^{els}$	$-ARTz_i^2\left[\frac{I^{\frac{1}{2}}}{1+BaI^{\frac{1}{2}}}+\frac{m_M z_M^2}{2bBI}\right]$
	μ_0^{els}	$ART\left(\frac{2}{3}I^{\frac{3}{2}}\sigma\left(BaI^{\frac{1}{2}}\right)\frac{M_0}{\rho_0}+\frac{M_0 m_M z_M^2}{bB}\right)$

$$\sigma = \frac{3}{x^3}\left\{(1+x) - 2\ln(1+x) - \frac{1}{1+x}\right\}$$

Physical	$\mu_{i\neq 0}^{phy}$	$2RT\sum_{i\neq 0}\beta_{i,j}m_j$
	μ_0^{phy}	$-M_0RT\sum_{i\neq 0}\sum_{j\neq 0}\beta_{i,j}m_i m_j$
Swelling	$\mu_{i\neq 0}^{swe}$	0
	μ_0^{swe}	$\overline{V_0}E_b^0\left[1 - \frac{\frac{d(\phi_M)}{2} - R_{domain}(\phi_M)}{\frac{d^0}{2} - R_{domain}^0}\right]$
Steric	$\mu_{i\neq 0}^{stc}$	$\frac{RTa_i}{d(\phi_M) - d^0}$
	μ_0^{stc}	0

[a] x_i is the mole fraction of species i. The subscript 0 represents the solvent, and subscript M represents the polymer electrolyte. α_0 and α_i are the ratios of free solvent and unbound ions, respectively, after solvation to before solvation. α_i^∞ is the fraction of unsolvated i in the limit of infinite dilution. I ($= \frac{\rho_0}{2n_0M_0}\sum_{i\neq 0,M} z_i^2 n_i$) is the ionic strength, excluding fixed-charge groups in the membrane. a is the distance of closest approach between ions. A is the Debye-Huckel limiting slope (= 1.177 $m^{3/2}$ $mol^{-1/2}$ for water at 298 K), and B is the Debye-Huckel solvent parameter (= 3.291 $m^{3/2}$ $mol^{-1/2}$ nm^{-1} for water at 298 K). b is the spacing between charged groups in the membrane. m_i is the molality of species i. $\beta_{i,j}$ is a specific interaction parameter between species i and j. $\beta_{i,j} = 0$ for species with like charge, is < 0 for favorable short-range interactions, and is > 0 for unfavorable interactions. E_b^0 is the Young's Modulus of the dry polymer. R_{domain} and d are the hydrophilic domain size and spacing in the ionomer and are both functions of the membrane volume fraction (ϕ_M) with the superscript 0 denoting properties of the dry ionomer.

3.3.3 Exchange of Species Across Phases

The exchange of ions and solvent between the solution and ionomer phase is another critical physical phenomenon that must be simulated to characterize fully the chemical

microenvironments in electrochemical synthesis devices. Invoking the conservation of chemical potential for an ideal solution (Eq. (33)) for all species across phases, as well as the condition of electroneutrality ($\Sigma z_i c_i = 0$), the equilibrium of species concentration across phases can be calculated using the framework of ideal Donnan equilibrium,[118]

$$c_i^M = \mathrm{c_i^0} \exp\left(\frac{-z_i F(\phi_i^M - \phi_i^0)}{RT}\right), \tag{35}$$

where $\Delta\phi_D = \phi_i^M - \phi_i^0$ is the ideal Donnan potential defined as the difference in electrostatic potential between the membrane and solution phases, c_i^M is the concentration of species *i* in the membrane phase, and $\mathrm{c_i^0}$is the concentration of species *i* in the solution phase. It should be noted that the above treatment does not explicitly resolve the double layer at the phase boundary. To account for such features requires more sophisticated nanoscale models. It is important to note that ideal Donnan equilibrium does not predict any change in concentration for neutral species (*e.g.,* the solvent) across the ionomer/solution interface because Donnan equilibrium is based on purely on electrostatics. Therefore, in continuum models that employ ideal Donnan equilibrium to calculate ionic species concentrations, a separate treatment of solvent uptake is commonly employed that accounts for water activity gradients in confined polymer electrolyte domains, as well as the effects of osmotic pressure driving forces.[11, 12, 49, 67, 102, 117]

Most electrochemical synthesis models treat solvent uptake using a semi-empirical[49, 67] or thermodynamic model[119-121] that is parameter fit using experimental thermogravimetric analysis (TGA) data. The developed expression relates solvent content in the membrane (λ_0), defined as the ratio of moles of solvent to moles of fixed charge sites in the membrane, to solvent activity. The use of λ_0 is convenient because many membrane properties are reported or tabulated as a function of λ_0. Therefore, solvent uptake isotherms can be used to model membrane properties

as a function of the solvent activity. Weng *et al.*[49] demonstrated this methodology in a CO_2 reduction study, which simulated the water uptake in a Tokayuma A201 ionomer (**Figure 9**).[122]

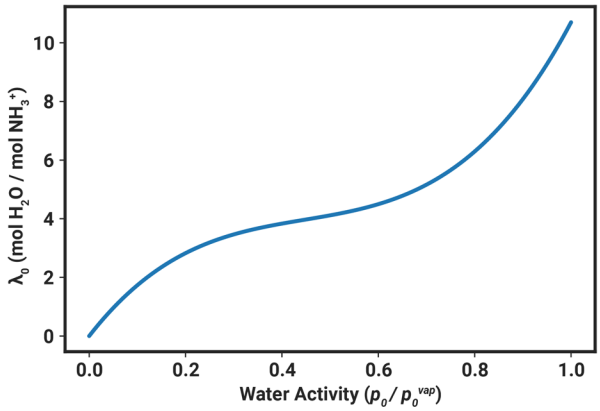

Figure 9: Water uptake isotherm for Tokuyama A201 anion exchange ionomer. The isotherm was fit using data originally shown in Peng *et al.* 2018.[122] Figure adapted from Weng *et al.* 2020 with permission.[67] Copyright 2020 Royal Society of Chemistry.

Important to note is that a membrane in equilibrium with a vapor phase solvent at unit activity exhibits different solvent content than one in equilibrium with an aqueous phase or mixed aqueous and vapor-phase solvent. This phenomenon is referred to as Schroeder's Paradox and results from variations in the polymer swelling for a membrane in contact with an aqueous or vapor phase that result from the difference in internal pressure exerted by liquid or vapor phase water.[116, 123-126] Therefore, because multiphase flow is common in electrochemical synthesis systems, the semi-empirical treatment of solvent content must account for Schroeder's Paradox, as shown below,

$$\lambda_0 = \lambda_{0,V}|_{a_0=1} + \left(\lambda_{0,L} - \lambda_{0,V}|_{a_0=1}\right)S, \tag{36}$$

where λ_0 is the solvent content of the membrane, $\lambda_{0,V}|_{a_0=1}$ is the solvent content of the membrane in contact with vapor phase solvent at unit activity, and $\lambda_{0,L}$ is the solvent content of the membrane in content with a pure aqueous phase solvent. S is an empirical relation related roughly to the interior surface energies and water-phase network.[126] It is important to note that

this formulation is only valid for membranes that exhibit phase separated morphologies. While most cation-exchange ionomers are phase separated, most anion-exchange membranes do not exhibit substantial phase separation.[127] An example saturation curve taken from Weng *et al.* for Tokuyama A201 is shown in **Figure 10**.

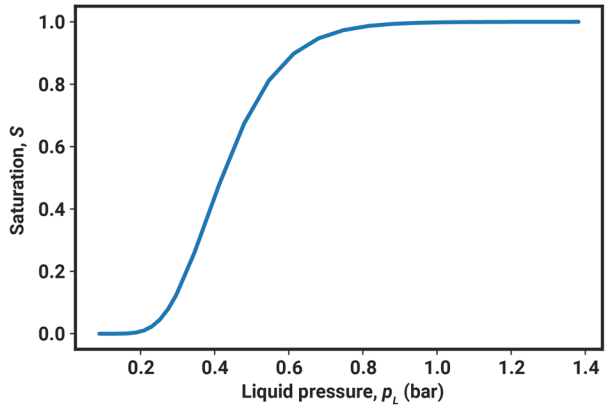

Figure 10: Saturation curve for Tokuyama A201 anion exchange ionomer. *S* is water saturation and p_L is the pressure of the liquid phase. Adapted with permission from Weng *et al.*[49] Copyright 2020 Royal Society of Chemistry.

When modeling species uptake for non-ideal membranes more generally, it becomes convenient to consider an electroneutral sum of two species (*i* and *j*) and solve the conservation of electrochemical potential across the phase boundary. Accounting for non-idealities is necessary to model properly the partitioning of different ionic species into the ionomer phase, which has shown to impact the selectivity of electrochemical synthesis.[128-131] The tendency for *i* and *j* to sorb into the ionomer phase is defined as the partitioning coefficient, Γ_{ij},.

$$\Gamma_{ij} = \frac{x_i^M \left(x_j^M\right)^{-\frac{z_i}{z_j}}}{x_i^0 \left(x_j^0\right)^{-\frac{z_i}{z_j}}} = \exp\left(\frac{\left(\mu_i^{ex,0} - \mu_i^{ex,M}\right) - \frac{z_i}{z_j}\left(\mu_j^{ex,0} - \mu_j^{ex,M}\right)}{RT}\right), \tag{37}$$

where μ_i^{ex} is the sum of all excess chemical potentials. Γ_{ij} is conveniently independent of electrostatic potential and represents the product of contributions from each excess potential

term. If $\Gamma_{ij} = 1$, the oppositely charged ions partition into the membrane following ideal Donnan equilibrium. If $\Gamma_{ij} > 1$, *i* and *j* favorably partition into the membrane, and if $\Gamma_{ij} < 1$, partitioning is unfavorable. For a neutral species *i*, the *j* terms disappear, and the ratio of mole fraction across the phase boundary is defined purely by the difference in excess chemical potential of the neutral species across the boundary.

3.3.4 Speciation

The thermodynamics of electrochemical-synthesis systems are governed by the physical properties of the distinct species present, including the solvent, free ions, ion pairs, neutral reactants and undissociated acids. Therefore, a complete thermodynamic model of an electrochemical system requires a complete specification of component speciation. For instance, in the electrochemical reduction of CO_2, the reaction of fed CO_2 with hydroxide anions forms bicarbonate anions, which can further dissociate to form carbonate anions. These reactions are responsible for parasitic CO_2 consumption and subsequent crossover of (bi)carbonate anions through anion-exchange membranes in CO_2 reduction devices. Tracking the (bi)carbonate anion formation in the ionomer is critical to modeling ion transport as well as single-pass conversion efficiency,[49, 132] because CO_2 can react with OH^- anions at the cathode to form (bi)carbonates and cross over to the anode, where H^+ generation from water oxidation reforms CO_2 that leaves the cell unreacted.[133] Similarly, speciation can be used to rationalize interacting ion transport and phenomena such as solvation and subsequent solvent transport. Additionally, the inclusion of dissociation reactions is necessary to describe accurately the local pH due to possible pH buffering capacity, which can greatly impact local microenvironment and product distributions.[134, 135] The equilibrium constants of these homogeneous reactions are defined as[107]

$$K_{\mathrm{i}} = \prod\left(a_i^{s_i}\right) = \exp\left(-\frac{\Delta G^0}{RT}\right), \tag{38}$$

where ΔG^0 is the free energy change of a given dissociation reaction in the standard state. (Note that the values of these equilibrium constants change with the choice of reference state.) A list of common buffer reactions in electrochemical synthesis and their equilibrium constants for a standard reference at 298 K is given in **Table 4**.

Table 4: Expressions for equilibrium constants of common dissociation reactions at 298 K using a standard reference in aqueous electrolyte.

Reaction	K_{i}	Ref.
$CO_{2(aq)} + H_2O \leftrightarrow H^+ + HCO_3^-$	4.27×10^{-7}	[136]
$HCO_3^- \leftrightarrow H^+ + CO_3^{2-}$	4.58×10^{-11}	[136]
$CO_{2(aq)} + OH^- \leftrightarrow HCO_3^-$	4.27×10^{7}	[136]
$HCO_3^- + OH^- \leftrightarrow H_2O + CO_3^{2-}$	4.58×10^{3}	[136]
$H_2CO_3 \leftrightarrow H^+ + HCO_3^-$	4.3×10^{-7a}	[137]
$H_2O \leftrightarrow H^+ + OH^-$	1.0×10^{-14}	[137]
$HCOOH_{(aq)} \leftrightarrow H^+ + HCOO^-$	1.77×10^{-4}	[138]
$CH_3COOH_{(aq)} \leftrightarrow H^+ + CH_3COO^-$	1.77×10^{-5}	[137]
$HOOCCOOH_{(aq)} \leftrightarrow H^+ + HOOCCOO^-$	3.47×10^{-2}	[139]
$HOOCCOO^- \leftrightarrow H^+ + OOCCOO^{2-}$	3.98×10^{-5}	[139]

$H_3PO_{4(aq)} \leftrightarrow H^+ + H_2PO_4^-$	7.52×10^{-3}	[137]
$H_2PO_4^- \leftrightarrow H^+ + HPO_4^{2-}$	6.23×10^{-8}	[137]
$HPO_4^{2-} \leftrightarrow H^+ + PO_4^{3-}$	4.8×10^{-13}	[137]
$H_2SO_{4(aq)} \leftrightarrow H^+ + HSO_4^-$	1.0×10^{3}	[140]
$HSO_4^- \leftrightarrow H^+ + SO_4^{2-}$	1.02×10^{-2}	[137]
$H_3BO_3 \leftrightarrow H^+ + H_2BO_3^-$	5.75×10^{-10}	[141]
$H_2BO_3^- \leftrightarrow H^+ + HBO_3^{2-}$	1.8×10^{-13}	[142]
$HBO_3^{2-} \leftrightarrow H^+ + BO_3^{3-}$	1.6×10^{-14}	[142]
$NH_3 + H_2O \leftrightarrow NH_4^+ + OH^-$	1.78×10^{-5}	[143]

[a]While the pK_a of the first carbonic acid dissociation is commonly noted as 6.37 (as is consistent with the value in the table). Recent work has suggested that the pK_a is actually substantially more acidic, with a pK_a of 3.49 due to the very fast equilibrium with CO_2.[144]

Work by Divekar *et al.* suggests that the rate coefficients and the unimolecular K_a of the buffer reactions change when measured in an ionomer environment as opposed to an aqueous solution.[145] However, the magnitude of these changes has not been widely reported or established. Future work should seek to characterize these values for implementation in the development of continuum models.

Lastly, it is important to note that Onsager demonstrated that the equilibrium for reactions that lead to the net generation and consumption of charge is strongly impacted by the local electric field. These field-enhanced dissociation kinetics are particularly relevant for modeling the dissociation of water at bipolar membrane (BPM) or in neutral water inside porous domains

in the high-field region at ionomer/ionomer or ionomer/water interfaces, as field-enhanced dissociation changes observed pH gradients (e.g., in BPMs).[117, 146] Additionally, these effects may be relevant in modeling the local pH near an electrolyte/metal interface due to the high electric fields achieved in the double layer.[70] To incorporate this effect into the homogeneous reaction kinetics, the equilibrium constant is modeled as a function of the local electric field.[147-149] The dependence of the equilibrium constant on the electric field is given by,[150]

$$K_a(E) = K_a^0 \frac{\left(\sum_{m=0}^{\infty} \frac{1}{m!(m+1)!}(2\beta E)^m\right)\cosh(\tau\beta E)\cosh(\tau)^{\beta E}}{1+\frac{1-\exp\left(-\frac{1}{\sigma}\right)}{2}\left(\sigma^2\beta E+(4.97\sigma)\frac{\sinh(0.0835\sigma\beta E)}{\cosh^2(0.0835\sigma\beta E)}\right)}. \quad (39)$$

In the above equation, K_a^0 is the equilibrium constant under zero electric field, E is the local electric field, and τ is a lumped parameter:

$$\tau = -0.128\ln(\cosh(0.235\sigma)) + 5.72\sigma^2, \quad (40)$$

where σ is dimensionless bond length defined as the bond length divided by the Bjerrum length.

$$\sigma = \frac{0.58\text{ nm}}{2l_b}, l_b = \frac{eF}{8\pi\varepsilon_{H_2O}RT} \quad (41)$$

In the above definition, e is the elementary charge, F is Faraday's constant, R is the ideal-gas constant, ε_{H_2O} is the dielectric permittivity of water, and T is the absolute temperature. The value of 0.58 nm represents the length at which the hydroxide and hydronium ions separate in water.[150] βE is a dimensionless electric field strength given as

$$\beta E = \frac{l_b F}{RT}E. \quad (42)$$

3.4 Transport

3.4.1 Mass Transport in Porous Electrodes

Electrochemical-synthesis devices typically mediate multicomponent and multiphase mass transfer of products and reactants. In such systems, it is necessary to ensure mass

conservation for each species as well as for each phase. The conservation of moles for each species can be written based on Eq. **(6)** for a discrete control volume within the porous electrode device,[12]

$$\frac{\partial \varepsilon_k c_{i,k}}{\partial t} + \nabla \cdot \mathbf{N}_{\boldsymbol{i,k}} = R_{i,k}. \tag{43}$$

In the above equation, ε_k is the volume fraction of phase k, $c_{i,k}$ is concentration of species i in phase k, $\mathbf{N}_{i,k}$ is the molar flux of species i in phase k, and $R_{i,k}$ is the total volume specific rate of generation of species i in phase k through reactions and phase change. While Eq. (43) is mole-based, an analogous mass-based conservation equation is also used in literature.

For a dilute system, only interactions between the mobile chemical species and the solvent are considered in the molar flux term. The diffusion term is estimated using Fick's law and the total molar flux is usually expressed as[151]

$$\mathbf{N}_{i,k} = -D_{i,k}^{eff} \nabla c_{i,k} + c_{i,k} \mathrm{v}_k^*, \tag{44}$$

where $D_{i,k}^{eff}$ is the effective diffusion coefficient of species i in phase k and v_k^* is the molar-averaged velocity of phase k[151]

$$\mathbf{v}_k^* = \frac{\sum_i \boldsymbol{N}_{i,k}}{c_{T,k}}, \tag{45}$$

where $c_{T,k}$ is the total concentration of phase k. The effective diffusivity $D_{i,k}^{eff}$ takes into account the phase volume fraction and tortuosity[152]

$$D_{i,k}^{eff} = \frac{\varepsilon_k}{\tau_k} D_{i,k}, \tag{46}$$

where $D_{i,k}$ is the molecular diffusivity of species i in the solvent and τ_k is the tortuosity of phase k. To simulate mass transfer of a gaseous species in a porous medium with pore sizes that are smaller than the mean free-path, Knudsen diffusivity must be considered. The diffusivity is then estimated as a combination of molecular and Knudsen diffusivity[152]

$$\frac{1}{D_{i,k}} = \frac{1}{D_{m_{i.k}}} + \frac{1}{D_{K_{i,k}}}. \tag{47}$$

$D_{m_{i,k}}$ is the molecular diffusivity of species *i* in phase *k*, which can be expressed for gases at low pressure using the following expression developed from kinetic theory and corresponding states arguments:[151]

$$D_{m_{i,k}} = \frac{a}{p}\left(\frac{T}{\sqrt{T_{cA}T_{cB}}}\right)^{b} \left(p_{c,A}p_{c,B}\right)^{\frac{1}{3}}\left(T_{c,A}T_{c,B}\right)^{\frac{5}{12}}\left(\frac{1}{M_A}+\frac{1}{M_B}\right)^{\frac{1}{2}}, \tag{48}$$

In the above expression, a and b are empirical constants with values of $a = 2.745 \times 10^{-4}$ $[\frac{\mathrm{cm}^2}{\mathrm{s}}\mathrm{atm}^{\frac{1}{3}}\mathrm{K}^{-\frac{5}{6}}\left(\frac{\mathrm{g}}{\mathrm{g-mol}}\right)^{\frac{1}{2}}]$, and $b = 1.823$ for nonpolar gas pairs. M_i, $T_{c,i}$, and $p_{c,i}$ represent the molar mass, critical temperature, and critical pressure of species *i,* respectively. For definitions of molecular diffusivity for gases at high pressure or molecules in aqueous solvent, more complicated, often empirical relationships are used, some expressions can be found in the text by Bird, Stewart and Lightfoot.[151]

In Eq. (47), $D_{K_{i,k}}$ is the Knudsen diffusivity[152]

$$D_{K_{i,k}} = \frac{2r_0}{3}\sqrt{\frac{8RT}{\pi M_i}}, \tag{49}$$

where r_0 is the pore radius and M_i is the molar mass of species i.

For a concentrated multi-component mixture, one must additionally consider solute/solute friction and interactions, which are neglected when using Fick's law. Hence, a Stefan-Maxwell framework is usually implemented,[153, 154] In this framework, the sum of the driving force is equal to the sum of the frictional forces acting on species *i* due to its motion relative to other species,

$$\boldsymbol{d_i} = \sum_{j \neq i} K_{ij}(\boldsymbol{v_j} - \boldsymbol{v_i}), \tag{50}$$

where $\boldsymbol{d_i}$ is the driving force per unit volume acting on a given species *i,* K_{ij} is a coefficient that represents the extent of frictional interaction between species *i* and *j* (where $K_{ij} = K_{ji}$ by Newton's third law of motion), and $\boldsymbol{v_i}$ is the velocity of species *i* relative to a reference velocity.

The left-hand side of Eq. (50) can be replaced with the following expression for a general driving force.

$$\boldsymbol{d_i} = c_i \left[\nabla \mu_i - \frac{M_i}{\rho} \nabla p - \boldsymbol{X_i} + \frac{M_i}{\rho} \sum_j \boldsymbol{X_j} c_j + \bar{S}_i \nabla \mathbf{T} \right] \tag{51}$$

The first term results from transport along chemical potential gradients, the second term is due to gradients in the thermodynamic pressure, the third and fourth terms arise due to external body forces per mole (*e.g.,* gravity), and the last term results from thermal diffusion. However, because thermal diffusion is typically small relative to other effects, this term can usually be neglected,[11, 111] resulting in the following form for the isothermal transport of species *i.*

$$\sum_{j \neq i} K_{ij}(\boldsymbol{v_j} - \boldsymbol{v_i}) = c_i \left[\nabla \mu_i - \frac{M_i}{\rho} \nabla p - \boldsymbol{X_i} + \frac{M_i}{\rho} \sum_j \boldsymbol{X_j} c_j \right] \tag{52}$$

It is important to note that for electrochemical synthesis devices with large temperature gradients, the effects of thermal diffusion will likely need to be considered.

Accounting for friction from a porous medium has been implemented differently in the literature. A commonly used framework in the modeling of porous media is the Dusty Gas Model (DGM)[155]; however, recently several discrepancies have been pointed out in this model.[156] Therefore, improved models such as the Binary Friction Model (BFM)[156] and Modified Binary Friction Model (MBFM)[152] have been developed. In the MBFM, Eq. (52) can be expressed as,[152]

$$\boldsymbol{\nabla} p_{i,k} = RT \sum_{\substack{j=1 \\ j \neq i}}^{n} \left(\frac{p_{i,k}\mathbf{N_{j,k}} - p_{j,k}\mathbf{N_{i,k}}}{p_k D_{ij}^{eff}} \right) - RT \left[D_{K_{i,k}} + \frac{k_k}{\chi_i} \right]^{-1} \mathbf{N_{i,k}}, \tag{53}$$

where $p_{i,k}$ is partial pressure of i and k_k is the permeability of phase k. The binary diffusion coefficients shown above can be related to the frictional coefficients (Eq. (50)) according to

$$D_{ij} = \frac{RT c_i c_j}{K_{ij} c_T}. \tag{54}$$

The effective binary diffusivity between i and j is symmetric due to Onsager reciprocity and is given as:

$$D_{ij}^{eff} = D_{ji}^{eff} = \frac{\varepsilon_k}{\tau_k} D_{ij} = \frac{\varepsilon_k}{\tau_k} D_{ji}. \tag{55}$$

The parameter χ_i is expressed as,

$$\chi_i = \frac{\mu M_i^{\frac{1}{2}}}{\sum_j p_{j,k} M_j^{\frac{1}{2}}}, \tag{56}$$

where μ is the mixture viscosity, which can be obtained using the Chapman-Enskog formulation.[157]

For a multi-component system with N species, one needs to determine n partial pressures ($p_{i,k}$), concentrations ($c_{i,k}$), or mole/mass fractions. In solving for these quantities, $(N-1)$ mole conservation equations can be invoked, leaving one additional degree of freedom. The final equation required to satisfy the degrees of freedom is the mixture mole fraction constraint.

$$\sum_{i=1}^{n} x_i = 1, \tag{57}$$

To determine the macroscale pressure, a hydrodynamic equation is required, which is typically Darcy's law[12]

$$\mathbf{v} = -\frac{\mathrm{k_k}}{\mu}\boldsymbol{\nabla} p_k, \tag{58}$$

where $\mathbf{v}$ is the mass-averaged velocity.

The total rate of generation of species i in Eq. (43) can be expressed as

$$R_{i,k} = -\sum_{n} A_{s,k} s_{n_{i,k}} \frac{i_n}{n_n F} + \sum_{l} A_{l,k} r_{i,l\to k} + \varepsilon_k \sum_{m} s_{m_{i,k}} R_{m_{i,k}}\,. \tag{59}$$

The first term describes the consumption of species i through various electrochemical reactions. $A_{s,k}$ is the specific area of the interface between electronically conducting phase (s) and phase k, $s_{n_{i,k}}$ is the stoichiometry of the n^{th} electrochemical reaction of species i in phase k, n_n is the number of electrons involved in l^{th} electrochemical reaction, and i_n is the transfer current between phases. The negative sign of this term assumes that consumption of species i produces current; a more detailed explanation of the kinetics is provided in Section 3.5. The

second term describes the source term due to phase transfer. $r_{i,l\to k}$ is the area specific rate of phase transfer of species i from phase l to phase k and $A_{l,k}$ is the interfacial area between phases l and k. The rate of phase transfer across a phase boundary can be obtained as,[102]

$$r_{i,l\to k} = k_{i,l\to k}\left(\mu_{i,l} - \mu_{i,k}\right), \tag{60}$$

where $k_{i,lk}$ is the transfer rate constant and $\mu_{i,l}$ and $\mu_{i,k}$ are the chemical potentials of species i in phase l and k, respectively. A large value of $k_{i,lk}$ is often used to ensure equilibrium between the two phases. Finally, the last term in Eq. (59) describes the generation of species i through homogeneous volumetric chemical reactions, where $R_{m_{i,k}}$ is the volume specific rate of generation of species i in phase k via the m^{th} chemical reaction. It is relevant to note that Eq. (59) does not include terms for heterogeneous adsorption of species i on a solid surface, but would take a form similar to that of the phase transfer term.

3.4.2 Charge Transport

The charge transport in an electrochemical-synthesis system follows the same conservation equation framework as Eq. (6),

$$\frac{\partial}{\partial t}\varepsilon_k z_i F c_{i,k} + \boldsymbol{\nabla}\cdot z_i F \mathbf{N}_{i,k} = z_i F R_{i,k}, \tag{61}$$

where z_i is charge of species i, F is Faraday's constant. $R_{i,k}$ is the rate of generation of species i through electrochemical and/or homogeneous reactions and can be estimated using Eq. (59). Because the model calculates the fluxes and local concentrations of each ionic species, when charge separation is determined by coupling these ionic species conservation equations with the Poisson equation (discussed later), the physics and capacitance of the diffuse double layer are calculated directly within a given phase k. However, it is important to note that the model does

not account for specific adsorption and desorption processes in the inner and outer Helmholtz planes explicitly, and a more sophisticated model is required to capture those multi-scale phenomena.

The overall charge conservation, which can be obtained by summing Eq. (61) over all phases and species, is also an important quantity. In many cases in electrochemical synthesis, the relevant processes to be simulated are macroscale ($\geq 10\,\mu m$) and at steady state, for which charge separation is negligible and there can be no net generation or consumption of total charge. For these cases, the overall charge conservation equation reduces to

$$\frac{\partial}{\partial t} F \sum_k \varepsilon_k \sum_i z_i c_{i,k} = -\nabla \cdot F \sum_k \sum_i z_i \mathbf{N}_{i,k}. \tag{62}$$

The current density in each phase is defined as

$$\mathbf{i}_k = F \sum_i z_i \mathbf{N}_{i,k}. \tag{63}$$

Furthermore, charge neutrality must be observed in each phase as well at steady state,

$$\sum_i z_i c_{i,k} = 0. \tag{64}$$

The overall assumption of charge neutrality in the domain relies on the assumption that there is no definite charge separation in the domain. The double layers near the phase boundaries (*e.g.,* between carbon and ionomer), however, may have charging/discharging during dynamic operations and therefore a charge separation can occur. One can neglect this when simulation domains are large enough that the double-layer volume is negligible and the timescales under

consideration are larger than charge/discharge cycles (~10 ms)[89, 158]. For small length and timescales, when charge separation cannot be neglected, Poisson's equation is used,[159]

$$\nabla^2 \phi_{\mathrm{k}} = -\frac{\rho_{\mathrm{e}}}{\varepsilon_0}, \tag{65}$$

where ϕ_{k} is the electric potential of phase k, ε_0 is the permittivity of the medium, and ρ_e is the net charge density defined as

$$\rho_e = F \sum_i z_i c_i. \tag{66}$$

The estimation of the flux of charged species depends on whether a dilute or concentrated solution approach is used. In the dilute-solution approach, the flux from diffusion, convection, and migration under electric field are linearly superimposed without accounting for any interaction between the various species; the net flux is given by the Nernst-Planck equation[159]

$$\mathbf{N}_{i,k} = -\varepsilon_k D_{i,k} \boldsymbol{\nabla} c_{i,k} + c_{i,k} \mathbf{v}_k^* - \varepsilon_k \frac{z_i D_{i,k} F c_{i,k}}{RT} \boldsymbol{\nabla} \phi_k. \tag{67}$$

This equation is sometimes also written in terms of mobility as

$$\mathbf{N}_{i,k} = -\varepsilon_k D_{i,k} \boldsymbol{\nabla} c_{i,k} + c_{i,k} \mathbf{v}_k^* - \varepsilon_k z_i u_{i,k} F c_{i,k} \boldsymbol{\nabla} \phi_k, \tag{68}$$

where Nernst-Einstein relation is used to define the mobility of ion i in phase k and is only valid at infinite dilution.

$$u_i = \frac{D_i}{RT} \tag{69}$$

The total ionic current in phase k can be obtained as[160]

$$\mathbf{i}_k = F\sum_i z_i \mathbf{N}_{i,k} = -\varepsilon_k F\sum_i z_i D_{i,k}\nabla c_{i,k} - \varepsilon_k F^2 \sum_i z_i^2 u_{i,k}\, c_{i,k}\nabla\phi_k + F\sum_i z_i c_{i,k}\mathbf{v}_k^*. \quad (70)$$

Since no net charge convection can occur due to charge neutrality, the above equation reduces to

$$\begin{aligned}\mathbf{i}_k &= -\varepsilon_k F\sum_i z_i D_{i,k}\nabla c_{i,k} - \varepsilon_k F^2 \sum_i z_i^2 u_{i,k}\, c_{i,k}\nabla\phi_k \\ &= -\varepsilon_k F\sum_i z_i D_{i,k}\nabla c_{i,k} - \varepsilon_k \kappa_k \nabla\phi_k,\end{aligned} \quad (71)$$

where κ_k is ionic conductivity of phase k

$$\kappa_k = F^2 \sum_i z_i^2 u_{i,k}\, c_{i,k}. \quad (72)$$

Under pure migration (no concentration gradients), Eq. (71) reduces to Ohm's law

$$\mathbf{i}_k = -\kappa_k \nabla\phi_k. \quad (73)$$

The Nernst-Plank equation framework is easy to use as it requires the knowledge of only N diffusivities ($D_{i,k}$); however, it relies on the assumption of a dilute solution. For thorough understanding of multi-ion transport in a solution, a more rigorous concentrated-solution theory approach is required, which accounts for all binary interactions among all components. The concentrated-solution theory for charge transport also utilizes the Stefan-Maxwell framework, similar to the mass-transport relation described in the previous section (**Section 3.4.1** Eqs. (51)-(52)).

Prior studies have redefined the Stefan-Maxwell equations in terms of experimentally measurable properties,

$$\mathbf{N}_{i,k} = -\frac{t_{i,k}\kappa_k}{z_i F^2}\frac{\boldsymbol{\nabla}\mu_{n,k}}{z_n} - \sum_j \left(\alpha_{ij,k} + \frac{t_{i,k}t_{j,k}\kappa_k}{z_i z_j F^2}\right)\boldsymbol{\nabla}\mu_{j,n,k}, \tag{74}$$

where $t_{i,k}$ is transference number of species i in phase k, $\alpha_{ij,k}$ is the transport coefficient between species i and j. $\mu_{i,n,k}$ is the electrochemical potential of species i relative to species n[161]

$$\mu_{i,n,k} = \mu_{i,k} - \frac{z_i}{z_n}\mu_{n,k}. \tag{75}$$

Equation (74) can also be expressed in terms of current density as[160]

$$\mathbf{N}_{i,k} = \frac{t_{i,k}\mathbf{i}_k}{z_i F} - \sum_j \alpha_{ij,k}\boldsymbol{\nabla}\mu_{j,n,k}. \tag{76}$$

The coefficients $\alpha_{ij,k}$ are symmetric, which results in $\frac{(N-1)N}{2}$ independent coefficients. Several of the $\alpha_{ij,k}$'s and $t_{i,k}$'s can be related to experimental measurements of conductivity, transference numbers, electro-osmotic coefficients, and diffusion coefficients. Furthermore, a few of the coefficients, such as interactions between same charges, can be safely neglected due to electrostatic repulsions; however, even with the available measurements and the neglected parameters, several of the transport parameters remain unknown for a variety of systems. Prior work has presented detailed theoretical frameworks to estimate several of these parameters.[116, 162] Overall, even though the concentrated-solution approach is more rigorous, it is often difficult to implement due to a lack of interaction parameter values or expressions.

For the simple case of a single ion in a polymer electrolyte, the concentrated-solution framework simplifies. Such conditions may exist in water electrolyzers where only protons or hydroxide ions are present. The concentrated-solution-theory framework in such cases reduces to[163]

$$\mathbf{i}_k = -\kappa_k \nabla \phi_k - \frac{\kappa_k \xi_k}{F} \nabla \mu_{w,k}, \tag{77}$$

$$\mathbf{N}_{w,k} = -\frac{\kappa_k \xi_k}{F} \nabla \phi_k - \left(\alpha_k + \frac{\kappa_k \xi_k^2}{F^2} \right) \nabla \mu_{w,k}, \tag{78}$$

where $\mu_{w,k}$ is chemical potential of water in the electrolyte, α_k is the water diffusion coefficient in electrolyte, κ_k is the conductivity of pure polymer electrolyte, and ξ_k is the electroosmotic coefficient. This framework is extensively used in fuel cells and water electrolyzers.[11, 126]

While a concentrated-solution framework like the one shown in Eq. (74) may be infeasible for multi-ion mixtures due to the number of coefficients, the single-ion model shown above can be extended to account for multiple ions.[12] The flux of species i can be expressed as

$$\mathbf{N}_{i,k} = -x_{i,k} \frac{\kappa_{i,k}}{z_i F} \nabla \phi_k - x_{i,k} \frac{\kappa_{i,k} \xi_{i,k}}{z_i^2 F^2} \nabla \mu_{w,k} - D_{i,k} c_t \nabla x_{i,k}, \tag{79}$$

where $x_{i,k}$ is the mole fraction of species i, $\kappa_{i,k}$ is the limiting electrolyte conductivity when saturated with ion i, $D_{i,k}$ is the diffusion coefficient of species i in solution and c_t is the total ion concentration. The water transport is then obtained as[12]

$$\mathbf{N}_{w,k} = -\sum_i x_{i,k} \frac{\kappa_{i,k} \xi_{i,k}}{z_i F} \nabla \phi_k - \left(\alpha_k + \sum_i x_{i,k} \frac{\kappa_{i,k} \xi_{i,k}^2}{z_i^2 F^2} \right) \nabla \mu_{w,k}. \tag{80}$$

This framework is ultimately a compromise between the dilute and concentrated solution framework that relies on an assumption of parallel transport of each ionic species i, and only considers interactions between the mobile species and the solvent because the solvent is concentrated. However, it neglects species-species frictional interactions, assuming dilute solute. This assumption may breakdown when the ionic species concentrations are high enough such that inter-species interactions become dominant.

The electron transport in the system is modeled using Ohm's law,[164]

$$\mathbf{i}_s = -\sigma_s^{eff} \nabla \phi_s, \tag{81}$$

where σ_s^{eff} is the effective electronic conductivity and ϕ_s is the electronic potential.

3.4.3 Energy Transport

For energy transport, Eq. (6) can be expressed as[12]

$$\begin{aligned} &\rho_k C_{p,k} \left(\frac{\partial T_k}{\partial t} + \mathbf{v}_k^* \cdot \nabla T_k \right) + \left(\frac{\partial \ln p_k}{\partial \ln T_k} \right)_{p_k, x_{i,k}} \left(\frac{\partial p_k}{\partial t} + \mathbf{v}_k^* \cdot \nabla p_k \right) \\ &= Q_{k,p} - \nabla . \boldsymbol{q}_k - \bar{\bar{\boldsymbol{\tau}}} : \nabla \mathbf{v}_k^* + \sum_i \bar{H}_{i,k} \nabla \cdot \mathbf{J}_{i,k} + \sum_i \bar{H}_{i,k} R_{i,k}. \end{aligned} \tag{82}$$

The second term on the left side represents the energy due to reversible work; for the electrochemical systems of interest, it is negligible. $Q_{k,p}$ represents local heat transfer between phases. For these electrochemical systems, all phases at a point can be assumed to be in thermal equilibrium and therefore at the same temperature.[11] This results in elimination of $Q_{k,p}$. The term $\bar{\bar{\boldsymbol{\tau}}} : \nabla \mathbf{v}_k^*$ represents viscous dissipation and can also be safely neglected.[11] $\bar{H}_{i,k}$ is the specific enthalpy of the species i in phase k. The term $\bar{H}_{i,k} \nabla \cdot \mathbf{J}_{i,k}$ represents enthalpy change due to diffusion and the heat flux $\boldsymbol{q}_k$ is defined as:

$$q_k = \sum_i \bar{H}_{i,k} \mathbf{J}_{i,k} - k_{T,k}^{eff} \nabla T_k, \tag{83}$$

where the first terms on the right side represent the heat flux associated with mass transport. The second term on the right side represents the conductive heat flux. $k_{T,k}^{eff}$ is the effective thermal conductivity. Eliminating all the negligible terms and using Eq. (83) in Eq. (82) yields,

$$\rho_k C_{p,k} \frac{\partial T_k}{\partial t} = -\rho_k C_{p,k} \mathbf{v}_k^* \cdot \boldsymbol{\nabla} T_k + \boldsymbol{\nabla}.\left(k_{T,k}^{eff} \boldsymbol{\nabla} T_k\right) - \sum_i \boldsymbol{J_{i,k}} \cdot \boldsymbol{\nabla} \bar{H}_{i,k} + \sum_i \bar{H}_{i,k} R_{i,k}, \quad (84)$$

where $C_{p,k}$ is the specific heat capacity.

The last term on the right side of the above equation represents different heat sources in the system. In general, heat generation during electrochemical synthesis is caused by 3 different phenomena: electrochemical reactions, phase change, and homogeneous chemical reactions.

Heat in the electrochemical reaction is generated because of the reversible and irreversible thermodynamic changes. The irreversible heat can be easily estimated using the corresponding reaction overpotential ($\dot{Q}_{irrev,k} = \sum_l i_{v,l} \eta_l$) where $i_{v,l}$ is the current per volume (mA cm^{-3}). The reversible heat can be estimated by calculating the entropy change or by using the corresponding Peltier coefficient if available[12]

$$\dot{Q}_{rev,k} = \sum_l r_{i,l} \, \mathrm{T} \Delta s_l \simeq \sum_l i_{v,l} \Pi_l, \quad (85)$$

where Δs_l is the specific entropy change during l^{th} reaction and Π_l is associated Peltier coefficient. The heat due to phase change or adsorption/desorption is estimated as

$$\dot{Q}_{phase,k} = \sum_l r_{i,l \to k} \Delta H_{i,l \to k}, \quad (86)$$

where $\Delta H_{i,l \to k}$ is the specific enthalpy of phase change or adsorption/desorption from phase l to phase k.

Finally, the heat generation due to ohmic (Joule) heating is derived from the third term on the right side of Eq. (84) and can be derived as follows.

$$\dot{Q}_{ohm,k} = -\sum_i \boldsymbol{J_{i,k}} \cdot \boldsymbol{\nabla} \bar{H}_{i,k} = \boldsymbol{i}_k \cdot \boldsymbol{\nabla} \phi_k \tag{87}$$

Substituting in Ohm's law for the gradient of the electrostatic potential results in the final form for the Joule heating term.

$$\dot{Q}_{ohm,k} = \boldsymbol{i}_k \cdot \boldsymbol{\nabla} \phi_k = \frac{\mathbf{i}_k \cdot \mathbf{i}_k}{\kappa_k^{eff}}, \tag{88}$$

where κ_k^{eff} is the effective conductivity of phase k. Replacing all the source terms in Eq. (84) results in

$$\rho_k C_{p,k} \frac{\partial T_k}{\partial t} = -\rho_k C_{p,k} \mathbf{v}_k^* \cdot \boldsymbol{\nabla} T_k + \boldsymbol{\nabla} . \left(k_{T,k}^{eff} \boldsymbol{\nabla} T_k \right) + \sum_l i_{v,l} (\eta_l + \Pi_l) + \sum_l r_{i,l \to k} \Delta H_{i,l \to k} + \frac{\mathbf{i}_k \cdot \mathbf{i}_k}{\kappa_k^{eff}}. \tag{89}$$

Summing Eq. (89) over all phases, the overall energy conservation for the system is

$$\sum_k \rho_k C_{p,k} \frac{\partial T}{\partial t} = -\sum_k \rho_k C_{p,k} \mathbf{v}_k^* \cdot \boldsymbol{\nabla} T_k + \boldsymbol{\nabla} . \left(k_T^{eff} \boldsymbol{\nabla} T \right) + \sum_k \sum_l i_{v,l} (\eta_l + \Pi_l) + \sum_k \sum_l r_{i,l \to k} \Delta H_{i,l \to k} + \sum_k \frac{\mathbf{i}_k \cdot \mathbf{i}_k}{\kappa_k^{eff}}. \tag{90}$$

3.5 Kinetics

3.5.1 Electrochemical Reactions

Several source terms in the mass, charge, and energy balances (Eqs. (43), (61), and (82)) described above arise due to electrochemical reactions. Each chemical species can participate in multiple electrochemical reactions at the electrode surfaces. The total reaction rate of species i in phase k can be obtained as

$$r_{i,k} = \sum_{l} r_{i,k,l} = \sum_{l} s_{i,k,l} \frac{i_l}{n_l F}, \tag{91}$$

where $r_{i,k,l}$ is the rate of reaction of i in the l^{th} half-reaction (*e.g.,* hydrogen evolution, CO evolution, *etc.*) and i_l is the current production due to l^{th} reaction of species i in phase k. $s_{i,k,l}$ is the stoichiometry of i in the reaction and n_l is the number of electrons produced in the reaction such that the reaction can be expressed as,

$$\sum_{r=1}^{c} s_{r,k,l} A_r + n_l e^- \rightarrow \sum_{p=1}^{a} s_{p,k,l} A_p, \tag{92}$$

where s_i is the stoichiometric coefficient of species i, A_r's are the reactants (cathodic), and A_p's are products (anodic). The generation of anodic and cathodic products must balance to ensure mass and charge conservation.

The Butler-Volmer equation can be used to model the relationship between the current density and applied potential for a given, elementary electrochemical half-reaction, l.[111, 112]

$$i_l = i_{0,l} \left\{ \exp\left[\frac{(1-\beta) nF}{RT} \left(\phi_s - \phi_k - U_l \right) \right] - \exp\left[-\frac{\beta nF}{RT} \left(\phi_s - \phi_k - U_l \right) \right] \right\}, \tag{93}$$

where i_l is the area-specific transfer current density at the interface between solid phase s and electrolyte phase k due to the l^{th} reaction, and U_l is the local equilibrium potential for the l^{th} half-reaction defined by Eq **(22)**, which takes into account local variations in the activities of the reactant and product species. ϕ_s is the electrostatic potential within the solid electrode phase, and ϕ_k is the electrostatic potential within the electrolyte phase. Their difference represents the potential drop across the electrochemical double layer. β is the symmetry factor, which represents the fraction of applied potential that promotes the cathodic reaction. Similarly, $1 - \beta$

represents the fraction of applied potential that promotes the anodic reaction. For many elementary reactions, the symmetry factor is assumed to be $\frac{1}{2}$. The pre-factor, i_0, is known as the exchange current density, and can be written as follows:

$$i_{0,l} = nFk_a^{\beta}k_c^{1-\beta}\prod_{p=1}^{a}(a_p)^{s_{p,k,l}(\beta)}\prod_{r=1}^{c}(a_r)^{s_{r,k,l}(1-\beta)} \tag{94}$$

where k_a is the rate constant of the anodic direction, and k_c is the rate constant of the cathodic direction. $s_{r,k,l}$ and $s_{p,k,l}$ correspond to the stoichiometric coefficients of reactants (*r)* and products (*p*), respectively, in reaction *l* in phase *k*, as defined in Eq. (93). a_p and a_r correspond to the activities of the reactants and products of reaction *l* at the electrode surface.

When significant species concentration polarization occurs, the activity of each species at the electrode surface will differ from that in the bulk. In such circumstances it is useful to reference the exchange current density to the activities of the species in the device at the open circuit condition of the cell a_i^{ref} as opposed to the standard reference. Doing so divides and multiplies the $i_{0,l}$ in Eq. 94 to produce Eq. 95. In doing so, when the cell has no concentration polarization, the activity dependence (*i.e.,* mass transfer) terms in the i_0 become unity. Proper values for a_i^{ref} include the bulk electrolyte activity in an aqueous cell, or the channel or feed activity in a vapor fed device. It is important to note that conditions at open circuit are not equivalent to the standard conditions (unity activity) at which U_l^0 is referenced, because the bulk electrolyte or channel may not be at unity activity. Redefining the i_0 in this new reference state yields the following:

$$i_{0,l} = nFk_a^{\beta}k_c^{1-\beta}\prod_{p=1}^{a}(a_p^{ref})^{s_{p,k,l}(\beta)}\prod_{r=1}^{c}(a_r^{ref})^{s_{r,k,l}(1-\beta)}\prod_{p=1}^{a}\left(\frac{a_p}{a_p^{ref}}\right)^{s_{p,k,l}(\beta)}\prod_{r=1}^{c}\left(\frac{a_r}{a_r^{ref}}\right)^{s_{r,k,l}(1-\beta)} \tag{95}$$

In most cases in electrochemical synthesis, however, the assumption of a single elementary step is a poor one. Therefore, to model these complex systems with multiple reactions steps, we can either use a complete microkinetic model (discussed later), or we can invoke the quasi-equilibrium approximation on all steps other than a single rate determining step,[165] a simplifying assumption that enables the determination of a single rate expression. Doing so results in the following rate expression for the Butler-Volmer that is applicable to more complicated reaction networks.

$$i_l = i_{0,l}\left\{\exp\left[\frac{\alpha_{a,l}F}{RT}\left(\phi_s - \phi_k - U_l\ \right)\right] - \exp\left[-\frac{\alpha_{c,l}F}{RT}\left(\phi_s - \phi_k - U_l\ \right)\right]\right\}\exp\left(-\frac{E_{a,l}}{R}\left(\frac{1}{T}-\frac{1}{T_0}\right)\right) \qquad (96)$$

$\alpha_{a,l}$ and $\alpha_{c,l}$ are the anodic and cathodic transfer coefficients (which sum to 1 for an elementary reaction, but in more complex chemistries range from 0.2 to 2[111]), respectively, for the l^{th} reaction. These transfer coefficients can be related to the properties of the microkinetic mechanism as follows:

$$\alpha_a = \frac{n-s}{\nu} - q\beta_{s+1} \qquad (97)$$

$$\alpha_c = q\beta_{s+1} + \frac{s}{\nu} \qquad (98)$$

In the above expressions, q represents the number of electrons transferred in the rate-determining step, s represents the number of electrons transferred prior to the rate-determining step, $(s+1)$ represents the index of the rate-determining step itself, β_{s+1} is the symmetry factor of the rate-determining step, n is the number of electrons transferred in the overall reaction, and ν is the multiplicity of the rate-determining step (*i.e.,* how many times the rate-determining step must occur for the overall action to proceed). The sum of these transfer coefficients is $\alpha_{c,l} + \alpha_{a,l} = \frac{n}{\nu}$.

For the multi-step electrochemical reaction, the definition of i_0 also differs from that occurring in the single-elementary step model, and can be defined as,

$$i_{0,l} = {a_r^{ref}}^{\gamma_{r,k,l}} {a_p^{ref}}^{\gamma_{p,k,l}} \prod_r \left(\frac{a_r}{a_r^{ref}}\right)^{\gamma_{r,k,l}} \prod_p \left(\frac{a_p}{a_p^{ref}}\right)^{\gamma_{p,k,l}} nFk_{s+1,c} \prod_{j=1}^{s} K_{j,eq}^{\frac{1}{\nu}} \exp\left[-\frac{\alpha_c F}{RT} U_l^0\right], \quad (99)$$

where $k_{s+1,c}$ is the forward rate constant of the cathodic reaction of the rate-determining step, and $K_{i,eq}$ represents the equilibrium constant of the i^{th} step in the reaction mechanism. The continued product of the equilibrium constants of the individual kinetic steps prior to the rate determining step arises when determining the activity of the intermediate species in the rate determining step by invoking the quasi-equilibrium approximation. The last exponential term results when shifting from using the absolute voltage to the surface overpotential. This shift from absolute voltage to surface overpotential is explained thoroughly in the book of Newman and Thomas-Alyea.[111] Nonetheless, interested readers should contact the author for the full derivation of these generalized Butler-Volmer kinetics. $\gamma_{r,k,l}$ and $\gamma_{p,k,l}$ are the apparent rate orders of the reaction with respect to the reactants and products, respectively, defined below:

$$\gamma_{r,k,l} = \frac{\alpha_a}{n} s_{r,k,l} \quad (100)$$

$$\gamma_{p,k,l} = \frac{\alpha_c}{n} s_{p,k,l} \quad (101)$$

The last factor in Eq. (96) is an Arrhenius dependence that accounts for changes in the kinetics upon changes in temperature, where $E_{a,l}$ is the activation energy of the overall reaction.

The potential difference term in Eqs. (93) and (96) can be expressed as an electrode surface overpotential for a given half-reaction *l*,

$$\eta_{S,l} = \phi_s - \phi_k - U_l \quad .$$

(102)

It is important to note is that the surface overpotential $\eta_{S,l}$ is defined such that the driving force for the current density towards a particular reaction, l, is defined as the difference between the applied potential and the equilibrium potential of reaction l at the local conditions that exist at the electrode surface, rather than at standard state. If we return to the case-study discussed in **Section 3.3.1** where reaction l represents AN reduction, this overpotential is defined as:

$$\eta_{S,l} = \phi_s - \phi_k - \left[0.67\ [\mathrm{V}] - \frac{2.303RT}{F}\mathrm{pH} + \frac{RT}{F}\ln(a_{AN}) - \frac{RT}{2F}\ln(a_{ADN})\right]. \tag{103}$$

The Butler-Volmer kinetics detailed in Eq. (96) can be recast such that instead of referencing the overpotential to local, surface conditions, the overpotential is instead referenced to the standard state (unity activity of all products and reactants).

$$i_l = i_{0,l}\left[\prod_{p=1}^{a}\left(\frac{a_p}{a_p^{ref}}\right)^{s_{p,k,l}\frac{\alpha_{a,l}}{n}} \prod_{r=1}^{c}\left(\frac{a_r}{a_r^{ref}}\right)^{-s_{r,k,l}\frac{\alpha_{a,l}}{n}} \exp\left(\frac{\alpha_{a,l}F}{RT}(\phi_s - \phi_k - U_l^0)\right) - \prod_{r=1}^{c}\left(\frac{a_r}{a_r^{ref}}\right)^{s_{r,k,l}\frac{\alpha_{c,l}}{n}} \prod_{p=1}^{a}\left(\frac{a_p}{a_p^{ref}}\right)^{-s_{p,k,l}\frac{\alpha_{c,l}}{n}} \exp\left(-\frac{\alpha_{c,l}F}{RT}(\phi_s - \phi_k - U_l^0)\right)\right] \exp\left(-\frac{E_{a,l}}{R}\left(\frac{1}{T} - \frac{1}{T_0}\right)\right), \tag{104}$$

Recasting the expression simply extracts the Nernstian correction out from the exponential, but doing so has implications for the apparent reaction orders observed. For the case where local conditions are referenced, the apparent reaction orders are $\gamma_{r,k,l}$ or $\gamma_{p,k,l}$ for the cathodic and anodic reactions, respectively. However, when standard conditions are referenced, the apparent reaction orders are $\frac{s_{r,k,l}}{\nu}$ and $\frac{s_{p,k,l}}{\nu}$ for the cathodic and anodic reactions, respectively (as can be seen by substituting in the expression for i_0). Thus, when choosing and measuring reaction orders for the reactants and products, one must be wary of their choice of referencing (to local conditions or to standard conditions) within the definition of overpotential used.

Returning to the definition where surface conditions are used, and considering isothermal operation, which will be the case for many systems in electrochemical synthesis, equation (96) can be then rewritten as,

$$i_l = i_{0,l}\left[\exp\left(\frac{\alpha_{a,l}F}{RT}\eta_S\right) - \exp\left(-\frac{\alpha_{c,l}F}{RT}\eta_S\right)\right] \tag{105}$$

When certain desired reactions are sluggish in nature, one must operate further away from their reference potentials to achieve appreciable current densities. Consequently, the magnitude of the overpotential η is large for these electrochemical reactions. Depending on a positive or negative overpotential, either the cathodic or anodic term of Eq. (96) becomes negligible, resulting in the well-known Tafel equation,

$$i_l = \begin{cases} i_{0,l}\exp\left(\frac{\alpha_{a,l}F}{RT}\eta_S\right) & \text{If } \alpha_a F\eta_S \gg RT, \\ -i_{0,l}\exp\left(-\frac{\alpha_{c,l}F}{RT}\eta_S\right) & \text{If } \alpha_c F\eta_S \ll -RT. \end{cases} \tag{106}$$

As written, when the potential at an electrode is highly positive when compared to the equilibrium potential, the anodic reaction is driven. Conversely, when the potential a given electrode is highly negative when compared to the equilibrium potential, the cathodic reaction is driven. Most commonly, Tafel kinetics are used to model the sluggish anodic oxygen-evolution or cathodic CO_2 reduction reactions commonly found electrochemical-synthesis systems.

Both the Butler-Volmer and Tafel kinetics assume that the reaction is controlled by a particular rate-determining step. In reality, however, most reactions occur in multiple steps, and the rate-determining step can change with the operating potential and local reaction environment. Furthermore, since all reactions happen at the same catalyst sites, competition between different species can affect adsorption of different reactants and intermediate species to the surface. One

may use multi-step reaction kinetics to account for changes in operating potential and reaction conditions on the kinetics, but this comprehensive microkinetic framework has not been developed for many electrochemical-synthesis reactions. Notwithstanding, one can still account for competition between parallel reactions by incorporating surface coverage effects into a traditional single rate-determining-step framework (*i.e.*, Butler-Volmer or Tafel kinetics). To do so, one must assume that each reaction proceeds through a particular rate-determining step, and that the remaining faster steps give rise to negligible surface coverages of the reaction intermediates due to an assumed high-turnover frequency. The balance on the total available reaction sites is

$$\sum_{l} \theta_l = 1, \tag{107}$$

where θ_l is the surface coverage of the intermediate species in l^{th} reaction. The surface coverage of each intermediate can be obtained using an isotherm (*e.g.,* Langmuir)[166, 167]

$$\theta_l = \frac{\exp\left(\frac{\alpha'_{a,l}F}{RT}\eta_{int,l}\right)}{\exp\left(\frac{\alpha'_{a,l}F}{RT}\eta_{int,l}\right) + \exp\left(-\frac{\alpha'_{c,l}F}{RT}\eta_{int,l}\right)}, \tag{108}$$

where $\alpha'_{a,l}$ and $\alpha'_{c,l}$ are fitting coefficients. $\eta_{int,l}$ can be defined as

$$\eta_{int,l} = \phi_s - \phi_k - U_{int,l}, \tag{109}$$

where $U_{int,l}$ is the equilibrium potential for the rate-determining step of the l^{th} reaction. These coefficients and the equilibrium potential can be obtained by fitting the experimentally collected kinetics data.

Figure 11 shows a typical Langmuir isotherm coverage for different equilibrium potentials. Once the coverages of the intermediates are known, the reaction rates can be corrected to account for the surface coverage. For example, anodic Tafel kinetics can be modified as

$$i_l = i_{0,l}\theta_l \exp\left(\frac{\alpha_{a,l}F}{RT}\eta_l\right). \tag{110}$$

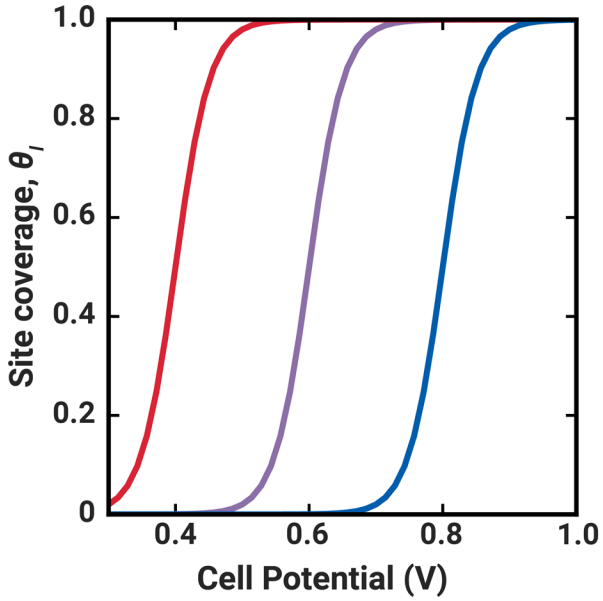

Figure 11: A typical Langmuir isotherm (Eq (108)) showing change of surface coverage with operating potential. Different lines represent the adsorption isotherms for the intermediates of different rate-determining steps with different equilibrium potentials ($U_{int,l}$).

To model completely the competing electrochemical reaction pathways occurring in an electrochemical-synthesis device without loss of generality, one must employ a microkinetic model.[20, 168, 169] The microkinetic model is used to calculate the concentrations of all surface species and relate them to concentration of reactants and products in the outer Helmholtz plane (OHP) that participate in each step of a given microkinetic mechanism. An example of a reaction scheme is shown in **Figure 12** for the electrochemical CO reduction over a Cu catalyst. Microkinetic models typically employ DFT-derived parameters to describe the free energy of

adsorption for each step in the assumed mechanism and can be used to predict catalytic activity of a broad range of electrochemical reactions.[169]

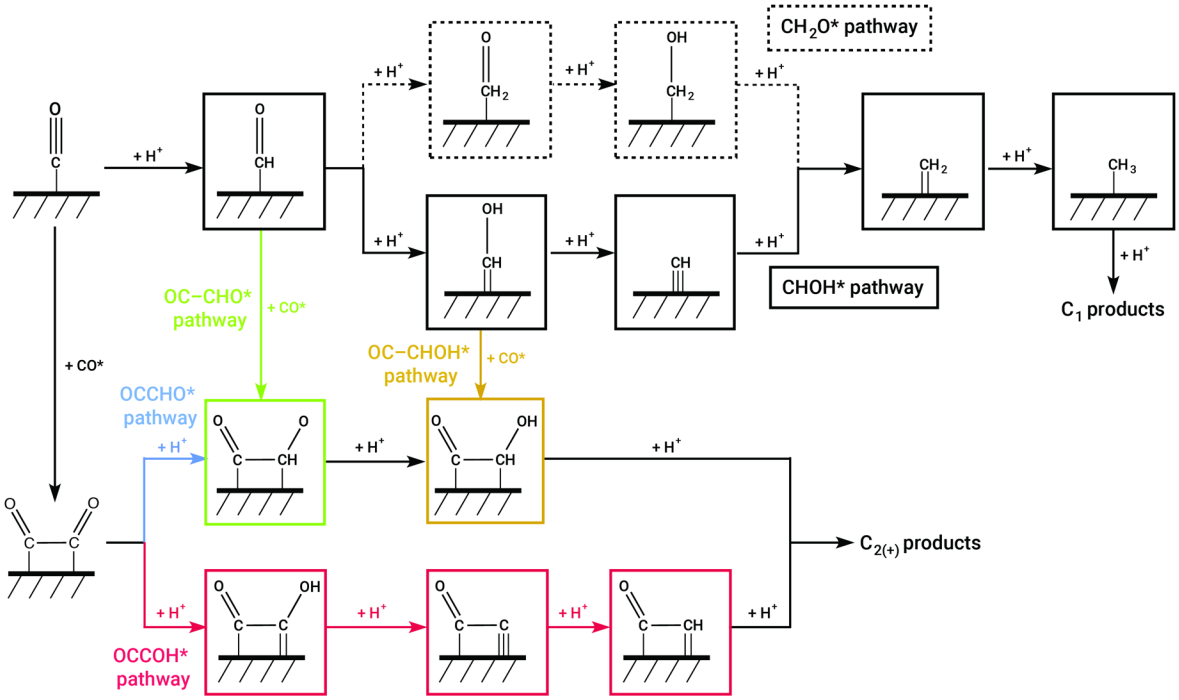

Figure 12: Potential microkinetic pathways of CO reduction on copper catalysts. Adapted with permission from Liu *et al.*[134] Copyright Creative Commons 2019 http://creativecommons.org/licenses/by/4.0/.

Consider the first two elementary steps in the mechanism outlined by Liu *et al.* for electrochemical CO reduction on Cu.[134]

$$CO_{(g)} + * \rightleftharpoons CO^* \tag{111}$$

$$CO^* + H^+ + e^- \rightleftharpoons CHO^* \tag{112}$$

The rate of these elementary steps can be written as follows.

$$r_1 = k_1 a_{CO(g)} \theta_* - k_{-1} \theta_{CO} \tag{113}$$

$$r_2 = k_2 \exp\left(-\frac{\beta_2 F}{RT} V\right) a_{H^+} \theta_{CO} - k_{-2} \exp\left(\frac{1-\beta_2}{RT} FV\right) \theta_{CHO} \quad (114)$$

Reaction 2 (Eq. (111)) possesses an overpotential-dependent exponential term due to the charge transfer. While shown here for only the first two steps in the mechanism, the complete microkinetic model would determine rates for every microkinetic step in the mechanism. From these rate expressions, the overall current density can be calculated as

$$i = -\frac{nFr_i}{\nu_i}, \quad (115)$$

where r_i is the rate of charge transfer step *i,* and ν_i is the stoichiometric number of charge transfer step *i*. The condition that this current density must be equivalent at a given applied potential for all elementary charge-transfer steps is used to solve for local coverages and concentrations and assumes a pseudo steady state. The microkinetic model can be used to obtain Tafel parameters for any given reaction condition and can thus be easily compared to experiment. The key advantage of this technique for electrocatalytic application is that, unlike the Butler-Volmer analysis which uses overall reactions and assumes rate-determining steps and surface coverages, the microkinetic model makes no such simplifying assumptions. The microkinetic model dictates the coverages of all adsorbed species involved in each elementary step in the reaction pathway for the chosen mechanism. The impact of pH, mass transport, site blocking, adsorbate-adsorbate interactions, etc. can be incorporated by coupling the activities and coverages derived in the microkinetic model to a multi-scale continuum transport model of the electrical double layer and mass-transport boundary layers.

3.5.2 Homogeneous Reactions

In electrochemical systems for which speciation reactions (see **Section 3.3.4**) are not in thermodynamic equilibrium, the reaction source term in Eq. (43) also includes the generation and consumption of species through homogeneous reactions that occur throughout the modeled domain. While these reaction terms are often neglected, the source terms resulting from these reactions are particularly relevant in electrochemical-synthesis applications. Works by Hashiba *et al.* and Singh *et al.* elucidate that the buffering capacity of these reactions substantially impacts the local pH and reactant concentration in electrochemical CO_2 reduction,[68, 170] and work by Bui *et al.* demonstrates that titration currents generated by the buffering of species in a bipolar-membrane electrolyzer drastically impacts its electrochemical behavior.[117]

The forward rate constants for common buffer reactions in electrochemical synthesis and their sources are given in **where** $\mathrm{sn_i}$ are the stoichiometric coefficient of species *i* in reaction *n*, wherein $\mathrm{s_{n_i}} < 0$ corresponds to reactants of the overall reaction, and $\mathrm{s_{n_i}} > 0$ corresponds to

$$k_{-i} = \frac{k_i}{K_i}, \tag{116}$$

products of the overall reaction.

Table 5. The reverse rate constants for these reactions can be calculated through using the equilibrium constants for these reactions given in **Table 4**,

where k_i and k_{-i} are the forward and reverse rate constants of reaction i, respectively. The rate of consumption or generation through homogeneous reactions can be written as

$$R_{B,i} = \sum_n s_{n_i} \left(k_n \prod_{s_{n_i}<0} a_i^{-s_{n_i}} - \frac{k_n}{K_n} \prod_{s_{n_i}>0} a_i^{s_{n_i}} \right) \tag{117}$$

where s_{n_i} are the stoichiometric coefficient of species i in reaction n, wherein $s_{n_i} < 0$ corresponds to reactants of the overall reaction, and $s_{n_i} > 0$ corresponds to products of the overall reaction.

Table 5: Expressions for forward rate constants of common dissociation reactions at 298 K using a standard reference.[a]

Reaction	k_i	Unit[a]	Ref.
$CO_{2(aq)} + H_2O \leftrightarrow H^+ + HCO_3^-$	3.71×10^{-2}	M s^{-1}	136
$HCO_3^- \leftrightarrow H^+ + CO_3^{2-}$	59.44	M s^{-1}	136
$CO_{2(aq)} + OH^- \leftrightarrow HCO_3^-$	2.23×10^3	M s^{-1}	136
$HCO_3^- + OH^- \leftrightarrow H_2O + CO_3^{2-}$	6.0×10^9	M s^{-1}	136
$H_2CO_3 \leftrightarrow H^+ + HCO_3^-$	2.0×10^4	M s^{-1}	171
$H_2O \leftrightarrow H^+ + OH^-$	8.9×10^{-4}	M s^{-1}	150
$HCOOH_{(aq)} \leftrightarrow H^+ + HCOO^-$	4.0×10^5	M s^{-1}	67
$CH_3COOH_{(aq)} \leftrightarrow H^+ + CH_3COO^-$	7.97×10^5	M s^{-1}	171
$HSO_4^- \leftrightarrow H^+ + SO_4^{2-}$	1.0×10^9	M s^{-1}	171
$NH_3 + H_2O \leftrightarrow NH_4^+ + OH^-$	6.1×10^5	M s^{-1}	171

[a]Because the form of the source term used in Eq. (117) employs unitless species activities to determine the rate of generation or consumption, the rate constants listed here must all possess identical units required for consistency with the equation for conservation of moles (M s^{-1}) (Eq.

(43)). In reactions where water is a reactant, this formulation requires a correction factor of 55 M from reported values to account for the fact that 55 M water possesses unit activity in the aqueous phase (where these constants are measured).

It is once again important to note that the values of these rate constant have been shown to depend strongly on the local reaction environment.[145, 172] For this reason, there is variance in the measured values for these rate constants. Additionally, these rate constants are dependent on the local electric field due to the Second Wien Effect (as discussed in **Section 3.3.4**)—a phenomenon which becomes particularly relevant in bipolar membranes or in the electrical double layer.[173-175] Proper models of electrochemical synthesis should aim to provide sensitivity analyses on the values of these rate parameters to account for the inconsistency in experimentally reported values.

Lastly, the dependence of these buffer reaction source terms on the concentration of the products and reactants makes the mass conservation equations (Eq. (43)) in electrochemical synthesis models highly nonlinear. Consequently, convergence issues have limited the development of complex electrochemical synthesis models that incorporate buffer kinetics. One way to make CO_2 reduction models converge more easily is to make simplifying assumptions regarding the (bi)carbonate equilibrium. For pH values >12 (as is the case for KOH electrolytes) the bicarbonate buffer is broken, This assumption is made because only carbonate species are observed beyond pH 12 experimentally.[176] therefore, the following reaction can be considered irreversible,[177]

$$CO_{2(aq)} + 2OH^- \rightarrow CO_3^{2-} \tag{118}$$

Accordingly, the rate of the homogeneous reaction is only a function of CO_2 and hydroxide concentrations as follows,

$$-r_{CO_2} = kC_{\mathrm{CO_2}}C_{\mathrm{OH^-}} \quad (119)$$

This framework for modeling the (bi)carbonate equilibrium is far simpler than accounting for all (bi)carbonate equilibrium reactions (which are shown in the first 5 rows of **Table 4**). Moore *et al*. used this simplifying assumption in a resolved pore model to predict mass transfer and kinetic control regimes for aqueous CO_2 reduction in highly alkaline electrolyte.[178] By neglecting the reversibility of the (bi)carbonate equilibrium, the authors showed that the consumption of CO_2 by homogeneous reactions, surface reactions, and reactions at a triple-phase can be compared using a simple reaction-diffusion equation. This reduction in complexity made the results of the model more physically interpretable, and was made because only carbonate species are observed beyond pH 12 experimentally.[176] We note that further work should aim to assess more rigorously the impacts of these (bi)carbonate buffer reactions and their rate constants on electrochemical performance and mass transport in order to verify the validity of these assumptions.

3.6 Model Parameterization

3.6.1 Transport Parameters in Electrochemical Synthesis

Knowledge of the transport parameters is crucial for implementing the different equations discussed in previous sections, especially since many have nonlinear dependences on independent variables. The transport parameters available in literature are obtained either through theoretical estimates, experimental measurements, or assumptions. While there have been several articles devoted to reporting different transport properties,[127] most of the transport properties are specific to the materials being used in the electrochemical systems; *e.g.,* the thermal conductivity of the porous transport layer is dependent on the materials and manufacturing method. Therefore, one must take care in obtaining properties for new material sets. Furthermore, while some transport properties have been measured with high accuracy and

certainty in literature, several transport properties show significant uncertainties and spread in data.

3.6.1.1 Mass-Transport Parameters

The bulk binary diffusion coefficients D_{ij} of different gas pairs are obtained either using kinetic theory of gases[179] or using Wilke coefficient relationships.[180] In porous electrodes, the effective diffusivity is reduced due to reduction in pore space and tortuous pore path (Eq (55)).

Effective diffusivity of carbon-based gas-diffusion layers and microporous layers have been extensively measured in fuel-cell literature with high accuracy.[181-185] Pore-scale imaging and subsequent diffusion simulations are also used for estimating effective diffusivities.[185-191] For estimating convective transport, the permeability of a phase is estimated as,

$$k_k = k_{k,0} k_{k,rel}, \tag{120}$$

where $k_{k,0}$ is the absolute permeability (which depends only on structure) and $k_{k,rel}$ is the relative permeability (accounting for partial saturations). Absolute permeability of carbon-based porous layers has been measured and reported in literature,[192-196] and is often anisotropic with through-plane almost an order of magnitude smaller than in-plane for fibrous media.[192, 197] Pore-scale modeling and Stokes flow simulation can also be used to estimate the permeability of partially and fully saturated porous layers, or perhaps measured in special setups where one can visualize the water distribution[96]. Relative permeability of a phase is usually expressed as a function of saturation, *S* (the fraction of pores filled with liquid).

$$k_{k,rel} = {S_k}^{\beta_{sat}}, \tag{121}$$

where the exponent β_{sat} can obtained by fitting to experimental or simulation data and S_i is the saturation of phase k.[184, 198-200] The properties are highly dependent on the volume fraction,

additives, structure, and operating conditions and therefore can be different than the ones shown in the table. For fiber-based gas diffusion layers, the values of β_{sat} can range from 2-5; for particle-based gas diffusion layers (*e.g.* catalyst layers), the β_{sat} can range from 1.5 to 3.[197, 201] For fiber-based gas diffusion layers, $k_{k,0}$ is of the order of magnitude 10^{-11} m^2 whereas for particle-based gas diffusion layers (*e.g.* catalyst layers), $k_{k,0}$ is of the order of magnitude 10^{-13} m^2.[197, 201] It is lastly important to note that there exist multidimensional anisotropies present in these porous materials that are not fully captured by the above formulation for the transport parameters.[188]

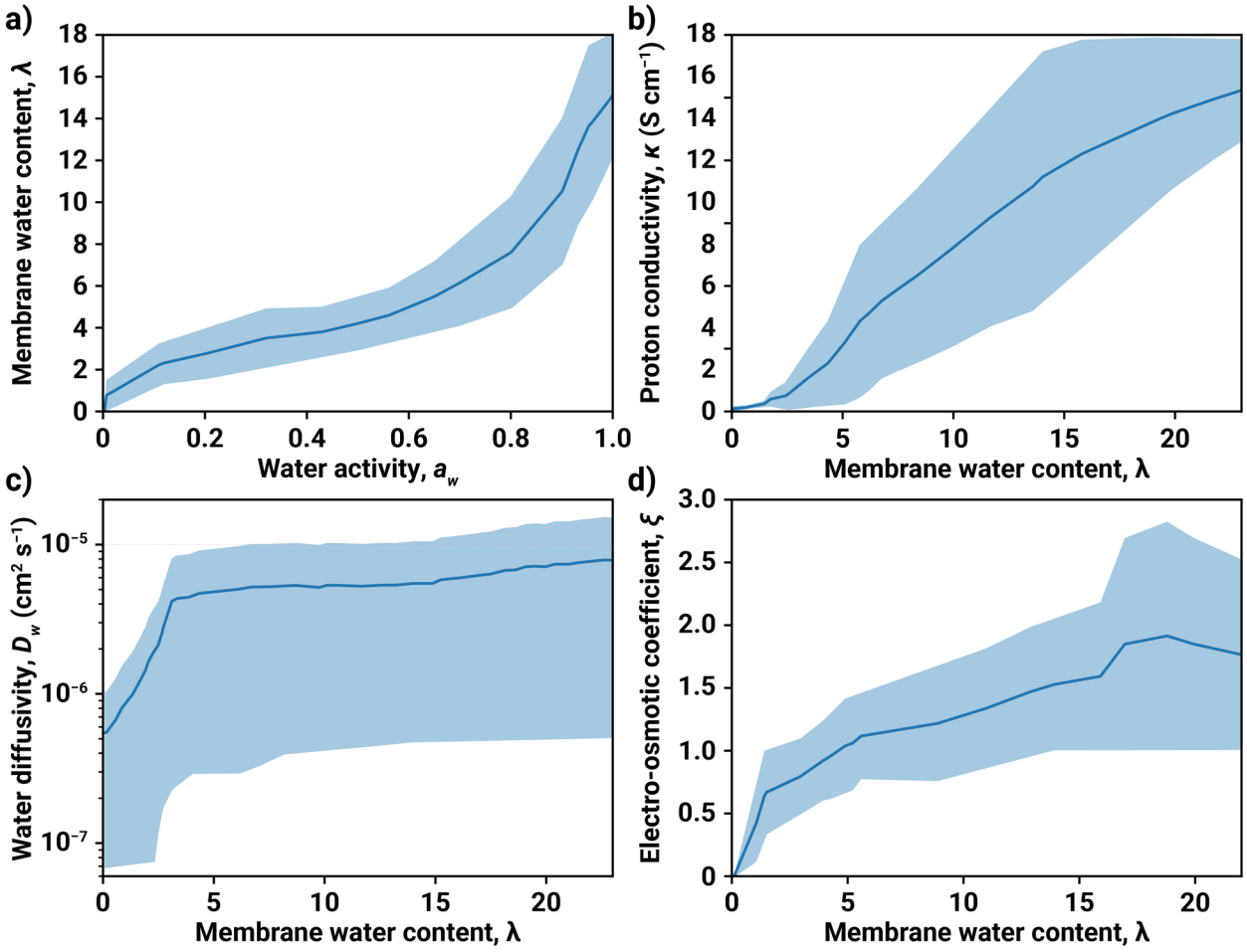

Figure 13. Range of proton-conducting-membrane properties reported in literature at 25 to 30 ºC.[127] The shaded zone shows the spread and the solid line the average values. (a) Membrane

water content, (b) Proton conductivity, (c) Membrane water diffusivity, and (d) Electro-osmotic coefficient.

3.6.1.2 Charge-Transport Parameters

Electron transport is characterized using effective electronic conductivity σ_s^{eff}. For most components, the bulk electronic conductivity of all the layers is in the order of 10^4 S/m.[164] For ionic transport in the polymer electrolyte, hydration plays a crucial part. The different transport properties, *e.g.,* ionic conductivity and diffusivity are dependent on the membrane water-uptake parameter commonly denoted as λ (moles of water per mol of fixed ionic sites). Proton-conducting membranes such as Nafion have been studied in detail, providing a large data set; however, a significant spread has been observed in the measured values of membrane properties. **Figure 13** shows the spread of measured membrane properties as reported by Kusoglu *et al.*[202] and Vetter *et al.*[203] Even though the membrane-transport properties are dependent on water content, it can be seen in **Figure 13a** that the membrane water content has a large spread and therefore associated uncertainty in measurement. Furthermore, the dependence of transport properties on the water content itself is not known with high certainty as shown in **Figure 13(b-d)**. For concentrated multi-ion systems, the transference numbers t_i must also be known. There have been few measurements of cationic transference numbers in proton conducting membranes.[204, 205] Recently, Crothers *et al.*[116, 160, 162] presented a detailed theoretical model for estimating several of the membrane properties, which are not easily available from experimental data. While significant literature data exists for proton-conducting membranes, limited data is available for anion-exchange-membrane transport properties.[206]

3.6.1.3 Heat-Transport Parameters

The primary mode of heat transport in electrochemical systems is via heat conduction. The effective thermal conductivity of any porous layer is

$$k_T^{eff} = k_{T,dry}^{eff} + S_L k_L, \tag{122}$$

where $k_{T,dry}^{eff}$ is the bulk conductivity measured in dry state, S_L is water fraction/saturation, and k_L is thermal conductivity of water. This expression is derived by assuming parallel pathways for heat transport: One through both the liquid-filled pores in the porous material, and another through the solid fraction of the porous material itself (either solid ionomer or solid electrode volume). The dry state thermal conductivity of carbon-based GDLs, catalysts layers, and polymer electrolytes are around 1.4, 0.27, and 0.2 $\mathrm{W/m \cdot K}$, respectively.[198]

3.6.2 Electrochemical Kinetic Parameters

One set of key fitting parameters employed in continuum models of electrochemical synthesis is the kinetic parameters for the electrochemical reactions that occur on the catalytic surfaces. Because most models employ simplified Butler-Volmer or Tafel equations to model these surface reactions (Eqs. (96) and (106)), the most common fitting parameters include the exchange current density (i_0) and the cathodic transfer coefficient (α_c). These parameters are typically the most sensitive when fitting and facilitating agreement between the polarization curves or product distributions collected experimentally and those simulated through continuum modeling. **Figure 14** displays a distribution of Butler-Volmer kinetic parameters for electrochemical CO_2 reduction on various catalyst (Cu, Ag, Au, and Sn) employed in various continuum models of electrochemical CO_2 reduction;[49, 60, 66, 67, 74, 78, 135, 170, 207-212] the specific values used for these figures can be found in **Table 6.** When examining the fit parameters in

these distributions, the spread in the fit values, even across a single catalyst, are quite large, even though some variation in these parameters is expected due to the drastically different experimental architectures and condition (*e.g.,* the choice of the electrolyte cation, which greatly impacts selectivity).[129, 213-215] For instance, in the case of CO_2 reduction to ethanol on Cu, there is a variance in the fit exchange current densities of twenty-five orders of magnitude, and the transfer coefficients vary from 0.02 to 1.1. Additionally, the kinetics measured in aqueous electrolytes may vary from those in vapor-fed porous electrode systems, limiting the direct translatability of parameters measured in the aqueous phase to vapor-phase systems. In particular, for porous catalyst layers that employ ionomers, the chemistry of the ionomer coating can drastically impact the reaction kinetics at the catalyst surface.[216, 217]

Nevertheless, the extreme variation, and sometimes nonphysical values, observed across simulation fits suggests the need for more rigorous methods of fitting. It has recently been shown that the distribution of sites on a monometallic catalyst can lead to severe changes in the observed kinetic parameters.[3, 218] When plotting the fit exchange current densities against the fit transfer coefficients, a weak trend can be observed, where larger transfer coefficients typically imply smaller exchange current densities. While this trend is too weak to make any major claims, the seemingly coupled nature of these two parameters could imply the existence of multiple, equally good fits to a single set of experimental polarization data, wherein multiple combinations of transfer coefficient or exchange current densities result in equally good fits of a simulation to experimental results, possibly as a result of the mathematical coupling of these parameters as seen in the Tafel kinetics (see Eq. (106)). This challenge motivates the need for greater statistical rigor of the chosen kinetic parameters—electrochemical kinetic parameters determined using more controlled experiments and then applied within continuum models present promise for

greater standardization and transferability of simulation results. For example, Agbo *et al.* developed a unique algorithm to calculate Tafel kinetic parameters that takes an experimentally measured polarization curve and calculates every possible Tafel slope across the dataset, ultimately developing a distribution of potential Tafel slopes from which the most probable Tafel slope can be chosen.[219] However, such a procedure requires a large amount of data to be accurate,[101] which is not currently available and especially for porous-electrode systems; this data insufficiency restricts the use of the algorithm by Agbo *et al.* to electrochemical reactions with 100% selectivity, where product quantification is not necessary.

Table 6: Fit kinetic parameters across various continuum models of electrochemical CO_2 reduction on various catalysts assuming Tafel kinetics (see Eq. (106)) at ambient conditions.[a]

Product	α_C	$\log_{10}(i_0[\text{mA cm}^{-2}])$	Ref.
CO (Cu)	0.08	6.99	McCallum[207]
C_2H4 (Cu)	0.1	5.04	McCallum[207]
H_2 (Cu)	0.08	5.72	McCallum[207]
EtOH (Cu)	0.07	4.73	McCallum[207]
H_2 (Cu)	0.14	−1.20	Bui[135]
CO (Cu)	0.35	−2.70	Bui[135]
HCOOH (Cu)	0.43	−5.45	Bui[135]
C_2H_4 (Cu)	0.41	−11.29	Bui[135]
EtOH (Cu)	0.43	−12.07	Bui[135]
PrOH (Cu)	0.4	−12.01	Bui[135]
AllylOH (Cu)	0.49	−14.47	Bui[135]
CH_4 (Cu)	0.84	−17.39	Bui[135]
CO (Ag)	0.44	−3.33	Weng 1[60]
H_2 (Ag)	0.36	−5.94	Weng 1[60]
CO (Ag)	1	−8.67	Weng 2[49]
H_2 (Ag)	0.44	−7.60	Weng 2[49]
CO (Cu)	0.17	0.41	Weng 3[67]
H_2 (Cu)	0.28	−2	Weng 3[67]
HCOOH (Cu)	0.37	−0.66	Weng 3[67]
C_2H_4 (Cu)	0.67	−5.72	Weng 3[67]
EtOH (Cu)	0.74	−7.92	Weng 3[67]
PrOH (Cu)	0.75	−8.31	Weng 3[67]

H_2 (Cu)	0.69	−7.66	Weng 4[67]
CO (Cu)	0.1	−3.96	Weng 4[67]
HCOOH (Cu)	0.24	−6.27	Weng 4[67]
C_2H_4 (Cu)	0.69	−12.47	Weng 4[67]
EtOH (Cu)	1.1	−18.85	Weng 4[67]
CH_4 (Cu)	1.13	−17.07	Weng 4[67]
H_2 (Cu)	0.258	-2	Chen[74]
C_2H_4 (Cu)	0.35	−7.93	Chen[74]
CH_4 (Cu)	1.33	−17.46	Chen[74]
CO (Ag)	0.33	−4.48	Kas[78]
H_2 (Ag)	0.33	−6.47	Kas[78]
CO (Ag)	0.4	−1.15	Yang[66]
H_2 (Ag)	0.23	−2.82	Yang[66]
HCOOH (Ag)	0.4	−1.05	Yang[66]
H_2 (Sn)	1.0	−2.80	Wang[208]
HCOOH (Sn)	0.1	−2	Wang[208]
CO (Ag)	0.285	−3.82	Singh[170]
CO (Ag)	0.5	−2.95	Delacourt[209]
H_2 (Ag)	0.4	−3.80	Delacourt[209]
CO (Ag)	0.76	−5.81	Delacourt[209]
H_2 (Ag)	0.88	−10.24	Delacourt[209]
CO (Au)	0.7	−2.95	Delacourt[209]
H_2 (Au)	0.46	−4.16	Delacourt[209]
H_2 (Ag)	0.95	−10.15	Suter[211]
CO (Ag)	0.29	−6.00	Suter[211]
H_2 (Ag)	0.95	−10.04	Suter[211]
CO (Ag)	0.29	−6.08	Suter[211]
CO (Ag)	0.128	−0.41	Gutierrez[212]
H_2 (Ag)	0.137	−1.85	Gutierrez[212]
CO (Ag)	0.139	−0.33	Gutierrez[212]
H_2 (Ag)	0.114	−1.57	Gutierrez[212]
CO (Cu)	0.16	1.61	Gutierrez[212]
H_2 (Cu)	0.249	−5.14	Gutierrez[212]
HCOOH (Cu)	0.235	2.56	Gutierrez[212]
CH_4 (Cu)	0.042	−4.26	Gutierrez[212]
C_2H_4 (Cu)	0.005	1.07	Gutierrez[212]
EtOH (Cu)	0.023	3.37	Gutierrez[212]
CO (Cu)	0.037	−1.41	Gutierrez[212]
H_2 (Cu)	0.067	−1.28	Gutierrez[212]
HCOOH (Cu)	0.368	−1.89	Gutierrez[212]
C_2H_4 (Cu)	0.028	−3.77	Gutierrez[212]
EtOH (Cu)	0.033	−5.03	Gutierrez[212]

[a]For H_2 evolution reactions, only the alkaline H_2 evolution pathway kinetics are shown and compared in the table above. H_2 from direct proton reduction possesses different kinetic parameters, and this reaction pathway is rarely modeled in CO_2R models because they possess highly alkaline pHs at the cathode. For i_0s that are temperature dependent, they are tabulated at 298 K.

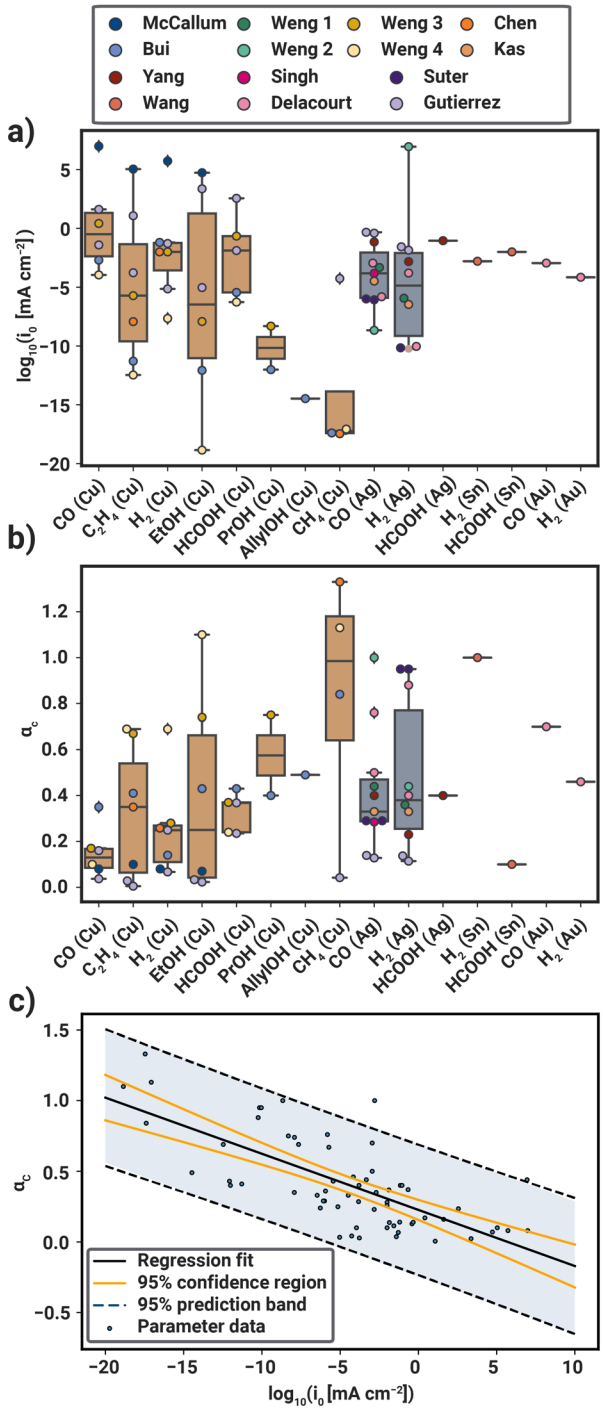

Figure 14: Distribution of parameters used in continuum-based models of CO_2 reduction catalysts assuming Tafel kinetics (see Eq. (106)) at ambient conditions:[49, 60, 66, 67, 74, 78, 135, 170, 207-212] **(a)** Exchange-current-density distributions and **(b)** cathodic transfer coefficient distributions. The color of box and whisker plot represents the catalyst used; color of the individual points in the swarm plot corresponds to the dataset from which the data was taken. It is important to note that the H_2-evolution kinetics shown here are only for the alkaline (H_2O) pathway. **(c)** Plot of fit exchange current density and transfer coefficient, displaying a weak trend (R^2 = 0.54). The

shaded region represents the 95% prediction band, and the solid orange lines demarcate the 95% confidence interval. See **Table 6** for a table of the values used to construct these distributions.

Recent work by Limaye *et al.* (**Figure 15**) has attempted to address this challenge in determining Tafel slopes for electrochemical kinetics using an automated kinetic fitting approach that fit experimental data to a Tafel equation modified to account for mass transport effects. In this automated kinetic fitting approach, a Bayesian statistical model evaluated a distribution of possible exchange current densities, limiting current densities, and Tafel slopes and assessed the probability for that distribution to be descriptive of the experimental data with the Tafel-equation model (Eq. (106)). The combination of Tafel slopes, limiting current, and exchange current densities with the greatest probability of describing data is chosen as the most probable Tafel slope. (**Figure 15a**) Interestingly, while there was relatively strong agreement between the experimentally reported Tafel slope and the Tafel slope reported using Limaye's algorithm, there were still some substantive discrepancies (**Figure 15b**). Most notably, whereas the experimentally reported values clustered on values associated with well-known kinetic steps (*i.e.,* 120 mV decade^{-1} for the first one-electron transfer to CO_2 in CO_2R), the modeled Tafel slopes did not collapse upon these values, suggesting researcher-bias towards these cardinal values overstated their prevalence in the data (**Figure 15d**). The authors refer to these values of the Tafel slope that are associated with known kinetic steps as "cardinal" values. It is important to note, however, that the work by Limaye did not separate the Tafel slopes explicitly by product formed, fitting a Tafel slope to the total current density, and also did not separate out data by catalyst type. Clearer trends could possibly be observed if the data was separated by these criteria. These rigorous statistical fitting methods should be employed when parameterizing kinetics in electrochemical synthesis, to avoid similar data misrepresentation and to assess the validity of fit electrochemical kinetic parameters more adequately.

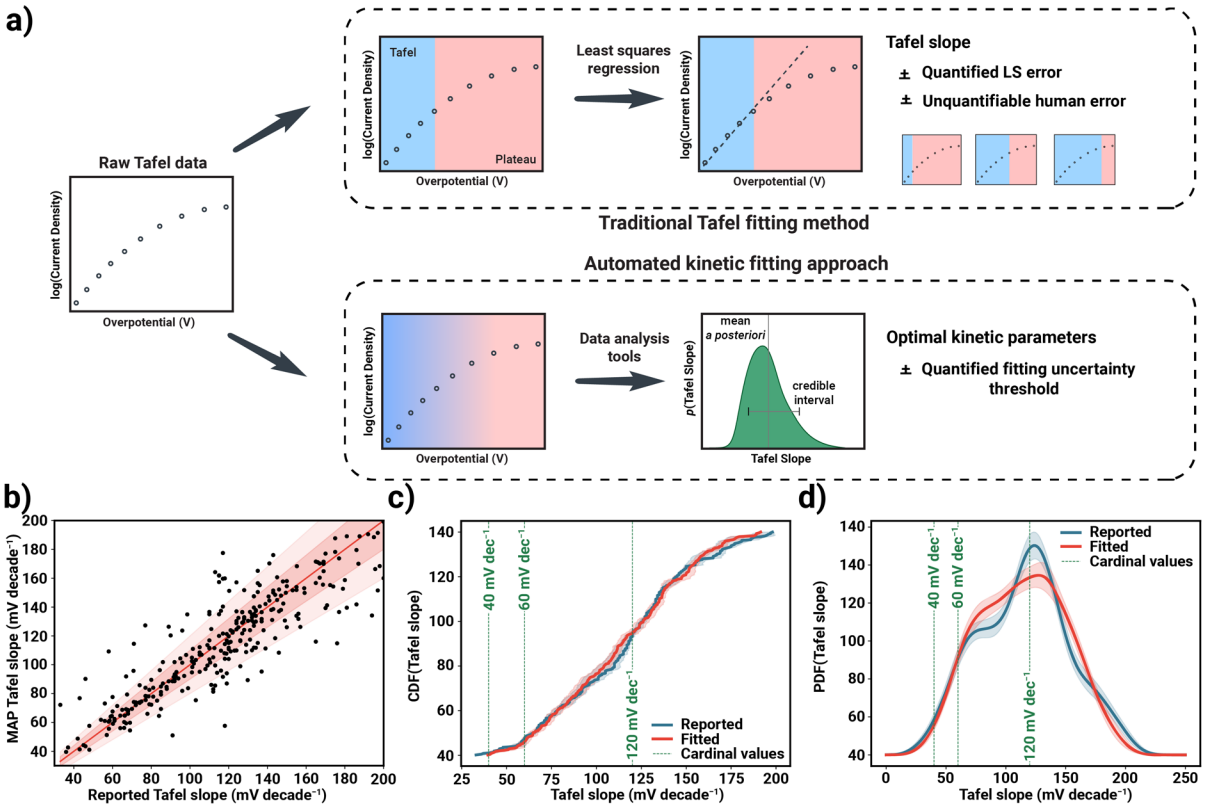

Figure 15: (a) Overview of kinetic fitting algorithm developed by Limaye *et al.*[101] **(b)** Comparison of algorithmically fit kinetic parameters to experimentally reported kinetics. **(c)** Cumulative distribution function of experimentally reported and algorithmically fit Tafel slopes. **(d)** Comparison of distribution of experimentally reported and algorithmically fit Tafel slopes. Adapted with permission from Limaye *et al.*[101] Copyright Creative Commons 2021 http://creativecommons.org/licenses/by/4.0/.

3.7 Sample Modeling Approach

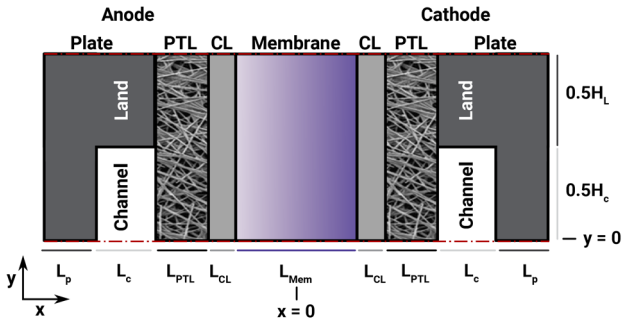

Figure 16. Schematic of a 2-D modeling domain for a typical electrochemical-synthesis device.

The approach used to estimate the system state is highly dependent on the cell geometry, configuration, model-dimensionality, and mathematical framework to describe the underlying physical phenomena. In this section, a steady-state, 2-D macroscale example is selected to showcase the typical implementation of the equations described in section 3. **Figure 16** shows the schematic of a typical 2-D macroscale modeling domain for electrochemical-synthesis devices, where the along-the-channel direction is ignored (*i.e.*, differential conditions). This latter assumption can happen in two cases: i) at high flow rates where the reactions occurring within the system cannot change channel flow conditions or the overall system; and ii) when only a small length along the third dimension is considered,[164] where the net changes are negligible. Furthermore, one can assume symmetry at the midpoint (in *y*-direction) of the channels and land, which reduces the simulation domain by half in the *y*-direction. In a macroscale approach, volume-averaged properties are used and all phases are considered to exist within all control volumes. Also, all of the interfacial phenomena such as surface reactions, adsorption/desorption can be converted to homogeneous volumetric reactions by utilizing a specific interfacial area. **Table 7** shows the conservation and transport equations for this system assuming a dilute gas mixture. The different source terms are described in **Table 8**. The sign of the source terms must be adjusted based on whether it is a generation or consumption term. Finally, **Table 9** provides a set of boundary conditions to be used for the solution of the differential-equation system.

Table 7. Conservation and transport equations for the sample electrochemical-synthesis cell

Physics	**Equations**	**Domain**
Gas diffusion	$\nabla \cdot \mathrm{N}_i = R_{i,rxn} + R_{i,phase}$ $\mathrm{N}_i = -D_i^{eff} \nabla c_i + c_i \mathrm{v}^*$	PTLs, CLs
Gas convection	$\nabla \cdot \rho_G \mathrm{v}^* = \sum_i (R_{i,rxn} + R_{i,phase})$	PTLs, CLs

	$\mathrm{v}^* = -\frac{k_o k_{G,rel}}{\mu_G}\nabla p_G$	
Liquid transport	$\nabla \cdot \rho_L \mathrm{v}_\mathrm{L}^* = R_{cond} + \sum_i R_{L,i,rxn}$ $\mathrm{v}_\mathrm{L}^* = -\frac{k_0 k_{L,rel}}{\mu_L}\nabla p_L$	PTLs, CLs
Ionic transport	$\boldsymbol{\nabla} \cdot \mathrm{N}_i = (R_{i,rxn} + R_{i,desorption})$ $\mathrm{N}_i = -x_i \frac{\kappa_i}{z_i F}\boldsymbol{\nabla}\phi_k - x_i \frac{\kappa_i \xi_i}{z_i^2 F^2}\boldsymbol{\nabla}\mu_w - D_i C_t \boldsymbol{\nabla} x_i$ $\mathrm{N}_w = -\sum_i x_i \frac{\kappa_i \xi_i}{z_i F}\boldsymbol{\nabla}\phi_k - \left(\alpha_k + \sum_i x_i \frac{\kappa_i \xi_i^2}{z_i^2 F^2}\right)\boldsymbol{\nabla}\mu_w$	CLs, Membrane
Electron transport	$\nabla \cdot i_s = j_{rxn}$ $i_s = -\sigma_s^{eff}\nabla\phi_s$	Plate, PTLs, CLs
Heat transport	$\nabla \cdot q = \dot{Q}$ $q = -k_T^{eff}\nabla T$	All layers

Table 8. Source terms for the conservation equations in different layers of the cell

Source Term (Expression)	**Plates**	**PTL**	**CL**	**Membrane**
Electrochemical reaction of species i, $R_{i,rxn}$			$\sum_l s_{i,l}\frac{i_l}{n_l F}$	
Phase change of species i to pore, $R_{i,phase}$		$k_{i,l}(\mu_{i,l} - \mu_{i,p})$	$k_{i,l}(\mu_{i,l} - \mu_{i,p})$	
Condensation of liquid water, R_{cond}		$k_{ec}(\mu_V - \mu_L)$	$k_{ec}(\mu_V - \mu_L)$	
Rate of desorption of species i from pore to ionomer		$k_{ad}(\mu_{i,p} - \mu_{i,m})$	$k_{ad}(\mu_{i,p} - \mu_{i,m})$	
Rate of current generation, j_{rxn}			$a_v i_l$ i_l defined in Eq. (96)	
Heat generation, $\dot{Q}$	$\dot{Q}_{ohm,solid}$	$\dot{Q}_{ohm,solid} + \dot{Q}_{phase,pore} +$	$\dot{Q}_{ohm,solid} + \dot{Q}_{ohm,ionomer} + \dot{Q}_{phase,pore} + \dot{Q}_{rev} + \dot{Q}_{irrev}$	$\dot{Q}_{ohm,ionomer}$

Table 9. Boundary conditions for different physics in the electrochemical-synthesis model

Physics	**Boundary conditions**
Gas diffusion	$c_i\|_{x=-L_{PTL}-L_{CL}-0.5L_{mem}} = c_{\text{i,anode,channel}}$ $c_i\|_{x=L_{PTL}+L_{CL}+0.5L_{mem}} = c_{\text{i,cathode,channel}}$ $N_i\|_{x=-0.5L_{mem}} = N_i\|_{x=0.5L_{mem}} = 0$
Gas convection	$p_G\|_{x=-L_{PTL}-L_{CL}-0.5L_{mem}} = p_{\text{G,anode,channel}}$ $p_G\|_{x=L_{PTL}+L_{CL}+0.5L_{mem}} = p_{\text{G,cathode,channel}}$ $\text{v}^*\|_{x=-0.5L_{mem}} = \text{v}^*\|_{x=0.5L_{mem}} = 0$
Liquid transport	For liquid saturated cell: $p_L\|_{x=-L_{PTL}-L_{CL}-0.5L_{mem}} = p_{\text{L,anode,channel}}$ $p_L\|_{x=L_{PTL}+L_{CL}+0.5L_{mem}} = p_{\text{L,cathode,channel}}$ For dry cell: $\text{v}_\text{L}^*\|_{x=-L_{PTL}-L_{CL}-0.5L_{mem}} = 0$ $\text{v}_\text{L}^*\|_{x=L_{PTL}+L_{CL}+0.5L_{mem}} = 0$ For all conditions: $\text{v}_\text{L}^*\|_{x=-0.5L_{mem}} = \text{v}_\text{L}^*\|_{x=0.5L_{mem}} = 0$
Ionic transport	$N_i\|_{x=-0.5L_{mem}-L_{CL}} = N_i\|_{x=0.5L_{mem}+L_{CL}} = 0$
Electron transport	For potentiostatic: $\phi_s\|_{x=-L_P-L_C-L_{PTL}-L_{CL}-0.5L_{mem}} = V_{applied}$ For galvanostatic: $\mathbf{n}\cdot\sigma_{plate}\nabla\phi_s\|_{x=-L_P-L_C-L_{PTL}-L_{CL}-0.5L_{mem}} = i_{applied}$ Always: $\phi_s\|_{x=L_P+L_C+L_{PTL}+L_{CL}+0.5L_{mem}} = 0$ $\mathbf{n}\cdot\sigma_{plate}\nabla\phi_s\|_{x=-0.5L_{mem}} = \mathbf{n}\cdot\sigma_{plate}\nabla\phi_s\|_{x=0.5L_{mem}} = 0$
Heat transport	$T\|_{x=-L_P-L_C-L_{PTL}-L_{CL}-0.5L_{mem}} = T_{an,out}$ $T\|_{x=L_P+L_C+L_{PTL}+L_{CL}+0.5L_{mem}} = T_{ca,out}$ $T\|_{x=-L_C-L_{PTL}-L_{CL}-0.5L_{mem},y<0.5H_C} = T\|_{x=-L_{PTL}-L_{CL}-0.5L_{mem},y<0.5H_C}$ $= T\|_{y=0.5H_C,(-L_C-L_{PTL}-L_{CL}-0.5L_{mem}<x<-L_{PTL}-L_{CL}-0.5L_{mem})}$ $= T_{\text{an,ch}}$ $T\|_{x=L_C+L_{PTL}+L_{CL}+0.5L_{mem},y<0.5H_C} = T\|_{x=L_{PTL}+L_{CL}+0.5L_{mem},y<0.5H_C}$ $= T\|_{y=0.5H_C,(L_{PTL}+L_{CL}+0.5L_{mem}<x<L_C+L_{PTL}+L_{CL}+0.5L_{mem})}$ $= T_{\text{ca,ch}}$
All	$\left.\frac{\partial(*)}{\partial y}\right\|_{y=0} = \left.\frac{\partial(*)}{\partial y}\right\|_{y=0.5H_C+0.5H_L} = 0$

3.8. Applied-Voltage Breakdown (a.k.a. Power Loss Analysis)

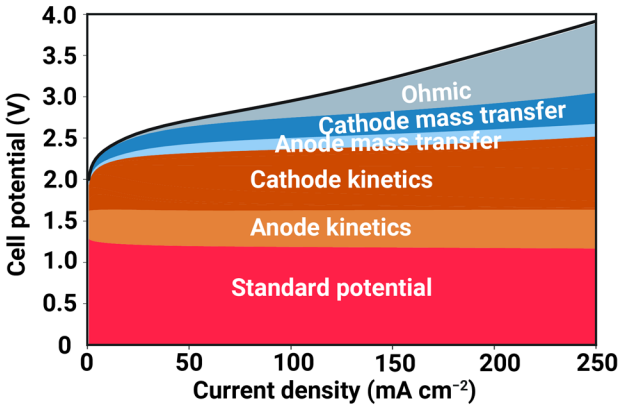

Figure 17. Example of an applied-voltage breakdown developed through power-loss analysis. Adapted with permission from Weng *et al.*[67] Copyright 2020 Royal Society of Chemistry.

A crucial benefit of macroscale simulation is that it enables the breakdown of a measured or simulated polarization curve into a series of voltage contributions that sum to the overall polarization curve, thereby enabling a clearer understanding of the limiting processes within an electrochemical device.[77] The power-loss-analysis based method breaks the overall applied potential into the contributions from the sources. Because of this, mathematical expressions for these overpotential contributions from each mechanism must be derived from first principles. This analysis is referred to as "power-loss analysis" because these expressions are derived by determining the power loss throughout the modeled domain due to each mechanism normalized by the total current density to determine a power-loss-based overpotential contribution. The individual voltage-loss contributions are defined as follows. For greater depth regarding applied-voltage analysis, please view our recent tutorial review on this topic.[77]

In the definition of the voltage-loss breakdown, the choice of model of the kinetics becomes relevant, as it dictates the form of the expression for the mass-transport and kinetic losses. In the following analysis, the concentration-dependent Tafel expression is used (Eq. (106)). For an anodic reaction, the Tafel kinetics can be rearranged, such that the mass-transport

effects are placed within the exponential to derive a total overpotential η_T (for a cathodic reaction, the sign on the total overpotential would change to be negative, as shown in Eq. (106)). This is achieved by using logarithmic identity to move the activity dependent terms in the definition of i_0 (Eq. (99)) into the exponential of the Tafel expression (Eq. (106)), adding them to the surface overpotential to arrive at the total overpotential.

$$\eta_T = \phi_s - \phi_k - U_l \; + \frac{RT}{\alpha_{a,l}F}\left(\sum_p \gamma_{p,k,l} \ln\left(\frac{a_p}{a_p^{ref}}\right) + \sum_r \gamma_{r,k,l} \ln\left(\frac{a_r}{a_r^{ref}}\right)\right) \tag{123}$$

The total overpotential can be further divided into a kinetic (*i.e.,* surface) overpotential, η_S, and a concentration overpotential, η_C. The surface overpotential describes the electrochemical driving force required to drive the Tafel kinetics, and the concentration overpotential describes potential losses due to concentration gradients within the electrochemical cell.

$$\eta_S = \phi_s - \phi_k - U_l \tag{124}$$

$$\eta_C = \frac{RT}{\alpha_{a,l}F}\left(\sum_p \gamma_{p,k,l} \ln\left(\frac{a_p}{a_p^{ref}}\right) + \sum_r \gamma_{r,k,l} \ln\left(\frac{a_r}{a_r^{ref}}\right)\right), \tag{125}$$

where a_p is the activity of anodic reactant p, a_p^{ref} is the activity of reactant p at the open circuit condition (channel activity for vapor-fed systems or bulk electrolyte activity for liquid-fed systems as discussed in **Section 3.5.1**), and $\gamma_{p,k,l}$ is the rate order of reactant p in phase k in reaction l. The concentration overpotential, η_C, must be referenced to open circuit conditions, because if the device is operating at open circuit, there are no fluxes in the cell and the concentration overpotential must tend to 0. Often, we ignore the contribution due to the second term in the concentration overpotential, (associated with the transport of cathodic species away

from the anodic electrode), because we can assume they immediately bubble out of the electrolyte or that their activity in the channel is negligible.

Now, to determine the applied voltage loss in the overall cell due to kinetics, we integrate the product of the surface overpotential and the local volumetric current density over the volume of both catalyst layers, summing over all reactions, and dividing by the total volumetric current density.

$$\eta_{kinetic} = \sum_l \frac{\int_{CL} i_{v,l}\eta_S dL}{\int_{CL} i_v dL} = \sum_l \frac{\int_{CL} i_{v,l}\,(\phi_s - \phi_k - U_l\ )dL}{\int_{CL} i_v dL}, \tag{126}$$

where $i_{v,rxn}$ is the local volumetric current source in A m^{-3}. dL represents a differential length along the through-plane of the catalyst layer.

The mass-transport-overpotential losses are derived by similar power-loss integration of η_C and account for voltage losses due to variations in local pH, as well as any other concentration overpotentials within the catalyst layer

$$\eta_{\text{mass transport,k}} = \sum_l \frac{\int_{CL} i_{v,l}\,\eta_C dL}{\int_{CL} i_v dL} = \sum_l \frac{\int_{CL} i_{v,l} \frac{RT}{\alpha_{a,l}F}\left(\sum_p \gamma_{p,k,l} \ln\left(\frac{a_p}{a_p^{ref}}\right) + \sum_r \gamma_{r,k,l} \ln\left(\frac{a_r}{a_r^{ref}}\right)\right) dL}{\int_{CL} i_v dL}. \tag{127}$$

The voltage loss due to ohmic resistances is determined by integrating the power-loss as defined by Ohm's Law over both the catalyst layer and membrane domains and dividing by the total current density,

$$\eta_{\text{ohmic}} = \frac{\int_{\text{CL+MEM}} \frac{i_M^2}{\kappa^{\text{eff}}} dL}{\int_{CL} i_v dL}, \tag{128}$$

where i_M is the local ionic current density in A m^{-2} and κ^{eff} is the effective ionic conductivity of the ionomer, which varies with respect to the local conditions (*e.g.,* water content, temperature) as described in **Sections 3.4** and **3.6.1**, and must be integrated over.

These individual contributions (Eqs. (126)-(128)) will sum to be equal to the overall polarization curve by definition. It is important to note that the above analysis is written for a 1-D model. To extend the above definitions to higher dimensions, higher-dimensional integration will be required, along with additional normalization by the relevant length scales.

3.9. Computational Methods

Predicting the state and behavior of the electrochemical-synthesis systems requires solving the mathematical equations discussed in **Section 3.** General Aspects and Equations. While analytical solutions can be obtained for simplified limiting-case scenarios,[220] as has been done in other electrochemical systems such as fuel cells,[221-226] the complexity and nonlinearity (especially the various properties) of the equations necessitates numerical solution. These nonlinearities are exacerbated by the homogeneous reactions including buffers, that can make the problem quite stiff. Both finite-element-method (FEM) and finite-volume-method (FVM) frameworks have been used for discretization. While FEM provides a generalized framework for solving any type of differential equations with high accuracy, FVM methods are naturally suited for solving conservation equations. In either framework, the discretized equations for the time independent part can be presented as system of nonlinear equations

$$[A(\mathbf{x})]\mathbf{x} = \boldsymbol{b}(\mathbf{x}), \tag{129}$$

where $[A(\mathbf{x})]$ is the variable dependent (nonlinear) coefficient matrix, $\mathbf{x}$ is the variable vector and $b(\mathbf{x})$ is the variable-dependent right-side vector. The solution for $\mathbf{x}$ can be obtained by direct

inversion of matrix A (for smaller problem sizes) or by iterative methods.[227] Due to nonlinearity, Picard's method, Newton-Raphson method, or secant method is typically used.[228] Finally, the transient equation is normally solved using Euler's method or Crank-Nicholson time stepping.[228, 229]

In literature, the FEM or FVM numerical frameworks have been implemented in either commercial software, open-source packages, or using in-house coding. Commercially, software such as COMSOL®[164, 198, 230-232] and ANSYS-Fluent®[233-235] have been extensively used to simulate the multiphysics equations for electrochemical systems. Other commercial software such as STAR-CCM+®[236, 237], AVL-FIRE[238, 239] and CFD-ACE[240, 241] also have functionality for simulating electrochemical systems. Open-source frameworks like openFCST[242] and openFuelCell[243], which are built upon open-source libraries such as deal.II[244] and openFOAM[245-248] respectively, can be used for simulating synthesis systems. Finally, several in-house numerical implementations have been reported, albeit primarily for fuel-cell systems.[249-251]

4. Survey of Macroscale Models Employed for Modeling Porous-Electrode Devices

The physics and theory described in **Section 3** constitute the framework for models of electrochemical devices. In this section, we review literature to explore electrochemical-synthesis cell models at various length and timescales. The goal of the current section is to present the utility and limitations of each modeling approach, while providing guidelines for the development of integrated models that can predict product distributions, electrochemical performance, and failure mechanisms.

4.1 Modeling of Porous Electrodes

Because the phenomena in porous electrodes for electrochemical synthesis occur over multiple relevant length scales, this section is broken down into models at these various scales. First, we review models of porous electrodes at the scale of a pore, nanostructure, or agglomerate to understand how the physics at the nanoscale can be translated directly to observables at the macroscale. Next, we discuss the use of high-fidelity porous-media models, which attempt to link these model formulations to account for phenomena occurring at a wide range of length scales. Lastly, we explore models at the macroscale, which treat the porous electrode as a homogeneous, volume-averaged continuum to ease computational cost when simulating these complex electrodes at full, macroscale.

4.1.1 Continuum Models of Pores, Nanostructure and Agglomerates

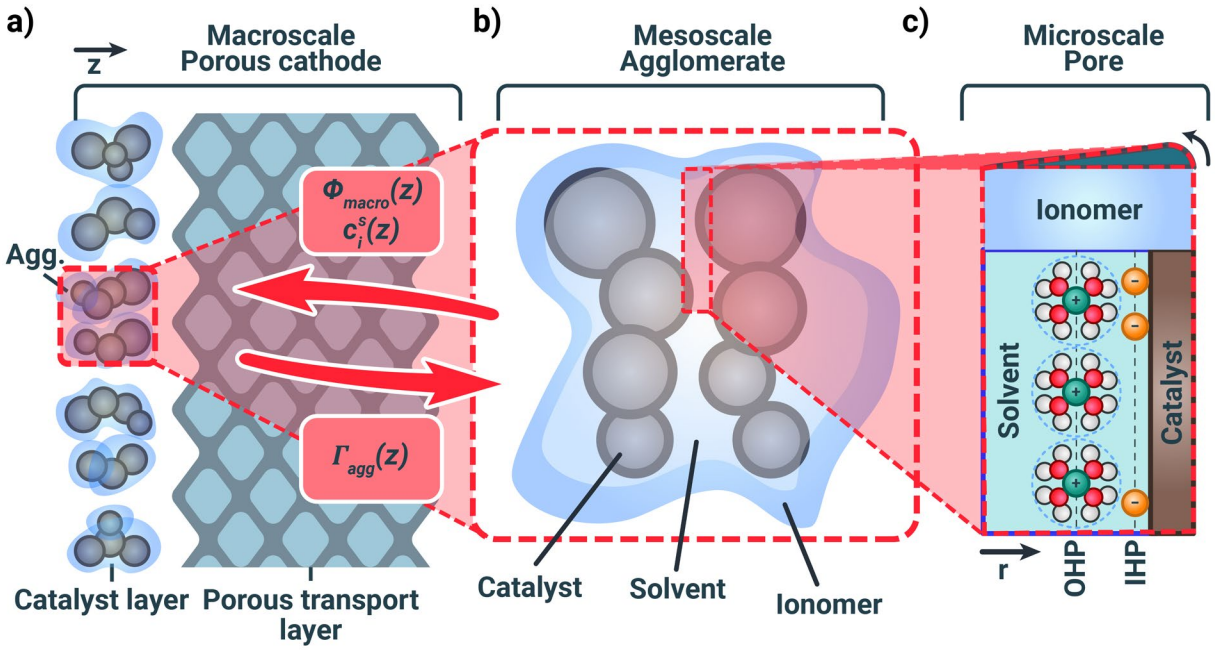

Figure 18: (a) Schematic depicting a porous electrode. **(b)** Zoomed in schematic of an agglomerate of catalyst particles that are bound by ionomer and filled with water or solvent. **(c)** Further zoomed in schematic of continuum-level description of a single pore with the electrical double layer illustrated. Boxes and arrows between panels **(a)** and **(b)** represent the mathematical constructs that can be used to link scales.

Transport within porous electrodes is complex because of the multitude of phases that coexist in catalyst layers, as well as charging and species adsorption that occurs on the catalyst surfaces (**Figure 18**). Pore-level modeling aims to resolve gradients in ion concentration, and ionic and electric potentials by simulating mass and charge transport in discrete pores. A characteristic feature of pore-level models is that they account for electric double layers (EDLs), which occur at the interface of a charged electrode in contact with an electrolyte phase. Ions and dipoles reorient either towards or away from the solid electrode and specific adsorption occurs, resulting in space-charge region with their own associated potential gradients. Consequently, capturing the EDL effects in electrochemical synthesis models is usually necessary to accurately characterize the local ionic environment at the catalyst surface.[252-254]

There are various EDL models in the literature, with Guoy-Chapman-Stern-Grahame (GCSG) theory being perhaps the most widely used. GCSG theory conceptually divides the electrolyte portion of the EDL into diffuse and Stern layers (**Figure 18c**). The Stern layer is theorized as an infinitely thin layer of ions that specifically adsorb to a solid electrode. The inner Helmholtz plane (IHP) passes through the adsorbed ions and the outer Helmholtz plane (OHP) passes through the center of the closest fully-solvated ions to the electrode.[255] When explicitly modeling the double layer, the potential difference between the metal and OHP defines the overpotential:

$$\eta = (\phi_m - \phi_{OHP}) - (\phi_m - \phi_{OHP})_{eq} \tag{130}$$

where ϕ_m is the metal potential, ϕ_{OHP} is the OHP potential and the last term is their difference at equilibrium (*i.e.*, no applied potential). If the OHP potential is known, this overall expression for the reaction overpotential can be used in the Butler-Volmer equation to determine the reaction rate of the electrochemical-synthesis reaction. This modification to the Butler-Volmer equation is commonly referred to as the Frumkin correction.[256] Beyond the OHP is the diffuse layer, which extends to the bulk solution and is composed of electrolyte and solvated ions. As the distance from the solid phase increases, the charge in the diffuse layer approaches the charge-neutral bulk electrolyte. The Poisson-Nernst-Planck (PNP) equation, which results from combining Eqs. (65) and (67), is used to determine charge and ion concentration profiles throughout the domain.

The Stern layer generally is assumed to be free of ions, as specific energies of adsorption are difficult to measure and with non-poisoning electrolyte one can assume only water dipoles present in the Stern layer. To account for water dipoles preferential orientation within the Stern layer, one can reduce the relative dielectric constant within the Stern layer to below 80 (to 6-10 for example).[257] Generally, with these modifications, Stern layer addition to the PNP equations

ensures the EDL is saturated with water at high applied potentials. Without the Stern layer addition, a modified PNP needs to be used to account for the finite size of ions crowded in the double-layer.[69-71] The variables that the PNP solves for are the ion concentrations and potentials.

The potential of zero charge (PZC) and charging dynamics of the solid phase are important physical parameters that PNP models for electrochemical synthesis must consider. The PZC is broadly defined here as the potential at which the solid phase carries zero electron charge. Consequently, the potential that is measured across the interface at the PZC potential is due exclusively to aligned water dipoles and electron spillover effects.[258] Without accounting for these corrections, PNP models implicitly assume a PZC value 0 V, which is generally not the case for catalysts used in electrochemical synthesis.[259, 260] The fuel-cell community has integrated PZC values into GCSG-type models and their results are highly sensitive to the PZC, and whether the PZC is in the operating potential window, because this parameter determines the degree of metal charging and associated ion distributions.[261-264] For example, Huang *et al.* showed non-monotonic surface charging of Pt electrodes and associated ion distributions,[263] which necessitated accounting for surface oxide dipoles and their contribution to the charge and potential drop across the interface. These studies established that the PZC is a critical parameter for modeling EDLs in pore-level models.

Some catalysts used for electrochemical synthesis, such as Au or Cu, can exist in several oxidation states that effect the PZC.[265] Recent studies coupled electrokinetics (streaming current/streaming potentials)[266, 267] and electrochemical measurements to determine zeta potential, which is the potential at the OHP (under certain conditions), to understand better surface charging and PZC. The PZC is incorporated into these models as a boundary condition, where instead of ϕ_m one would apply $\phi_m - \phi_{pzc}$. The second boundary condition for Poisson

equation is the electrolyte bulk potential, which is taken to be 0 vs. RHE, as the solution is electroneutral. However, EDLs formed at catalyst layer surfaces can overlap with each other when confined in small pores.[268, 269] Therefore, one must be careful of choosing the location in the model for the bulk solution to accurately characterize EDLs in porous electrodes.

Perhaps the most significant challenge in the development of the EDLs and pore-scale models is integrating them with the high-fidelity porous network or continuum volume-averaged models.[131] Agglomerate models (**Figure 18b**) are used as a bridge between the catalyst-layer continuum level and pore-scale models.[74, 270-272] Catalysts particles that may be coated by ionomer aggregate and form agglomerated structures, that are often assumed to be spherical.[74] The interstices within the agglomerates can be filled with liquid electrolyte, thin ionomer films, partial water layers, or vapor, but are often assumed to be macro-homogeneous and thus an effective conductivity is used or it is assumed to be isopotential.[167] On the surface of an agglomerate, either a thin film of water or ionomer is present to conduct ions and dissolved gas (in the case of liquid-filled pores) into agglomerate core. An effectiveness factor can then be defined as a ratio of the actual reaction rate from the agglomerate to the idealized reaction rate, if the interior pores of the agglomerate were exposed to the surface conditions (concentration, pressure, potential etc.) or the bulk conditions if an overall effectiveness factor is being used. For a first-order reaction, the simultaneous diffusion and reaction in the agglomerate can be solved analytically to yield the following expression for the effectiveness factor:

$$E_r = \frac{1}{\phi_L}\left(\frac{1}{\tanh\,(3\phi_L)} - \frac{1}{3\phi_L}\right) \tag{131}$$

where the Thiele's modulus, ϕ_L, for a spherical agglomerate is

$$\phi_L = \frac{r_{agg}}{3}\sqrt{\frac{k_c}{D_{eff}}} \tag{132}$$

where r_{agg} is the radius of agglomerate, k_c is the reaction rate, D_{eff} is the effective reactant diffusion coefficient within the agglomerate. The effectiveness factor can be used to link a mesoscale agglomerate model to a macroscale continuum averaged model using a scaling term on the current density source term for the electrochemical reactions in the continuum model. For example, one can use Equation (92) (*i.e.,* the Butler-Volmer equation) to determine the partial current density for product *i* under idealized conditions ($i_{l,ideal}$) when the reactant and solvent activities equal to that of the bulk solution. Then, one can calculate the actual current density after correcting for the effectiveness factor as follows,

$$i_l = E_r i_{l,ideal} \tag{133}$$

Chen *et al.*[74] used the above framework to link the agglomerate- and macroscales to account for agglomerate effects within a continuous GDE framework to assess the impact of agglomerate size on COR and CO_2R. In this work, they bridged the continuum and agglomerate models with an effectiveness factor but neglected the effects of the EDL at the interior pore scale. Throughout the study, Chen *et al.* explored the pH and CO_2R reaction rates through the length of the catalyst layer, concluding that the agglomerate size has significant effect on current density, with larger agglomerates reducing the CO_2R current density (**Figure 19**). This work presents a good first step towards the development of multiscale models for CO_2R that capture meso- and macroscale effects on the local current densities.

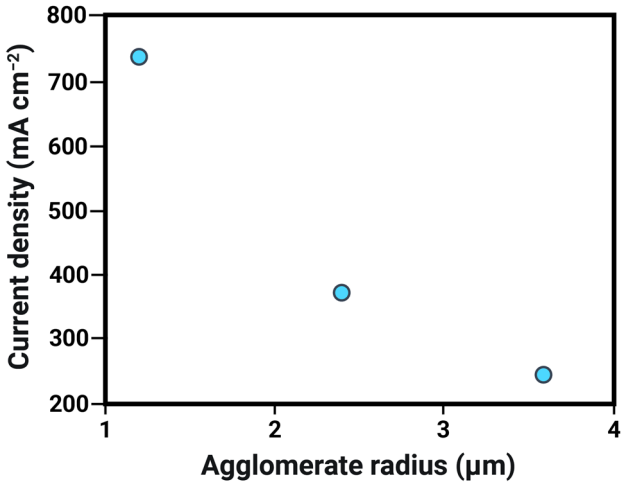

Figure 19: Impact of agglomerate size on CO_2R current density via modeling of a MEA architecture. Adapted from work by Chen *et al.*[74] Copyright 2020 The Electrochemical Society ("ECS").

Sadeghi *et al.*[273] developed a modeling framework where transport and reaction kinetics within the micro- and mesopores of the agglomerates were resolved with a PNP-type EDL model. This pore-scale model was then fed into an agglomerate model, which subsequently informed a macroscale volume-averaged model. The overall CL effectiveness factor was calculated as:

$$\Gamma_{CL} = \Gamma_{np}\Gamma_{stat}\frac{\int_0^{CL}\Gamma_{agg}(z)dz}{L_{CL}} \tag{134}$$

where Γ_{np} is the effectiveness factor responsible for bridging the pore- and agglomerate-scales. It can be calculated as the ratio of current density within the pores divided by the idealized current density (on the surface of agglomerate). Γ_{stat} was described in their model as an empirical parameter that arises due to the inhomogeneous ionomer distribution and the connectivity of the interior pore network. The last term is the effectiveness factor of agglomerates, which accounts for the various agglomerate sizes and the thin film of solvent or ionomer surrounding the

agglomerate. The form of the terms in this expression can be retrofitted for a multitude of electrochemical-synthesis systems depending on the physics, reactions, and morphologies studied. Γ_{np} will change based on the chosen pore geometries, as well as the gas and ion concentrations, and bulk electrolyte potentials. Γ_{stat} can account for the statistical distributions in the size and number of these pores, their location, and how many of them are flooded vs. dry. All of these inhomogeneities at the pore- and agglomerate-scales have substantial repercussions for the local environments and thus the product distributions observed in electrochemical synthesis. The model by Sadeghi *et al.* (**Figure 20**) shows that, even at a moderate current density of 0.2 A cm^{-2}, Γ_{agg} is less than 0.25 throughout the catalyst layer, indicating poor utilization of the catalytic active sites. This result provides the impetus to better understand and optimize the microstructure of catalyst layers to reduce mass transfer limitations in catalyst particle agglomerates.[274-276]

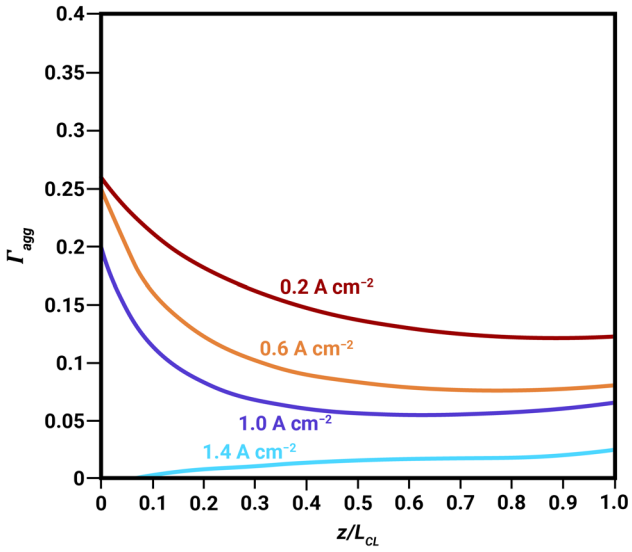

Figure 20: Agglomerate effectiveness factor (Γ_{agg}; Eq. (134)) as a function of position and total current density. $z/L_{CL} = 0$ is the CL interface with membrane, whereas $z/L_{CL} = 1$ is the interface with the PTL. Adapted from work by Sadeghi *et al.*[273] Copyright 2013 The Electrochemical Society ("ECS").

Recently, Moore *et al.* employed pore-scale simulation to analyze mass transport within the pores of an unsupported Ag catalyst layer without ionomer in a vapor-fed CO_2 electrolyzer (**Figure 21**).[178] The aim was to simulate the pore scale and determine if common assumptions employed in volume-averaged macroscale models of porous electrodes (see **Section 4.1.3**) were valid for electrochemical CO_2 reduction. Namely, to validate the common assumption that there are no radial gradients within a catalyst pore, and that the concentration at the reacting surface is equivalent to that within the electrolyte in the pore (*i.e.,* the effectiveness factor is 1). The authors identified three distinct mass-transport regimes in the catalyst-layer pores. In the first, which they refer to as "bulk-reaction control", the homogeneous reaction of CO_2 to form (bi)carbonate anions is the primary consumer of CO_2 (**Figure 21b, e**). In the second, referred to therein as "surface-reaction control", the electrochemical reaction of CO_2 to CO at the surface of the catalyst is the dominant phenomenon, and the entirety of the catalyst pore (*i.e.,* the solid-electrolyte or double-phase boundary) is active for CO_2 reduction (**Figure 21c, e**). In the third, referred to as "triple-phase-region (TPR) control", CO_2 reduction primarily occurs at the triple-phase interface between the vapor phase, liquid electrolyte, and solid catalyst (**Figure 21d, e**). They find that the assumption of a unity effectiveness factor at ambient conditions is sound for all cases except for TPR control, where the high rates of CO_2 reduction at the triple-phase boundary result in significant radial gradients within the catalyst pore. Using a mass-transport-regime phase diagram (**Figure 21f-g**), where the pore radius and CO evolution current density are the axes, they demonstrated that for low to moderate current densities and small pore radii, transport within the catalyst pore can be described by either the bulk or surface reaction regimes, consistent with prior assumptions made in the literature.[49, 60] Additionally, the work supports the concept that CO_2 reduction occurs at double-phase boundaries more often than at triple-phase

boundaries.[50] More interesting, however, is that they find that a change in the catalyst pore pH by one unit (pH 14 to 13) drastically changes the transport behavior of CO_2 within the pore. Lowering the pH results in a much larger region of surface-reaction control, and substantially mitigates the parasitic consumption of CO_2 within the pore by bulk reactions, enhancing CO_2R.

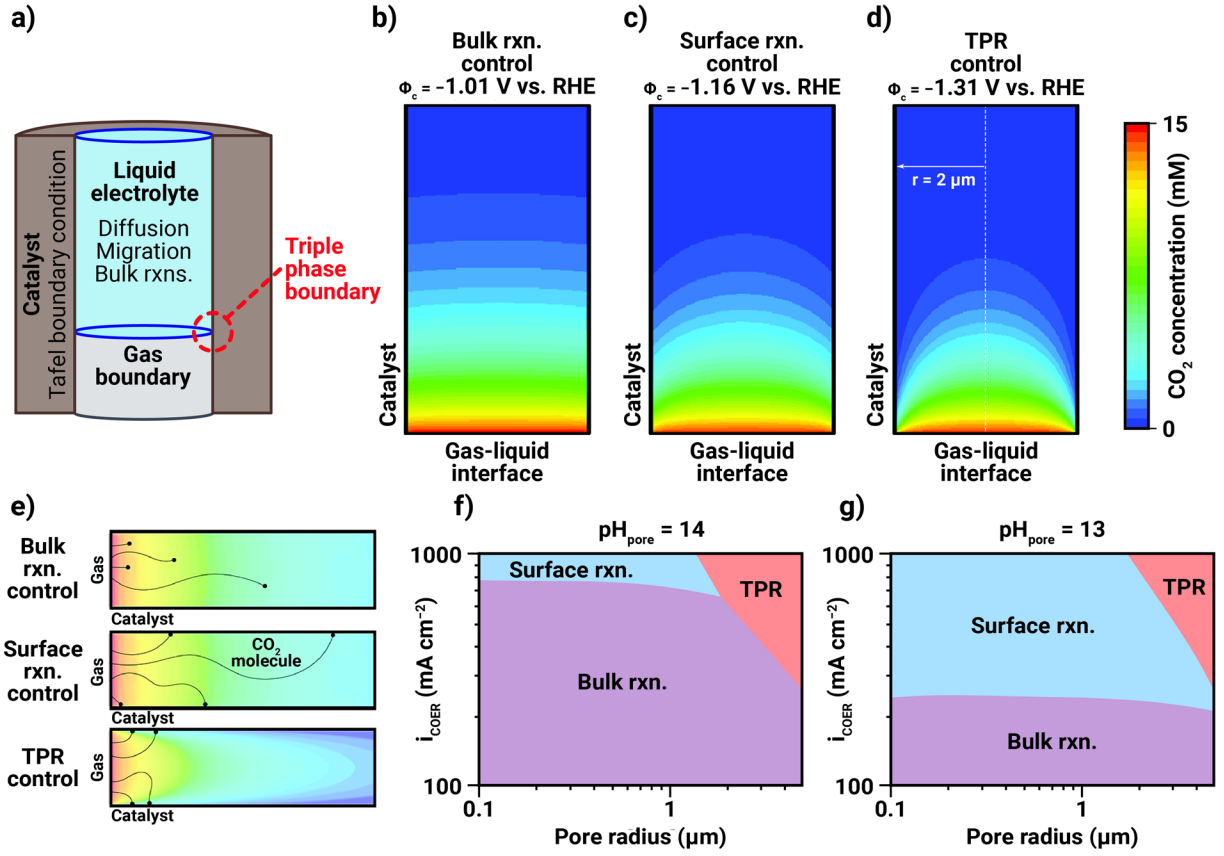

Figure 21: Simulation of an Ag catalyst pore in an unsupported catalyst layer for vapor-fed electrochemical CO_2 reduction. **(a)** Modeled domain: cylindrical domain where CO_2 reduction occurs at the outer catalyst surface. Mass transport is modeled in the liquid electrolyte. CO_2 concentration distributions within a singular catalyst pore for three distinct mass transport control regimes: **(b)** bulk reaction control, **(c)** surface reaction control, and **(d)** triple phase region (TPR) control. **(e)** Schematic depiction of the three mass transport control regimes. Phase diagram for mass transport regimes as a function of pore radius and CO evolution current density (i_{COER}) for a pore pH (pH_{pore}) of **(f)** 14 and **(g)** 13. Adapted from work by Moore *et al.*[178] Copyright 2021 American Chemical Society.

4.1.2 High-fidelity Porous-Media Models

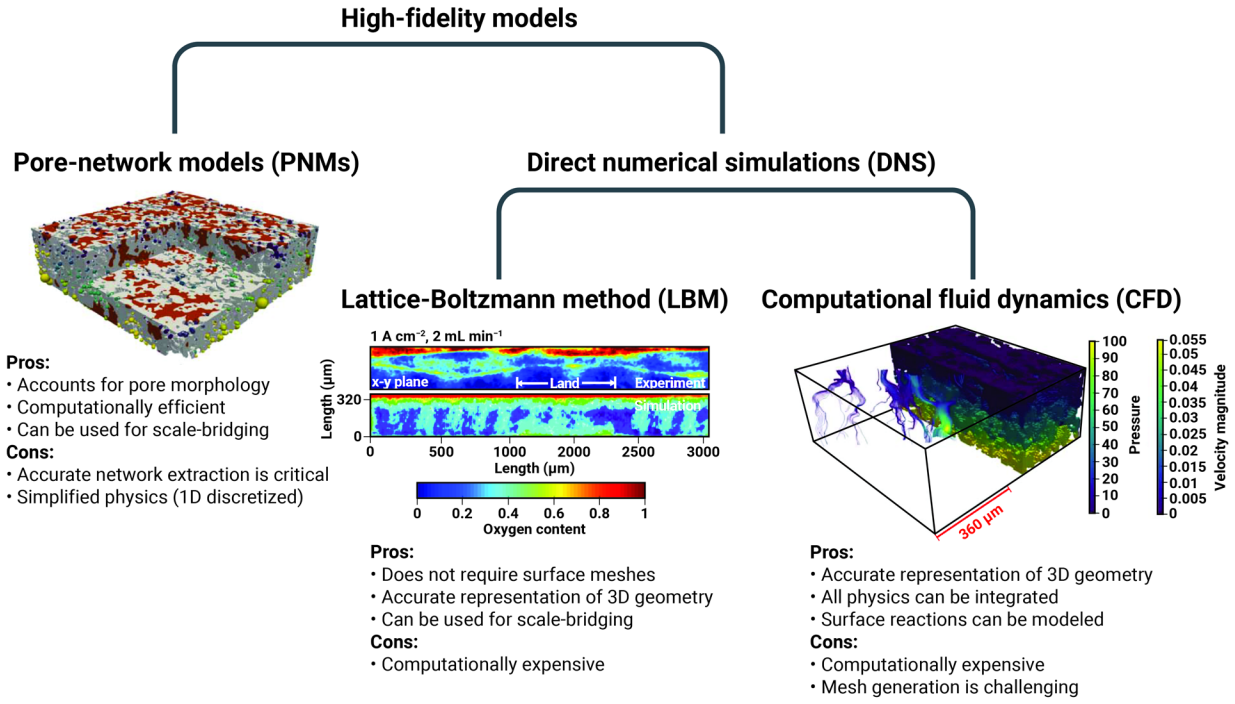

Figure 22: Schematic depiction of various high-fidelity models for porous transport layers along with pros and cons of each class of model. Adapted with permission from works by Jung *et al.*[277] (Copyright 2021 Jung et al.) and Satjaritanun *et al.*[278] (Copyright 2021 Satjaritanun et al.).

CLs and PTLs are morphologically complex multiscale media with pores ranging from micro (1 to 10 nm), meso (10 nm to 1 □m) to macro (1 to 100 □m) scales. Continuum models are not well suited to describe local heterogeneities that include variations in pore sizes and shapes, dead-ends, chemical or wettability variations, etc. High-fidelity porous-media models can overcome these bottlenecks and account for heterogeneities, but care must be taken in their implementation because they are often numerically expensive. The two main classes of high-fidelity models are pore-network models (PNM) and direct-numerical simulations (DNS), as shown by **Figure 22**, where the latter category consists of Lattice-Boltzmann-method (LBM) and computational-fluid-dynamics (CFD) methods.

A PNM relies on a statistical description of the medium (typically obtained through imaging or advanced formation algorithms) and reduced-order physics-based descriptions for the linkages between the network nodes. These linkages essentially represent the resistance to transport through the network. Advanced PNMs also incorporate source terms at the nodes in the network to account for catalyst sites. The network architecture and use of reduced order equations allows for hundreds of pores to be evaluated and solved in a relatively computationally efficient manner. PNMs can be used for a single-phase transport, for example to extract diffusivity, permeability or other domain properties or for two-phase transport, where gas transport within electrolyte can be described. PNMs in electrochemical-synthesis literature have mostly been applied to water electrolysis.[95, 277, 279-281] Dual PNMs (D-PNMs) have been proposed in geological community,[282] but have yet to be implemented in the electrochemical-synthesis community.

LBM is a mesoscopic method that solves Navier-Stokes equations at the macroscale, while considering interparticle forces at the microscale. One of the advantages of the method is that it does not need to track interfaces for two-phase systems, resulting in better solution convergence, compared to CFD methods. Like PNMs, LBM models have been mostly applied to study water and oxygen transport in the PTL of water electrolyzers.[283, 284] LBM is applied over the reconstructed 3-D domain, commonly obtained with x-ray computed tomography, FIB-SEM or other imaging tools.[96] While application of LBM beyond computational fluid dynamics and calculation of the flow field are still quite rare, LBM has recently been applied in the electrochemical community to study both species transport in porous components and their reactivity.[285, 286] Kamali *et al.* developed a boundary condition for simulation of a surface reaction rate possessing a reaction order of 1. This boundary condition was called “half-way

bounce back" and was validated against an analytical reaction diffusion solution. Satjaritanun *et al.* further extended the LBM approach to model the catalyst layer using an agglomerate model.[287]

DNS have been sparsely used to model electrochemical synthesis porous electrodes, primarily due to their higher computational cost compared to PNM, although they are inherently the most accurate and can capture heterogeneities. Suter and Haussener[211] reported an experimentally-validated, 3-D-mesoscale model of Ag inverse opal structures for CO_2 reduction in potassium bicarbonate electrolyte (**Figure 23**). The physics of the model accounted for diffusion of species in pore space, bulk reactions in the electrolyte, and surface reactions. Using this 3-D model of the porous electrode, they determined that increasing the roughness factor of the electrode enhanced CO FE and suppressed H_2 FE (**Figure 23b**), elucidating that increasing the roughness factor induced substantial concentration gradients within the pore domains (**Figure 23c**), due to the trapping of OH^- within pores further from the bulk electrolyte. Additionally, they found that increasing film thickness and decreasing pore size trapped more anions, resulting in higher CO FE (**Figure 23d**). This work highlights how the 3-D-geometry of a porous electrode can result in drastic changes in the local microenvironment and thus the observed product distributions in an electrochemical-synthesis device. Overall, there are several approaches to modeling the relevant porous media, and the approach to be taken depends on the questions being asked. While DNS provides the most rigorous descriptions, its computational cost in terms of convergence and meshing limits its applicability. Pore-network models provide some consideration of the pore network, usually in terms of transport processes, and can go to full layer length scales, but is these models ultimately use statistical representations of the

medium and often reduced physics. Finally, volume-averaged macro-homogeneous approaches do not account explicitly for pore structures but can involve complex physics at multiple length scales as discussed in the next section.

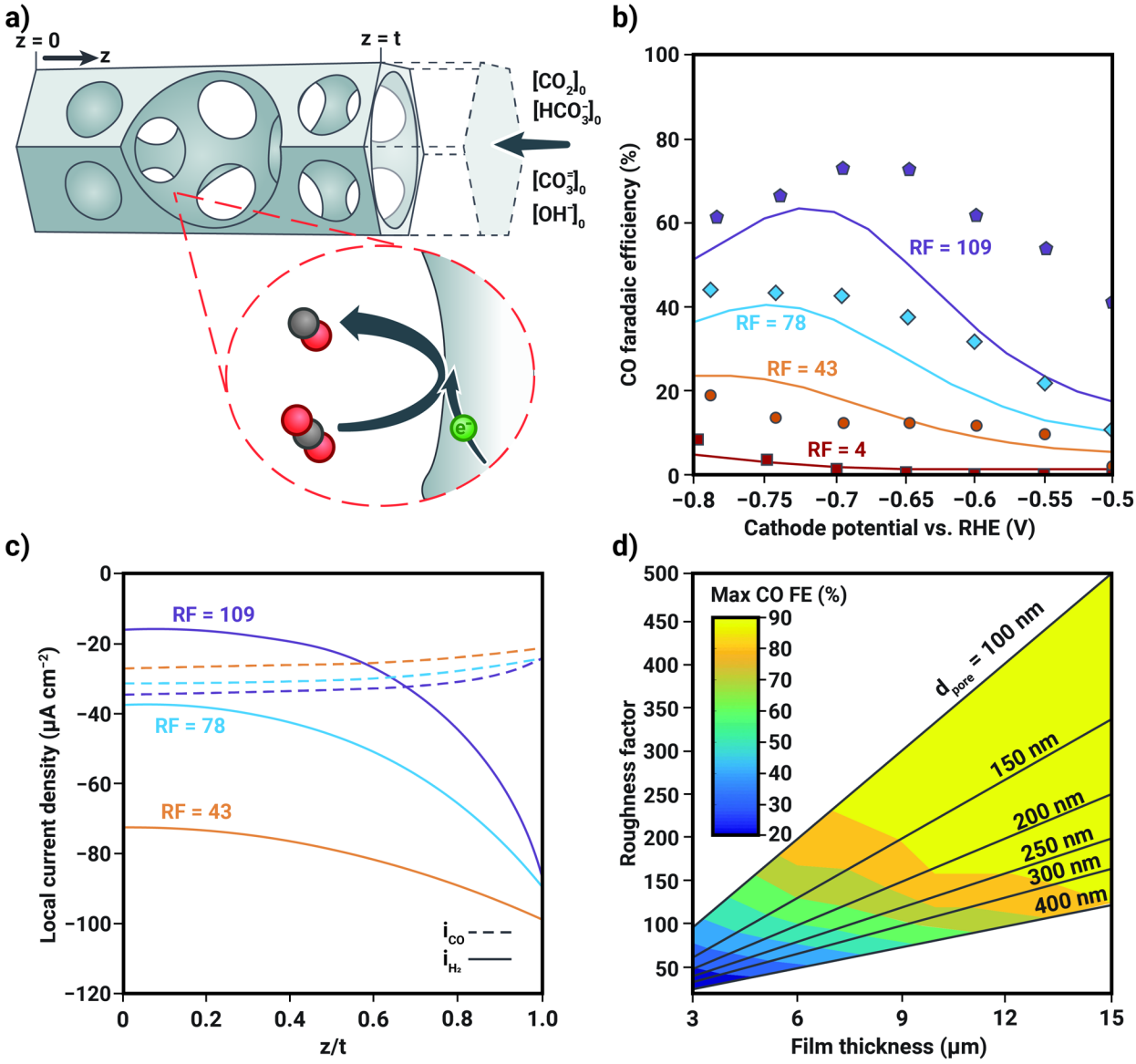

Figure 23: Results of a complete 3-D DNS of an Ag mesoporous electrode. **(a)** Modeled geometry. **(b)** Impact of roughness factor (RF) on CO FE as simulated and validated by experiment. Experimental data shown as markers, simulation in solid lines. **(c)** Local current density within a pore as a function of location within the porous network for multiple roughness factors. Solid lines represent H_2 current densities; dashed lines represent CO current densities. **(d)** Impact of pore radius and film thickness on the maximum achievable CO FE. Adapted with permission from Suter *et al.*[211] Copyright 2017 Royal Society of Chemistry.

4.1.3 Macroscale Modeling

Macroscale models are used to describe transport and reaction processes that occur at larger length scales and can be applied across the entire domain of an electrochemical-synthesis device or porous electrode (**Figure 24a**). This feature enables macroscale models to produce results that are easily compared to experimental observables (*i.e.,* FEs and polarization curves). More importantly, while the high-fidelity models presented in the previous subsections (4.1.1 and 4.1.2) do enable deeper, more accurate understanding of the impact of heterogeneities and local phenomena within the porous electrode, the volume-averaged models enable investigation of the material and reactor-design parameter space albeit with perhaps limited microscale physics, which can be upscaled using surrogate models or fits from the hi-fidelity ones.

Existing macroscale models consider a variety of dimensionalities (1-D, 2-D, 2-D + 1, and 3-D). Lower dimensional models (*i.e.,* 1-D and 2-D) are the simplest models, but have been demonstrated to simulate potential and species-concentration gradients effectively across porous catalyst and transport layers in the through-plane direction.[74, 288] To reduce computational cost, these types of models represent 3-D porous electrodes with volume-averaged parameters that are interpretable in 1-D and 2-D reference frames (**Figure 24**). For example, mass-transfer resistances that depend on the pore-size distribution and connectivity of the porous medium are often estimated using Darcy's law (Eq. (58)), which describes transport of viscous fluid within a porous medium, with nominal porosity and tortuosity values. This volume-averaged approach implicitly neglects double-layer effects, pore-network heterogeneities, and other microkinetic phenomena. For these reasons, macroscale models rely on effective transport properties that can be measured experimentally or determined computationally if morphology of the domains is known. Experimentally measured effective transport properties such as thermal conductivity,

effective gas diffusivity, and permeability can be directly used in Eqs. (83), (44), and (58), respectively, to describe transport. Alternatively, one can use bulk transport coefficients and correct them for transport in porous media as is done in Eq. (46), where effective properties are obtained when bulk transport parameters are corrected with porosity and tortuosity values. Additionally, these models need to incorporate interfacial transport resistances, such as thermal contact resistances or mass-transport resistance of ionomer thin films; it is also important that experiments performed to obtain electrochemical kinetic parameters are designed to account for mass-transfer effects.[101]

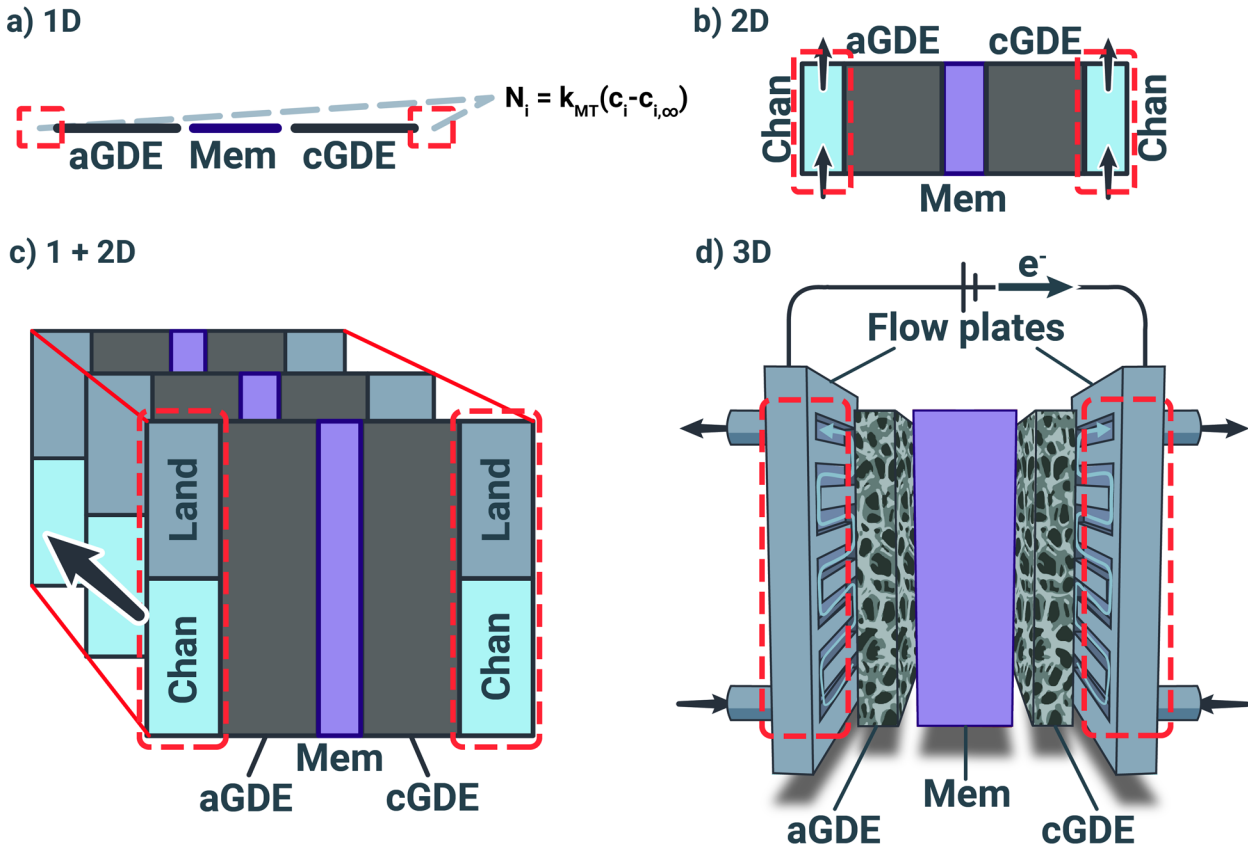

Figure 24: Schematic depicting the modeling of a porous electrode device with various dimensionalities of the simulated flow: **(a)** 1-D, **(b)** 2-D, **(c)** 1 + 2-D along-the-channel, and **(d)** 3-D.

Steady-state macroscale models of electrochemical-synthesis systems are sufficient to describe polarization behavior, spatial distributions of chemical species along various dimensions, temperature distribution, and reaction selectivity. However, transient models (which are rarer in the literature) are required when simulating pulsed electrolysis, where either potential or current is varied over short-time intervals, which has been shown in several experimental works as an effective way to reach higher FE values for various products.[289-291] Two-phase models are necessary for most of the electrochemical-synthesis systems where reactants and products co-exist in gaseous and liquid forms.

Several macroscale models exist for porous electrodes used in electrochemical-synthesis devices.[49, 60, 67, 68] The majority of these models investigate gas-diffusion-electrode (GDE) architectures, which consist of carbon diffusion media with a deposited catalyst layer. For the volume-averaged approach, several morphological properties of the porous diffusion media and catalyst layers need to be known including porosity, pore-size distribution, tortuosity, and wettability (through water-retention curves) (See **Section 3.6.1**). To model catalyst layers containing ionomers, an ionomer volume fraction must be known to determine the volume of water- and ion-transport pathways.

Delacourt and Newman reported the first macroscale model for a CO_2 reduction electrolyzer with a porous silver electrode.[210] This 1-D model was developed with a framework for reducing numerical complexity: fast kinetic processes (*i.e.,* buffer reactions and mass transfer at the gas/liquid interface) were assumed to be at equilibrium, which eliminated terms from the conservation equations. The catalyst layers were also considered as interfaces instead of distinct domains and therefore heterogeneous concentration gradients within the porous catalyst layer were neglected.[71] This simplified model was used to investigate the effect of potential and local

pH on CO_2 reduction, and to quantify the consumption of CO_2 via equilibrium with (bi)carbonate anions and electrochemical reactions. The model results generally agreed with experimental data at low current densities, but the two sets of data diverged at high current densities.

One of the most challenging aspects to macroscopic modeling of porous electrodes is a description of two-phase equilibria and transport between liquid water and water vapor and water that exists within ionomer or membrane phases. For volume-averaged macroscale models, liquid-water saturation (the fraction of pore volume filled with liquid) is an output parameter and capillary pressure (difference between liquid- and gas-phase pressures) is the independent parameter. These functions yield water-retention curves, which have also been mapped out experimentally for a wide range of commercial carbon diffusion media.[201, 292] Data for catalyst layers is much more challenging to obtain, largely because of the higher surface area and electrowetting phenomena, which modulates hydrophobicity as a function of potential.[293] Therefore, the water fraction and distribution within catalyst layers is one of the large uncertainties associated with multiphase volume-averaged macroscale models. Currently, experimental methods are still not sufficiently precise to measure water or electrolyte content in the catalyst layer as a function of potential.[294]

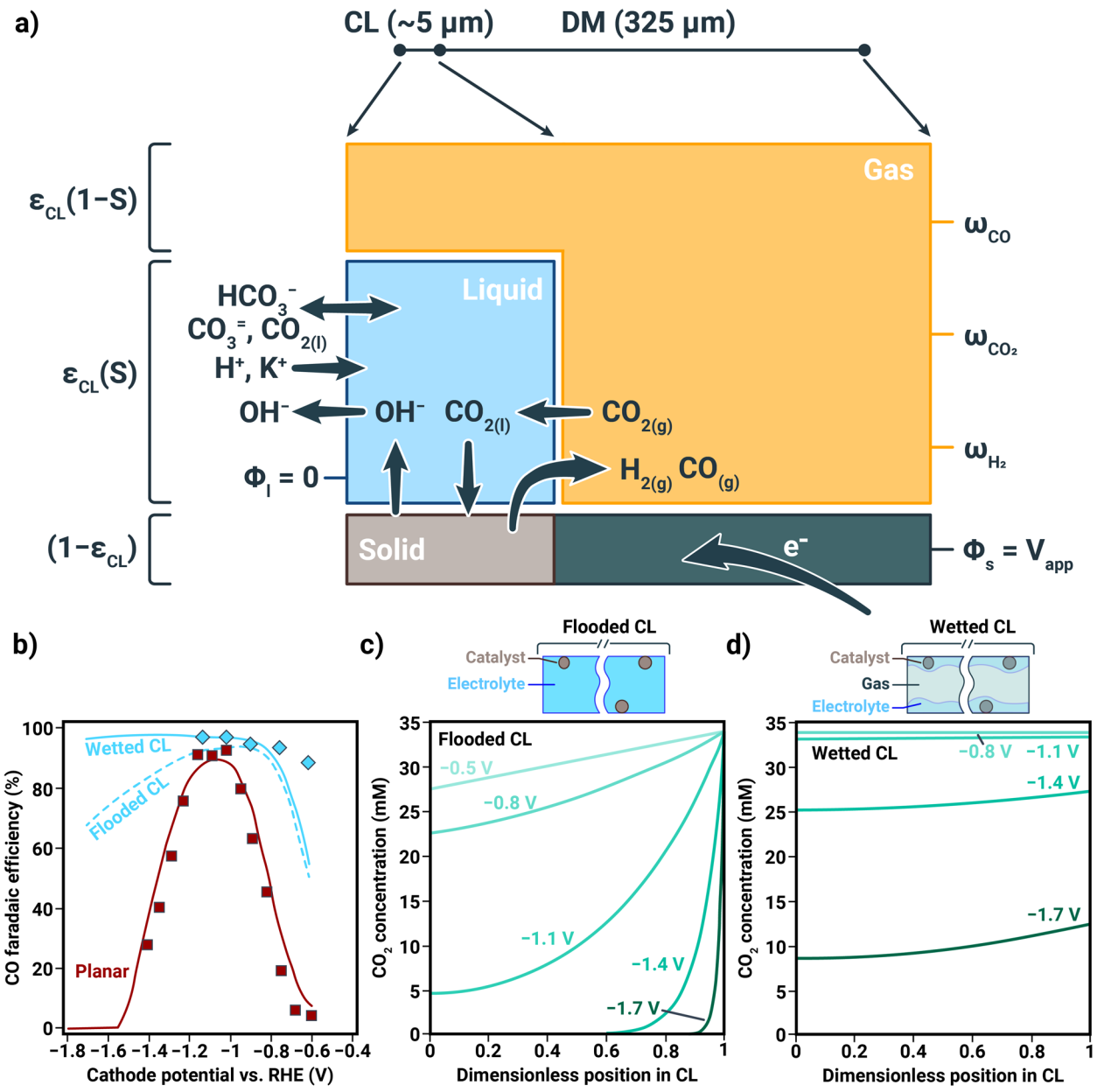

Figure 25: (a) Schematic depiction of a volume-averaged modeling domain for a Ag gas-diffusion electrode **(b)** Modeled (solid lines) and experimental (markers) CO FE for a planar electrode, as well as a flooded and partially wetted catalyst layer. Modeled local CO_2 concentration for various applied potentials for a **(c)** flooded and **(d)** partially wetted catalyst layer. Adapted with permission from Weng *et al.*[60] Copyright 2018 Royal Society of Chemistry.

Because the liquid content in the catalyst layer cannot be measured easily, modeling is particularly useful for elucidating the impact of liquid saturation on electrochemical synthesis. Weng *et al.*[60] were the first to simulate three water saturation states for the catalyst layer of a

silver GDE for CO_2 reduction: a flooded catalyst layer, uniformly-wetted catalyst layer, and a catalyst layer that is described by a water-retention curve. The results demonstrated that flooding significantly reduced the FE for CO formation at high current densities (>100 mA cm^{-2}) because of an uneven distribution of CO_2 and enhanced competition from HER. In 2020, a 1-D steady-state volume-averaged model was developed for full CO_2 reduction cell with a copper catalyst at the cathode.[67] The model contained the physics of water evaporation/condensation, capillary effects and liquid-phase transport to determine water saturation throughout the porous electrode more accurately. A correction to the intrinsic catalyst surface area, a_s^0 , was included to account for accumulation of liquid water blocking the path of reactants to catalyst sites:

$$a_{s,k} = (1 - S_{CL})a_s^0 \tag{135}$$

where, S_{CL} is the liquid saturation of the catalyst layer and $a_{s,k}$is the corrected specific interfacial surface area. The volume fractions of the medium *m* were calculated from the intrinsic porosity:

$$\varepsilon_{S,m} = 1 - \varepsilon_m^0 \tag{136}$$

$$\varepsilon_{I,m} = \varepsilon_m^0 \times f_{I,m} \tag{137}$$

$$\varepsilon_{L,m} = \varepsilon_m^0\left(1 - f_{I,m}\right) \times S_m \tag{138}$$

$$\varepsilon_{G,m} = \varepsilon_m^0(1 - f_{I,m})(1 - S_m) \tag{139}$$

where *S*, *I*, and *G* are solid, ionomer, and gas phases, respectively, and *f* is the volume fraction of ionomer in the pore space. The medium can be a catalyst or diffusion medium. The model showed that catalyst-layer thickness and surface area were not significant (within the parameter range of the model) because the system was not kinetically limited below 250 mA cm^{-2} current

density. Yang *et al.*[66] applied a similar isothermal, steady-state model for CO_2 reduction to formate anions and CO. They found that increasing the CO_2 velocity along the flow channel by 200 to 400% from its baseline value (3.85×10^{-3} m s^{-1}) increased the product yield. However, the product yield remained constant as the velocity was increased further from 400 to 1000% of the baseline value because the increases in local CO_2 concentration resulting from operating at higher flow velocity were offset by reductions in the total catalyst-layer pressure.

Kim *et al.*[89] conducted experiments for pulsed electrolysis of CO_2 reduction on a copper foil, and experimentally demonstrated that pulsing cathodic potentials between −1.15 and −0.8 V vs. SHE increased the total current density and the FE for C_{2+} products and decreased the FE for H_2 and C_1 products. Bui *et al.*[135] used a 1-D transient model of a Cu electrode and 100 □m thick mass-transport boundary layer with 0.1 M $CsHCO_3$ to simulate Kim's data. This model incorporated the effects of local pH and CO_2 concentration on the reaction kinetics. An important finding of the simulations is that a combination of pH, CO_2 concentration, and overpotential result in increased C_{2+} FEs. This work also identified an ideal pulse shape with an average cathodic potential of –0.975 V vs. RHE that increases the pH, without sacrificing the selectivity to C_{2+} products.

CO_2 and CO reduction on copper was also modeled for a flow-through porous-electrode architecture by Chen et al.[74] The authors' macroscale model simulated and compared the concentration profiles and catalyst activities associated with different electrode architectures (*i.e.,* planar, nanostructured, and porous). Owing to thinner boundary layers and higher electrochemically active surface areas (ECSAs), the porous electrodes achieved higher CO_2 reduction activity than the planar and nanostructured electrodes. The porous electrodes also yielded higher FE values for ethylene than the planar or nanostructured electrodes because they

exhibited higher pH values that suppressed methane formation (**Figure 26a**), especially closer to the current collector. In contrast, ethylene generation was independent of position in the electrode because the electrochemical kinetics are explicitly independent of pH (**Figure 26b**).[3] The effect of CO surface coverages was also simulated, and it was shown that high CO surface coverage boosts both methane and ethylene formation rates. These studies collectively demonstrate the utility of macroscale models for relating a combination of factors on the porous-electrode activity and selectivity.

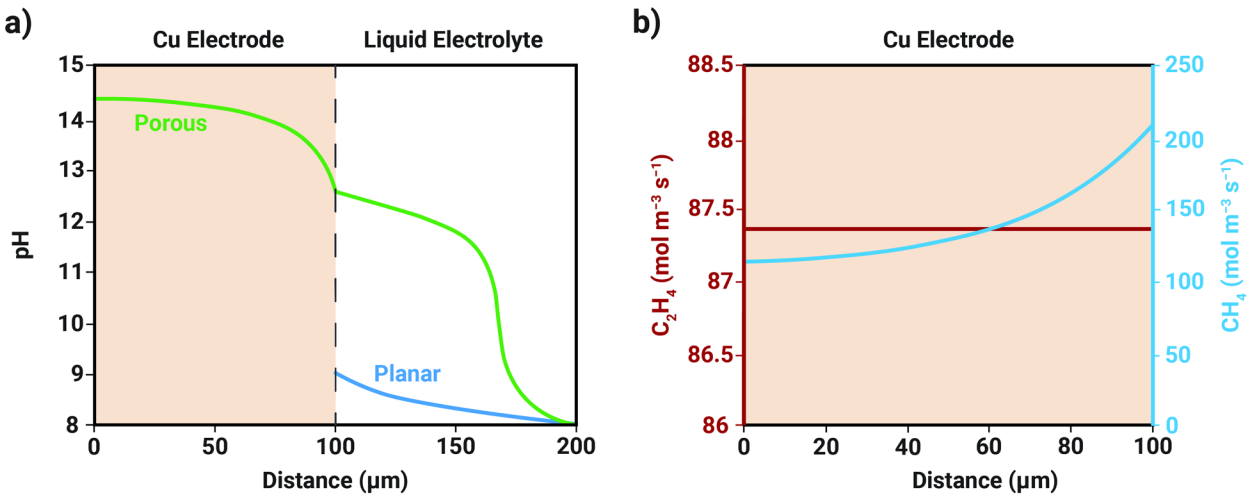

Figure 26: (a) Simulated comparison of local pH within a porous electrode and a planar electrode performing electrochemical CO_2 reduction at a cathodic potential of −1.65 V vs. SHE with an electrolyte solution of bulk pH = 8. **(b)** Simulated spatial variation in ethylene and methane generation within a porous electrode. Adapted with permission from work by Chen *et al.* [74] Copyright 2020 The Electrochemical Society ("ECS").

4.2 Modeling of Ionomers and Membranes

Key to the development of devices for electrochemical synthesis is the choice of solid electrolyte or ionomer, which exists in both thin-film (in catalyst layer) and membrane (as a separator) forms. The ionomer serves two primary purposes: first to, provide pathways for ionic conduction between the electrodes; second, to prevent the crossover of evolved product gases between electrode chambers.[49, 127]

Most modern electrochemical synthesis devices can be characterized as using one of four different ionomer types (**Figure 27b**): a cation-exchange membrane (CEM), an anion-exchange membrane (AEM), a reverse-bias bipolar membrane (RB-BPM), or a forward-bias bipolar membrane (FB-BPM). Recent work has demonstrated that the choice of membrane type can have a significant impact on the local environments achieved within an electrochemical-synthesis device.[170, 217] Additionally, the use of CEMs or BPMs has been shown to negate the effects of parasitic carbonate crossover in devices for electrochemical CO_2 reduction.[295, 296] Continuum modeling can be used to elucidate the mechanism and rate of species transport. Furthermore, such models can help determine the optimal configuration and material property design targets for a given electrochemical-synthesis scheme. In the following section, macroscale models for ion-exchange membranes will be evaluated and discussed within the context of electrochemical synthesis.

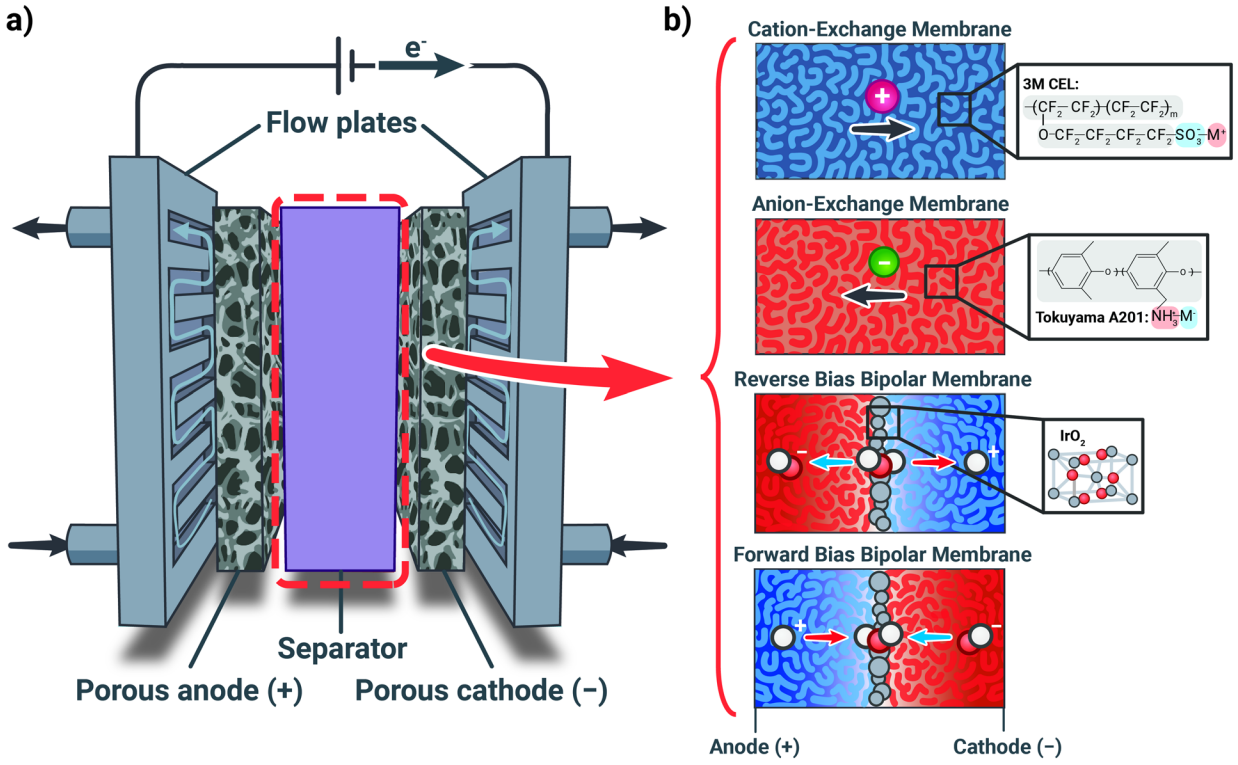

Figure 27: (a) Schematic depicting a typical porous electrode device. **(b)** Schematics describing the various types of ion-exchange membranes employed in electrochemical synthesis: cation-exchange membranes (CEMs), anion-exchange membranes (AEMs), reverse bias bipolar membranes (RB-BPMs), and forward bias bipolar membranes (FB-BPMs). Insets depict example chemical structures for CEMs, AEMs, and interfacial BPM catalysts.

4.2.1 Models of Cation-Exchange Membranes

CEMs have long been utilized in electrochemical devices such as proton-exchange-membrane fuel cells due to their high protonic conductivity and low gas permeability, which minimizes crossover of the product or reactant gas species.[297, 298] The prototypical CEM (Nafion) is comprised of a hydrophobic backbone (*e.g.,* PTFE) with charged, hydrophilic sidechains attached (*e.g.,* sulfonic-acid groups),[127] see inset in **Figure 27b**. CEMs are defined by their equivalent weight (defined as the mass of dry polymer per mole of fixed charged sites) or the inverse of their ion-exchange capacity. Typical CEMs phase separate, with water or solvent uptake occurring and transporting in the hydrophilic domains, providing a pathway for ion transport.[127] Key to understanding CEMs employed in electrochemical synthesis is the partitioning of cations and water in the CEM, because their local concentrations severely impact synthesis performance. A well hydrated membrane is required to facilitate cationic transport and avoid severe ohmic losses at high current densities, and a CEM exchanged with protons is substantially more conductive than one exchanged with other alkali cations.[160] At the same time, in CO_2R, a membrane with a lower water content and exchanged with Cs^+ cations maximizes the selectivity to C_{2+} products.[217] A membrane with lower water content reduces the selectivity to less desirable H_2, whereas the hydrated Cs^+ cations can pack tightly in the double-layer due to their smaller solvated-radius, enhancing the local electric field and improving the adsorption of intermediates for valuable CO_2R products.[130, 131, 215, 217] These performance tradeoffs underscore the need to design CEMs with carefully tailored microenvironments that can balance both efficiency and selectivity objectives required in electrochemical synthesis.

Many prior studies have sought to understand electrolyte transport in CEMs employed for various applications,[116, 160-162, 299-311] with the aim of developing membranes that selectively transport desirable species and limit the movement of contaminants, additives, or other redox species that worsen device performance.[312] The extensive work of Kamcev and Freeman provides significant insights into the thermodynamics and transport of ionic species and solvent in CEMs.[304-309, 313] In their earlier work, they developed a thermodynamic model for ion sorption in CEMs that, given the parameters of the CEM fixed-charge concentration and the Manning parameter (a dimensionless spacing between fixed charge groups), is capable of predicting the co- and counter-ion sorption within a CEM to a remarkable degree of accuracy for a wide variety of monovalent and divalent electrolyte solutions.[306, 308, 313] The key finding in this set of studies is the importance of thermodynamic non-idealities when calculating ion-partitioning in CEMs. In particular, the inclusion of Manning condensation (the condensing of counter-ions onto the fixed-charge groups of the CEM) was required to achieve agreement and predictive power with experimental data. For CEMs with a high degree of inhomogeneity, the Manning parameter had to be fit experimentally, but for those with poor phase separation, Manning parameters calculated from theory were sufficient to describe experimental data. This effect and subsequent slower diffusivities also needed to be incorporated to fit transport data when modeled using a Nernst-Planck framework, as per Eq. (67).[305, 309]

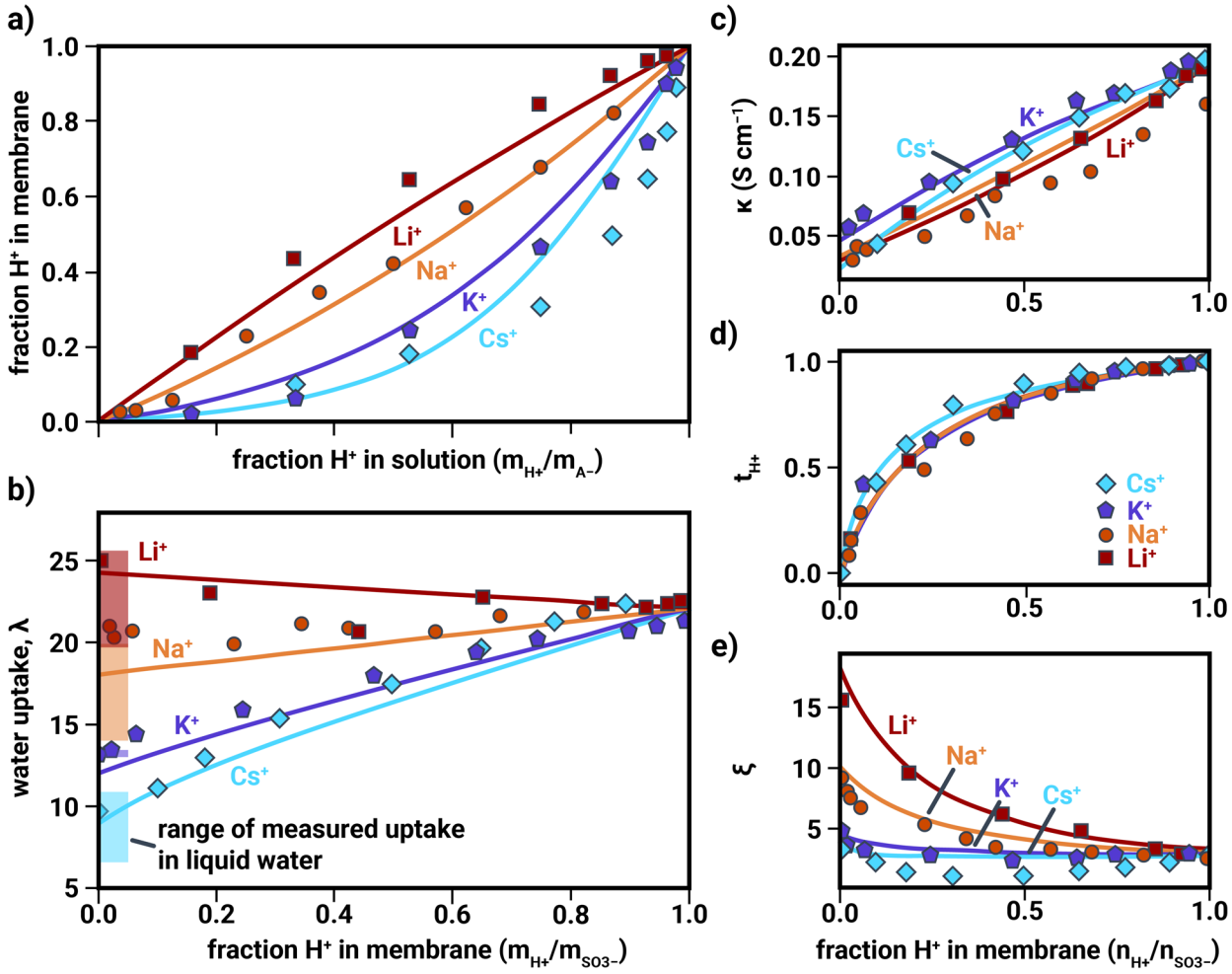

Figure 28: Summary of modeling ion and species exchange in membranes. **(a)** Partitioning of various alkali cations between the membrane and the exchange solution. **(b)** Water uptake, **(c)** conductivity, **(d)** proton transference number, and **(e)** electro-osmotic coefficient for a CEM exchanged with various cations. Markers represent experimental data; simulation is denoted by solid lines. Adapted from work by Crothers *et al.*[116, 160] (Copyright 2020 Crothers et al.), with experimental data adapted from Okada *et al*[314].

Recently, Crothers *et al.* expanded upon the work of Kamcev and Freeman through the development of a modeling framework for the transport and thermodynamics of multiple ions in a CEM.[116, 160, 162] This set of studies is particularly relevant for electrochemical synthesis because it specifically explores the uptake and transport of all alkali cations along with that of the solvent (water) in Nafion CEMs. In the first study by Crothers *et al.*, a thermodynamic model was developed that solved for ion and solvent uptake between the electrolyte and ionomer phases.

Nonidealities were accounted for using excess Gibbs free-energy terms (see **Table 3**) that explicitly account for solvation, electrostatic interactions, short-range physical interactions, polymer swelling, and steric interactions with the polymer.[116] The thermodynamic model was able to predict ion partitioning and water uptake (**Figure 28**) for CEMs exchanged with different alkali cations. The model also elucidated differences in partitioning resulting primarily from more favorable physical interactions of sulfonate moieties with alkali cations going from Li^+ to Cs^+ (**Figure 28a**). Additionally, these favorable interactions reduce the driving force for water to solvate and dilute the A^+-SO_3^- pairs, resulting in an opposite trend of water uptake compared to ion partitioning, with Cs^+-exchanged Nafion exhibiting the lowest water uptake and Li^+-exchange Nafion exhibiting the greatest water uptake (**Figure 28b**).

The framework developed by Crothers *et al.* was further employed to examine ionic transport in CEMs by taking the solvent uptake and ion concentrations solved for under thermodynamic equilibrium and simulating the full multi-component transport equations with Stefan-Maxwell-Onsager concentrated-solution theory, as described in **Section 3.4.1** Eqs. (51)-(52).[160] The model was suitably predictive of ionic conductivity, transference number, and electroosmotic coefficient (**Figure 28**) for all alkali cations and for a wide range of membrane ion concentrations. It demonstrated that the conductivity increases significantly as the fraction of protons in the membrane increases due to the enhanced mobility of protons compared to alkali cations (**Figure 28c**). Additionally, because protons are much more mobile than alkali cations, the transference number for protons is high (> 0.5) except for in the case of nearly complete exchange with alkali cations (**Figure 28d**). Lastly, the electroosmotic coefficient decreases when the membrane goes from the H^+-form to an alkali cation-form, and further decreases moving from Li^+ to Cs^+. This result is primarily due to the higher mobility of protons than alkali cations

and the lower water uptake moving from Li^+ to Cs^+. The results of this work and those of the work by Kamcev and Freeman underscore the importance of considering non-idealities when modeling multi-ion uptake and transport in CEMs, and they highlight the predictive power of such models for understanding CEM performance. The understanding developed in these studies can be leveraged to develop novel CEMs and operating conditions for electrochemical-synthesis applications.

The role of water activity in CEMs is critical and has been further evaluated for MEA devices utilized for both water-vapor electrolysis[163] and CO_2 reduction,[315] as well as extensively in the fuel-cell literature.[202] Work by Shafaque *et al.* used a semi-empirical model for water uptake in the CEM that used water-volume-fraction data collected by neutron radiography at different cross sections in the membrane to estimate the water-content gradients across the CEM in a CEM-CO_2 electrolyzer with a liquid-fed anode.[315] The work demonstrated poor hydration at the center of CEM when the cathodic CO_2 feed was not fully humidified, and that the conductivity of the CEM, and thus its performance, could be substantially enhanced through the use of a humidified CO_2 feed. Interestingly, this behavior was not observed in the work of Fornaciari *et al.,* which modeled CEM performance using a continuum model of an MEA water-vapor electrolyzer.[163] The model demonstrated that when the humidity of the cathode and anode feeds were lowered, the water content, and thus the conductivity, were also lowered, resulting in worse electrochemical performance due to greater ohmic losses (**Figure 29a**). However, the model also demonstrated that a fully humidified anode is sufficient to hydrate the cathode in water-vapor electrolysis (**Figure 29b)** at elevated temperature, as the membrane resistance was similar in the case of both a 65% anode | 65 % cathode relative-humidity feed as well as for a 98% anode | 30 % cathode relative-humidity feed. Furthermore, the model deconvoluted

contributions to the water flux, demonstrating that the high transport coefficient resulting from the electroosmotic transport of water in the fully humidified anode case is sufficient to hydrate the cathode and avoid mass-transport limitations (**Figure 29c)**; however, such effects become more complicated in CO_2R and AEMs as discussed in the next section due to higher consumption of water as a reactant as well as opposite direction for the electroosmotic flow. The results of these studies underscore the substantial utility of macroscale modeling to understand CEM performance and to inform the development of next-generation membranes and devices for electrochemical synthesis.

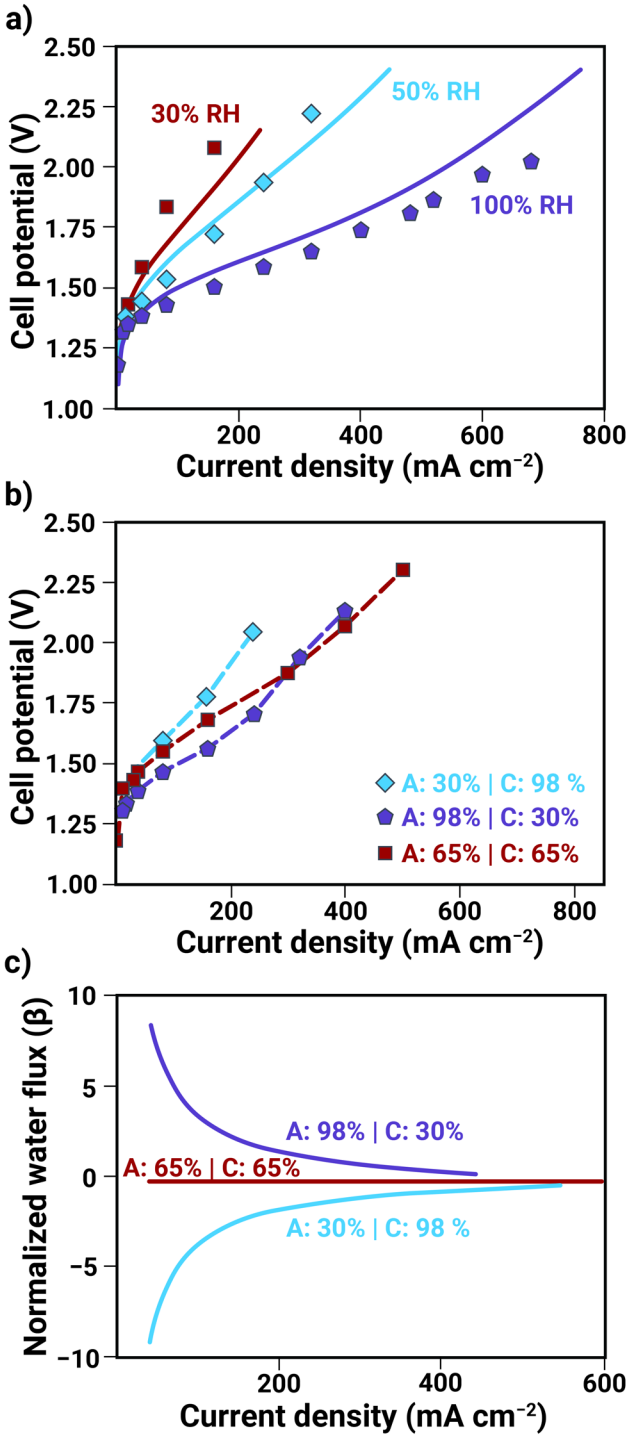

Figure 29: (a) Measured (markers) and simulated (solid lines) impact of water activity on electrochemical performance of a vapor-fed water electrolyzer. **(b)** Effect of asymmetrically varying water activity at each electrode. **(c)** Simulated water transport coefficient in the membrane for various water activities at each electrode. Adapted from work by Fornaciari *et al.*[163] (Copyright 2020 Fornaciari et al.).

4.2.2 Models of Anion-Exchange Membranes

A substantial number of MEA devices for electrochemical CO_2R have employed AEMs due to their ability to support the high pH environments required to suppress the selectivity to unwanted H_2 in CO_2R devices. Like CEMs, AEMs are typically copolymers with charged, hydrophilic side chains. Unlike CEMs, however, the charged moieties possess a fixed positive charge (*e.g.,* imidazolium), which facilitate selective anion transport (**Figure 27c**).[316] It is also important to note that most AEMs are significantly more amorphous than the polycrystalline PFSA CEMs.[308, 313] The amorphous nature of Sustainion and other similar AEMs facilitates greater gas solubility, permeability, and water uptake when compared to Nafion.[217] The enhanced gas permeability and solubility are desirable for CO_2R in the catalyst layer (but not as a separator) because they enable greater local concentrations of CO_2, enhancing mass transport.[217] However, AEMs in CO_2R are afflicted by parasitic carbonate crossover: CO_2 fed to the electrolyzer reacts with OH^- in the electrolyte, forming (bi)carbonate anions that then cross through the AEM and are reconverted to CO_2 at the less alkaline anode.[132, 317] This phenomenon results in very poor utilization of the fed CO_2 (< 8 %) for CO_2 electrolyzers employing AEMs (**Figure 30**).[318] Macroscale modeling can be used to further understand crossover in these systems and provide recommendations in the development of AEMs that maximize single-pass CO_2 conversion. For example, Weng *et al.* modeled this phenomenon in a CO_2 electrolyzer and calculated at most a single-pass utilization of 50% due to stoichiometric neutralization of the CO_2 feedstock with OH^- and transport of CO_3^{2-} through the AEM. This model has been corroborated by experimental studies which also show a limit of 43% single-pass conversion of CO_2 into CO in neutral media.[319]

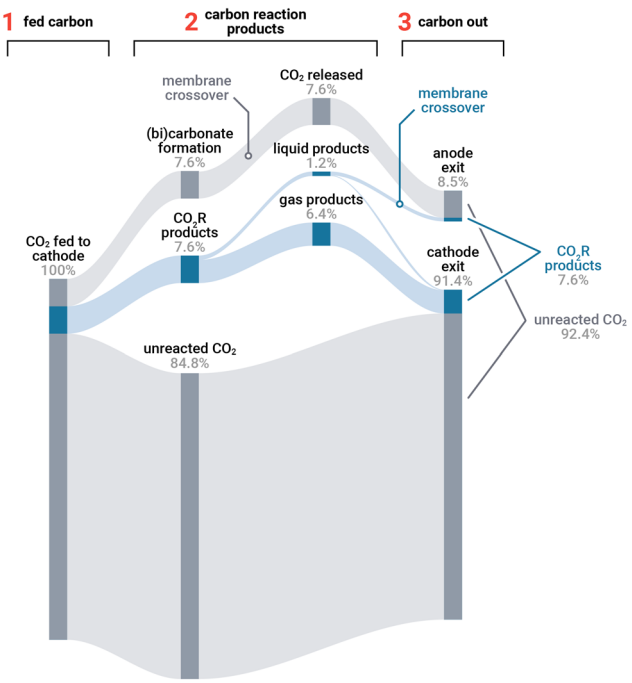

Figure 30: Sankey diagram representing the carbon mass balance for a typical AEM-based CO_2 electrolyzer. Of the total carbon that is fed to the cathode, 7.8% is converted into a reduced product (e.g., ethylene), 8.5% is emitted as CO_2 at the anode after crossing the AEM as (bi)carbonates, and 84.8% exits the cathode unreacted. Adapted with permission from work by Lees *et al.*[318] Copyright 2021 Springer Nature.

Like CEMs, understanding ion-partitioning and solvent uptake are critical in the development of next-generation AEMs for electrochemical synthesis, particularly with an emphasis on understanding the partitioning of OH^- ions and carbonate species. Work by Kamcev and Freeman also explored ion partitioning in AEMs with the Manning-theory framework discussed in section 4.1.2 [308, 313] They found that, unlike for CEMs, where the Manning parameter was employed as an adjustable parameter, the homogeneous structure of AEMs enabled the Manning parameter predicted from theory to be accurate over a wide-array of electrolytes.[308, 313] This result again highlights the importance of considering non-idealities when calculating phase equilibria in macroscale models of ion-exchange membranes

Models developed for tracking carbonate transport in AEMs have been employed to explore CO_2 contamination in AEM fuel cells,[320-322] and, more recently, in CO_2R to mitigate

carbonate transport in these systems.[49, 207] Recent work by Weng *et al.* used an Nernst-Planck framework with ideal Donnan equilibrium in a continuum model to simulate $CO_3^{=}$, HCO_3^{-}, and OH^{-} profiles within the AEM of an Ag-MEA CO_2 electrolyzer for the generation of CO from CO_2 (**Figure 31**).[49] Measuring ionic content of the AEM with a comparable degree of spatial resolution would be incredibly challenging experimentally, emphasizing the importance of models of similar nature to understand ionic partitioning in electrochemical-synthesis systems. The results of their study demonstrated that $CO_3^{=}$ ions comprise over 50% of the ionic species within the AEM at industrially relevant current densities of 500 and 1000 mA cm^{-2} (**Figure 31a-b**), and that the conversion of CO_2 to value-added products is limited to less than 10 % due to parasitic carbonate crossover (**Figure 31c**). The authors suggest that reducing the rate of CO_2 consumption by introducing homogeneous buffer reactions could drastically reduce crossover. Lastly, water management in the AEM was modeled, demonstrating that substantial dehydration of the membrane occurs (**Figure 31d**), which reduces electrochemical performance of the Ag-MEA, although it can be mitigated by increased temperature or thinner AEM.

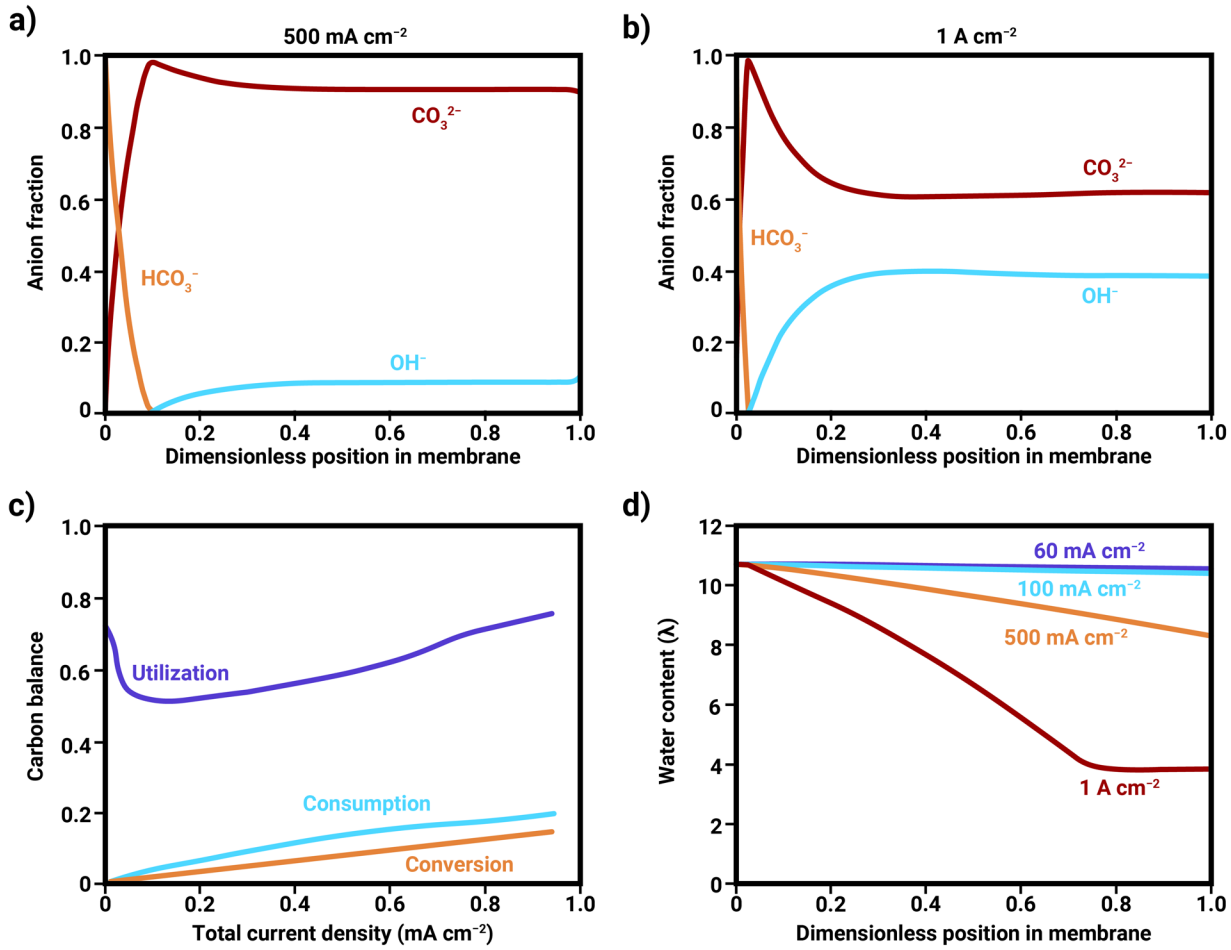

Figure 31: Simulated anion fraction at **(a)** 500 mA cm^{-2} and **(b)** 1 A cm^{-2} within an AEM employed in an Ag-MEA for electrochemical CO_2 reduction. **(c)** Modeled utilization, consumption, and conversion of CO_2 in the Ag-MEA as simulated. **(d)** Local water content (λ) within the AEM at various applied current densities. Adapted with permission from Weng *et al.*[49] Copyright 2019 Royal Society of Chemistry.

Recent work by McCallum *et al.*, expanded upon the Weng *et al.* models to optimize properties of AEMs for maximizing CO_2 utilization in electrochemical CO_2R over a Cu catalyst with a liquid bicarbonate anode feed.[207] By performing a sensitivity analysis on the AEM properties (membrane thickness and background charge), the authors were able to identify that the use of an as-thin-as-possible AEM would be optimal for mitigating crossover, because H^+ ions generated at the anode could diffuse through the thin AEM and neutralize carbonates species in the cathode stream. Additionally, a greater bicarbonate diffusion gradient develops

from the feed towards the cathode when the AEM is thinned, further enhancing utilization. These works further underscore the capacity of modeling to understand and elucidate methods to mitigate crossover.

4.2.3 Models of Bipolar Membranes

BPMs, in which a CEM and AEM are stacked with a water-dissociation catalyst in between them, present an exciting opportunity to control individually the pH at each electrode in an electrochemical-synthesis device, as well as to block parasitic carbonate and proton crossover.[323] Recent work by Patru *et al.*[324] and Blommaert *et al.*[325] investigated the performance of electrochemical CO_2R under both forward- and reverse-bias BPM orientations. Patru *et al.* observed better selectivity and mitigated crossover in forward bias. Conversely, Blommaert *et al.* observed that the best crossover and selectivity were for reverse bias. These contrasting results underscore the emerging need to understand better BPMs applied to electrochemical synthesis, of which continuum modeling plays a critical role due to the experimental complexity of interrogating such architectures and materials.

Many studies have sought to model the electrochemical behavior of BPMs.[117, 146, 150, 326-331] However, very few have modeled the BPM in pH gradients relevant to electrochemical-synthesis applications. In a recent study by Bui *et al.*, the authors modeled the BPM with as a continuum using a Poisson-Nernst-Planck framework under four distinct pH gradients relevant to electrochemical-synthesis applications, with strong agreement to experimental data using a single set of adjustable parameters (**Figure 32**).[117] They discovered that the current density in the plateau region of measured BPM polarization curves is dominated by co- and counter-ion crossover, and that the current density past the breakdown region of the curve was dominated by water dissociation. They then performed sensitivity analysis on the critical BPM properties,

discerning that the optimal BPM possesses a high ion-exchange capacity to maximize field-assisted water dissociation, and a thinner CEL than AEL layer to mitigate ohmic and water-transport losses while still blocking co-ion crossover.[117]

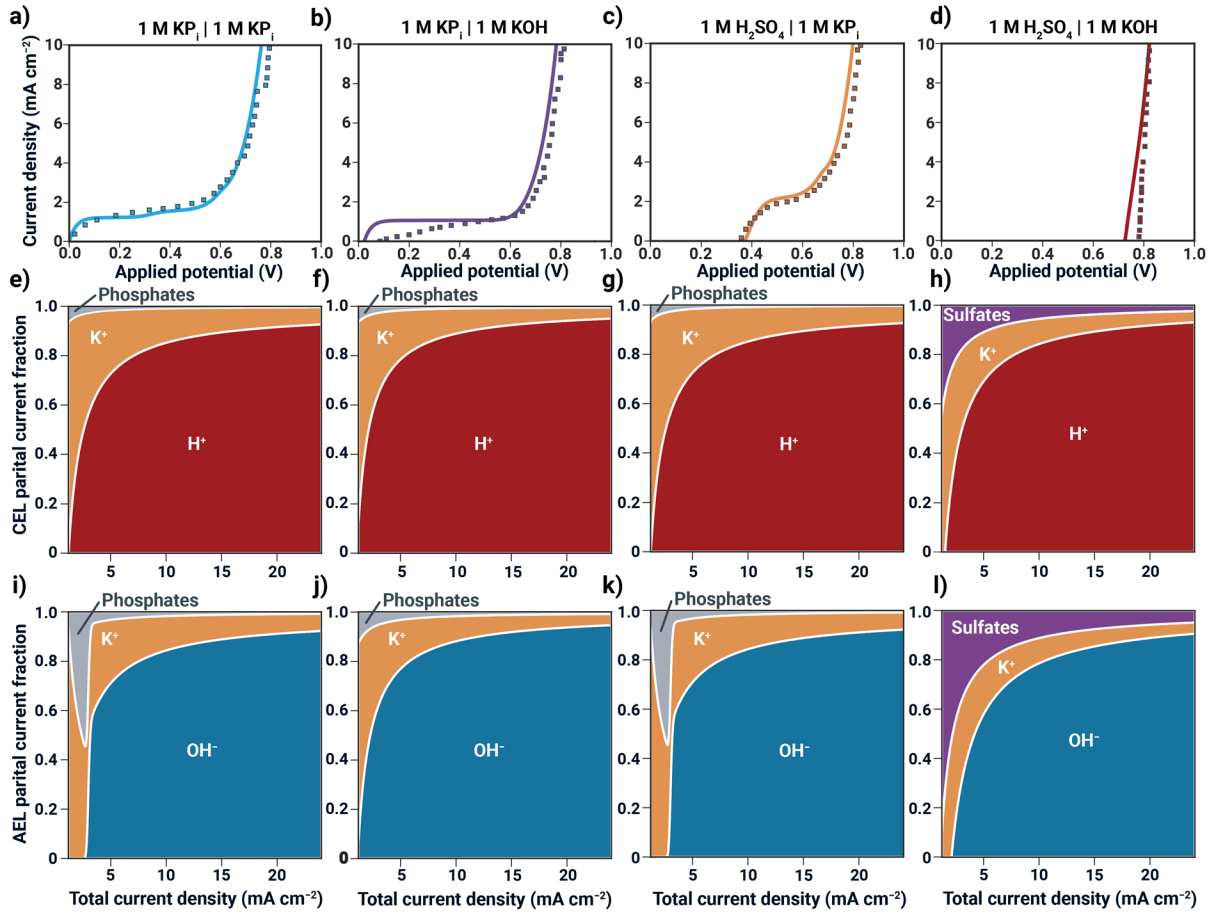

Figure 32: (a-d) Experimental (markers) and simulated (solid lines) polarization curves for a BPM under various applied pH gradients. Partial-current-density contributions of various ions to measured current in the **(e-h)** CEL and **(i-l)** AEL of the BPM. Adapted with permission from work by Bui *et al.*[117] Copyright 2020 American Chemical Society.

Lin *et al.* developed a similar multi-ion transport model that also explicitly modeled the interfacial junction profiles of the water-dissociation catalyst.[329] They found that the catalyst layer primarily serves to screen the electric field in the junction and accelerate water dissociation through field enhancement (Eqs. (39)-(42)). Explicit modeling of the catalyst layer further enabled the authors to perform sensitivity analysis on the catalyst-layer properties and provide

concrete guidance in the development of next-generation BPMs, demonstrating a slight sensitivity to catalyst-layer thickness, with increasing catalyst-layer thickness resulting in poorer performance. Similar to the work of Bui *et al.*, they found that increasing the ion-exchange capacity substantially improved water-dissociation catalyst performance. Additionally, when deconvoluting water dissociation current and co-ion current, they found that increasing the ion-exchange capacity also blocked the transport of co-ions by electrostatic repulsion. Nonetheless, additional work is still necessary to model these BPM materials in the context of complete electrochemical-synthesis devices and at higher current densities, as well as with co- and counter- ions more relevant to electrochemical synthesis, such as carbonates.

4.3 Modeling of Flow Plates

Flow plates are graphitic or metallic plates with engraved flow patterns that are used to deliver reactants and remove products from the electrodes of a device. Efficient convective mass transfer within flow plates is key to increasing electrochemical-synthesis activity and mitigating overpotentials. Continuum models are useful for generating optimized flow-plate designs because they can link flow-plate geometry (*e.g.,* flow pattern, channel length, and channel-to-land ratio) to electrochemical device efficiency. Coupling continuum modeling with advanced manufacturing is projected to accelerate reactor design for electrochemical synthesis.[76]

Approaches to modeling flow plates for electrochemical synthesis devices stem mainly from fuel-cell and flow-battery studies.[12] In simple 1-D models (**Figure 24a**), the flow plate is not explicitly considered.[49, 60, 67] Instead, a mass-transfer correlation that depends on the bulk concentration in the flow plate is often used as a boundary condition to describe the flux of reactant at the flow-plate/electrode interface. This type of boundary condition assumes that the chemical composition of the fluid in the flow plate is not affected by the reaction and is

homogeneous along the channel. 2-D cross-sectional models can more accurately represent the flow plate by simulating the land and channel at the flow-plate/electrode interface.[332-334] These differential models account for convective transport under the landing, but they do not quantify variations along the length of the flow channel.[335] Consequently, other 2-D models (**Figure 24b**) have been developed to quantify spatial variations along the flow path,[336-339] but these so-called "along-the-channel" models neglect land/channel effects. Kas *et al.* developed an "along-the-channel" 2-D model that was used to map the spatial activity gradients within a CO_2 electrolyzer cathode (**Figure 33**).[78] The authors demonstrated the effects of CO_2 reduction, (bi)carbonate reactions, and pressure drops on CO_2 transport in the in-plane and through-plane directions. The analysis highlighted the tradeoffs between high and low CO_2 flow rates: high CO_2 flow rates enable higher CO_2 reduction rates, but they also cause higher ohmic resistances and lower single-pass CO_2 conversion.

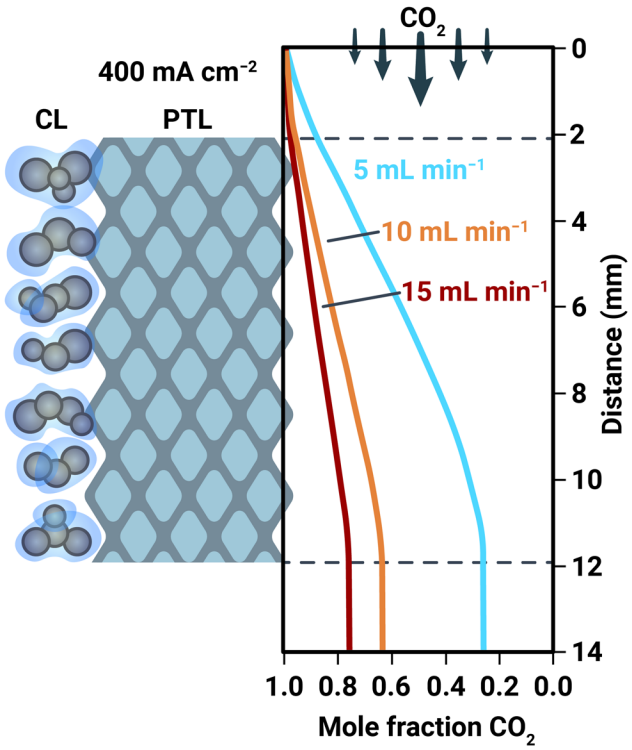

Figure 33: Change in local CO_2 mole fraction in the flow channel of a CO_2R device for various CO_2 flow rates at an applied current density of 400 mA cm^{-2} as simulated by a 2-D continuum model. Adapted from work by Kas *et al.*[78] Copyright 2021 American Chemical Society.

Pseudo 3-D models or "1+2-D models" have been developed to simulate simultaneously along-the-channel and land/channel effects (**Figure 24c**).[320, 321, 335, 340, 341] This approach entails solving 2-D cross-sectional models for the electrode with boundary conditions that vary along the flow path. The 2-D solutions are solved iteratively with mass-, charge, and heat-conservation equations (**Section 3.4**) or the flow channel to enable approximation of a 3-D geometry. Of course, true 3-D models are needed to model multicomponent mass transfer comprehensively in the flow plates (**Figure 24d**), as 1+2-D models cannot capture relevant transport phenomena such as under-the-land flow common in interdigitated and serpentine flow channels.[340, 342, 343] However, these models are generally too computationally intensive to bridge with device-scale models for electrochemical synthesis without sacrificing significant physics. Laminar flow is often assumed for gas transport within flow-field,[344] but for low kinematic viscosity of gases this assumption can break down and turbulent flow may need to be considered. 3-D models also need to be selected carefully to model flow in the channels and within the porous adjacent domains. Recent study in the field of redox flow batteries has attempted to directly model the effects of multidimensional flow within the flow field on electrochemical performance, namely to understand the optimal flow profiles and flow field geometries to maximize performance.[345, 346] Work by Knudsen *et al.*, even demonstrates that turbulent flow regimes exist in localized regions of the flow field (*e.g.,* the conduits connecting the inlet and outlet to the individual channels.[345] Notwithstanding, 3-D flow-plate models have been developed for CO_2 reduction, and these models are capable of tracking water activity and CO_2 depletion along the flow channel.[63] Humidifying the CO_2 feed reduced electroosmotic flow of water and yielded a more uniform water distribution in the flow channel (**Figure 34**). It is important to note, however, that a major

gap exists in studies that directly model turbulence due to multiphase or bubbly flows that are often present and relevant in electrochemical synthesis. Future work in the field should aim to model more fully turbulence induced by the multiphase flows often present in electrochemical synthesis systems, where reagents and products are both sparingly soluble in the aqueous electrolyte.

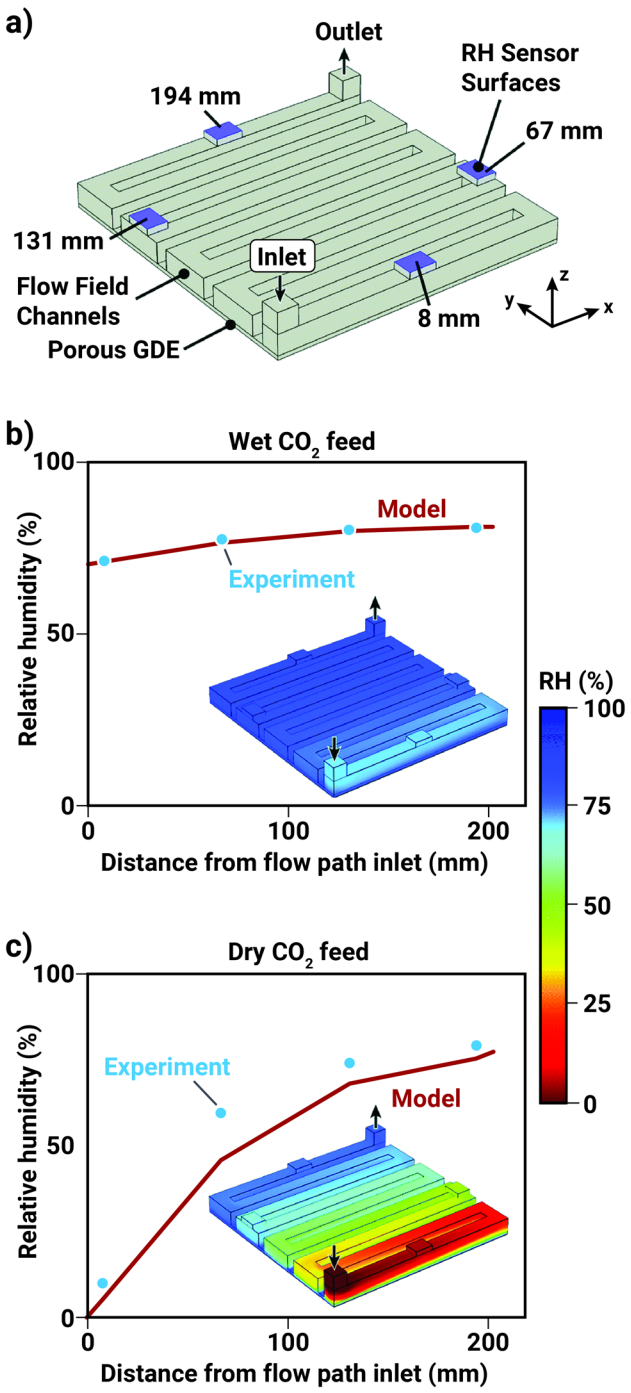

Figure 34: (a) Schematic of a 3-D-continuum model of transport in a flow channel of a CO_2R device. Experimentally measured (markers) and simulated (solid lines) relative humidity at various points along-the-channel for operation with a **(b)** wet CO_2 feed and a **(c)** dry CO_2 feed. Adapted from work by Wheeler *et al.*[63] Copyright 2019 Royal Society Chemistry.

Continuum models of flow plates can be used to answer several open design questions for electrochemical devices. For example, how do homogeneous reactions, which occur in the

relatively well-mixed flow plate, inhibit or intensify the reactants concentration at the electrode? How does the flow plate geometry influence the rate of consecutive electrochemical reactions (*i.e.,* the reduction of CO_2 to CO followed by the reduction of CO into multi-carbon products)? The role of the flow plate in managing water transport for these systems is also unresolved. It is our contention that these questions can be answered by developing robust "1+2-D models" that provide reasonable estimations of 3-D solutions while mitigating computational costs. These types of models can be adapted based on fuel-cell literature, and existing electrochemical-synthesis models. Theory and experiment-based flow-plate design are certain to play a role in advancing the efficiency of electrochemical-synthesis devices.

4.4 Modeling of Device Architecture

The prior subsections established the utility of continuum models of electrochemical-synthesis devices to understand the local environments and phenomena occurring within various components of the overall device. Once these simulations at the component level are well established and understood, the physics of each component can be integrated into full-cell models that are capable of not only modeling the physics within a single component, but also facilitating understanding of how the interplay between these individual components (*e.g.,* the mass and phase transfer of reactants and products through different components, heat transfer across the full cell, etc.) impact local environments and performance. An example of this study is the comparative work by Weng *et al.* for different device architecture for electrochemical CO_2 reduction on Ag[49] and Cu[67] catalysts as shown in **Figure 35**. In the aqueous-GDE cell, aqueous electrolyte feeds are fed to both the anode and cathode, and an electrolyte buffer layer is placed in between the electrode and the ion-exchange membrane. In the exchange-MEA, the anode is fed with an aqueous electrolyte feed whereas the cathode is fed is a 100% RH vapor phase feed.

Lastly, in the full-MEA, both anode and cathode are fed with 100% RH vapor phase feeds. Through macroscale simulation, the authors determined that both full-MEA and exchange-MEA cells required substantially reduced applied cell potential than the aqueous-GDE system due to the lack on a liquid electrolyte layer between the electrodes. Between the full-MEA and exchange-MEA systems, it was found that the exchange-MEA required substantially reduce applied potential than the full-MEA due to dehydration effects during operating of the ionomer in the full-MEA leading to substantial ohmic losses in the membrane. However, the exchange-MEAs may become limited in applicability due to the precipitation of K_2CO_3 at the cathode because K^+ from the anode moves to the cathode to neutralize OH^- ions generated from CO_2 reduction.[49] To overcome the water and precipitation issues, the authors suggest either fully humidified feeds at higher temperature or use of a liquid and not electrolyte exchange layer. Subsequent work by Weng *et al.* with Cu catalyst explored this concept by incorporating an energy balance, and demonstrated that the performance between full-MEAs and exchange-MEAs is relatively insignificant at 350 K due to better hydration of the ionomer and enhanced transport properties.[67] Additionally, the authors demonstrated that the increase in temperature positively affects products that possess higher activation energy, thus enabling significant and disproportionate gains in C_{2+} generation efficiency operating at high temperature.

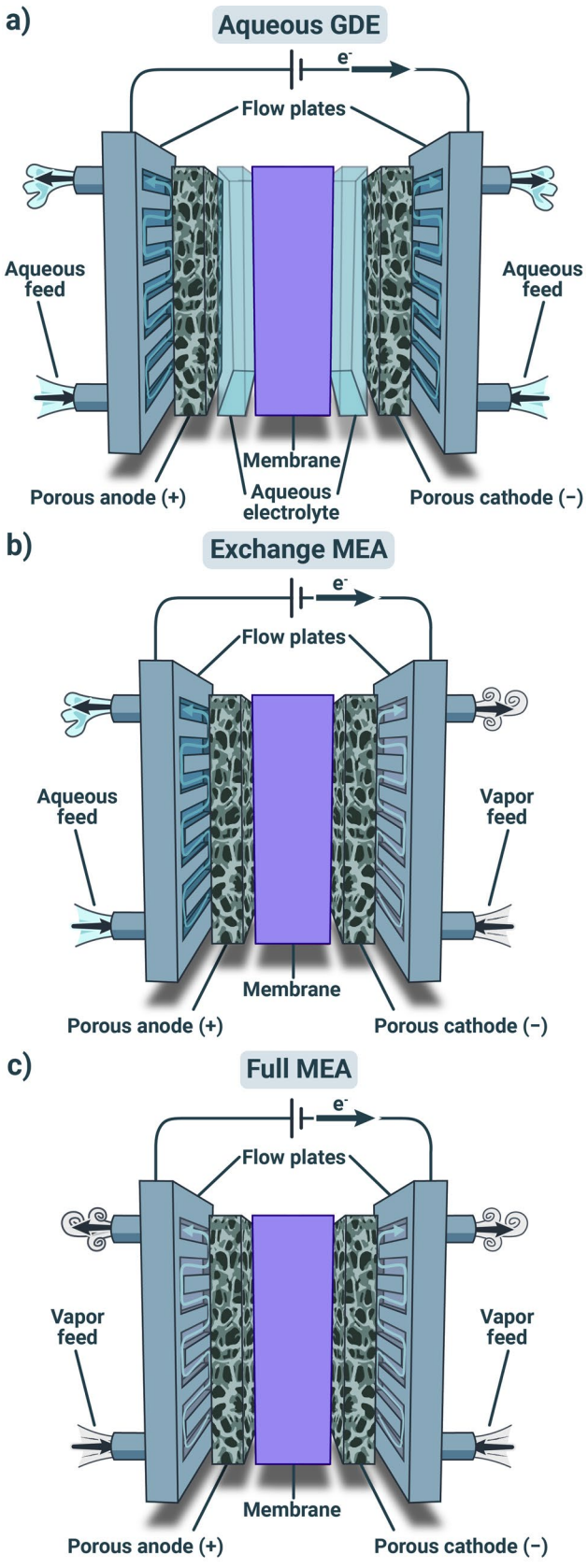
a)
Aqueous GDE
e-
Flow plates
Aqueous feed
Aqueous feed
Membrane
Porous anode (+)
Aqueous electrolyte
Porous cathode (−)
b)
Exchange MEA
e-
Flow plates
Aqueous feed
Vapor feed
Membrane
Porous anode (+)
Porous cathode (−)
c)
Full MEA
e-
Flow plates
Vapor feed
Vapor feed
Membrane
Porous anode (+)
Porous cathode (−)

Figure 35: Depiction of various device architectures employing porous electrodes used for electrochemical synthesis. **(a)** Aqueous-GDE, **(b)** Exchange-MEA, and **(c)** Full-MEA architecture for electrochemical synthesis.

Beyond the exploration of how to leverage thermal management to enhance device performance and selectivity, the work also provided insight regarding device design for CO_2R on Cu using applied-voltage-breakdown analysis (see **Section 3.8.1**). Through this analysis on the full Cu-MEA system, the authors identified the main losses being the kinetics and ohmic losses at higher current densities due to the dehydration. They also explore the impact of catalyst-layer thickness. When the catalyst layer was made thinner, because the kinetic overpotential within the cathode is increased due to a larger ionic potential gradient, the selectivity to C_{2+} products was increased due to their higher cathodic transfer coefficients and thus increased sensitivity to the local ionic potential. Thus, the work shows that thinner catalyst layers can be used to enhance C_{2+} selectivity without any thermodynamic penalties at the device scale. The full-cell simulation, coupled with the technique of applied-voltage-breakdown analysis, provides concrete recommendations to rationalize and guide the performance and design of electrochemical-synthesis cells and related porous electrodes.

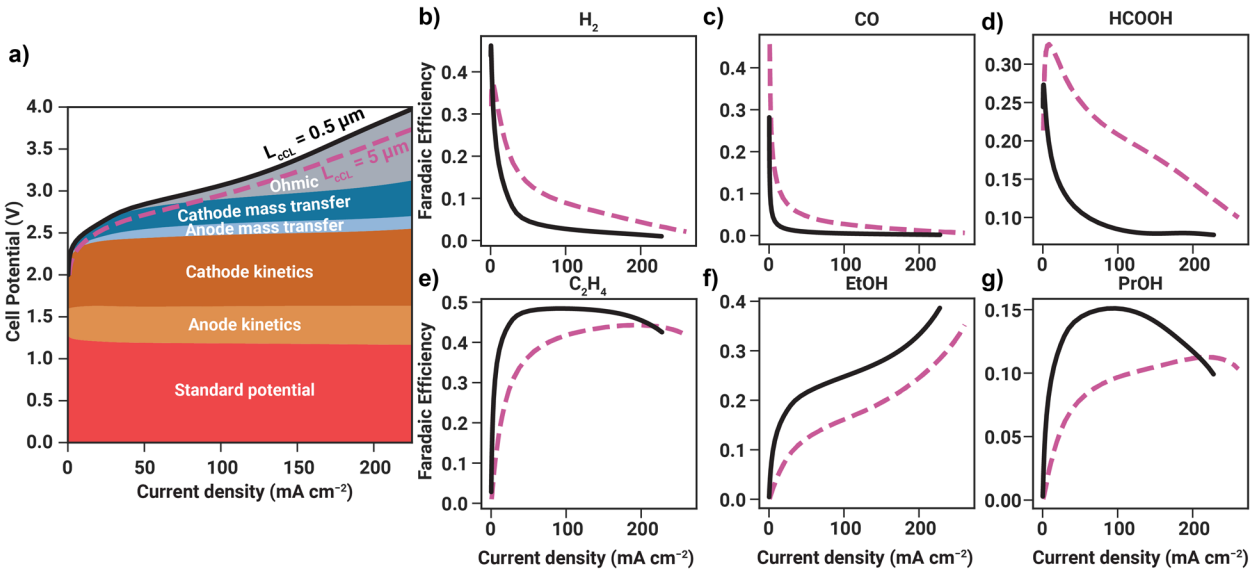

Figure 36: (a) The effect of reducing the cCL thickness from 5 to 0.5 µm on the *iV*-characteristics of a CO_2 electrolyzer utilizing a copper catalyst and applied-voltage breakdown of Cu-MEA system. Overall polarization curve from original 5 µm cCL is shown in grey dashes. (b-g) Faradaic efficiencies to various hydrocarbon products as a function of applied current for both 5 µm (grey dashed lines) and 0.5 µm (solid black lines) thick cCL. Adapted from work by Weng *et al.*[67] Copyright 2020 Royal Society of Chemistry.

5. Future Directions

5.1 Bridging Length Scales

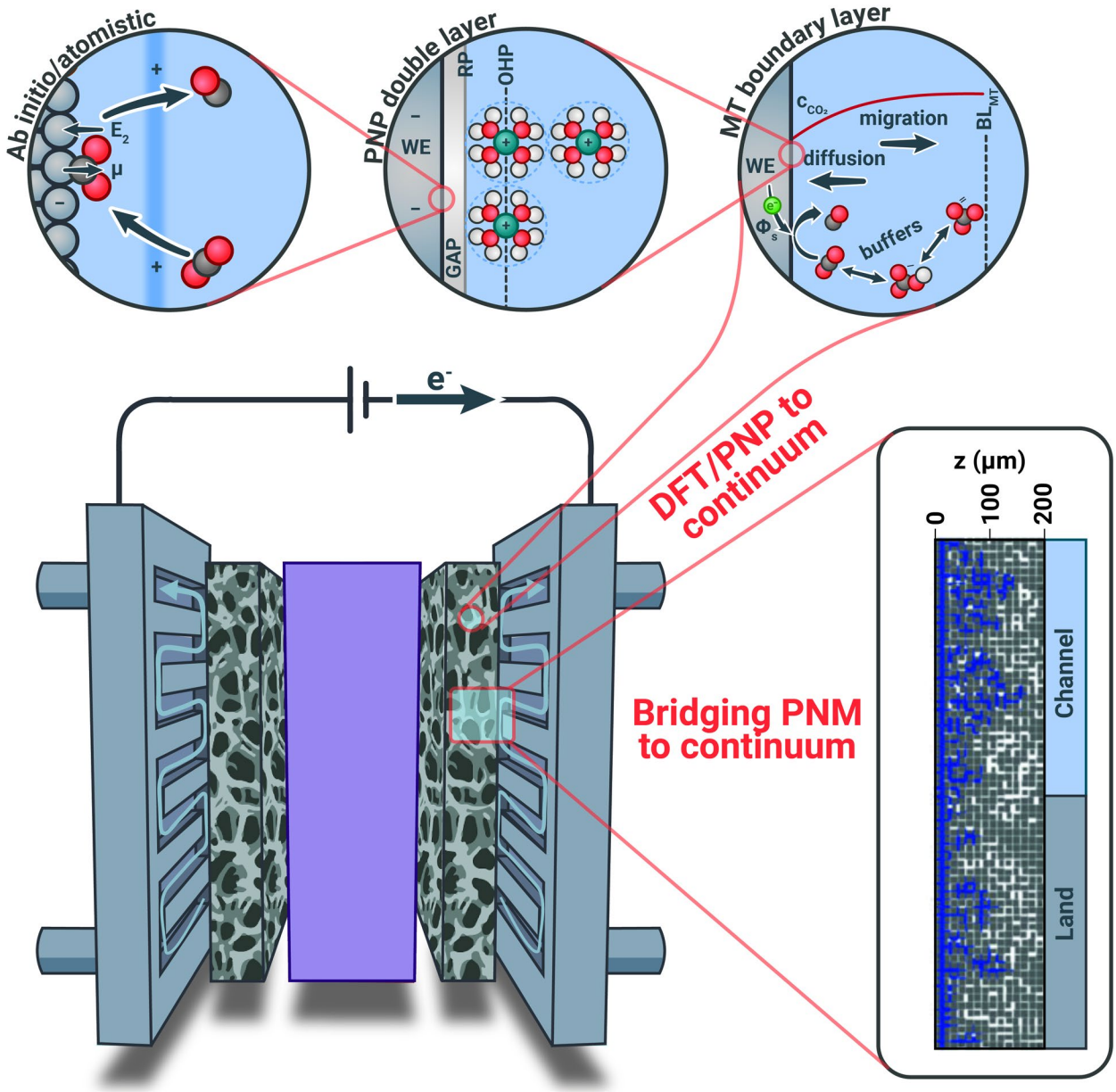

Figure 37: Schematic depiction of scale-bridging. **(Top Row)** Insets depicting bridging from *ab-initio* or atomistic models to Poisson-Nernst Planck continuum models of the double-layer to continuum models of the mass-transport boundary layer. **(Bottom Row)** Device schematic. Inset depicting bridging of high-fidelity pore-network models to continuum-scale device models adapted with permission from Medici *et al.*[347] Copyright 2016 Wiley-VCH Verlag GmbH & Co.

Multiscale modeling or scale-bridging (**Figure 37**) is one of the most challenging aspects of modeling electrochemical-synthesis cells and porous electrodes since it requires combining phenomena occurring from very disparate length scales to model the cell fully (see **Sections 4.1.1-4.1.3** for a description of various porous electrode models at varying scales). Traditionally these linkages are made by upscaling the more detailed microscale models in terms of fluxes to the macroscale ones that provide concentration and other scalar boundary conditions. Currently, very little research is done in the field of electrochemical synthesis on all of the above links, and new model methodologies need to be developed or leveraged from adjacent fields to fill in some of these gaps.

Some studies have explored integrated DFT and continuum models to extend DFT calculations beyond vacuum to account for interface polarization on CO_2R.[348-350] Weitzner *et al.*[351] created a comprehensive DFT-continuum model based on effective screening medium method and the reference-interaction-site model (EST-RISM) to understand the impact of electrolyte composition on CO adsorption free energies. The EST-RISM uses a classical description of the liquid electrolyte and Green's function to model electrified interfaces. The model predicts spatial distributions of ions and potentials at the interface and in the solution. While DFT-continuum model captured the surface state and EDLs, upscaling EDLs results into pore-scale models is the next stage. Ringe *et al*.[265] used DFT to determine surface- and voltage-charge-dependent mean-field microkinetics. They coupled these results to classical PNP model of EDLs, including the impact of ion-ion repulsion and finite-ion-size effect. The model explained the influence of hydrated alkali cation size on the rate-limiting steps involved in CO_2 reduction over Ag and Cu.

The next level of scale-bridging consists of upscaling high-fidelity pore-scale models into volume-averaged continuum models.[352] The goal of the upscaling process is to translate properties obtained with either PNMs, 3-D models or agglomerate-type models into lower fidelity continuum model, which describes other components in the electrochemical cell, and are typically 2-D. Coupled continuum and PNMs previously implemented for fuel cells have yet to be extended to electrochemical synthesis.[347, 353] The framework developed by Zenyuk *et al.*[353] and Medici *et al.*[347] took advantage of computationally rapid steady-state 2-D continuum models (**Section 4.1.3**) and PNMs (**Section 4.1.2**) to capture water and gas distributions in the diffusion media and its impact on overall cell performance. Bridging between LBM and finite-volume has also been accomplished to capture better the detailed water distributions, including perhaps reactions.[278, 354, 355] Such descriptions can provide detailed distributions of phases and ions, which is critical for understanding the local reaction environment. However, these studies are nascent and remain too computationally intensive for detailed sensitivity exploration. As the recognition of the importance of local conditions and multiscale phenomena (*e.g.,* EDL, macroscale transport, microkinetics) on cell performance becomes more apparent, there is a need to explore and exercise more multiscale modeling methodologies include perhaps the development of surrogate models.

5.2 Modeling Cell and Component Durability

The majority of the current research and modeling for analysis and optimization of electrochemical-synthesis systems is based on exploring, explaining, and predicting performance of the various cells, components, and architectures. While this makes sense currently, deployment of the technologies will readily require understanding the timescale issues and lifetime (most electrochemical-synthesis porous electrodes have only been operated on the 10-

100's of hours and not the required 1000-10000's of hours required in industry).[316, 356-360] In the related fields of fuel cells, chlor-alkali, *etc*. such longer lifetimes have been achieved. While there is some understanding of the degradation mechanisms in those fields, a truly predictive lifetime model has yet to be established.[361, 362] Thus, there is a need to discover the degradation mechanisms and their synergistic effects on lifetime, which can be aided by modeling but there is also a dearth of relevant data.

The models for changes at and around the catalyst are perhaps the first that need to be developed due to the importance of the local microenvironment on the local synthesis activity. This is especially true since these conditions are expected to be very heterogeneous in the porous electrodes (as noted in **Sections 3.4** and **4.1),** thus resulting in various stressors and conditions that could lead to poisoning, precipitation, reconfiguration, etc. For example, the model of Weng *et al*. predicted points where precipitation will occur (**Figure 38**), thus limiting electrolyte feed compositions.[49] The accumulation of such ions over time will likewise cause increased mass-transport limitations, and one must consider rebalancing and regeneration schemes, the implementation of which is ideally suited for modeling. The low reducing potential or even pulsed and cycling creates changes in the catalyst structure that can lead to dissolution as well as just surface area changes over time, which will impact product selectivity and rate (see **Section 3.5**). Detailed surface models at the microscale can again help inform these changes, which could be linked through surrogate models or various upscaling to predict overall lifetime or changes at longer length scales. Such multi timescale modeling is a key challenge for the community.

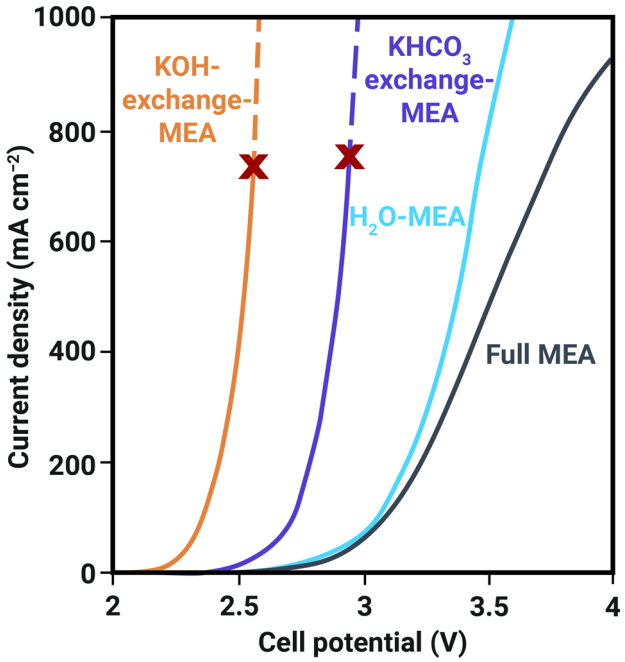

Figure 38: Simulated polarization curves for various configurations of Ag-MEA devices performing CO_2 reduction to CO. Red "x"s represent the potential at which point salt precipitation occurs. Adapted from work by Weng et al.[49] Copyright 2020 Royal Society of Chemistry.

In terms of other degradation phenomena, the polymer electrolytes are not necessarily going to be stable in the various conditions. The strong pH environments will induce leaching of the various catalyst materials, which could reduce the critical ion (*e.g.,* OH^-) fluxes and retard performance. Also, the strong oxidizing potentials at the anode and just the existence of high-energy intermediates during the synthesis reactions could induce membrane chemical degradation, and changes in the water balance can result in mechanical degradation due to swelling cycles, and often these are synergistic. Some models do exist for such impacts in the fuel-cell and water-electrolysis literature,[127] but their applicability to the complex environments and conditions in electrochemical synthesis have not been explored, especially in terms of failure and rare events such as pinholes and increased crossover. Finally, there is a need to understand how these various degradation phenomena act in concert, as they do not occur in isolation. To

this end, real-world long-term testing is important, but there is often a lack of such data. Thus, accelerated stress tests are developed, which isolate key stressors and amplify them so that the failure occurs faster without inducing any new degradation modes. Predictive models and machine learning can provide critical insights into the development of such tests and especially their acceleration factors, and such analysis is at the forefront of modeling activities currently.

5.3 Machine Learning

The majority of the current modeling work for analysis and optimization of electrochemical systems has focused on physics-based modeling. While insightful, physics-based modeling is often limited by the high computational cost for detailed models, especially when considering multi-dimensional, multiscale models like those discussed above (*e.g.,* **Section 5.1**). Furthermore, the performance and durability of these systems depends on numerous, convoluted parameters, and a multi-parameter optimization is even more difficult due to computational limitations. A macroscale electrochemical cell model has upwards of 50 input parameters (material choices, device design and geometry, current, voltage, *etc.*). Conventional regression-based fitting methods are therefore not suitable for these systems.

Machine learning is a discipline involving algorithms that use available data about the system to learn its behavior and to obtain input-output correlations.[363] Machine-learning algorithms have already been proven as versatile and promising tools in image processing and identification. In energy sciences, machine learning has primarily been used in material characterization and screening, leading to discovery of new materials.[364-366] Ultimately, however, one would hope that machine-learning algorithms could be used to predict device performance and durability given an understanding of material and design inputs. Unfortunately, to date there have been limited studies in uses of machine learning for predicting system performance. The

few available studies have focused on simply fitting the polarization data for a few input parameters.[367, 368] As discussed above, current multiscale, multi-dimensional system models are too computationally intensive for full parametric optimization or for use in system-level control scenarios. Coupling machine learning with multiscale modeling could enable more rapid predictions, because the use of machine learning could enable greater predictive power with substantially fewer evaluations of a given multiscale model. Using advanced methods like deep learning can also enable better understanding of some previously unobserved physical phenomena that are contained in the training datasets. Machine learning could also assist in understanding cell durability by predicting state of health and remaining life when the physics of durability are incorporated or with the relevant data sets of property and material changes over time (see **Section 5.2**).[369]

When using machine-learning tools in electrochemical-synthesis systems, one must ensure that the learning captures and is consistent with the general physics of the system and is not solely representative of the data. **Figure 39a** shows a hypothetical data set that contains some noise in measurement. The data is plotted as "Input" vs. "Output", but this representation could be generalized to any of the multitude of input and output combinations in electrochemical synthesis, such as polarization curves, product distributions, *etc.* A machine-learning model with correct training can identify the underlying trend while ignoring the noise, enabling predictive understanding of system behavior. However, overtraining the model will simply result in a data fit that, while representative of the measured data, does not provide any insights about the physical behavior of the data. Furthermore, since the over-fitted models do not capture the general trend, they are usually inaccurate for extrapolation and prediction outside of the training range, as also seen in **Figure 39b**. As the model is over-trained, the accuracy of training

increases (better fit to the individual points); however, the accuracy on testing data decreases as the model is not able to predict the accurate trend. Physics-constrained learning is another way to use the efficiency of machine-learning methods, while accounting for the underlying physics. In constrained methods, the training is run while minimizing the violation of associated physics equations. [370] So far, there has not been any work on using the constrained methods in electrochemical systems leaving a vast research domain unexplored, although some progress has been made in using these methods to deconvolute complex reaction networks in combustion and similar chemical systems.[371-373]

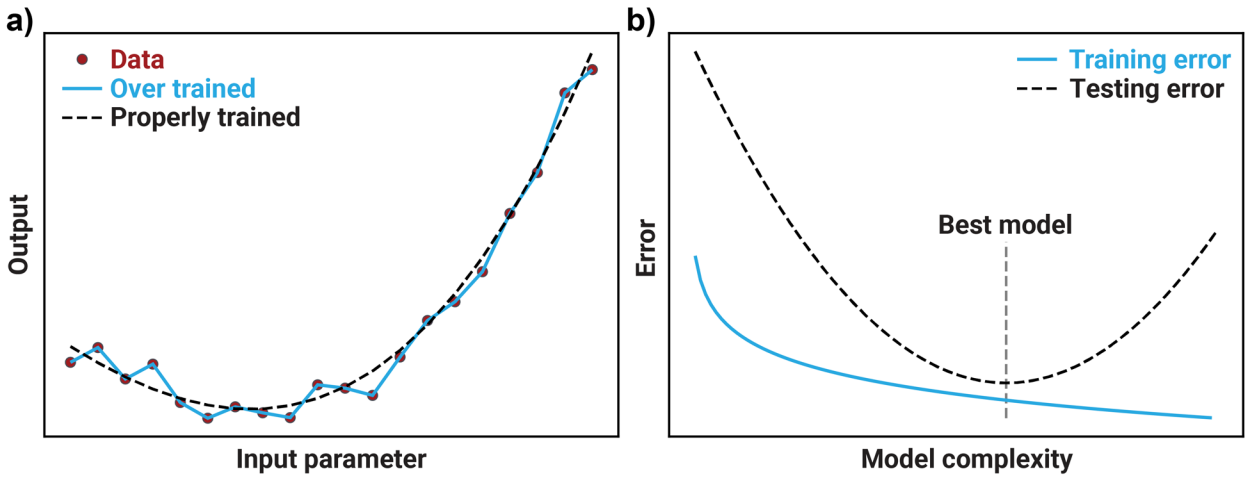

Figure 39. Effect of machine-learning complexity on prediction accuracy. **(a)** Illustration of a correctly trained and over-trained data set. **(b)** Effect of model complexity on training and testing error.

One interesting application of machine-learning methods in the field of electrochemical synthesis is the work of Blanco *et al.* on optimizing pulse shapes for the pulsed electrochemical synthesis of adiponitrile (ADN).[374] In the electrochemical synthesis of ADN, two equivalents of acetonitrile (AN) react at the electrode surface to form ADN, where propionitrile (PN) is an undesired side product resulting from the reaction of one equivalent of AN with water. The authors found that they could drastically enhance the production rate of ADN by pulsing the

applied-voltage signal, switching between a cathodic potential hold where the ADN synthesis occurred, and a rest potential hold where no reactions occurred at the electrode. They used continuum modeling to demonstrate that the pulsed potential enabled the local concentration of AN at the electrode surface to be regenerated during the rest time. However, due to the chosen time scale of the pulses (< 100 ms), the phenomena occurring in the EDL were incredibly relevant, and limited the applicability of the model to predict the optimal pulse shape. This challenge motivated the use of machine learning (via an advanced neural network (ANN)), combined with a systematic experimental campaign, to determine an optimal combination of cathodic and rest times (**Figure 40**). Using the ANN to predict behavior in the regions in between experimental measurements on the parameter space of the cathodic and rest times, the ANN identified a region of maximum selectivity that when validated experimentally, enabled improvements of 30 and 325 % in the AND production rate and selectivity, respectively. This study demonstrates the utility of machine learning to perform advanced correlative studies and predict optimal regions of performance for electrochemical synthesis, while minimizing the number of measurements needed to be taken to access these optima.

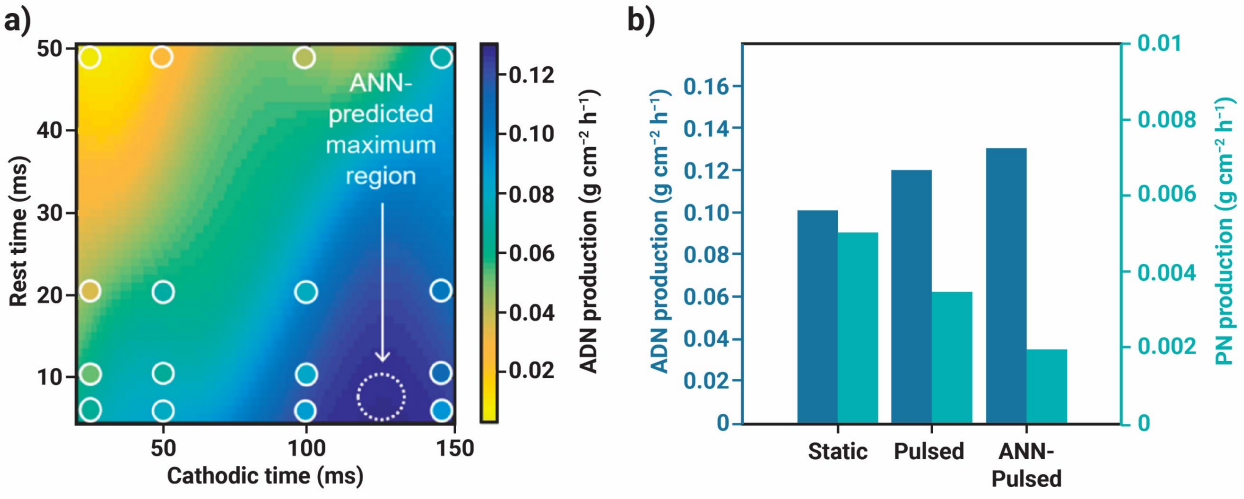

Figure 40. Use of machine learning to optimize the pulsed electrosynthesis of ADN. **(a)** Contour plot of ADN production rate as a function of the cathodic and rest times. Systematic experiments

are demarcated as markers, and the ANN prediction is overlayed as the color map. **(b)** Production rates of ADN and PN for the static, optimal experimental pulsed, and the ANN-optimized pulsed electrosynthesis. Adapted with permission from Blanco *et al.* 2019.[374] Copyright 2019 National Academy of Sciences.

5.4 Topology Optimization for Porous-Electrode Design

Topology optimization is a mathematical technique that optimizes the spatial distribution of material in a given domain in order to achieve certain physical constraints while minimizing a pre-defined objective function.[375-378] This method has been long used by mechanical and civil engineers to minimize the amount of material used for a given application, while still achieving certain mechanical strength or durability targets.[375, 379-381] There are numerous methods to perform topology optimization; however, the most ubiquitous class is referred to as density methods[375]. Less common are approaches referred to as discrete methods, which are seldom used because they require 2D-gradient information of the discretized objective function, which is often poorly defined or nearly impossible to calculate.[378] The following section provides the reader with a cursory overview of the major topology optimization schemes and their potential applications to electrochemical systems; for an in depth review and tutorial of the mathematics of the subject, the authors refer the reader to the seminal review by Sigmund and Maute.[378]

In density techniques, the optimal topology is determined by systematically varying the material density within the individual unit cells of a finitely discretized domain. Common implementations of these techniques include the Simplified Isotropic Material with Penalization (SIMP) or the Rational Approximation of Material Properties (RAMP). In these approaches, the domain is first discretized, a density parameter ($0 \leq \rho_i \leq 1$) is defined that is related to the material property to be optimized (*e.g.,* mass density, Young's modulus, *etc.*) by a parametrized penalization relationship defined based on the method chosen, and an initial guess of the optimal topology is made. The penalization relationship in these methods smooths the gradient of the

objective function to facilitate more facile calculation of the optimization. Then, a finite-element analysis (FEA) is performed to assess the performance of the structure by way of the objective function. In each successive iteration, the algorithm optimizes the density of each unit cell, uses the optimized density parameter to solve for the new values of the material properties based on the penalization relationship, and then performs FEA of the entire domain once more. The optimization is continued until convergence is achieved and no subsequent changes in the unit-cell densities leads to further minimization of the objective function.[375, 377] This scheme is shown schematically in **Figure 41** for the simple problem of minimizing the amount of material in a steel beam supporting a given vertical load.

In discrete methods, the density function to be optimized exists as a discrete, binary variable ($\rho_i = 0\ or\ 1$). This definition poses a substantial challenge, because the optimization function for a binary variable has a gradient that is nearly impossible calculate. This challenge can be circumvented by using gradients defined from continuous variables rather than the discrete density function to inform discrete changes in the design. Nonetheless, these methods are prone to problems with convergence and stability. The most common branch of discrete methods is the evolutionary structural optimization (ESO) methods. The ESO method progressively removes unneeded material from a structure. As in density approaches, the domain is discretized, and an initial guess of the optimized topology is made. A "rejection criterion" is defined that identifies ineffective material (like the parameterization in density methods), and in each successive iteration, this material is removed from the domain in a discrete design change. The optimization continues until convergence is achieved.[381] Schematically, this method looks nearly identical to SIMP with one key distinction: Because the method can only remove unneeded material, the convergence plot for ESO must be monotonically decreasing.

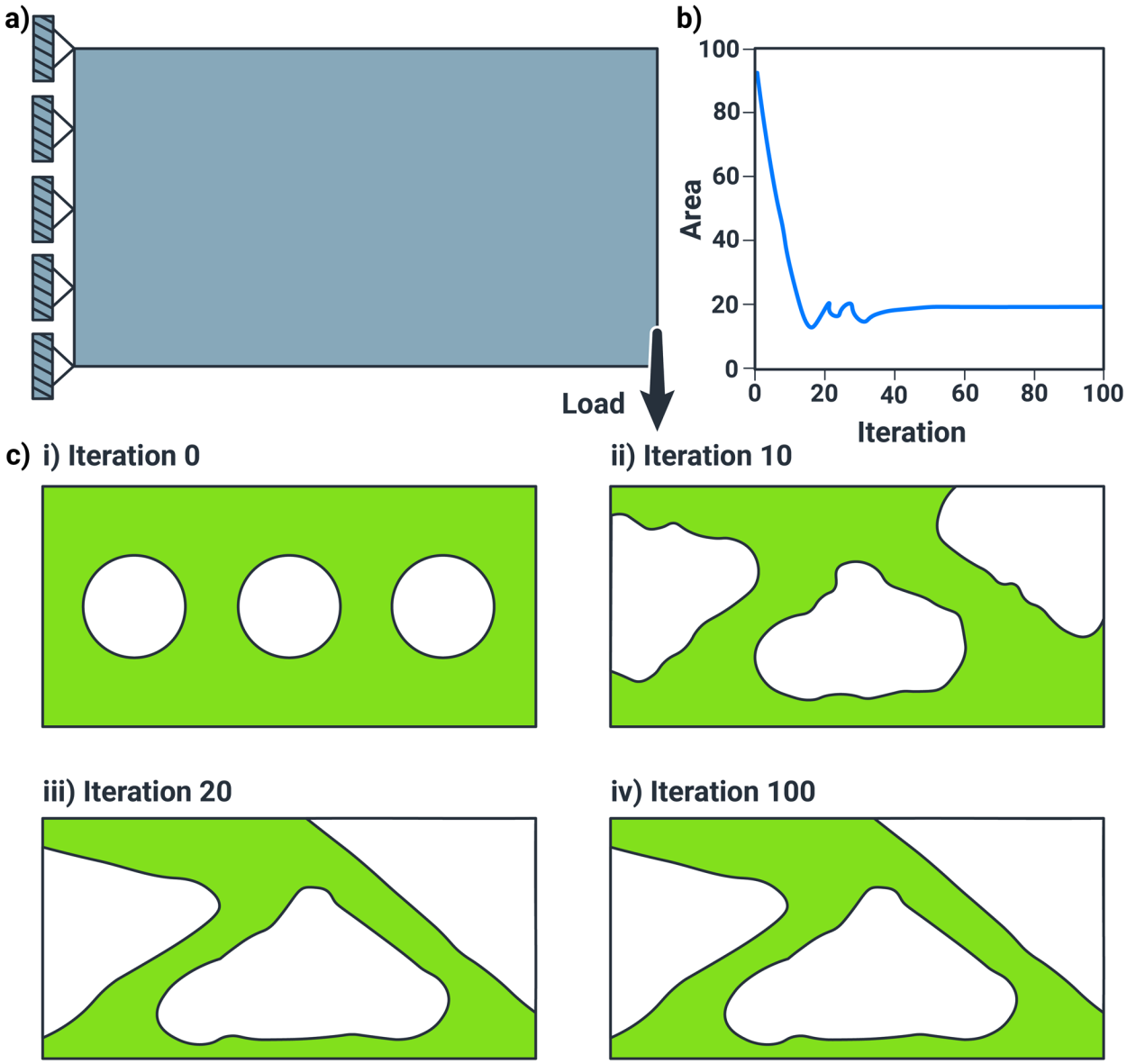

Figure 41: Depiction of a SIMP topology-optimization scheme. **(a)** The desired optimization problem: A short steel beam that must support a given vertical load using a minimal amount of material. **(b)** Convergence of the cross-sectional area of the steel beam as a function of the number of topology optimization iterations. **(c) (i-iv)** Geometry of the steel beam throughout the topology optimization process. An initial guess of the optimized topology **(i)** is made, and the optimizer minimizes the required material while still complying to the load constraint, iterating until an optimal geometry is found.

Topology optimization has immense potential to optimize the structure of porous electrodes for electrochemical applications. With the rise of high-resolution additive-manufacturing techniques,[382, 383] the design space for porous electrodes has been revolutionized;

multiple recent studies have demonstrated the capacity to 3-D-print porous electrodes for electrochemical applications,[88, 384-394] with some possessing improved mass-transport properties compared to conventional porous electrodes.[88, 386, 387, 392, 394, 395] Topology optimization interfaces well with these advanced-manufacturing techniques,[376, 396] and the ability to manufacture complex porous electrodes motivates the development of topology optimized electrodes for a variety of electrochemical applications.

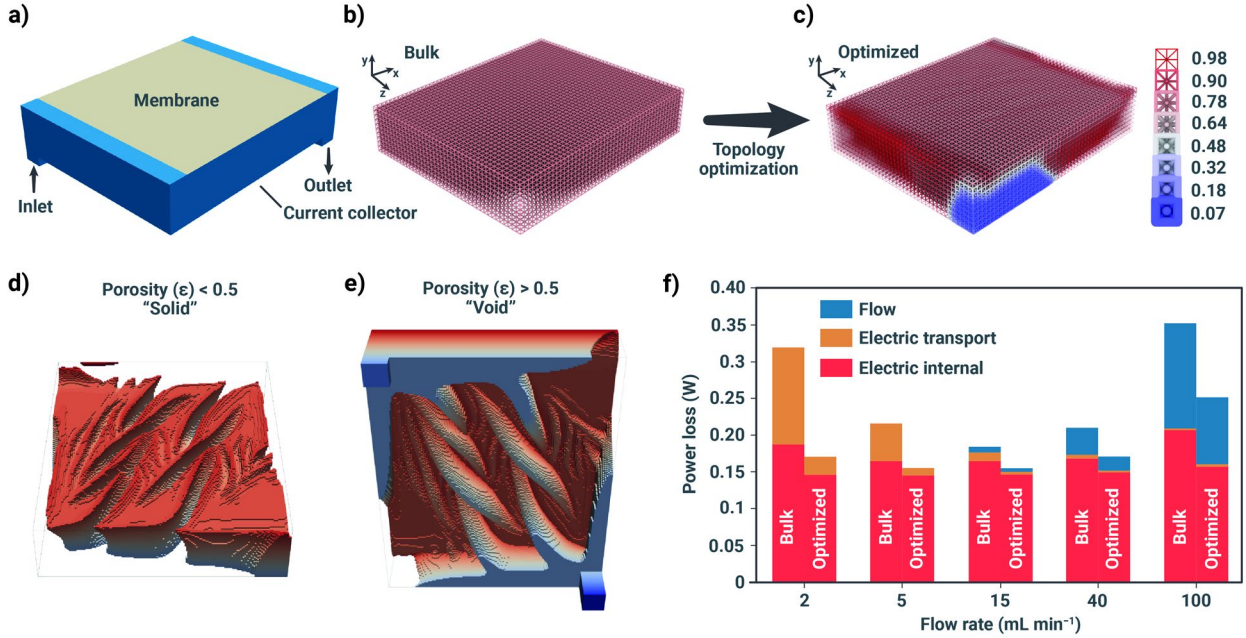

Figure 42: Application of topology optimization to minimize the power loss in the negative half-cell of a redox flow battery. **(a)** 3-D-schematic of the modeled domain. **(b)** Depiction of a "bulk" porous electrode, comprised of regular, isotruss unit cells with a constant porosity (ε). **(c)** Depiction of an "optimized" porous electrode, comprised of isotruss unit cells with variable ε (varied by changing rod radii) that has been optimized by topology optimization. Color bar depicts ε as a function of rod radii. Red shades correspond to high ε and thinner rods, blue shades correspond to lower ε and thicker rods. **(d, e)** Optimized porous electrode split into a "solid" **(d)** portion with $\varepsilon < 0.5$, and a "void" **(e)** portion with $\varepsilon > 0.5$. **(f)** Comparison of power loss exhibited in "bulk" and "optimized" porous electrodes operated with a flow rate of 15 mL min^{-1} at 400 mA cm^{-2}. Adapted from work by Beck *et al.*[397] (Copyright Elsevier 2021)

Topology optimization have already been employed for electrochemical systems with great success. Recent studies have used topology optimization to develop optimized flow

plates[398, 399] that exhibit higher voltage efficiency than their traditional counterparts for flow batteries and fuel cells. Additionally, recent work by Roy *et al.* has demonstrated the use of topology optimized porous electrodes that minimize potential losses at an electrode performing a generalized Faradaic reaction.[400] In these studies, the objective functions used for the topology optimization were the minimization of power loss[399, 400] or the maximization of mass transport to the electrode surface,[398] and the continuum-scale model is used to evaluate the performance of the system to ensure constraints are met as well as to optimize the objective function.

In addition to formal implementations of topology optimization, initial studies by Golmon *et al.* on Li-ion batteries demonstrated that improvements in discharge capacity of 61% could be achieved by optimizing the porosity and pore radius distribution in functionally graded porous electrodes to maximize usable battery capacity.[401] Herein, the term functionally graded refers to a component for which a critical material property (*i.e.,* porosity, pore size or radius, lattice structure, *etc.*) is variable throughout the material.[402, 403] Additionally, due to the high cost of the Pt catalyst commonly used in PEMFCs, a great deal of recent study has sought to perform optimizations to develop functionally-graded porous catalyst layers with minimal amounts of catalyst material that still achieve performance targets.[404, 405] It is important to note that these works (and others like it), which optimize an underlying material parameter, are not true topology optimizations because they do not formally add or remove material. Nonetheless, they are algorithmically quite similar, and the systematic development of such functionally graded materials offers substantial potential for application to electrochemical systems.

Perhaps the most intriguing application of computational design optimization to electrochemical synthesis is that implemented by Beck *et al.* to optimize mass transport in the negative chamber of a redox flow battery (**Figure 42a**).[397] In this work, the authors optimized a

3-D-porous electrode comprised of regular, isotruss unit cells with a given porosity (ε), controlled by the radii of the rods that constitute a given isotruss cell (**Figure 42b**). The topology-optimization algorithm, which is essentially a modified implementation of SIMP, minimizes power loss within the cell by systematically changing the porosity in each unit cell (**Figure 42c**). Furthermore, in this study, the geometry of the entire negative chamber is optimized. In other words, the flow plate and porous electrode are optimized simultaneously. The optimization was performed for multiple flow regimes at 400 mA cm^{-2}, and the best performing electrode from the study is shown in **Figure 42d-e**. For improved visualization, the electrode is split into a "solid" fraction comprised of all unit cells with $\varepsilon < 0.5$, and a "void" fraction comprised of all unit cells with $\varepsilon > 0.5$. As shown in **Figure 42d-e**, the optimized electrode possesses wide porous channels for distributing flow near the current collector that mimic the function of a flow plate, that become smaller, more porous, and more frequent as the membrane is approached to mimic the function of the diffusion media. This geometry ensures optimal mass transport within the porous electrode. It is important to note that, while the electrode has been optimized into a somewhat intuitive flow plate-diffusion media stack, the geometry of that stack is highly nonintuitive and represents an optimum that would not be achieved by traditional manufacturing or human-led adaptation. Additionally, as shown in **Figure 42f**, all topology optimized electrodes across all mass-transport regimes exhibited substantially reduced power loss when compared to their traditionally manufactured "bulk" counterparts, demonstrating the utility of this technique to enhance substantially the performance of electrochemical devices.

Key to topology optimization in these systems is an established relationship between microstructure and the device performance that comes in the form of a validated continuum model. Therefore, the implementation of these techniques to optimize porous electrodes in

electrochemical synthesis requires the development of continuum models that can adequately relate local properties to overall performance, as outlined in this review. A necessary caveat is that these continuum models will have a higher degree of complexity than the flow battery and fuel cell continuum models employed in the previous applications of electrochemical topology optimization, due to the presence of out-of-equilibrium homogeneous reactions, an increase in the number of modeled species, and competing surface reaction chemistries. Therefore, for these systems, topology optimization, which is already computationally expensive, will likely incur substantial computational cost. Additionally, the objective functions employed (power loss and local concentrations) previously for electrochemical topology optimization will likely be insufficient, and new objective functions that account for both device efficiency and product selectivity to a certain product, such as the energy efficiency of a given product, will need to be employed. Nonetheless, once these challenges are addressed, topology optimization presents an excellent opportunity to use continuum modeling to substantially optimize mass transport and performance of devices for electrochemical synthesis.

6. Conclusions

Porous electrodes have been engineered and designed for efficient energy conversion at high rates. They are the critical component within electrochemical-synthesis devices, but involve structures and phenomena that are inherently multicomponents, multiscale, and coupled, resulting in complex interplays between species concentrations, operating conditions, material properties, kinetic mechanisms, *etc*. Mathematical modeling is ideally suited to elucidate and explain the various experimental observations in terms of performance, product distribution, *etc.* In this review, we explore the underlying phenomena and models used in electrochemical-synthesis cells and porous electrodes, with a focus on the underlying physics and governing

phenomena and highlighting various applications and modeling methodologies. A roadmap is provided for developing continuum models at various length scales for different electrochemical synthesis device components. The analysis of the literature suggests that balancing complexity and predictive power is necessary for selecting an appropriate model framework and parameterization strategy. Throughout, it is clear the importance of the local chemical microenvironment near the catalyst surface on overall cell performance.

While density-functional-theory models can be used to determine surface reaction parameters (*e.g.,* Tafel slopes and exchange current densities) by simulating idealized molecular interactions at the electrocatalyst/electrolyte interface, these simulations do not inform how mass and charge dictates the chemical microenvironment throughout electrochemical-synthesis devices. It is therefore necessary to quantify transport phenomena in porous electrodes to link experimental observations with physics-based theories accurately and perform mathematical optimization on design parameters. Continuum-scale modeling, which has long been used to study porous electrodes for a multitude of energy applications, is a demonstrated strategy for elucidating physical phenomena in porous electrodes at various scales and exploring design parameters at a much higher throughput than experimental techniques. The trade-offs between different modeling approaches are highlighted throughout and the need and challenge for the development of new models that bridge length scales, determine device durability, and leverage machine learning and topology optimization noted. This review presented the breadth of continuum modeling tools to the electrochemical-synthesis community, which should facilitate richer insights into device operation and guide experimental studies that seek to optimize porous-electrode architectures.

7. Acknowledgements

This material is based on work performed by the Liquid Sunlight Alliance, which is supported by the U.S. Department of Energy, Office of Science, Office of Basic Energy Sciences, Fuels from Sunlight Hub under Award Number DE-SC0021266. JCB acknowledges funding from the National Science Foundation Graduate Research Fellowship under Grant No. DGE 1752814 and the National Defense Science and Engineering Graduate (NDSEG) Fellowship Program, sponsored by the Army Research Office (ARO). The authors would like to acknowledge Wilson A. Smith, Recep Kas, and Paige Brimley for their contribution to our discussion of modeling porous electrodes. We would also like to acknowledge Fraser G. L. Parlane for his assistance with generating figures for the manuscript.

8. Nomenclature

Roman

a_i	Activity of species i
a	Distance of closest approach between ions
A	Area (m^2)
A	Debye-Huckel limiting slope
B	Debye-Huckel solvent parameter
c_i	Concentration of species i (M)
C_p	Heat capacity (J mol^{-1} K^{-1})
d	Ionomer hydrophilic domain spacing (m)
D_i	Diffusivity of species i (m^2 s^{-1})
E	Electric field (V m^{-1})
E^0	Standard reduction potential (V)
E_b^0	Young's Modulus (kg m^{-1} s^{-2})
E_a	Activation energy (J mol s^{-1})
E_r	Reaction effectiveness factor
e	Elementary charge (C)
$f_{l,m}$	Volume fraction of ionomer in catalyst pores
F	Faraday constant (C mol^{-1})
G	Gibbs free energy (J mol^{-1})
H	Enthalpy (J mol^{-1})
$\boldsymbol{i}$	Current density (mA cm^{-2})
i_0	Exchange current density (mA cm^{-2})
i_v	Current density per volume (mA cm^{-3})
$\boldsymbol{J}_{i,k}$	Flux density of species i in phase k, relative to the mass-average velocity of phase k (mol m^{-2} s^{-1})
IEC	Ion exchange capacity (mmol g^{-1})
k	Mass transfer coefficient (mol^2 m^{-5} s^{-1} J^{-1})
k_B	Boltzmann constant (J K^{-1})
k_k	Permeability (m^2)
k_n	Forward rate constant of reaction n (mol m^{-3} s^{-1})
k_T	Thermal conductivity (J cm^{-2} K^{-1})
K_n	Equilibrium constant in reaction n
K_{ij}	Stefan Maxwell frictional interaction coefficient (kg m^{-3} s^{-1})
L	Length (m)
l_B	Bjerrum Length (m)
M_i	Molar mass of species i (g mol^{-1})
n_i	Number of electrons in reaction i
$\boldsymbol{N_i}$	Molar flux of species i (mol m^{-2} s^{-1})
p	Thermodynamic pressure (bar)
Q	Energy source term (J m^{-3} s^{-1})

$\boldsymbol{q}$	Heat flux (J m^{-2} s^{-1})
r	Radius (m)
R	Ideal gas constant (J mol^{-1} K^{-1})
R_i	Reaction source term for species i (mol m^{-3} s^{-1})
R_{domain}	Hydrophilic domain size (m)
s_i	Stoichiometric coefficient of species i in reaction n
S	Saturation
t_i	Transference number of species i
T	Temperature (K)
U	Cell potential (V)
u_i	Mobility of species i (m^2 V^{-1} s^{-1})
v	Velocity (m s^{-1})
V	Voltage
$\overline{V_i}$	Partial molar volume of species i (m^3 mol^{-1})
x	1-dimensional position variable (m)
x_i	Mole fraction of species i
z_i	Charge of ion i

Greek

α_i	Ion fraction
$\alpha_{ij,k}$	Ion transport coefficient (mol^2 s kg^{-1} m^{-3})
$\alpha_{a\ or\ c,n}$	Anodic or cathodic transfer coefficient of reaction n
β	Non-dimensional electric field scaling factor (m V^{-1})
β_n	Symmetry factor of reaction step n
$\beta_{i,j}$	Specific interaction parameter between ions
Γ_{ij}	Partition coefficient of ions
Γ_{CL}	Catalyst effectiveness factor
ε	Dielectric permittivity (F m^{-1})
ε_k	Volume fraction of phase k
η	Overpotential (V)
θ	Surface coverage
κ	Ionic conductivity (S m^{-1})
λ	Water content
μ_i	Chemical potential of species i (J mol^{-1})
μ	Mixture viscosity (kg m^{-1} s^{-1})
ξ	Electro-osmotic coefficient
Π	Peltier coefficient (J C^{-1})
ρ	Density (g cm^{-3})
σ	Dimensionless dissociation bond length
σ_s	Electronic conductivity (S m^{-1})
ϕ	Electrostatic potential (V)

ϕ_L	Thiele Modulus
ϕ_M	Membrane volume fraction
τ	Tortuosity
$\bar{\bar{\boldsymbol{\tau}}}$	Viscous stress tensor (N m^{-2})

Subscript

a	Anodic
agg	Agglomerate
an	Anodic
app	Applied
c	Cathodic
ca	Cathodic
char	Characteristic
eff	Effective
G	Gas phase
K	Knudsen
$l \rightarrow k$	Phase transfer from phase *l* to *k*
L	Liquid phase
m	Molecular
mem	Membrane
M	Value in membrane
p	Product
r	Reactant
rev	Reversible
s	Solid phase
T	Total
v	Volumetric
w	Value in water

Superscript

0	Intrinsic value or standard state
*	Molar averaged
E	Electric field dependence
els	Electrostatic
ex	Excess property
id	Ideal
M	Value in membrane
phys	Physical
ref	Evaluated at reference

slv	Solvation
stc	Steric
swe	Swelling

Acronyms

ADN	Adiponitrile
AEL	Anion exchange layer
AEM	Anion exchange membrane
AN	Acrylonitrile
AVB	Applied voltage breakdown
BPM	Bipolar membrane
CEL	Cation exchange layer
CEM	Cation exchange membrane
CFD	Computational fluid dynamics
CL	Catalyst layer
CO_2R	Carbon dioxide reduction
D-PNM	Dual pore-network models
DFT	Density functional theory
DNS	Direct numerical simulation
EDL	Electrical double layer
EE	Energy efficiency
ESO	Evolutionary structural optimization
EST-RIM	Effective screening medium method and the reference-interaction-site model
FB	Forward bias
FE	Faradaic efficiency
FIB-SEM	Focused ion beam scanning electron microscopy
GCSG	Guoy-Chapman-Stern-Grahame
HER	Hydrogen evolution reaction
HPLC	High performance liquid chromatography
IEM	Ion-exchange membrane
IHP	Inner Helmholtz Plane
LBM	Lattice-Boltzmann ,ethod
LHV	Lower heating value
NMR	Nuclear magnetic resonance
OHP	Outer Helmholtz Plane
PTL	Porous transport layer
PNM	Pore-network models

PNP	Poisson Nernst Planck
PZC	Point of zero charge
RB	Reverse bias
RH	Relative humidity
RHE	Real hydrogen electrode
SHE	Standard hydrogen electrode
SIMP	Solid isotropic material with penalization
VE	Voltage efficiency
WD	Water dissociation

9. Author Biographies

Justin Bui was born in 1997 in Fairfax, VA and received his B. Sc. In Chemical Engineering from Columbia University in 2019. At Columbia, his thesis focused on the development of additively manufactured devices for membraneless seawater electrolysis under the guidance of Dr. Daniel Esposito supported by the Goldwater Scholarship. Currently, he is pursuing his Ph. D. at the University of California, Berkeley under the direction of Prof. Alexis Bell and Dr. Adam Weber working within the Liquid Sunlight Alliance at Lawrence Berkeley National Laboratory. His dissertation work, which is funded by the NSF and NDSEG Fellowships, focuses on the simulation and optimization of microenvironments in devices for the electrochemical conversion of CO_2 to value-added products.

Eric W. Lees was born in 1995 in Calgary, Canada and he obtained his B. Sc. In Chemical Engineering Co-op from the University of Alberta in 2018. During his undergraduate degree, Eric investigated ethanol production from yeast lysates under the supervision Prof. Dominic Sauvageau and completed internships at Enerplus, Schlumberger, ERCO Worldwide, and Nexen CNOOC Ltd. Eric is currently pursuing his Ph. D. as an NSERC Alexander Graham Bell Scholar in Prof. Curtis P. Berlinguette's group at the University of British Columbia. Eric's Ph. D. research seeks to use electrochemistry, process engineering, and materials science to reduce the costs of CO_2 capture and electrochemical conversion.

Lalit Pant was a postdoctoral fellow in the Energy Technologies Area (ETA) at Lawrence Berkeley National Lab (LBNL). His research focused on using numerical modeling for performance and durability diagnostics in fuel cells and other electrochemical devices as part of FC-PAD and M2FCT consortiums. He received his B. Tech. from IIT Delhi, INDIA in 2009 and his M. Sc. And Ph. D. from University of Alberta, Canada in 2016. His Ph. D. work was focused on understanding pore-scale transport in electrodes using stochastic reconstructions. Currently, he is an assistant professor in the Department of Sustainable Energy Engineering at Indian Institute of Technology (IIT) Kanpur, India.

Iryna Zenyuk holds a B.S. (2008) in mechanical engineering from the New York University Tandon School of Engineering. She continued her studies at Carnegie Mellon University, where she earned M.S. (2011) and Ph.D. (2013) in Mechanical engineering. Her graduate work focused on fundamental understanding of electric double layers in electrochemical energy-conversion systems. After a postdoctoral fellowship at Lawrence Berkeley National Laboratory in the Electrochemical Technologies Group, Zenyuk joined the faculty of the Mechanical Engineering Department at Tufts University in 2015. In July 2018, she joined the Department of Chemical and Biomolecular Engineering at the University of California, Irvine, where she is also an Associate Director of the National Fuel Cell Research Center. At UC Irvine, Zenyuk's group works on enabling energy solutions by researching low-temperature hydrogen fuel-cells, Li-metal batteries and electrolyzers. Zenyuk works on design strategy encompassing novel materials, diagnostic tools and device-level testing. She is a recipient of the NSF CAREER award (2017), Interpore society Fraunhofer Award for Young Researchers (2017), Research Corporation for Science Advancement, Scialog Fellow in Advanced Energy Storage (2017-

2019), Electrochemical Society (ECS) Toyota Young Investigator Award (2018), UCI Samueli School of Engineering Early Career Faculty Excellence in Research Award (2019) and ECS Energy Technology Division Srinivasan Young Investigator Award (2021). Zenyuk published over 70 journal publications and delivered more than 80 invited presentations on topics of energy conversion and storage.

Alexis T. Bell received his Sc. D. in Chemical Engineering from the Massachusetts Institute of Technology, after which he joined the Department of Chemical and Biomolecular Engineering at the University of California, Berkeley, where he is currently the Dow Professor of Sustainable Chemistry. His research includes experimental and theoretical studies of heterogeneous catalysis, with a recent emphasis on the electrochemical oxidation of water and the reduction of carbon dioxide.

Adam Z. Weber received his B.S. and M.S. degrees in Chemical Engineering from Tufts University and a PhD from U.C. Berkeley, after which he joined Lawrence Berkeley National Laboratory, where he is currently the leader of the Energy Conversion Group and Co-Director of the Million Mile Fuel Cell Truck Consortium. His research interests include experimental and theoretical studies of fuel cells, electrolyzers, carbon-dioxide reduction, redox flow batteries, and related electrochemical devices and their components, with a focus on structure-function relationships, transport phenomena, and electrochemical engineering.

10. References

1. Apodaca, L.E. *Mineral Commodity Summaries - Ammonia*; 2016.

2. Intergovernmental Panel on Climate Change. *Climate Change 2014: Synthesis Report*; 2014.

3. Nitopi, S.; Bertheussen, E.; Scott, S. B.; Liu, X. Y.; Engstfeld, A. K.; Horch, S.; Seger, B.; Stephens, I. E. L.; Chan, K.; Hahn, C., et al., Progress and Perspectives of Electrochemical CO2 Reduction on Copper in Aqueous Electrolyte. *Chem. Rev.* **2019,** *119*, 7610-7672.

4. Geyer, R.; Jambeck, J. R.; Law, K. L., Production, Use, and Fate of All Plastics Ever Made. *Sci. Adv.* **2017,** *3*, 19-24.

5. Barton, J. L., Electrification of the Chemical Industry. *Science* **2020,** *368*, 1181-1182.

6. Schiffer, Z. J.; Manthiram, K., Electrification and Decarbonization of the Chemical Industry. *Joule* **2017,** *1*, 10-14.

7. Miller, D. J.; Houle, F. A., Membranes for Solar Fuel Devices. In *Integrated Solar Fuel Generators*, Royal Society of Chemistry: Cambridge, UK, 2018; Vol. 22, p 341.

8. Singh, M. R.; Haussener, S.; Weber, A. Z., Continuum-scale Modeling of Solar Water-splitting Devices. In *Integrated Solar Fuel Generators*, Royal Society of Chemistry: Cambridge, UK, 2019; Vol. 22, pp 500-536.

9. Carmo, M.; Fritz, D. L.; Mergel, J.; Stolten, D., A Comprehensive Review on PEM Water Electrolysis. *Int J Hydrogen Energ* **2013,** *38*, 4901-4934.

10. Shiva Kumar, S.; Himabindu, V., Hydrogen Production by PEM Water Electrolysis – A Review. *Mater. Sci. Energy Technol.* **2019,** *2*, 442-454.

11. Weber, A.; Newman, J., Modeling Transport in Polymer-Electrolyte Fuel Cells. *Chem. Rev.* **2004,** *104*, 4679-4726.

12. Weber, A. Z.; Borup, R. L.; Darling, R. M.; Das, P. K.; Dursch, T. J.; Gu, W. B.; Harvey, D.; Kusoglu, A.; Litster, S.; Mench, M. M., et al., A Critical Review of Modeling Transport Phenomena in Polymer-Electrolyte Fuel Cells. *J. Electrochem. Soc.* **2014,** *161*, F1254-F1299.

13. Xiang, C. X.; Weber, A. Z.; Ardo, S.; Berger, A.; Chen, Y. K.; Coridan, R.; Fountaine, K. T.; Haussener, S.; Hu, S.; Liu, R., et al., Modeling, Simulation, and Implementation of Solar-Driven Water-Splitting Devices. *Angew. Chem.* **2016,** *55*, 12974-12988.

14. Cindrella, L.; Kannan, A. M.; Lin, J. F.; Saminathan, K.; Ho, Y.; Lin, C. W.; Wertz, J., Gas Diffusion Layer for Proton Exchange Membrane Fuel Cells—A Review. *J. Power Sources* **2009,** *194*, 146-160.

15. Park, S.; Lee, J. W.; Popov, B. N., A Review of Gas Diffusion Layer in PEM Fuel Cells: Materials and Designs. *Int. J. Hydrogen Energy* **2012,** *37*, 5850.

16. Shojaeefard, M. H.; Molaeimanesh, G. R.; Nazemian, M.; Moqaddari, M. R., A Review on Microstructure Reconstruction of PEM Fuel Cells Porous Electrodes for Pore Scale Simulation. *Int J Hydrogen Energ* **2016,** *41*, 20276-20293.

17. Resasco, J.; Bell, A. T., Electrocatalytic CO2 Reduction to Fuels: Progress and Opportunities. *Trends Chem.* **2020,** *2*, 825-836.

18. Goldman, M.; Lees, E. W.; Prieto, P. L.; Mowbray, B. A. W.; Weekes, D. M.; Reyes, A.; Li, T.; Salvatore, D. A.; Smith, W. A.; Berlinguette, C. P., Electrochemical Reactors. In *Carbon Dioxide Electrochemistry: Homogeneous and Heterogeneous Catalysis*, The Royal Society of Chemistry: 2021; pp 408-432.

19. Garg, S.; Li, M. R.; Weber, A. Z.; Ge, L.; Li, L. Y.; Rudolph, V.; Wang, G. X.; Rufford, T. E., Advances and Challenges in Electrochemical CO2 Reduction Processes: An Engineering and Design Perspective Looking Beyond New Catalyst Materials. *J. Mater. Chem. A* **2020,** *8*, 1511-1544.

20. Singh, M. R.; Goodpaster, J. D.; Weber, A. Z.; Head-Gordon, M.; Bell, A. T., Mechanistic Insights into Electrochemical Reduction of CO2 over Ag Using Density Functional Theory and Transport Models. *Proc. Natl. Acad. Sci. U.S.A.* **2017,** *114*, E8812-E8821.

21. Nie, X.; Luo, W.; Janik, M. J.; Asthagiri, A., Reaction Mechanisms of CO2 Electrochemical Reduction on Cu(111) Determined with Density Functional Theory. *J. Catal.* **2014,** *312*, 108-122.

22. Liu, X.; Xiao, J.; Peng, H.; Hong, X.; Chan, K.; Nørskov, J. K., Understanding Trends in Electrochemical Carbon Dioxide Reduction Rates. *Nat. Commun.* **2017,** *8*, 15438.

23. Ross, M. B.; De Luna, P.; Li, Y.; Dinh, C.-T.; Kim, D.; Yang, P.; Sargent, E. H., Designing Materials for Electrochemical Carbon Dioxide Recycling. *Nat. Catal.* **2019,** *2*, 648-658.

24. Fan, L.; Xia, C.; Yang, F.; Wang, J.; Wang, H.; Lu, Y., Strategies in Catalysts and Electrolyzer Design for Electrochemical CO2 Reduction Toward C2+ Products. *Sci. Adv.* **2020,** *6*, eaay3111.

25. Burdyny, T.; Smith, W. A., CO2 Reduction on Gas-Diffusion Electrodes and Why Catalytic Performance Must be Assessed at Commercially-Relevant Conditions. *Energy Environ. Sci.* **2019,** *12*, 1442-1453.

26. Lim, C. F. C.; Harrington, D. A.; Marshall, A. T., Effects of Mass Transfer on the Electrocatalytic CO2 Reduction on Cu. *Electrochim. Acta* **2017,** *238*, 56-63.

27. Blanco, D. E.; Modestino, M. A., Organic Electrosynthesis for Sustainable Chemical Manufacturing. *Trends Chem.* **2019,** *1*, 8-10.

28. Orella, M. J.; Román-Leshkov, Y.; Brushett, F. R., Emerging Opportunities for Electrochemical Processing to Enable Sustainable Chemical Manufacturing. *Curr. Opin. Chem, Eng.* **2018,** *20*, 159-167.

29. Andrew, R. M., Global CO2 Emissions from Cement Production. *Earth Syst. Sci. Data* **2018,** *10*, 195-217.

30. *Mineral Commodity Summaries - Aluminum*; 2017.

31. Association, W. S., World Steel in Figures. **2018**.

32. Elgowainy, A.; Han, J.; Cai, H.; Wang, M.; Forman, G. S.; DiVita, V. B., Energy Efficiency and Greenhouse Gas Emission Intensity of Petroleum Products at US Refineries. *Environ. Sci. Technol.* **2014,** *48*, 7612-7624.

33. *Global Production Capacity of Ethylene 2014-2024*; statista, 2020.

34. *Global Production Capacity of Methanol 2018-2030*; statista, 2021.

35. *Production Capacity of Ammonia Worldwide in 2018 and 2030*; statista, 2021.

36. *Chemicals — Analysis*; International Energy Agency: 2018.

37. Botte, G. G., Electrochemical Manufacturing in the Chemical Industry. *Electrochem. Soc. Interface* **2014,** *23*, 49-55.

38. Comello, S.; Reichelstein, S.; Sahoo, A., The Road Ahead for Solar PV Power. *Renew. Sust. Energy Rev.* **2018,** *92*, 744-756.

39. Wiser, R.; Jenni, K.; Seel, J.; Baker, E.; Hand, M.; Lantz, E.; Smith, A., Expert Elicitation Survey on Future Wind Energy Costs. *Nat. Energy* **2016,** *1*, 8.

40. Baranzini, A.; Goldemberg, J.; Speck, S., A Future for Carbon Taxes. *Ecol. Econ.* **2000,** *32*, 395-412.

41. Kyriakou, V.; Garagounis, I.; Vourros, A.; Vasileiou, E.; Stoukides, M., An Electrochemical Haber-Bosch Process. *Joule* **2020,** *4*, 142-158.

42. De Luna, P.; Hahn, C.; Higgins, D.; Jaffer, S. A.; Jaramillo, T. F.; Sargent, E. H., What Would It Take for Renewably Powered Electrosynthesis to Displace Petrochemical Processes? *Science* **2019,** *364*.

43. Jouny, M.; Luc, W.; Jiao, F., General Techno-Economic Analysis of CO2 Electrolysis Systems. *Ind. Eng. Chem. Res.* **2018,** *57*, 2165-2177.

44. Smith, W. A.; Burdyny, T.; Vermaas, D. A.; Geerlings, H., Pathways to Industrial-Scale Fuel Out of Thin Air from CO2 Electrolysis. *Joule* **2019,** *3*, 1822-1834.

45. Cooper, W. C., Advances and Future Prospects in Copper Electrowinning. *J. Appl. Electrochem.* **1985,** *15*, 789-805.

46. O'Brien, T. F.; Bommaraju, T. V.; Hine, F., Chlor-Alkali Technologies. In *Handbook of Chlor-Alkali Technology: Volume I: Fundamentals, Volume II: Brine Treatment and Cell Operation, Volume III: Facility Design and Product Handling, Volume IV: Plant Commissioning and Support Systems, Volume V: Corrosion, Environmental Issues, and Future Development*, Springer US: Boston, MA, 2005; pp 387-442.

47. Capdevila-Cortada, M., Electrifying the Haber–Bosch. *Nat. Catal.* **2019,** *2*, 1055-1055.

48. Gao, Y.; Neal, L.; Ding, D.; Wu, W.; Baroi, C.; Gaffney, A. M.; Li, F., Recent Advances in Intensified Ethylene Production—A Review. *ACS Catalysis* **2019,** *9*, 8592-8621.

49. Weng, L.-C.; Bell, A. T.; Weber, A. Z., Towards Membrane-Electrode Assembly Systems for CO2 Reduction: A Modeling Study. *Energy Environ. Sci.* **2019,** *12*, 1950-1968.

50. Nesbitt, N. T.; Burdyny, T.; Simonson, H.; Salvatore, D.; Bohra, D.; Kas, R.; Smith, W. A., Liquid–Solid Boundaries Dominate Activity of CO2 Reduction on Gas-Diffusion Electrodes. *ACS Catal.* **2020,** *10*, 14093-14106.

51. Birdja, Y. Y.; Perez-Gallent, E.; Figueiredo, M. C.; Gottle, A. J.; Calle-Vallejo, F.; Koper, M. T. M., Advances and challenges in understanding the electrocatalytic conversion of carbon dioxide to fuels. *Nat. Energy* **2019,** *4*, 732-745.

52. Yoshio, H.; Katsuhei, K.; Shin, S., Production of CO and CH4 in Electrochemical Reduction of CO2 at Metal Electrodes in Aqueous Hydrogencarbonate Solution. *Chem. Lett.* **1985,** *14*, 1695-1698.

53. Yoshio, H.; Katsuhei, K.; Akira, M.; Shin, S., Production of Methane and Ethylene in Electrochemical Reduction of Carbon Dioxide at Copper Electrode in Aqueous Hydrogencarbonate Solution. *Chem. Lett.* **1986,** *15*, 897-898.

54. Yang, K. L.; Kas, R.; Smith, W. A., In Situ Infrared Spectroscopy Reveals Persistent Alkalinity near Electrode Surfaces during CO2 Electroreduction. *J. Am. Chem. Soc.* **2019,** *141*, 15891-15900.

55. Gupta, N.; Gattrell, M.; MacDougall, B., Calculation for the Cathode Surface Concentrations in the Electrochemical Reduction of CO2 in KHCO3 Solutions. *J. Appl. Electrochem.* **2006,** *36*, 161-172.

56. Weekes, D. M.; Salvatore, D. A.; Reyes, A.; Huang, A.; Berlinguette, C. P., Electrolytic CO2 Reduction in a Flow Cell. *Acc. Chem. Res.* **2018,** *51*, 910-918.

57. Newman, J. S.; Tobias, C. W., Theoretical Analysis of Current Distribution in Porous Electrodes. *J. Electrochem. Soc.* **1962,** *109*, 1183-1191.

58. Smith, R. B.; Bazant, M. Z., Multiphase Porous Electrode Theory. *J. Electrochem. Soc.* **2017,** *164*, E3291-E3310.

59. Higgins, D.; Hahn, C.; Xiang, C. X.; Jaramillo, T. F.; Weber, A. Z., Gas-Diffusion Electrodes for Carbon Dioxide Reduction: A New Paradigm. *ACS Energy Lett.* **2019,** *4*, 317-324.

60. Weng, L. C.; Bell, A. T.; Weber, A. Z., Modeling Gas-diffusion Electrodes for CO2 Reduction. *Phys Chem Chem Phys* **2018,** *20*, 16973-16984.

61. Bidault, F.; Brett, D. J. L.; Middleton, P. H.; Brandon, N. P., Review of Gas Diffusion Cathodes for Alkaline Fuel Cells. *J. Power Sources* **2009,** *187*, 39-48.

62. Bui, J. C.; Kim, C.; King, A. J.; Romiluyi, O.; Kusoglu, A.; Weber, A. Z.; Bell, A. T., Engineering Catalyst−Electrolyte Microenvironments to Optimize the Activity and Selectivity for the Electrochemical Reduction of CO2 on Cu and Ag. *Acc. Chem. Res.* **2022,** https://doi.org/10.1021/acs.accounts.1c00650.

63. Wheeler, D. G.; Mowbray, B. A. W.; Reyes, A.; Habibzadeh, F.; He, J.; Berlinguette, C. P., Quantification of Water Transport in a CO2 Electrolyzer. *Energy Environ. Sci.* **2020,** *13*, 5126-5134.

64. Reyes, A.; Jansonius, R. P.; Mowbray, B. A. W.; Cao, Y.; Wheeler, D. G.; Chau, J.; Dvorak, D. J.; Berlinguette, C. P., Managing Hydration at the Cathode Enables Efficient CO2 Electrolysis at Commercially Relevant Current Densities. *ACS Energy Lett.* **2020,** *5*, 1612.

65. Liu, C. P.; Saha, P.; Huang, Y.; Shimpalee, S.; Satjaritanun, P.; Zenyuk, I. V., Measurement of Contact Angles at Carbon Fiber-Water-Air Triple-Phase Boundaries Inside Gas Diffusion Layers Using X-ray Computed Tomography. *ACS Appl. Mater. Interfaces* **2021,** *13*, 20002-20013.

66. Yang, Z.; Li, D.; Xing, L.; Xiang, H.; Xuan, J.; Cheng, S.; Yu, E. H.; Yang, A., Modeling and Upscaling Analysis of Gas Diffusion Electrode-Based Electrochemical Carbon Dioxide Reduction Systems. *ACS Sustainable Chem. Eng.* **2021,** *9*, 351-361.

67. Weng, L.-C.; Bell, A. T.; Weber, A. Z., A Systematic Analysis of Cu-Based Membrane-Electrode Assemblies for CO2 Reduction through Multiphysics Simulation. *Energy Environ. Sci.* **2020,** *13*, 3592-3606.

68. Hashiba, H.; Weng, L. C.; Chen, Y. K.; Sato, H. K.; Yotsuhashi, S.; Xiang, C. X.; Weber, A. Z., Effects of Electrolyte Buffer Capacity on Surface Reactant Species and the Reaction Rate of CO2 in Electrochemical CO2 Reduction. *J. Phys. Chem. C* **2018,** *122*, 3719-3726.

69. Bohra, D. Modeling the Carbon Dioxide Electrocatalysis System. Delft Institute of Technology, 2020.

70. Bohra, D.; Chaudhry, J. H.; Burdyny, T.; Pidko, E. A.; Smith, W. A., Modeling the Electrical Double Layer to Understand the Reaction Environment in a CO2 Electrocatalytic System. *Energy Environ. Sci.* **2019,** *12*, 3380-3389.

71. Bohra, D.; Chaudhry, J. H.; Burdyny, T.; Pidko, E. A.; Smith, W. A., Mass Transport in Catalytic Pores of GDE-Based CO2 Electroreduction Systems. *chemrxiv*, DOI: 10.26434/chemrxiv.13073348.v1 (accessed 2021-01-31).

72. Kas, R. K.; Yang, K. L.; Bohra, D.; Kortlever, R.; Burdyny, T.; Smith, W. A., Electrochemical CO2 Reduction on Nanostructured Metal Electrodes: Fact or Defect? *Chem. Sci.* **2020,** *11*, 1738-1749.

73. Chen, Y.; Lewis, N. S.; Xiang, C., Modeling and Simulation of the Spatial and Light-Intensity Dependence of Product Distributions in an Integrated Photoelectrochemical CO2 Reduction System. *ACS Energy Lett.* **2016,** *1*, 273-280.

74. Chen, Y.; Lewis, N. S.; Xiang, C., Modeling the Performance of A Flow-Through Gas Diffusion Electrode for Electrochemical Reduction of CO or CO2. *J. Electrochem. Soc.* **2020,** *167*.

75. Ni, M., An Electrochemical Model for Syngas Production by Co-electrolysis of H2O and CO2. *J. Power Sources* **2012,** *202*, 209-216.

76. Corral, D.; Feaster, J. T.; Sobhani, S.; DeOtte, J. R.; Lee, D. U.; Wong, A. A.; Hamilton, J.; Beck, V. A.; Sarkar, A.; Hahn, C., et al., Advanced Manufacturing for Electrosynthesis of Fuels and Chemicals from CO2. *Energy Environ. Sci.* **2021,** *14*, 3064-3074.

77. Gerhardt, M. R.; Pant, L. M.; Bui, J. C. M.; Crothers, A. R.; Ehlinger, V. M.; Fornaciari, J. C.; Liu, J.; Weber, A. Z., Methods—Practices and Pitfalls in Voltage Breakdown Analysis of Electrochemical Energy-Conversion Systems. *J. Electrochem. Soc.* **2021**.

78. Kas, R.; Star, A. G.; Yang, K.; Van Cleve, T.; Neyerlin, K. C.; Smith, W. A., Along the Channel Gradients Impact on the Spatioactivity of Gas Diffusion Electrodes at High Conversions during CO2 Electroreduction. *ACS Sustainable Chem. Eng.* **2021,** *9*, 1286-1296.

79. Zhang, T. Y.; Li, Z. Y.; Zhang, J. F.; Wu, J. J., Enhance CO2-to-C2+ products yield through spatial management of CO transport in Cu/ZnO tandem electrodes. *J. Catal.* **2020,** *387*, 163-169.

80. Burdyny, T.; Graham, P. J.; Pang, Y.; Dinh, C.-T.; Liu, M.; Sargent, E. H.; Sinton, D., Nanomorphology-Enhanced Gas-Evolution Intensifies CO2 Reduction Electrochemistry. *ACS Sustainable Chem. Eng.* **2017,** *5*, 4031-4040.

81. Li, J.; Wang, Z. Y.; McCallum, C.; Xu, Y.; Li, F. W.; Wang, Y. H.; Gabardo, C. M.; Dinh, C. T.; Zhuang, T. T.; Wang, L., et al., Constraining CO Coverage on Copper Promotes High-Efficiency Ethylene Electroproduction. *Nat. Catal.* **2019,** *2*, 1124-1131.

82. Jang, J.-Y.; Gan, Y.-F., Numerical Simulation of a Two-Phase Flow for the Acrylonitrile Electrolytic Adiponitrile Process in a Vertical/Horizontal Electrolysis Cell. *Energies* **2018,** *11*.

83. Fornaciari, J. C.; Primc, D.; Kawashima, K.; Wygant, B. R.; Verma, S.; Spanu, L.; Mullins, C. B.; Bell, A. T.; Weber, A. Z., A Perspective on the Electrochemical Oxidation of Methane to Methanol in Membrane Electrode Assemblies. *ACS Energy Lett.* **2020,** *5*, 2954-2963.

84. Lazouski, N.; Chung, M. J.; Williams, K.; Gala, M. L.; Manthiram, K., Non-aqueous Gas Diffusion Electrodes for Rapid Ammonia Synthesis from Nitrogen and Water-Splitting-derived Hydrogen. *Nat. Catal.* **2020,** *3*, 463-+.

85. Zhang, T.; Bui, J. C.; Li, Z.; Bell, A. T.; Weber, A. Z.; Wu, J., Highly Selective Reduction of Carbon Dioxide to Multicarbon Products via In-situ CO Management Using Segmented Tandem Electrodes. *Nat. Catal.* **2022,** *In Press*.

86. de Arquer, F. P. G.; Dinh, C. T.; Ozden, A.; Wicks, J.; McCallum, C.; Kirmani, A. R.; Nam, D. H.; Gabardo, C.; Seifitokaldani, A.; Wang, X., et al., CO2 Electrolysis to Multicarbon Products at Activities Greater than 1 A cm(-2). *Science* **2020,** *367*, 661-+.

87. She, X.; Zhang, T.; Li, Z.; Li, H.; Xu, H.; Wu, J., Tandem Electrodes for Carbon Dioxide Reduction into C2+ Products at Simultaneously High Production Efficiency and Rate. *Cell Reports Physical Science* **2020,** *1*.

88. Wicks, J.; Jue, M. L.; Beck, V. A.; Oakdale, J. S.; Dudukovic, N. A.; Clemens, A. L.; Liang, S.; Ellis, M. E.; Lee, G.; Baker, S. E., et al., 3D-Printable Fluoropolymer Gas Diffusion Layers for CO2 Electroreduction. *Adv. Mater.* **2021,** *33*, e2003855.

89. Kim, C.; Weng, L. C.; Bell, A. T., Impact of Pulsed Electrochemical Reduction of CO2 on the Formation of C2+ Products over Cu. *ACS Catal.* **2020,** *10*, 12403-12413.

90. Sedighian Rasouli, A.; Wang, X.; Wicks, J.; Lee, G.; Peng, T.; Li, F.; McCallum, C.; Dinh, C.-T.; Ip, A. H.; Sinton, D., et al., CO2 Electroreduction to Methane at Production Rates Exceeding 100 mA/cm2. *ACS Sustainable Chem. Eng.* **2020,** *8*, 14668-14673.

91. Smith, W.; Nesbitt, N., Water Activity Regulates CO2 Reduction in Gas-Diffusion Electrodes. *J. Phys. Chem. C.* **2021,** *125*, 13085-13095.

92. Lees, E. W.; Bui, J. C.; Song, D.; Weber, A. Z.; Berlinguette, C. P., Continuum Model to Define the Chemistry and Mass Transfer in a Bicarbonate Electrolyzer. *ACS Energy Lett.* **2022,** *7*, 834-842.

93. Onda, K.; Murakami, T.; Hikosaka, T.; Kobayashi, M.; Notu, R.; Ito, K., Performance analysis of polymer-electrolyte water electrolysis cell at a small-unit test cell and performance prediction of large stacked cell. *J. Electrochem. Soc.* **2002,** *149*, A1069-A1078.

94. Lee, B.; Lim, D.; Lee, H.; Lim, H., Which Water Electrolysis Technology is Appropriate?: Critical Insights of Potential Water Electrolysis for Green Ammonia Production. *Renew. Sust. Energy Rev.* **2021,** *143*.

95. Vorhauer, N.; Altaf, H.; Tsotsas, E.; Vidakovic-Koch, T., Pore Network Simulation of Gas-Liquid Distribution in Porous Transport Layers. *Processes* **2019,** *7*.

96. Zenyuk, I. V., Bridging X-Ray Computed Tomography and Computational Modeling for Electrochemical Energy-Conversion and –Storage. *Curr. Opin. Electrochem.* **2019,** *13*, 78-85.

97. Frensch, S. H.; Fouda-Onana, F.; Serre, G.; Thoby, D.; Araya, S. S.; Kær, S. K., Influence of the Operation Mode on PEM Water Electrolysis Degradation. *Int J Hydrogen Energ* **2019,** *44*, 29889-29898.

98. Paciok, P.; Schalenbach, M.; Carmo, M.; Stolten, D., On the Mobility of Carbon-supported Platinum Nanoparticles towards Unveiling Cathode Degradation in Water Electrolysis. *J. Power Sources* **2017,** *365*, 53-60.

99. Rakousky, C.; Reimer, U.; Wippermann, K.; Carmo, M.; Lueke, W.; Stolten, D., An Analysis of Degradation Phenomena in Polymer Electrolyte Membrane Water Electrolysis. *J. Power Sources* **2016,** *326*, 120-128.

100. Sun, S.; Shao, Z.; Yu, H.; Li, G.; Yi, B., Investigations on Degradation of the Long-term Proton Exchange Membrane Water Electrolysis Stack. *J. Power Sources* **2014,** *267*, 515-520.

101. Limaye, A. M.; Zeng, J. S.; Willard, A. P.; Manthiram, K., Bayesian Data Analysis Reveals No Preference for Cardinal Tafel Slopes in CO2 Reduction Electrocatalysis. *Nat Commun* **2021,** *12*, 703.

102. Weber, A.; Balliet, R.; Gunterman, H. P.; Newman, J., Modeling Water Management in Polymer Electrolyte Fuel Cells. In *Modern Aspects of Electrochemistry*, Springer: New York, USA, 2008.

103. Kakac, S.; Pramuanjaroenkij, A.; Zhou, X., A Review of Numerical Modeling of Solid Oxide Fuel Cells. *Int J Hydrogen Energ* **2007,** *32*, 761-786.

104. Hajimolana, S. A.; Hussain, M. A.; Daud, W. M. A. W.; Soroush, M.; Shamiri, A., Mathematical Modeling of Solid Oxide Fuel Cells: A Review. *Renew. Sust. Energy Rev.* **2011,** *15*, 1893-1917.

105. Beale, S. B.; Andersson, M.; Boigues-Muñoz, C.; Frandsen, H. L.; Lin, Z.; McPhail, S. J.; Ni, M.; Sundén, B.; Weber, A.; Weber, A. Z., Continuum Scale Modelling and Complementary Experimentation of Solid Oxide Cells. *Prog. Energy Combust. Sci.* **2021,** *85*.

106. Chen, Y.; Li, C. W.; Kanan, M. W., Aqueous CO2 Reduction at Very Low Overpotential on Oxide-Derived Au Nanoparticles. *J. Am. Chem. Soc.* **2012,** *134*, 19969-19972.

107. Koretsky, M. D., *Engineering and Chemical Thermodynamics*. 2nd ed.; Wiley: Hoboken, USA, 2013.

108. Blanco, D. E.; Dookhith, A. Z.; Modestino, M. A., Enhancing Selectivity and Efficiency in the Electrochemical Synthesis of Adiponitrile. *React. Chem. Eng.* **2019,** *4*, 8-16.

109. Zhang, Z.; Lees, E. W.; Ren, S.; Huang, A.; Berlinguette, C. P., Electrolytic Conversion of Bicarbonate Solutions to CO at >500 mA cm-2 and 2.2 V. *chemrxiv,* 2021-02-01, DOI: 10.26434/chemrxiv.13665074.v1 (accessed 2021-01-31).

110. Han, X.; Sheng, H.; Yu, C.; Walker, T. W.; Huber, G. W.; Qiu, J.; Jin, S., Electrocatalytic Oxidation of Glycerol to Formic Acid by CuCo2O4 Spinel Oxide Nanostructure Catalysts. *ACS Catal.* **2020,** *10*, 6741-6752.

111. Newman, J.; Thomas-Alyea, K. E., *Electrochemical Systems*. 3rd ed.; Wiley: Hoboken, NJ, 2004.

112. Bard, A. J.; Faulkner, L. R., *Electrochemical Methods: Fundamentals and Applications*. 2nd ed.; Wiley: Hoboken, NJ, 2001.

113. Cheng, W.-H.; de la Calle, A.; Atwater, H. A.; Stechel, E. B.; Xiang, C., Hydrogen from Sunlight and Water: A Side-by-Side Comparison between Photoelectrochemical and Solar Thermochemical Water-Splitting. *ACS Energy Lett.* **2021,** *6*, 3096-3113.

114. DeBethune, A. J.; Licht, T. S.; Swendeman, N., The Temperature Coefficients of Electrode Potentials: The Isothermal and Thermal Coefficients—The Standard Ionic Entropy and Electrochemical Transport of the Hydrogen Ion. *J. Electrochem. Soc.* **1959,** *106*, 616-625.

115. DeBethune, A. J.; Swendeman Loud, N. A., *Standard Aqueous Electrode Potentials and Temperature Coefficients at 25 C*. Skokie, IL, 1964.

116. Crothers, A. R.; Darling, R. M.; Kusoglu, A.; Radke, C. J.; Weber, A. Z., Theory of Multicomponent Phenomena in Cation-Exchange Membranes: Part I. Thermodynamic Model and Validation. *J. Electrochem. Soc.* **2020,** *167*.

117. Bui, J. C.; Digdaya, I.; Xiang, C. X.; Bell, A. T.; Weber, A. Z., Understanding Multi-Ion Transport Mechanisms in Bipolar Membranes. *ACS Appl. Mater. Interfaces* **2020,** *12*, 52509-52526.

118. Overbeek, J. T. G., The Donnan Equilibrium. *Prog. Biophys. Biophys. Chem.* **1956,** *6*, 57-84.

119. Futerko, P.; Hsing, I.-M., Thermodynamics of Water Vapor Uptake in Perfluorosulfonic Acid Membranes. *J. Electrochem. Soc.* **1999,** *146*, 2049-2053.

120. Meyers, J. P.; Newman, J., Simulation of the Direct Methanol Fuel Cell. *J. Electrochem. Soc.* **2002,** *149*.

121. Thampan, T.; Malhotra, S.; Tang, H.; Datta, R., Modeling of Conductive Transport in Proton-Exchange Membranes for Fuel Cells. *J. Electrochem. Soc.* **2000,** *147*.

122. Peng, J.; Roy, A. L.; Greenbaum, S. G.; Zawodzinski, T. A., Effect of CO2 Absorption on Ion and Water Mobility in an Anion Exchange Membrane. *J. Power Sources* **2018,** *380*, 64-75.

123. Kreuer, K.-D., The Role of Internal Pressure for the Hydration and Transport Properties of Ionomers and Polyelectrolytes. *Solid State Ionics* **2013,** *252*, 93-101.

124. Gostick, J. T.; Weber, A. Z., Resistor-Network Modeling of Ionic Conduction in Polymer Electrolytes. *Electrochim. Acta* **2015,** *179*, 137-145.

125. Weber, A. Z.; Newman, J., Transport in Polymer-Electrolyte Membranes - I. Physical Model. *J. Electrochem. Soc.* **2003,** *150*, A1008-A1015.

126. Weber, A. Z.; Newman, J., Transport in Polymer-Electrolyte Membranes - II. Mathematical Model. *J. Electrochem. Soc.* **2004,** *151*, A311-A325.

127. Kusoglu, A.; Weber, A. Z., New Insights into Perfluorinated Sulfonic-Acid Ionomers. *Chem Rev* **2017,** *117*, 987-1104.

128. Blanco, D. E.; Atwi, R.; Sethuraman, S.; Lasri, A.; Morales, J.; Rajput, N. N.; Modestino, M. A., Effect of Electrolyte Cations on Organic Electrosynthesis: The Case of Adiponitrile Electrochemical Production. *J. Electrochem. Soc.* **2020,** *167*.

129. Goyal, A.; Koper, M. T. M., The Interrelated Effect of Cations and Electrolyte pH on the Hydrogen Evolution Reaction on Gold Electrodes in Alkaline Media. *Angew. Chem.* **2021,** *60*, 13452-13462.

130. Resasco, J.; Lum, Y.; Clark, E.; Zeledon, J. Z.; Bell, A. T., Effects of Anion Identity and Concentration on Electrochemical Reduction of CO2. *ChemElectroChem* **2018,** *5*, 1064-1072.

131. Ringe, S.; Clark, E. L.; Resasco, J.; Walton, A.; Seger, B.; Bell, A. T.; Chan, K., Understanding Cation Effects in Electrochemical CO2 Reduction. *Energy Environ. Sci.* **2019,** *12*, 3001-3014.

132. Rabinowitz, J. A.; Kanan, M. W., The Future of Low-temperature Carbon Dioxide Electrolysis Depends on Solving One Basic Problem. *Nat Commun* **2020,** *11*, 5231.

133. Larrazábal, G. O.; Ma, M.; Seger, B., A Comprehensive Approach to Investigate CO2 Reduction Electrocatalysts at High Current Densities. *Acc. Mater. Res.* **2021,** *2*, 220-229.

134. Liu, X.; Schlexer, P.; Xiao, J.; Ji, Y.; Wang, L.; Sandberg, R. B.; Tang, M.; Brown, K. S.; Peng, H.; Ringe, S., et al., pH Effects on the Electrochemical Reduction of CO(2) Towards C2 Products on Stepped Copper. *Nat Commun* **2019,** *10*, 32.

135. Bui, J. C.; Kim, C.; Weber, A. Z.; Bell, A. T., Dynamic Boundary Layer Simulation of Pulsed CO2 Electrolysis on a Copper Catalyst. *ACS Energy Lett.* **2021**, 1181-1188.

136. Schulz, K. G.; Riebesell, U.; Rost, B.; Thoms, S.; Zeebe, R. E., Determination of the Rate Constants for the Carbon Dioxide to Bicarbonate Inter-conversion in pH-buffered Seawater Systems. *Marine Chem.* **2006,** *100*, 53-65.

137. Zumdahl, S.; DeCoste, D., Appendix 5. In *Chemical Principles*, 8th ed.; Cengage Learning: Boston, MA, 2016; p A22.

138. Riddick, J. A.; Bunger, W. B.; Sakano, T. K., *Organic Solvents. Techniques of Chemistry*. 4th ed.; Wiley: New York, USA, 1986.

139. Clayton, G. D.; Clayton, F. E., *Patty's Industrial Hygiene and Toxicology*. 3rd ed.; Wiley: New York, USA, 1981; Vol. 2.

140. Vollhardt, P., *Organic Chemistry: Structure and Function*. 5th ed.; W.H. Freeman: New York, NY, 2005.

141. Schubert, D., Boron Oxides, Boric Acid, and Borates. In *Kirk-Othmer Encyclopedia of Chemical Technology*, John Wiley and Sons: New York, NY, 2011.

142. Dalton, L. R. Table of Acid and Base Strength. (accessed October 23, 2021).

143. Bates, R. G.; Pinching, G. D., Acidic Dissociation Constant of Ammonium Ion at 0 to 50 C, and the Base Stength of Ammonia. *J. Res. Natl. Bur. Stand.* **1949,** *42*, 419-430.

144. Pines, D.; Ditkovich, J.; Mukra, T.; Miller, Y.; Kiefer, P. M.; Daschakraborty, S.; Hynes, J. T.; Pines, E., How Acidic Is Carbonic Acid? *J Phys Chem B* **2016,** *120*, 2440-51.

145. Divekar, A. G.; Park, A. M.; Owczarczyk, Z. R.; Seifert, S.; Pivovar, B. S.; Herring, A. M., A Study of Carbonate Formation Kinetics and Morphological Effects Observed on OH-Form of Pfaem When Exposed to Air Containing CO2. *ECS Trans.* **2017,** *80*, 1005.

146. Bui, J. C.; Corpus, K. R. M.; Bell, A. T.; Weber, A. Z., On the Nature of Field Enhanced Water Dissociation in Bipolar Membranes. *J. Phys. Chem. C* **2021,** *125*, 24974-24987.

147. Conroy, D. T.; Craster, R. V.; Matar, O. K.; Cheng, L. J.; Chang, H. C., Nonequilibrium Hysteresis and Wien Effect Water Dissociation at a Bipolar Membrane. *Phys. Rev. E. Stat. Nonlin. Soft Matter Phys.* **2012,** *86*, 056104.

148. Kaiser, V. The Wien Effect in Electric and Magnetic Coulomb systems - from Electrolytes to Spin Ice. TU Dresden, Dresden, 2015.

149. Kaiser, V.; Bramwell, S. T.; Holdsworth, P. C. W.; Moessner, R., Onsager's Wien effect on a lattice. *Nature Materials* **2013,** *12*, 1033-1037.

150. Craig, N. P. Electrochemical Behavior of Bipolar Membranes. University of California, Berkeley, 2013.

151. Bird, R. B.; Stewart, W. E.; Lightfoot, E. N., *Transport phenomena*. 2 ed.; Wiley: New York, USA, 2002.

152. Pant, L. M.; Mitra, S. K.; Secanell, M., A generalized mathematical model to study gas transport in PEMFC porous media. *IJHMT* **2013,** *58*, 70-79.

153. Lightfoot, E. N., *Transport phenomena and living systems: Biomedical applications of momentum and mass transfe*. Wiley: Ney York, USA, 1974.

154. Taylor, R.; Krishna, R., *Multicomponent Mass Transfer*. Wiley: 1993.

155. Mason, E. A.; Malinauskas, A. P., *Gas Transport in Porous Media: The Dusty Gas Model*. Elsevier: Amsterdam, 1983.

156. Kerkhof, P. J. A. M., A modified Maxwell-Stefan model for transport through inert membranes: The binary friction model. *The Chemical Engineering Journal and the Biochemical Engineering Journal* **1996,** *64*, 319-343.

157. Hirschfelder, J. O.; Curtiss, C. F.; Bird, R. B., *Molecular Theory of Gases and Liquids*. Wiley: 1954.

158. Casebolt, R.; Levine, K.; Suntivich, J.; Hanrath, T., Pulse check: Potential Opportunities in Pulsed Electrochemical CO2 Reduction. *Joule* **2021,** *5*, 1987-2026.

159. Israelachvili, J. N., *Intermolecular and Surface Forces*. Elsevier: New York, 2011.

160. Crothers, A. R.; Darling, R. M.; Kusoglu, A.; Radke, C. J.; Weber, A. Z., Theory of Multicomponent Phenomena in Cation-Exchange Membranes: Part II. Transport Model and Validation. *J. Electrochem. Soc.* **2020,** *167*.

161. Delacourt, C.; Newman, J., Mathematical Modeling of a Cation-Exchange Membrane Containing Two Cations. *J. Electrochem. Soc.* **2008,** *155*, B1210-B1217.

162. Crothers, A. R.; Darling, R. M.; Kushner, D. I.; Perry, M. L.; Weber, A. Z., Theory of Multicomponent Phenomena in Cation-Exchange Membranes: Part III. Transport in Vanadium Redox-Flow-Battery Separators. *J. Electrochem. Soc.* **2020,** *167*.

163. Fornaciari, J. C.; Gerhardt, M. R.; Zhou, J.; Regmi, Y. N.; Danilovic, N.; Bell, A. T.; Weber, A. Z., The Role of Water in Vapor-fed Proton-Exchange-Membrane Electrolysis. *J. Electrochem. Soc.* **2020,** *167*.

164. Pant, L. M.; Gerhardt, M. R.; Macauley, N.; Mukundan, R.; Borup, R. L.; Weber, A. Z., Along-the-channel modeling and analysis of PEFCs at low stoichiometry: Development of a 1+2D model. *Electrochim. Acta* **2019,** *326*, 134963.

165. Bockris, J. O.; Nagy, Z., Symmetry Factor and Transfer Coefficient: A Source of Confusion in Electrode Kinetics. *J. Chem. Ed.* **1973,** *50*, 839-843.

166. Langmuir, I., The Adsorption of Gases on Plane Surfaces of Glass, Mica and Platinum. *J. Am. Chem. Soc.* **1918,** *40*, 1361-1403.

167. Yoon, W.; Weber, A. Z., Modeling Low-Platinum-Loading Effects in Fuel-Cell Catalyst Layers. *J. Electrochem. Soc.* **2011,** *158*, B1007-B1018.

168. Kibria, M. G.; Edwards, J. P.; Gabardo, C. M.; Dinh, C. T.; Seifitokaldani, A.; Sinton, D.; Sargent, E. H., Electrochemical CO2 Reduction into Chemical Feedstocks: From Mechanistic Electrocatalysis Models to System Design. *Adv. Mater.* **2019,** *31*, e1807166.

169. Motagamwala, A. H.; Dumesic, J. A., Microkinetic Modeling: A Tool for Rational Catalyst Design. *Chem Rev* **2021,** *121*, 1049-1076.

170. Singh, M. R.; Clark, E. L.; Bell, A. T., Effects of Electrolyte, Catalyst, and Membrane Composition and Operating Conditions on the Performance of Solar-driven Electrochemical Reduction of Carbon Dioxide. *Phys. Chem. Chem. Phys.* **2015,** *17*, 18924-18936.

171. Eigen, M., Proton Transfer, Acid-Base Catalysis, and Enzymatic Hydrolysis. Part I: Elementary Processes. *Angew. Chem.* **1964,** *3*, 1-19.

172. Conrad, J.; Tremaine, P. R., Third Dissociation Constant of Phosphoric Acid in H2O and D2O from 75 to 300 Degrees C at p = 20.4 MPa Using Raman Spectroscopy and a Titanium-sapphire Flow Cell. *Phys Chem Chem Phys* **2021,** *23*, 10670-10685.

173. Onsager, L., Deviations from Ohm's Law in Weak. *J. Chem. Phys.* **1934,** *2*, 599-615.

174. Onsager, L.; Fuoss, R. M., Irreversible Processes in Electrolytes. Diffusion, Conductance, and Viscous Flow in Arbitrary Mixtures of Strong Electrolytes. *J. Phys. Chem.* **1932,** *36*, 2689-2778.

175. Kaiser, V.; Bramwell, S. T.; Holdsworth, P. C. W.; Moessner, R., Onsager's Wien Effect on a Lattice. *Nat. Mater.* **2013,** *12*, 1033-1037.

176. Zhong, H.; Fujii, K.; Nakano, Y.; Jin, F., Effect of CO2 Bubbling into Aqueous Solutions Used for Electrochemical Reduction of CO2 for Energy Conversion and Storage. *J. Phys. Chem. C.* **2014,** *119*, 55-61.

177. Fukunaka, Y.; Jiang, M. F.; Yamamoto, T.; Asaki, Z.; Kondo, Y., Nonuniformity of NaOH Concentration and Effective Bubble Diameter in CO2 Injection into Aqueous NaOH Solution. *Metall. Trans. B* **1989,** *20*, 5-12.

178. Moore, T.; Xia, X.; Baker, S. E.; Duoss, E. B.; Beck, V. A., Elucidating Mass Transport Regimes in Gas Diffusion Electrodes for CO2 Electroreduction. *ACS Energy Lett.* **2021**, 3600-3606.

179. Poling, B. E.; Prausnitz, J. M.; O'Connell, J. P., *The Properties of Gases and Liquids*. McGraw-Hill: New York, USA, 2001.

180. Fairbanks, D. F.; Wilke, C. R., Diffusion Coefficients in Multicomponent Gas Mixtures. *Ind. Eng. Chem. Res* **1950,** *42*, 471-475.

181. Lamanna, J. M.; Kandlikar, S. G., Determination of Effective Water Vapor Diffusion Coefficient in PEMFC Gas Diffusion Layers. *Int J Hydrogen Energ* **2011,** *36*, 5021-5029.

182. Zamel, N.; Li, X.; Shen, J., Correlation for the Effective Gas Diffusion Coefficient in Carbon Paper Diffusion Media. *Energy Fuels* **2009,** *23*, 6070-6078.

183. Zamel, N.; Astrath, N. G. C.; Li, X.; Shen, J.; Zhou, J.; Astrath, F. B. G.; Wang, H.; Liu, Z. S., Experimental Measurements of Effective Diffusion Coefficient of Oxygen-Nitrogen Mixture in PEM Fuel Cell Diffusion Media. *Chem. Eng. Sci.* **2010,** *65*, 931-937.

184. Hwang, G. S.; Weber, A. Z., Effective-Diffusivity Measurement of Partially-Saturated Fuel-Cell Gas-Diffusion Layers. *J. Electrochem. Soc.* **2012,** *159*, F683-F692.

185. Garcia-Salaberri, P. A.; Gostick, J. T.; Hwang, G.; Weber, A. Z.; Vera, M., Effective Diffusivity in Partially-Saturated Carbon-Fiber Gas Diffusion Layers: Effect of Local Saturation and Application to Macroscopic Continuum Models. *J. Power Sources* **2015,** *296*, 440-453.

186. Sabharwal, M.; Pant, L. M.; Putz, A.; Susac, D.; Jankovic, J.; Secanell, M., Analysis of Catalyst Layer Microstructures: From Imaging to Performance. *Fuel Cells* **2016,** *16*, 734-753.

187. Garcia-Salaberri, P. A.; Gostick, J. T.; Zenyuk, I. V.; Hwang, G.; Vera, M.; Weber, A. Z., On the Limitations of Volume-Averaged Descriptions of Gas Diffusion Layers in the Modeling of Polymer Electrolyte Fuel Cells. *Polymer Electrolyte Fuel Cells 17 (Pefc 17)* **2017,** *80*, 133-143.

188. Garcia-Salaberri, P. A.; Zenyuk, I. V.; Shum, A. D.; Hwang, G.; Vera, M.; Weber, A. Z.; Gostick, J. T., Analysis of Representative Elementary Volume and Through-Plane Regional Characteristics of Carbon-fiber Papers: Diffusivity, Permeability and Electrical/Thermal Conductivity. *Int J Heat Mass Tran* **2018,** *127*, 687-703.

189. Singh, R.; Akhgar, A. R.; Sui, P. C.; Lange, K. J.; Djilali, N., Dual-Beam FIB/SEM Characterization, Statistical Reconstruction, and Pore Scale Modeling of a PEMFC Catalyst Layer. *J. Electrochem. Soc.* **2014,** *161*, F415-F424.

190. Lange, K. J.; Sui, P. C.; Djilali, N., Pore scale simulation of transport and electrochemical reactions in reconstructed PEMFC catalyst layers. *J. Electrochem. Soc.* **2010,** *157*, B1434-B1442.

191. Siddique, N. A.; Liu, F., Process Based Reconstruction and Simulation of a Three-Dimensional Fuel Cell Catalyst Layer. *Electrochim. Acta* **2010,** *55*, 5357-5366.

192. Gostick, J. T.; Fowler, M. W.; Pritzker, M. D.; Ioannidis, M. A.; Behra, L. M., In-plane and Through-plane Gas Permeability of Carbon Fiber Electrode Backing Layers. *J. Power Sources* **2006,** *162*, 228-238.

193. Gurau, V.; Bluemle, M. J.; Castro, E. S. D.; Tsou, Y. M.; Jr, T. A. Z.; Jr, J. A. M., Characterization of Transport Properties in Gas Diffusion Layers for Proton Exchange Membrane Fuel Cells. 2. Absolute Permeability. *J. Power Sources* **2007,** *165*, 793-802.

194. Pant, L. M.; Mitra, S. K.; Secanell, M., Absolute Permeability and Knudsen Diffusivity Measurements in PEMFC Gas Diffusion Layers and Micro Porous Layers. *J. Power Sources* **2012,** *206*, 153-160.

195. Carrigy, N. B.; Pant, L. M.; Mitra, S.; Secanell, M., Knudsen diffusivity and permeability of pemfc microporous coated gas diffusion layers for different polytetrafluoroethylene loadings. *J. Electrochem. Soc.* **2013,** *160*, F81-F89.

196. Bresciani, F.; Casalegno, A.; Varisco, G.; Marchesi, R., Water Transport into PEFC Gas Diffusion Layer: Experimental Characterization of Diffusion and Permeation. *Int. J. Energy Res.* **2014,** *38*, 602-613.

197. Gostick, J. T.; Ioannidis, M. A.; Fowler, M. W.; Pritzker, M. D., Pore Network Modeling of Fibrous Gas Diffusion Layers for Polymer Electrolyte Membrane Fuel Cells. *J. Power Sources* **2007,** *173*, 277-290.

198. Zenyuk, I. V.; Das, P. K.; Weber, A. Z., Understanding Impacts of Catalyst-Layer Thickness on Fuel-Cell Performance via Mathematical Modeling. *J. Electrochem. Soc.* **2016,** *163*, F691-F703.

199. Bednarek, T.; Tsotridis, G., Calculation of Effective Transport Properties of Partially Saturated Gas Diffusion Layers. *J. Power Sources* **2017,** *340*, 111-120.

200. Moosavi, S. M.; Niffeler, M.; Gostick, J.; Haussener, S., Transport Characteristics of Saturated Gas Diffusion Layers Treated with Hydrophobic Coatings. *Chem. Eng. Sci.* **2018,** *176*, 503-514.

201. Gostick, J. T.; Ioannidis, M. A.; Fowler, M. W.; Pritzker, M. D., Wettability and Capillary Behavior of Fibrous Gas Diffusion Media for Polymer Electrolyte Membrane Fuel Cells. *J. Power Sources* **2009,** *194*, 433-444.

202. Kusoglu, A.; Weber, A. Z., New Insights into Perfluorinated Sulfonic-Acid Ionomers. *Chem. Rev.* **2017,** *117*, 987-1104.

203. Vetter, R.; Schumacher, J. O., Experimental Parameter Uncertainty in Proton Exchange Membrane Fuel Cell Modeling. Part I: Scatter in Material Parameterization. *J. Power Sources* **2019,** *438*, 227018.

204. Okada, T.; Ayato, Y.; Yuasa, M.; Sekine, I., The Effect of Impurity Cations on the Transport Characteristics of Perfluorosulfonated Ionomer Membranes. *J. Phys. Chem. B* **1999,** *103*, 3315-3322.

205. Okada, T.; Satou, H.; Okuno, M.; Yuasa, M., Ion and Water Transport Characteristics of Perfluorosulfonated Ionomer Membranes with H+ and Alkali Metal Cations. *J. Phys. Chem. B* **2002,** *106*, 1267-1273.

206. Li, Y. S.; Zhao, T. S.; Yang, W. W., Measurements of Water Uptake and Transport Properties in Anion-exchange Membranes. *Int J Hydrogen Energ* **2010,** *35*, 5656-5665.

207. McCallum, C.; Gabardo, C. M.; O'Brien, C. P.; Edwards, J. P.; Wicks, J.; Xu, Y.; Sargent, E. H.; Sinton, D., Reducing the Crossover of Carbonate and Liquid Products during Carbon Dioxide Electroreduction. *Cell Rep. Phys. Sci.* **2021**.

208. Wang, H.; Leung, D. Y. C.; Xuan, J., Modeling of a Microfluidic Electrochemical Cell for CO2 Utilization and Fuel Production. *Appl. Energy* **2013,** *102*, 1057-1062.

209. Delacourt, C.; Newman, J., Mathematical Modeling of CO2 Reduction to CO in Aqueous Electrolytes. *J. Electrochem. Soc.* **2010,** *157*.

210. Delacourt, C.; Newman, J., Mathematical Modeling of CO2 Reduction to CO in Aqueous Electrolytes II. Study of an Electrolysis Cell Making Syngas (CO + H-2) from CO2 and H2O Reduction at Room Temperature. *J. Electrochem. Soc.* **2010,** *157*, B1911-B1926.

211. Suter, S.; Haussener, S., Optimizing Mesostructured Silver Catalysts for Selective Carbon Dioxide Conversion into Fuels. *Energy Environ. Sci.* **2019,** *12*, 1668-1678.

212. Gutierrez, R. R.; Haussener, S., Modeling of Concurrent CO2and Water Splitting by Practical Photoelectrochemical Devices. *J. Electrochem. Soc.* **2016,** *163*, H1008-H1018.

213. Marcandalli, G.; Goyal, A.; Koper, M. T. M., Electrolyte Effects on the Faradaic Efficiency of CO2 Reduction to CO on a Gold Electrode. *ACS Catal* **2021,** *11*, 4936-4945.

214. Huang, B.; Rao, R. R.; You, S.; Hpone Myint, K.; Song, Y.; Wang, Y.; Ding, W.; Giordano, L.; Zhang, Y.; Wang, T., et al., Cation- and pH-Dependent Hydrogen Evolution and Oxidation Reaction Kinetics. *J. Amer. Chem. Soc. Au* **2021,** *1*, 1674-1687.

215. Resasco, J.; Chen, L. D.; Clark, E.; Tsai, C.; Hahn, C.; Jaramillo, T. F.; Chan, K.; Bell, A. T., Promoter Effects of Alkali Metal Cations on the Electrochemical Reduction of Carbon Dioxide. *J Am Chem Soc* **2017,** *139*, 11277-11287.

216. Wang, J.; Cheng, T.; Fenwick, A. Q.; Baroud, T. N.; Rosas-Hernandez, A.; Ko, J. H.; Gan, Q.; Goddard, W. A., III; Grubbs, R. H., Selective CO2 Electrochemical Reduction Enabled by a Tricomponent Copolymer Modifier on a Copper Surface. *J Am Chem Soc* **2021,** *143*, 2857-2865.

217. Kim, C.; Bui, J. C.; Luo, X.; Cooper, J.; Kusoglu, A.; Weber, A. Z.; Bell, A. T., Bi-layer Ionomer Coatings on Copper Tailor Catalyst Microenvironments for Selective CO2 Electrolysis to Multicarbon Products. *Nat. Energy* **2021,** *6*, 1026-1034.

218. Wang, L.; Nitopi, S. A.; Bertheussen, E.; Orazov, M.; Morales-Guio, C. G.; Liu, X.; Higgins, D. C.; Chan, K.; Nørskov, J. K.; Hahn, C., et al., Electrochemical Carbon Monoxide Reduction on Polycrystalline Copper: Effects of Potential, Pressure, and pH on Selectivity toward Multicarbon and Oxygenated Products. *ACS Catalysis* **2018,** *8*, 7445-7454.

219. Agbo, P.; Danilovic, N., An Algorithm for the Extraction of Tafel Slopes. *J. Phys. Chem. C.* **2019,** *123*, 30252-30264.

220. Blake, J. W.; Padding, J. T.; Haverkort, J. W., Analytical Modelling of CO2 Reduction in Gas-Diffusion Electrode Catalyst Layers. *Electrochim. Acta* **2021,** *393*.

221. Eikerling, M.; Kornyshev, A. A., Modelling the Performance of the Cathode Catalyst Layer of Polymer Electrolyte Fuel Cells. *J. Electroanal. Chem.* **1998,** *453*, 89-106.

222. Eikerling, M., Water Management in Cathode Catalyst Layers of PEM Fuel Cells. *J. Electrochem. Soc.* **2006,** *153*, E58-E70.

223. Shamardina, O.; Kulikovsky, A. A.; Chertovich, A. V.; Khokhlov, A. R., A Model for High-Temperature PEM Fuel Cell: The Role of Transport in the Cathode Catalyst Layer. *Fuel Cells* **2012,** *12*, 577-582.

224. Kulikovsky, A. A., How Important is Oxygen Transport in Agglomerates in a PEM Fuel Cell Catalyst Layer? *Electrochim. Acta* **2014,** *130*, 826-829.

225. Kulikovsky, A. A., Understanding Catalyst Layer Degradation in PEM Fuel Cell Through Polarization Curve Fitting. *Electrocatalysis* **2014,** *5*, 221-225.

226. Bernardi, D. M.; Verbrugge, M. W., Mathematical Model of a Gas Diffusion Electrode Bonded to a Polymer Electrolyte. *AIChE J.* **1991,** *37*, 1151-1163.

227. Horn, R. A.; Johnson, C. R., *Matrix Analysis*. 2 ed.; Cambridge University Press: New York, USA, 1985.

228. Leveque, R. J., *Finite Difference Methods for Ordinary and Partial Differential Equations*. 2 ed.; SIAM: Philadelphia, USA, 2007.

229. Butcher, J. C., *Numerical Methods for Ordinary Differential Equations*. 1 ed.; John Wiley & Sons: New York, USA, 2003.

230. COMSOL Multiphysics® v. 5.6. www.comsol.com (accessed October 23, 2021).

231. Balliet, R. J.; Newman, J., Cold Start of a Polymer-Electrolyte Fuel Cell I. Development of a Two-Dimensional Model. *J. Electrochem. Soc.* **2011,** *158*, B927-B938.

232. Goshtasbi, A.; Pence, B. L.; Ersal, T., Computationally Efficient Pseudo-2D Non-Isothermal Modeling of Polymer Electrolyte Membrane Fuel Cells with Two-Phase Phenomena. *J. Electrochem. Soc.* **2016,** *163*, F1412-F1432.

233. ANSYS Fluent. https://www.ansys.com/products/fluids/ansys-fluent (accessed October 23, 2021).

234. Dutta, S.; Shimpalee, S.; Zee, J. W. V., Three-dimensional Numerical Simulation of Straight Channel PEM Fuel Cells. *J. Appl. Electrochem.* **2000,** *30*, 135-146.

235. Sivertsen, B. R.; Djilali, N., CFD-based Modelling of Proton Exchange Membrane Fuel Cells. *J. Power Sources* **2005,** *141*, 65-78.

236. Star-CCM+. https://www.plm.automation.siemens.com/global/en/products/simcenter/STAR-CCM.html (accessed October 23, 2021).

237. Lopata, J. S.; Kang, Z.; Young, J.; Bender, G.; Weidner, J. W.; Cho, H.; Shimpalee, S., Considering Two-Phase Flow in Three-Dimensional Computational Fluid Dynamics Simulations of Proton Exchange Membrane Water Electrolysis Devices. *ECS Trans.* **2929,** *9*, 653-662.

238. AVL. http://www.avl.com/ (accessed October 23, 2021).

239. Haas, C.; Macherhammer, M.-G.; Klopcic, N.; Trattner, A., Capabilities and Limitations of 3D-CFD Simulation of Anode Flow Fields of High-Pressure PEM Water Electrolysis. *Processes* **2021,** *9*.

240. ESI. CFD-ACE+. http://www.esi-cfd.com/ (accessed October 23, 2021).

241. Klein, J.; Deseure, J.; Bultel, Y., Simulations of Heat and Mass Transfers in Tubular Solid Oxide Electrolysis Cell. *ECS TRans.* **2009,** *2*, 1305-1314.

242. openFCST: An open source fuel cell simulation toolbox. http://www.openfcst.org.

243. openFuelCell. https://openfuelcell.sourceforge.io/ (accessed October 23, 2021).

244. deal.II: A Finite Element Differential Equations Analysis Library. http://www.dealii.org/ (accessed October 23, 2021).

245. openFOAM. https://www.openfoam.com/ (accessed October 23, 2021).

246. Kone, J.-P.; Zhang, X.; Yan, Y.; Hu, G.; Ahmadi, G., CFD Modeling and Simulation of PEM Fuel Cell Using OpenFOAM. *Energy Procedia* **2018,** *145*, 64-69.

247. Choi, H.; Pharaoh, J. G.; Ryland, D.; Kettner, A.; Gnanapragasam, N., Computational Fluid Dynamics Modeling of Solid Oxide Electrolysis Cell. *ECS Trans.* **2913,** *1*, 3161-3170.

248. Askari, E.; Proulx, P.; Passalacqua, A., Modelling of Bubbly Flow Using CFD-PBM Solver in OpenFOAM: Study of Local Population Balance Models and Extended Quadrature Method of Moments Applications. *ChemEngineering* **2018,** *2*.

249. Wang, C. Y., A Fixed-grid Numerical Algorithm for Two-Phase Flow and Heat Transfer in Porous Media. *Numer. Heat Transf. B: Fundam.* **1997,** *32*, 85-105.

250. Weber, A. Z.; Darling, R. M.; Newman, J., Modeling Two-Phase behavior in PEFCs. *J. Electrochem. Soc.* **2004,** *151*, A1715-A1727.

251. Weber, A. Z. Modeling Water Management in Polymer-Electrolyte Fuel Cells. University of California, Berkeley, 2004.

252. Kornyshev, A. A., Double-Layer in Ionic Liquids: Paradigm Change? *J. Phys. Chem. B* **2007,** *111*, 5545-5557.

253. Bazant, M. Z.; Storey, B. D.; Kornyshev, A. A., Double Layer in Ionic Liquids: Overscreening versus Crowding. *Phys. Rev. Lett.* **2011,** *106*, 046102.

254. Hunter, R. J.; Wright, H. J. L., The Dependence of Electrokinetic Potential on Concentration of Electrolyte. *J. Colloid Interface Sci.* **1971,** *37*, 564-580.

255. Nakamura, M.; Sato, N.; Hoshi, N.; Sakata, O., Outer Helmholtz Plane of the Electrical Double Layer Formed at the Solid Electrode–Liquid Interface. *ChemPhysChem* **2011,** *12*, 1430-1434.

256. Frumkin, A., Wasserstoffüberspannung und Struktur der Doppelschicht. *Zeitschrift für Physikalische Chemie* **1933,** *164A*, 121-133.

257. Hunter, R. J., Chapter 2 - Charge and Potential Distribution at Interfaces. In *Zeta Potential in Colloid Science*, Hunter, R. J., Ed. Academic Press: 1981; pp 11-58.

258. Frumkin, A. N.; Petrii, O. A., Potentials of Zero Total and Zero Free Charge of Platinum Group Metals. *Electrochim. Acta* **1975,** *20*, 347-359.

259. Auer, A.; Ding, X.; Bandarenka, A. S.; Kunze-Liebhäuser, J., The Potential of Zero Charge and the Electrochemical Interface Structure of Cu(111) in Alkaline Solutions. *J. Phys. Chem. C.* **2021,** *125*, 5020-5028.

260. Liu, T.; Xi, C.; Dong, C.; Cheng, C.; Qin, J.; Hu, S.; Liu, H.; Du, X.-W., Improving Interfacial Electron Transfer via Tuning Work Function of Electrodes for Electrocatalysis: From Theory to Experiment. *J. Phys. Chem. C.* **2019,** *123*, 28319-28326.

261. Zenyuk, I. V.; Lister, S., Spatially-Resolved Modeling of Electric Double Layers for the Oxygen Reduction Reaction in Water-Filled Platinum Electrodes. *ECS Trans.* **2013,** *58*.

262. Zenyuk, I. V.; Litster, S., Modeling Ion Conduction and Electrochemical Reactions in Water Films on Thin-film Metal Electrodes with Application to Low Temperature Fuel Cells. *Electrochim. Acta* **2014,** *146*, 194-206.

263. Huang, J.; Zhou, T.; Zhang, J.; Eikerling, M., Double Layer of Platinum Electrodes: Non-monotonic Surface Charging Phenomena and Negative Double Layer Capacitance. *J. Chem. Phys.* **2018,** *148*, 044704.

264. Chan, K.; Eikerling, M., A Pore-Scale Model of Oxygen Reduction in Ionomer-Free Catalyst Layers of PEFCs. *J. Electrochem. Soc.* **2011,** *158*.

265. Ringe, S.; Morales-Guio, C. G.; Chen, L. D.; Fields, M.; Jaramillo, T. F.; Hahn, C.; Chan, K., Double Layer Charging Driven Carbon Dioxide Adsorption Limits the Rate of Electrochemical Carbon Dioxide Reduction on Gold. *Nat Commun* **2020,** *11*, 33.

266. Saha, P.; Zenyuk, I. V., Electrokinetic Streaming Current Method to Probe Polycrystalline Gold Electrode-Electrolyte Interface Under Applied Potentials. *J. Electrochem. Soc.* **2021,** *168*.

267. Saha, P.; Nam, C.; Hickner, M. A.; Zenyuk, I. V., Electrokinetic Streaming-Current Methods to Probe the Electrode–Electrolyte Interface under Applied Potentials. *J. Phys. Chem. C.* **2019,** *123*, 19493-19505.

268. Avid, A.; Zenyuk, I. V., Confinement Effects for Nano-electrocatalysts for Oxygen Reduction Reaction. *Curr. Opin. Electrochem.* **2021,** *25*, 100634.

269. Gao, Y.; Huang, J.-T.; Liu, Y.-w.; Chen, S., Charge Transport in Confined Concentrated Solutions: A Minireview. *Curr. Opin. Electrochem.* **2019,** *13*, 107-111.

270. Secanell, M.; Karan, K.; Suleman, A.; Djilali, N., Multi-Variable Optimization of PEMFC Cathodes Using an Agglomerate Model. *Electrochim. Acta* **2007,** *52*, 6318-6337.

271. Sadeghi, E.; Putz, A.; Eikerling, M., Effects of Ionomer Coverage on Agglomerate Effectiveness in Catalyst Layers of Polymer Electrolyte Fuel Cells. *J. Solid State Electrochem.* **2013,** *18*, 1271-1279.

272. Epting, W. K.; Litster, S., Effects of an Agglomerate Size Distribution on the PEFC Agglomerate Model. *Int J Hydrogen Energ* **2012,** *37*, 8505-8511.

273. Sadeghi, E.; Putz, A.; Eikerling, M., Hierarchical Model of Reaction Rate Distributions and Effectiveness Factors in Catalyst Layers of Polymer Electrolyte Fuel Cells. *J. Electrochem. Soc.* **2013,** *160*, F1159-F1169.

274. Berlinger, S. A.; Dudenas, P. J.; Bird, A.; Chen, X. K.; Freychet, G.; McCloskey, B. D.; Kusoglu, A.; Weber, A. Z., Impact of Dispersion Solvent on lonomer Thin Films and Membranes. *ACS Appl. Polym. Mater.* **2020,** *2*, 5824-5834.

275. Hatzell, K. B.; Dixit, M. B.; Berlinger, S. A.; Weber, A. Z., Understanding Inks for Porous-electrode Formation. *J. Mater. Chem. A* **2017,** *5*, 20527-20533.

276. Mu, Y. T.; Weber, A. Z.; Gu, Z. L.; Tao, W. Q., Mesoscopic Modeling of Transport Resistances in a Polymer-Electrolyte Fuel-Cell Catalyst Layer: Analysis of Hydrogen Limiting Currents. *Appl. Energy* **2019,** *255*.

277. Jung, S.; Sabharwal, M.; Jarauta, A.; Wei, F.; Gingras, M.; Gostick, J.; Secanell, M., Estimation of Relative Transport Properties in Porous Transport Layers Using Pore-Scale and Pore-Network Simulations. *J. Electrochem. Soc.* **2021,** *168*.

278. Satjaritanun, P.; Cetinbas, F. C.; Hirano, S.; Zenyuk, I. V.; Ahluwalia, R. K.; Shimpalee, S., Hybrid Lattice Boltzmann Agglomeration Method for Modeling Transport Phenomena in Polymer Electrolyte Membrane Fuel Cells. *J. Electrochem. Soc.* **2021,** *168*.

279. Altaf, H.; Vorhauer, N.; Tsotsas, E.; Vidaković-Koch, T., Steady-State Water Drainage by Oxygen in Anodic Porous Transport Layer of Electrolyzers: A 2D Pore Network Study. *Processes* **2020,** *8*.

280. Lee, J. K.; Lee, C. H.; Bazylak, A., Pore Network Modelling to Enhance Liquid Water Transport through Porous Transport Layers for Polymer Electrolyte Membrane Electrolyzers. *J. Power Sources* **2019,** *437*.

281. Lee, J. K.; Bazylak, A., Optimizing Porous Transport Layer Design Parameters via Stochastic Pore Network Modelling: Reactant Transport and Interfacial Contact Considerations. *J. Electrochem. Soc.* **2020,** *167*.

282. Xiong, Q.; Baychev, T. G.; Jivkov, A. P., Review of Pore Network Modelling of Porous Media: Experimental Characterisations, Network Constructions and Applications to Reactive Transport. *J. Contam. Hydrol.* **2016,** *192*, 101-117.

283. Satjaritanun, P.; O'Brien, M.; Kulkarni, D.; Shimpalee, S.; Capuano, C.; Ayers, K. E.; Danilovic, N.; Parkinson, D. Y.; Zenyuk, I. V., Observation of Preferential Pathways for

Oxygen Removal through Porous Transport Layers of Polymer Electrolyte Water Electrolyzers. *iScience* **2020,** *23*, 101783.

284. Paliwal, S.; Panda, D.; Bhaskaran, S.; Vorhauer-Huget, N.; Tsotsas, E.; Surasani, V. K., Lattice Boltzmann Method to Study the Water-oxygen Distributions in Porous Transport Layer (PTL) of Polymer Electrolyte Membrane (PEM) Electrolyser. *Int J Hydrogen Energ* **2021,** *46*, 22747-22762.

285. Kamali, M. R.; Sundaresan, S.; Van den Akker, H. E. A.; Gillissen, J. J. J., A Multi-component Two-phase Lattice Boltzmann Method Applied to a 1-D Fischer–Tropsch Reactor. *Chem. Eng. J.* **2012,** *207-208*, 587-595.

286. Molaeimanesh, G. R.; Akbari, M. H., A Three-dimensional Pore-scale Model of the Cathode Electrode in Polymer-Electrolyte Membrane Fuel Cell by Lattice Boltzmann Method. *J. Power Sources* **2014,** *258*, 89-97.

287. Satjaritanun, P.; Hirano, S.; Zenyuk, I. V.; Weidner, J. W.; Tippayawong, N.; Shimpalee, S., Numerical Study of Electrochemical Kinetics and Mass Transport inside Nano-Structural Catalyst Layer of PEMFC Using Lattice Boltzmann Agglomeration Method. *J. Electrochem. Soc.* **2019,** *167*.

288. Raciti, D.; Mao, M.; Wang, C., Mass Transport Modelling for the Electroreduction of CO2 on Cu Nanowires. *Nanotechnology* **2018,** *29*, 044001.

289. Jeon, H. S.; Timoshenko, J.; Rettenmaier, C.; Herzog, A.; Yoon, A.; Chee, S. W.; Oener, S.; Hejral, U.; Haase, F. T.; Roldan Cuenya, B., Selectivity Control of Cu Nanocrystals in a Gas-Fed Flow Cell through CO2 Pulsed Electroreduction. *J Am Chem Soc* **2021,** *143*, 7578-7587.

290. Jännsch, Y.; Leung, J. J.; Hämmerle, M.; Magori, E.; Wiesner-Fleischer, K.; Simon, E.; Fleischer, M.; Moos, R., Pulsed Potential Electrochemical CO2 Reduction for Enhanced Stability and Catalyst Reactivation of Copper Electrodes. *Electrochem. Commun.* **2020,** *121*.

291. Tang, Z.; Nishiwaki, E.; Fritz, K. E.; Hanrath, T.; Suntivich, J., Cu(I) Reducibility Controls Ethylene vs Ethanol Selectivity on (100)-Textured Copper during Pulsed CO2 Reduction. *ACS Appl. Mater. Interfaces* **2021,** *13*, 14050-14055.

292. Gostick, J. T.; Fowler, M. W.; Ioannidis, M. A.; Pritzker, M. D.; Volfkovich, Y. M.; Sakars, A., Capillary Pressure and Hydrophilic Porosity in Gas Diffusion Layers for Polymer Electrolyte Fuel Cells. *J. Power Sources* **2006,** *156*, 375-387.

293. Li, M.; Idros, M. N.; Wu, Y.; Burdyny, T.; Garg, S.; Zhao, X. S.; Wang, G.; Rufford, T. E., The Role of Electrode Wettability in Electrochemical Reduction of Carbon Dioxide. *J. Mater. Chem. A* **2021**, 19369-19409.

294. Kulkarni, D.; Normile, S. J.; Connolly, L. G.; Zenyuk, I. V., Development of Low Temperature Fuel Cell Holders for Operando X-ray Micro and Nano Computed Tomography to Visualize Water Distribution. *J. Phys. Energy* **2020,** *2*.

295. Li, T.; Lees, E. W.; Goldman, M.; Salvatore, D. A.; Weekes, D. M.; Berlinguette, C. P., Electrolytic Conversion of Bicarbonate into CO in a Flow Cell. *Joule* **2019,** *3*, 1487-1497.

296. Huang, J. E.; Li, F.; Ozden, A.; Rasouli, A. S.; Garcia de Arquer, F. P.; Liu, S.; Zhang, S.; Luo, M.; Wang, X.; Lum, Y., et al., CO2 Electrolysis to Multicarbon Products in Strong Acid. *Science* **2021,** *372*, 1074-1078.

297. Abdin, Z.; Webb, C. J.; Gray, E. M., Modelling and Simulation of a Proton Exchange Membrane (PEM) Electrolyser Cell. *Int J Hydrogen Energ* **2015,** *40*, 13243-13257.

298. Weber, A. Z.; Balasubramanian, S.; Das, P. K., Proton Exchange Membrane Fuel Cells. *Adv. Chem. Eng.* **2012,** *41*, 65-143.

299. Weber, A. Z.; Delacourt, C., Mathematical Modelling of Cation Contamination in a Proton-exchange Membrane. *Fuel Cells* **2008,** *8*, 459-465.

300. Yang, Y.; Pintauro, P. N., Multicomponent Space-Charge Transport Model for Ion-exchange Membranes with Variable Pore Properties. *Ind. Eng. Chem. Res.* **2004,** *43*, 2957-2965.

301. Skyllas-Kazacos, M.; Goh, L., Modeling of Vanadium Ion Diffusion Across the Ion Exchange Membrane in the Vanadium Redox Battery. *J. Membrane Sci.* **2012,** *399-400*, 43-48.

302. Pintauro, P. N.; Bennion, D. N., Mass Transport of Electrolytes in Membranes. 1. Developoment of Mathematical Transport Model. *Ind. Eng. Chem. Fundam.* **1984,** *23*, 230-234.

303. Narebska, A.; Kujawski, W.; Koter, S., Irreversible Thermodynamics of Transport Across Charged Membranes. *J. Membrane Sci.* **1986,** *30*, 125-140.

304. Kamcev, J.; Sujanani, R.; Jang, E.-S.; Yan, N.; Moe, N.; Paul, D. R.; Freeman, B. D., Salt Concentration Dependence of Ionic Conductivity in Ion Exchange Membranes. *J. Membrane Sci.* **2018,** *547*, 123-133.

305. Kamcev, J.; Paul, D. R.; Manning, G. S.; Freeman, B. D., Accounting for Frame of Reference and Thermodynamic Non-idealities when Calculating Salt Diffusion Coefficients in Ion Exchange Membranes. *J. Membrane Sci.* **2017,** *537*, 396-406.

306. Kamcev, J.; Paul, D. R.; Freeman, B. D., Effect of Fixed Charge Group Concentration on Equilibrium Ion Sorption in Ion Exchange Membranes. *J. Mater. Chem. A* **2017,** *5*, 4638-4650.

307. Kamcev, J.; Doherty, C. M.; Lopez, K. P.; Hill, A. J.; Paul, D. R.; Freeman, B. D., Effect of Fixed Charge Group Concentration on Salt Permeability and Diffusion Coefficients in Ion Exchange Membranes. *J. Membrane Sci.* **2018,** *566*, 307-316.

308. Kamcev, J.; Paul, D. R.; Freeman, B. D., Equilibrium Ion Partitioning Between Aqueous Salt Solutions and Inhomogeneous Ion Exchange Membranes. *Desalination* **2018,** *446*, 31-41.

309. Kamcev, J.; Paul, D. R.; Manning, G. S.; Freeman, B. D., Ion Diffusion Coefficients in Ion Exchange Membranes: Significance of Counterion Condensation. *Macromolecules* **2018,** *51*, 5519-5529.

310. Geise, G. M.; Paul, D. R.; Freeman, B. D., Fundamental Water and Salt Transport Properties of Polymeric Materials. *Prog. Polym. Sci.* **2014,** *39*, 1-42.

311. Ashraf Gandomi, Y.; Aaron, D. S.; Mench, M. M., Influence of Membrane Equivalent Weight and Reinforcement on Ionic Species Crossover in All-Vanadium Redox Flow Batteries. *Membranes (Basel)* **2017,** *7*.

312. Park, H. B.; Kamcev, J.; Robeson, L. M.; Elimelech, M.; Freeman, B. D., Maximizing the Right Stuff: The Trade-off Between >Membrane Permeability and Selectivity. *Science* **2017,** *356*.

313. Kamcev, J.; Galizia, M.; Benedetti, F. M.; Jang, E. S.; Paul, D. R.; Freeman, B. D.; Manning, G. S., Partitioning of Mobile Ions Between Ion Exchange Polymers and Aqueous Salt Solutions: Importance of Counter-ion Condensation. *Phys Chem Chem Phys* **2016,** *18*, 6021-31.

314. Okada, T.; Satou, H.; Okuno, M.; Yuasa, M., Ion and Water Transport Characteristics of Perfluorosulfonated Ionomer Membranes with H+ and Alkali Metal Cations. *J. Phys. Chem. B* **2002,** *106*, 1267-1273.

315. Shafaque, H. W.; Lee, C. H.; Fahy, K. F.; Lee, J. K.; LaManna, J. M.; Baltic, E.; Hussey, D. S.; Jacobson, D. L.; Bazylak, A., Boosting Membrane Hydration for High Current Densities in Membrane Electrode Assembly CO2 Electrolysis. *ACS Appl. Mater. Interfaces* **2020,** *12*, 54585-54595.

316. Kutz, R. B.; Chen, Q.; Yang, H.; Sajjad, S. D.; Liu, Z.; Masel, I. R., Sustainion Imidazolium-Functionalized Polymers for Carbon Dioxide Electrolysis. *Energy Technol.* **2017,** *5*, 929-936.

317. O'Brien, C. P.; Miao, R. K.; Liu, S.; Xu, Y.; Lee, G.; Robb, A.; Huang, J. E.; Xie, K.; Bertens, K.; Gabardo, C. M., et al., Single Pass CO2 Conversion Exceeding 85% in the Electrosynthesis of Multicarbon Products via Local CO2 Regeneration. *ACS Energy Lett.* **2021,** *6*, 2952-2959.

318. Lees, E. W.; Mowbray, B. A. W.; Parlane, F. G.; Berlinguette, C. P., Gas Diffusion Electrodes and Membranes for CO2 Reduction Electrolysers. *Nat. Rev. Mater.* **2021**, 55-64.

319. Jeng, E.; Jiao, F., Investigation of CO2 Single-pass Conversion in a Flow Electrolyzer. *React. Chem. Eng.* **2020,** *5*, 1768-1775.

320. Gerhardt, M. R.; Pant, L. M.; Shiau, H. S.; Weber, A. Z., Modeling Water Management and Carbon-Dioxide Contamination Effects in Anion-Exchange Membrane Fuel Cells. *ECS Trans.* **2018,** *86*, 15-24.

321. Gerhardt, M. R.; Pant, L. M.; Weber, A. Z., Along-the-Channel Impacts of Water Management and Carbon-Dioxide Contamination in Hydroxide-Exchange-Membrane Fuel Cells: A Modeling Study. *J. Electrochem. Soc.* **2019,** *166*, F3180-F3192.

322. Siroma, Z.; Watanabe, S.; Yasuda, K.; Fukuta, K.; Yanagi, H., Mathematical Modeling of the Concentration Profile of Carbonate Ions in an Anion Exchange Membrane Fuel Cell. *ECS Trans.* **2010,** *33*, 1935-1943.

323. Blommaert, M. A.; Aili, D.; Tufa, R. A.; Li, Q.; Smith, W. A.; Vermaas, D. A., Insights and Challenges for Applying Bipolar Membranes in Advanced Electrochemical Energy Systems. *ACS Energy Lett* **2021,** *6*, 2539-2548.

324. Pătru, A.; Binninger, T.; Pribyl, B.; Schmidt, T. J., Design Principles of Bipolar Electrochemical Co-Electrolysis Cells for Efficient Reduction of Carbon Dioxide from Gas Phase at Low Temperature. *J. Electrochem. Soc.* **2019,** *166*, F34-F43.

325. Blommaert, M. A.; Sharifian, R.; Shah, N. U.; Nesbitt, N. T.; Smith, W. A.; Vermaas, D. A., Orientation of a Bipolar Membrane Determines the Dominant Ion and Carbonic Species Transport in Membrane Electrode Assemblies for CO2 Reduction. *J. Mater. Chem. A* **2021,** *9*, 11179-11186.

326. Mareev, S. A.; Evdochenko, E.; Wessling, M.; Kozaderova, O. A.; Niftaliev, S. I.; Pismenskaya, N. D.; Nikonenko, V. V., A Comprehensive Mathematical Model of Water Splitting in Bipolar Membranes: Impact of the Spatial Distribution of Fixed Charges and Catalyst at Bipolar Junction. *J. Membrane Sci.* **2020,** *603*.

327. Digdaya, I. A.; Sullivan, I.; Lin, M.; Han, L.; Cheng, W. H.; Atwater, H. A.; Xiang, C., A Direct Coupled Electrochemical System for Capture and Conversion of CO2 from Oceanwater. *Nat Commun* **2020,** *11*, 4412.

328. Volgin, V. M.; Davydov, A. D., Ionic Transport through Ion-Exchange and Bipolar Membranes. *J. Membrane Sci.* **2005,** *259*, 110-121.

329. Lin, M.; Digdaya, I. A.; Xiang, C., Modeling the Electrochemical Behavior and Interfacial Junction Profiles of Bipolar Membranes at Solar Flux Relevant Operating Current Densities. *Sust. Energy Fuels* **2021**.

330. Wrubel, J. A.; Chen, Y.; Ma, Z.; Deutsch, T. G., Modeling Water Electrolysis in Bipolar Membranes. *J. Electrochem. Soc.* **2020,** *167*.

331. Grew, K. N.; McClure, J. P.; Chu, D.; Kohl, P. A.; Ahlfield, J. M., Understanding Transport at the Acid-Alkaline Interface of Bipolar Membranes. *J. Electrochem. Soc.* **2016,** *163*, F1572-F1587.

332. Natarajan, D.; Van Nguyen, T., A Two-Dimensional, Two-Phase, Multicomponent, Transient Model for the Cathode of a Proton Exchange Membrane Fuel Cell Using Conventional Gas Distributors. *J. Electrochem. Soc.* **2001,** *148*, A1324.

333. Nguyen, T. V.; White, R. E., A Water and Heat Management Model for Proton-Exchange-Membrane Fuel Cells. *J. Electrochem. Soc.* **1993,** *140*, 2178-2186.

334. Sun, W.; Peppley, B. A.; Karan, K., An Improved Two-Dimensional Agglomerate Cathode Model to Study the Influence of Catalyst Layer Structural Parameters. *Electrochim. Acta* **2005,** *50*, 3359-3374.

335. Pant, L. M.; Gerhardt, M. R.; Macauley, N.; Mukundan, R.; Borup, R. L.; Weber, A. Z., Along-the-Channel Modeling and Analysis of PEFCs at Low Stoichiometry: Development of a 1+2D Model. *Electrochim. Acta* **2020,** *346*, 134963.

336. Weber, A. Z.; Newman, J., Coupled Thermal and Water Management in Polymer Electrolyte Fuel Cells. *J. Electrochem. Soc.* **2006,** *153*, A2205.

337. Yi, J. S.; Nguyen, T. V., An Along-the-Channel Model for Proton Exchange Membrane Fuel Cells. *J. Electrochem. Soc.* **1998,** *145*, 1149-1159.

338. Yi, J. S.; Van Nguyen, T., Multicomponent Transport in Porous Electrodes of Proton Exchange Membrane Fuel Cells Using the Interdigitated Gas Distributors. *J. Electrochem. Soc.* **1999,** *146*, 38-45.

339. Weber, A. Z.; Newman, J., Effects of Membrane- and Catalyst-layer-thickness Nonuniformities in Polymer-Electrolyte Fuel Cells. *J. Electrochem. Soc.* **2007,** *154*, B405-B412.

340. Natarajan, D.; Van Nguyen, T., Three-dimensional Effects of Liquid Water Flooding in the Cathode of a PEM Fuel Cell. *J. Power Sources* **2003,** *115*, 66-80.

341. Kulikovsky, A. A., Quasi Three–Dimensional Modelling of the PEM Fuel Cell: Comparison of the Catalyst Layers Performance. *Fuel Cells* **2001,** *1*, 162-169.

342. Nie, J.; Chen, Y.; Cohen, S.; Carter, B. D.; Boehm, R. F., Numerical and Experimental Study of Three-dimensional Fluid Flow in the Bipolar Plate of a PEM Electrolysis Cell. *Int. J. Thermal Sci.* **2009,** *48*, 1914-1922.

343. Nie, J.; Chen, Y., Numerical Modeling of Three-dimensional Two-phase Gas–liquid Flow in the Flow Field Plate of a PEM Electrolysis Cell. *Int J Hydrogen Energ* **2010,** *35*, 3183-3197.

344. Xuan, L.; Wang, Y.; Mei, D.; Lan, J., Design and Modelling of 3D Bionic Cathode Flow Field for Proton Exchange Membrane Fuel Cell. *Energies* **2021,** *14*.

345. Knudsen, E.; Albertus, P.; Cho, K. T.; Weber, A. Z.; Kojic, A., Flow simulation and analysis of high-power flow batteries. *J. Power Sources* **2015,** *299*, 617-628.

346. Oh, K.; Kang, T. J.; Park, S.; Tucker, M. C.; Weber, A. Z.; Ju, H., Effect of flow-field structure on discharging and charging behavior of hydrogen/bromine redox flow batteries. *Electrochim. Acta* **2017,** *230*, 160-173.

347. Medici, E. F.; Zenyuk, I. V.; Parkinson, D. Y.; Weber, A. Z.; Allen, J. S., Understanding Water Transport in Polymer Electrolyte Fuel Cells Using Coupled Continuum and Pore-Network Models. *Fuel Cells* **2016,** *16*, 725-733.

348. Xiao, H.; Cheng, T.; Goddard, W. A., 3rd; Sundararaman, R., Mechanistic Explanation of the pH Dependence and Onset Potentials for Hydrocarbon Products from Electrochemical Reduction of CO on Cu (111). *J Am Chem Soc* **2016,** *138*, 483-6.

349. Gauthier, J. A.; Dickens, C. F.; Ringe, S.; Chan, K., Practical Considerations for Continuum Models Applied to Surface Electrochemistry. *ChemPhysChem* **2019,** *20*, 3074-3080.

350. Gauthier, J. A.; Dickens, C. F.; Heenen, H. H.; Vijay, S.; Ringe, S.; Chan, K., Unified Approach to Implicit and Explicit Solvent Simulations of Electrochemical Reaction Energetics. *J. Chem. Theory Comput.* **2019,** *15*, 6895-6906.

351. Weitzner, S. E.; Akhade, S. A.; Varley, J. B.; Wood, B. C.; Otani, M.; Baker, S. E.; Duoss, E. B., Toward Engineering of Solution Microenvironments for the CO2 Reduction Reaction: Unraveling pH and Voltage Effects from a Combined Density-Functional-Continuum Theory. *J. Phys. Chem. Lett.* **2020,** *11*, 4113-4118.

352. Liu, J.; García-Salaberri, P. A.; Zenyuk, I. V., Bridging Scales to Model Reactive Diffusive Transport in Porous Media. *J. Electrochem. Soc.* **2020,** *167*.

353. Zenyuk, I. V.; Medici, E.; Allen, J.; Weber, A. Z., Coupling Continuum and Pore-network Models for Polymer-electrolyte Fuel Cells. *Int J Hydrogen Energ* **2015,** *40*, 16831-16845.

354. Chen, L.; Feng, Y.-L.; Song, C.-X.; Chen, L.; He, Y.-L.; Tao, W.-Q., Multi-scale Modeling of Proton Exchange Membrane Fuel Cell by Coupling Finite Volume Method and Lattice Boltzmann Method. *Int J Heat Mass Tran* **2013,** *63*, 268-283.

355. Becker, J.; Wieser, C.; Fell, S.; Steiner, K., A Multi-scale Approach to Material Modeling of Fuel Cell Diffusion Media. *Int J Heat Mass Tran* **2011,** *54*, 1360-1368.

356. Dinh, C.-T.; Burdyny, T.; Kibria, M. G.; Seifitokaldani, A.; Gabardo, C. M.; García de Arquer, F. P.; Kiani, A.; Edwards, J. P.; De Luna, P.; Bushuyev, O. S., et al., CO2 Electroreduction to Ethylene via Hydroxide-Mediated Copper Catalysis at an Abrupt Interface. *Science* **2018,** *360*, 783-787.

357. Choi, W.; Won, D. H.; Hwang, Y. J., Catalyst Design Strategies for Stable Electrochemical CO2 Reduction Reaction. *J. Mater. Chem. A* **2020,** *8*, 15341-15357.

358. Li, L.; Ozden, A.; Guo, S.; Garci, A. d. A. F. P.; Wang, C.; Zhang, M.; Zhang, J.; Jiang, H.; Wang, W.; Dong, H., et al., Stable, Active CO2 Reduction to Formate via Redox-Modulated Stabilization of Active Sites. *Nat Commun* **2021,** *12*, 5223.

359. Liu, Z.; Yang, H.; Kutz, R.; Masel, R. I., CO2 Electrolysis to CO and O2 at High Selectivity, Stability and Efficiency Using Sustainion Membranes. *J. Electrochem. Soc.* **2018,** *165*, J3371-J3377.

360. Yin, Z.; Peng, H.; Wei, X.; Zhou, H.; Gong, J.; Huai, M.; Xiao, L.; Wang, G.; Lu, J.; Zhuang, L., An Alkaline Polymer Electrolyte CO2 Electrolyzer Operated with Pure Water. *Energy Environ. Sci.* **2019,** *12*, 2455-2462.

361. Borup, R. L.; Kusoglu, A.; Neyerlin, K. C.; Mukundan, R.; Ahluwalia, R. K.; Cullen, D. A.; More, K. L.; Weber, A. Z.; Myers, D. J., Recent Developments in Catalyst-Related PEM Fuel Cell Durability. *Curr. Opin. Electrochem.* **2020,** *21*, 192-200.

362. Borup, R. L.; Meyers, J. P.; Pivovar, B. S.; Kim, Y. S.; Mukundan, R.; Garland, N.; Myers, D.; Wilson, M.; Garzon, F.; Wood, D., et al., Scientific Aspects of Polymer Electrolyte Fuel Cell Durability and Degradation. *Chem. Rev.* **2007,** *107*, 3904-3951.

363. Wang, Y.; Seo, B.; Wang, B.; Zamel, N.; Jiao, K.; Adroher, X. C., Fundamentals, Materials, and Machine Learning of Polymer Electrolyte Membrane Fuel Cell Technology. *Energy & AI* **2020,** *1*, 100014.

364. Fanourgakis, G. S.; Gkagkas, K.; Tylianakis, E.; Froudakis, G. E., A Universal Machine Learning Algorithm for Large-Scale Screening of Materials. *J. Am. Chem. Soc.* **2020,** *142*, 3814-3822.

365. Krishnamurthy, D.; Weiland, H.; Barati Farimani, A.; Antono, E.; Green, J.; Viswanathan, V., Machine Learning Based Approaches to Accelerate Energy Materials Discovery and Optimization. *ACS Energy Lett.* **2019,** *4*, 187-191.

366. Gu, G. H.; Noh, J.; Kim, I.; Jung, Y., Machine Learning for Renewable Energy Materials. *J. Mater. Chem. A* **2019,** *7*, 17096-17117.

367. Han, I.-S.; Chung, C.-B., Performance Prediction and Analysis of a PEM Fuel Cell Operating on Pure Oxygen using Data-driven Models: A Comparison of Artificial Neural Network and Support Vector Machine. *Int J Hydrogen Energ* **2016,** *41*, 10202-10211.

368. Huo, W.; Li, W.; Zhang, Z.; Sun, C.; Zhou, F.; Gong, G., Performance Prediction of Proton-Exchange Membrane Fuel Cell Based on Convolutional Neural Network and Random Forest Feature Selection. *Energy Convers. Manage.* **2021,** *243*, 114367.

369. Ma, R.; Yang, T.; Breaz, E.; Li, Z.; Briois, P.; Gao, F., Data-driven Proton Exchange Membrane Fuel Cell Degradation Predication Through Deep Learning Method. *Appl. Energy* **2018,** *231*, 102-115.

370. Zhu, Y.; Zabaras, N.; Koutsourelakis, P.-S.; Perdikaris, P., Physics-constrained Deep Learning for High-dimensional Surrogate Modeling and Uncertainty Quantification without Labeled Data. *J. Comp. Phys.* **2019,** *394*, 56-81.

371. Blau, S. M.; Patel, H. D.; Spotte-Smith, E. W. C.; Xie, X.; Dwaraknath, S.; Persson, K. A., A Chemically Consistent Graph Architecture for Massive Reaction Networks Applied to Solid-Electrolyte Interphase Formation. *Chem Sci* **2021,** *12*, 4931-4939.

372. Blau, S. M.; Spotte-Smith, E. W. C.; Wood, B.; Dwaraknath, S.; Persson, K. A., Accurate, Automated Density Functional Theory for Complex Molecules Using On-the-fly Error

Correction. *chemrxiv,* 2020-10-12, DOI: 10.26434/chemrxiv.13076030.v1 (accessed 2021-01-31).

373. Spotte-Smith, E. W. C.; Yu, P.; Blau, S. M.; Prasher, R. S.; Jain, A., Aqueous Diels-Alder Reactions for Thermochemical Storage and Heat Transfer Fluids Identified Using Density Functional Theory. *J. Comput. Chem.* **2020,** *41*, 2137-2150.

374. Blanco, D. E.; Lee, B.; Modestino, M. A., Optimizing Organic Electrosynthesis through Controlled Voltage Dosing and Artificial Intelligence. *Proc. Natl. Acad. Sci. U.S.A.* **2019,** *116*, 17683-17689.

375. Bendsoe, M. P.; Sigmund, O., *Topology Optimization: Theory, Methods, and Applications*. 2nd ed.; Springer: Berlin, Germany, 2002.

376. Liu, J.; Gaynor, A. T.; Chen, S.; Kang, Z.; Suresh, K.; Takezawa, A.; Li, L.; Kato, J.; Tang, J.; Wang, C. C. L., et al., Current and Future Trends in Topology Optimization for Additive Manufacturing. *Struct. Multidiscipl. Opt.* **2018,** *57*, 2457-2483.

377. Rosinha, I. P.; Gernaey, K. V.; Woodley, J. M.; Krühne, U., Topology Optimization for Biocatalytic Microreactor Configurations. In *12th International Symposium on Process Systems Engineering and 25th European Symposium on Computer Aided Process Engineering*, 2015; pp 1463-1468.

378. Sigmund, O.; Maute, K., Topology Optimization Approaches. *Struct. Multidiscipl. Opt.* **2013,** *48*, 1031-1055.

379. Mici, J.; Rothenberg, B.; Brisson, E.; Wicks, S.; Stubbs, D. M., Optomechanical Performance of 3D-printed Mirrors with Embedded Cooling Channels and Substructures. In *Optomechanical Engineering 2015*, 2015; p 957306.

380. Zhang, W.; Zhou, Y., Feature-Driven Optimization Method and Applications. In *The Feature-Driven Method for Structural Optimization*, Elsevier: 2021; pp 157-240.

381. Xie, Y. M.; Steven, G. P., A Simple Evolutionary Procedure for Structural Optimization. *Comput. Struct.* **1993,** *49*, 885-896.

382. Laguna, O. H.; Lietor, P. F.; Godino, F. J. I.; Corpas-Iglesias, F. A., A Review on Additive Manufacturing and Materials for Catalytic Applications: Milestones, Key Concepts, Advances and Perspectives. *Mater. Des.* **2021,** *208*.

383. Moran, B. D. Large Area Projection Micro Stereolithography. 2016.

384. Ambrosi, A.; Shi, R. R. S.; Webster, R. D., 3D-printing for Electrolytic Processes and Electrochemical Flow Systems. *J. Mater. Chem. A* **2020,** *8*, 21902-21929.

385. Bui, J. C.; Davis, J. T.; Esposito, D. V., 3D-Printed Electrodes for Membraneless Water Electrolysis. *Sust. Energy Fuels* **2020,** *4*, 213-225.

386. Hereijgers, J.; Schalck, J.; Lölsberg, J.; Wessling, M.; Breugelmans, T., Indirect 3D Printed Electrode Mixers. *ChemElectroChem* **2019,** *6*, 378-382.

387. Lolsberg, J.; Starck, O.; Stiefel, S.; Hereijgers, J.; Breugelmans, T.; Wessling, M., 3D-Printed Electrodes with Improved Mass Transport Properties. *Chemelectrochem* **2017**.

388. Mooraj, S.; Qi, Z.; Zhu, C.; Ren, J.; Peng, S.; Liu, L.; Zhang, S.; Feng, S.; Kong, F.; Liu, Y., et al., 3D Printing of Metal-based Materials for Renewable Energy Applications. *Nano Research* **2020**.

389. Vaněčková, E.; Bouša, M.; Shestivska, V.; Kubišta, J.; Moreno-García, P.; Broekmann, P.; Rahaman, M.; Zlámal, M.; Heyda, J.; Bernauer, M., et al., Electrochemical Reduction of Carbon Dioxide on 3D Printed Electrodes. *ChemElectroChem* **2021,** *8*, 2137-2149.

390. Xu, X.; Tan, Y. H.; Ding, J.; Guan, C., 3D Printing of Next-generation Electrochemical Energy Storage Devices: from Multiscale to Multimaterial. *Energy Environ. Mater.* **2021**.

391. Yang, G.; Yu, S.; Kang, Z.; Dohrmann, Y.; Bender, G.; Pivovar, B. S.; Green, J. B.; Retterer, S. T.; Cullen, D. A.; Zhang, F.-Y., A Novel PEMEC with 3D Printed Non-conductive Bipolar Plate for Low-cost Hydrogen Production from Water Electrolysis. *Energy Convers. Manage.* **2019,** *182*, 108-116.

392. Zhu, C.; Liu, T.; Qian, F.; Han, T. Y.; Duoss, E. B.; Kuntz, J. D.; Spadaccini, C. M.; Worsley, M. A.; Li, Y., Supercapacitors Based on Three-Dimensional Hierarchical Graphene Aerogels with Periodic Macropores. *Nano Lett.* **2016,** *16*, 3448-56.

393. Arenas, L. F.; Ponce de León, C.; Walsh, F. C., 3D-printed Porous Electrodes for Advanced Electrochemical Flow Reactors: A Ni/stainless Steel Electrode and Its Mass Transport Characteristics. *Electrochem. Commun.* **2017,** *77*, 133-137.

394. Beck, V. A.; Ivanovskaya, A. N.; Chandrasekaran, S.; Forien, J. B.; Baker, S. E.; Duoss, E. B.; Worsley, M. A., Inertially Enhanced Mass Transport Using 3D-printed Porous Flow-through Electrodes with Periodic Lattice Structures. *Proc. Natl. Acad. Sci. U.S.A.* **2021,** *118*.

395. Kou, T.; Wang, S.; Shi, R.; Zhang, T.; Chiovoloni, S.; Lu, J. Q.; Chen, W.; Worsley, M. A.; Wood, B. C.; Baker, S. E., et al., Periodic Porous 3D Electrodes Mitigate Gas Bubble Traffic during Alkaline Water Electrolysis at High Current Densities. *Adv. Energy Mater.* **2020,** *10*.

396. Dudukovic, N. A.; Fong, E. J.; Gemeda, H. B.; DeOtte, J. R.; Ceron, M. R.; Moran, B. D.; Davis, J. T.; Baker, S. E.; Duoss, E. B., Cellular Fluidics. *Nature* **2021,** *595*, 58-65.

397. Beck, V. A.; Wong, J. J.; Jekel, C. F.; Tortorelli, D. A.; Baker, S. E.; Duoss, E. B.; Worsley, M. A., Computational Design of Microarchitected Porous Electrodes for Redox Flow Batteries. *J. Power Sources* **2021,** *512*, 230453.

398. Chen, C.-H.; Yaji, K.; Yamasaki, S.; Tsushima, S.; Fujita, K., Computational Design of Flow Fields for Vanadium Redox Flow Batteries via Topology Optimization. *J. Energy Storage* **2019,** *26*.

399. Behrou, R.; Pizzolato, A.; Forner-Cuenca, A., Topology Optimization as a Powerful Tool to Design Advanced PEMFCs Flow Fields. *Int J Heat Mass Tran* **2019,** *135*, 72-92.

400. Roy, T.; Salazar de Troya, M. A.; Worsley, M. A.; Beck, V. A., Topology Optimization for the Design of Porous Electrodes. *arXiv,* 2021-11-23, DOI: arXiv:2111.12059v1, (accessed 2021-01-31).

401. Golmon, S.; Maute, K.; Dunn, M. L., A Design Optimization Methodology for Li+ Batteries. *J. Power Sources* **2014,** *253*, 239-250.

402. Panesar, A.; Abdi, M.; Hickman, D.; Ashcroft, I., Strategies for Functionally Graded Lattice Structures Derived Using Topology Optimisation for Additive Manufacturing. *Additive Manufacturing* **2018,** *19*, 81-94.

403. Takezawa, A.; Zhang, X.; Kato, M.; Kitamura, M., Method to Optimize an Additively-manufactured Functionally-graded Lattice Structure for Effective Liquid Cooling. *Additive Manufacturing* **2019,** *28*, 285-298.

404. Babu, V.; Varghese, G.; Joseph, T. V.; Chippar, P., Optimization of graded catalyst layer to enhance uniformity of current density and performance of high temperature-polymer electrolyte membrane fuel cell. *Int J Hydrogen Energ* **2022,** *47*, 4018-4032.

405. Xing, L.; Shi, W.; Su, H.; Xu, Q.; Das, P. K.; Mao, B.; Scott, K., Membrane electrode assemblies for PEM fuel cells: A review of functional graded design and optimization. *Energy* **2019,** *177*, 445-464.

For Table of Contents Only